Dissertation
submitted to the
Combined Faculties of the Natural Sciences and Mathematics
of the Ruperto-Carola-University of Heidelberg, Germany
for the degree of
Doctor of Natural Sciences

Put forward by
Miguel Ferreira Cao
Born in: Ourense, Galicia (Spain)
Oral examination: November 23rd, 2017

Control and characterisation of a Rydberg spin system to explore many-body physics

Referees: **Prof. Dr. Matthias Weidemüller**
Prof. Dr. Selim Jochim

Abstract:
This thesis explores the implementation of a spin-1/2 system to realise quantum simulation of Heisenberg XX and XXZ models. The spins are mapped onto two high-lying atomic levels, so-called Rydberg states, in an ultracold sample of ^{87}Rb and coupled by a microwave field. Efficient synthesis and control of the driving field has been introduced in the setup in order to probe the spin dynamics with NMR sequences. Two- and three-photon excitation schemes are implemented to prepare the Rydberg spins. In order to spatially resolve the Rydberg excitation dynamics, a new imaging technique is employed, which uses the depletion of absorption in presence of Rydberg atoms to detect their distribution in the atomic cloud, revealing the emergence of spatial order of the Rydberg excitations due to strong van der Waals interactions. To benchmark the validity of this platform, the coherence of the spin ensemble is measured by Ramsey techniques in the low-density regime, where the single-spin dynamics accurately describes the observations. Despite the black-body redistribution of Rydberg spins setting a limit for the T_2^* time of the spin system, the coherence is measured to persist over long timescales on the order of 130 µs. Thus, scaling up the density of spins, first signatures of dipolar many-body effects for $|nS\rangle - |nP\rangle$ (XX) and $|nS\rangle - |(n+1)S\rangle$ (XXZ) spin combinations have been observed.

Zusammenfassung:
Diese Arbeit beschreibt die Implementierung und Charakerisierung eines Spinsystems um einen Quantensimulator des Heisenberg XX und XXZ Hamiltonians zu realisieren. Die Spins werden auf zwei hoch gelegenen Atomniveaus abegbildet, diese sogenannten Rydberg Zustände werden in einem ultrakalten Gas von ^{87}Rb angeregt und mittels Mikrowellenstrahlung gekoppelt. Eine effiziente Synthese und Kontrolle des angelegten Feldes wurde in der Versuchsanordnung eingeführt um die Spindynamik mit NMR Sequencen zu proben. Zwei- oder Drei-Photon Anregungsschemata sind implementiert um die Rydberg-Spins zu preparieren. Um die Dynamik der Rydberg-Anregungung räumlich aufzulösen, wurde eine neue Abbildungsmethode angewendet, die die Verringerung der Absorption in Gegenwart von Rydberg-Atomen nutzt. Dies zeigte die Entstehung räumlicher Ordnung durch Vander-Waals-Wechselwirkungen. Um die Gültigkeit dieser Plattform zu überprüfen, wurde die Kohärenz des Spin-Ensembles mittels der Ramsey-Methode bei geringer Dichte gemessen, bei der die Einzelspindynamik genau die Beoabachtungen beschreibt. Abgesehen von der Schwarzkörper-Umverteilung der Rydberg-Spins, die eine Grenze für die T_2^* Zeit des Spin-Systems setzt, besteht die Kohärenz über lange Zeitskalen von etwa 130 µs. Durch ein Hochskalieren der Spindichte konnten erste Signaturen von dipolaren Vielkörpereffekten für $|nS\rangle - |nP\rangle$ (XX) und $|nS\rangle - |(n+1)S\rangle$ (XXZ) Spinkombinationen beobachtet werden.

This thesis is based on the following manuscripts and publications:

- **Interaction-Enhanced Imaging of Rydberg P states**
  V. Gavryusev, M. Ferreira-Cao, A. Kekić, G. Zürn and A. Signoles
  Eur. Phys. J. ST **225**, 15 (2016)

- **Density matrix reconstruction of three-level atoms via Rydberg electromagnetically induced transparency**
  V. Gavryusev, A. Signoles, M. Ferreira-Cao, G. Zürn, C. S. Hofmann, G. Günter, H. Schempp, M. Robert-de-Saint-Vincent, S. Whitlock and M. Weidemüller
  J. Phys. B **49**, 16 (2016)

Contents

Chapter 1

Introduction

Simulating the evolution of many-body quantum mechanical problems has been demonstrated to be a titanic task with classical numerical methods due to the large amount of memory required to store information about large physical systems, which increases exponentially with the amount of particles. To solve this problem, Feynman envisaged to implement so-called "quantum computers" [Feynman, 1982], devices based on quantum elements that would potentially allow to process a huge amount of information in a limited physical resource. Such strategy stimulated the development of two different types of controllable quantum platforms which are able to mimic the behaviour of other quantum systems: digital quantum simulators and analog quantum simulators [Buluta and Nori, 2009; Hauke *et al.*, 2012; Georgescu *et al.*, 2014]. The first type is based on the implementation of universal quantum gates which may compose any arbitrary operation on a quantum state [Lloyd, 1996], constituting then suitable platforms for quantum information processing [García-Ripoll *et al.*, 2005]. On the other hand, analog quantum simulators leverage the idea of emulating the quantum behaviour of a system by mapping the Hamiltonian which governs its evolution onto another well-controlled quantum platform [Somaroo *et al.*, 1999].

One of the most successful approaches to quantum simulations relies on the use of cold quantum matter. The development of laser cooling and trapping techniques [Wineland *et al.*, 1978; Ashkin, 1978; Raab *et al.*, 1987; Lett *et al.*, 1988] enabled the exploration of physics at ultra-low temperatures, where the many-body dynamics is dominated by the quantum nature of constituent. This was demonstrated by the first realisation of degenerate Bose-Einstein [Bradley *et al.*, 1995; Anderson *et al.*, 1995; Davis *et al.*, 1995] and Fermi gases [DeMarco and Jin, 1999]. Thereafter, ultracold quantum matter has been broadly used to study quantum properties of condensed-matter systems which are otherwise hard to access at the microscopic level, e.g. the

Bose- and Fermi-Hubbard models for high-T_c superconductivity and superfluidity, proposed [Jaksch *et al.*, 1998; Hofstetter *et al.*, 2002] and explored [Greiner *et al.*, 2002; Köhl *et al.*, 2005] with ultracold atoms in optical lattices and exchange amongst lattice sites. Such achievements allowed to explore the superfluid to Mott-insulator phase transition [Greiner *et al.*, 2002] or the BEC-BCS crossover [Greiner *et al.*, 2003; Bartenstein *et al.*, 2004] and are good candidates to explain superfluidy behaviour and high-T_c superconductivity in other materials. Thus, they constitute the basis for analog quantum simulations of complex condensed-matter systems in the many-body regime [Bloch *et al.*, 2008; Bloch *et al.*, 2012].

In order to simulate quantum magnetism with cold matter, the spin-spin interactions must be emulated. Neutral atoms trapped in optical lattices have been employed as a platform to simulate the transverse Ising model, where the spin-spin interactions can be emulated through a combination of on-site interactions and tunneling amongst the lattice sites [Simon *et al.*, 2011; Struck *et al.*, 2011]. Here, the pseudo-spin is mapped on the occupation number of each lattice site. Apart from the enormous contributions of cold trapped ions in the development of quantum computing [Kielpinski *et al.*, 2002; Debnath *et al.*, 2016], they have been proposed as an alternative route for quantum simulation due to the versatility of the Coulomb interaction, capable to engineer a large variety of Hamiltonians [Barreiro *et al.*, 2011; Blatt and Roos, 2012]. One of the most outstanding features of such system is the formation of the so-called Coulomb crystal due to the strong Coulomb repulsion between the ions. This has been employed to implement Ising-type models with tunable long-range interaction [Britton *et al.*, 2012], recently demonstrating entanglement of hundreds of spins [Bohnet *et al.*, 2016].

Another magnetic spin system which stimulates interest since long time is the Heisenberg model of magnetism [Heisenberg, 1928], which describes the properties and phases of coupled magnetic dipoles as spin-spin interactions amongst particles in a lattice. However, only the evolution of the one-dimensional chain is exactly solvable by means of the Bethe-Ansatz in one spatial dimension [Bethe, 1931; Yang and Yang, 1966], whereas different spin configurations require complex approximated methods. A generalisation of the Heisenberg model is the quantum Heisenberg XXZ Hamiltonian, which can be simulated using dipolar-interacting polar molecules or Rydberg atoms and is expected to show rich far-from-equilibrium dynamics and correlations [Hazzard *et al.*, 2013; Hazzard *et al.*, 2014a; Hazzard *et al.*, 2014b]. By mapping the spin-1/2 system onto two rotational states, a dipolar-interacting spin-exchange XX Hamiltonian has been mimicked in a two-dimensional lattice [Yan *et al.*, 2013], where the dipole-dipole interactions present $\propto 1/R^3$ scaling. Nevertheless,

the cooling process of two species and generation and control of polar molecules in a lattice is technically very demanding and the Hamiltonians are difficult to tune [Moses *et al.*, 2015].

In this thesis, I realise a versatile spin-1/2 platform for analog quantum simulation of Heisenberg-type many-body Hamiltonians with Rydberg atoms. Such atoms excited to highly-lying electronic states are ideal to explore many-body physics of interacting spins, as they offer long-range electric dipole-dipole interactions, either attractive or repulsive, with strength much higher than any of the previously discussed systems. This is a consequence of their large dipole moments [Gallagher, 1994; Saffman *et al.*, 2010]. The strength and long-range character of such interactions can be vastly tuned by the appropriate selection of quantum states and by externally applied fields. Interaction effects can be strong enough during the Rydberg atom preparation to compete with the laser coupling strength, leading to the Rydberg blockade (dipolar or van der Waals) of the excitation [Comparat and Pillet, 2010; Löw *et al.*, 2012], which generates strongly correlated many-body states. Since only one Rydberg atom can be excited within a certain critical distance, spatial order may emerge from the preparation of Rydberg spins. Evidences of this phenomenon have been observed [Heidemann *et al.*, 2007; Gaëtan *et al.*, 2009; Urban *et al.*, 2009; Dudin *et al.*, 2012; Barredo *et al.*, 2014], resulting in suppression of the excitation dynamics [Singer *et al.*, 2004; Tong *et al.*, 2004; Vogt *et al.*, 2006; Vogt *et al.*, 2007] or the sub-Poissonian counting statistics [Reinhard *et al.*, 2008; Viteau *et al.*, 2012; Hofmann *et al.*, 2013]. The effect can be leveraged to implement quantum information protocols and to create universal quantum gates [Jaksch *et al.*, 2000; Isenhower *et al.*, 2010; Saffman *et al.*, 2010; Saffman, 2016].

Such ground-Rydberg system has been mapped onto an Ising-type model with $|\downarrow\rangle$ as the ground state and $|\uparrow\rangle$ as the Rydberg level in the frozen gas regime [Robicheaux and Hernández, 2005; Weimer *et al.*, 2008; Schachenmayer *et al.*, 2010; Lesanovsky, 2011], revealing signatures of crystalline structure [Schwarzkopf *et al.*, 2011; Schauß *et al.*, 2012].

I focus on mapping the spin-1/2 system onto two different levels within the Rydberg manifold [Ryabtsev *et al.*, 2005; Carter and Martin, 2013; Hermann-Avigliano *et al.*, 2014]. Here, spins with different angular momenta (e.g. $|nS\rangle$ and $|nP\rangle$ present direct dipole-exchange $\propto 1/R^3$ coupling [Afrousheh *et al.*, 2004; Afrousheh *et al.*, 2006a] which allows to map a long-range XX model [Bettelli *et al.*, 2013], whereas two spins on states with identical angular momenta (e.g. $|nS\rangle$ and $|n'S\rangle$) give access to the Heisenberg XXZ with both spin-exchange and Ising $\propto 1/R^6$ terms [van Bijnen and Pohl, 2015; Whitlock *et al.*, 2017]. To benchmark the validity

of this flexible platform, the coherence of the system is observed in the low density regime, where interaction effects are negligible and a single spin model can be used as a reference. The coherence time of the quantum simulation platform is measured to persist over sufficiently large timescales to explore interaction-induced dynamics, which is characterised by means of Ramsey [Ramsey, 1990] and NMR [Ernst, 1992] techniques. Scaling up the number of spins leads to our first evidences of many-body effects on the XX and XXZ Heisenberg dynamics. Alternative platforms with few Rydberg-spins located in two-dimensional trap arrays currently investigate the few body aspects of the described spin-exchange XX [Barredo *et al.*, 2015] and Ising [Labuhn *et al.*, 2016] models.

To spatially resolve the excitation dynamics of Rydberg atoms and characterise their preparation, I developed an imaging technique that allows to measure the distribution of Rydberg spins despite their lack of interaction with the imaging optical field. In this scheme, one can spatially resolve the depletion of absorptive atoms in presence of pre-excited spins and thus quantify the local number of spins in different regions of the atomic cloud. With this technique, I observe the saturation of the excitation dynamics due to van der Waals interactions, which reveals the emergence of long-range order of the spins.

Outline

This work is structured in several chapters which comprise the key aspects of my research. Chapter 2.1 reviews the extreme properties of Rydberg atoms and the types of interactions arising between them, followed by a brief description of the experimental apparatus (Section 2.4) and the implementation of refined microwave control of Rydberg-Rydberg transitions for state-tomography experiments (Sec. 2.5). Then, Ch. 3 offers a detailed analysis of three different excitation schemes and of the detection methods that allow to create and probe the Rydberg spin system. In particular, a detailed study of the spatial population distribution excited by two-photon (either resonant or off-resonant from intermediate levels) schemes addressing nS-states is presented and a three-photon off-resonant excitation scheme of nP-states is introduced. In Ch. 4, the platform to study Rydberg spin-spin interactions and the main features which describe its dynamics are discussed, demonstrating an excellent coherence and control of the quantum state in the non-interacting regime. Then, our first investigations of many-body effects on XX and XXZ models are presented in Ch. 5. Finally, Ch. 6 discusses the latest developments on an advanced imaging technique called Interaction-Enhanced Imaging, that can potentially resolve the temporal evolution and spatial correlations of few or even single Rydberg spins.

Chapter 2

Ultracold Rydberg atomic gases: properties and experimental manipulation

The study of the emission spectra of highly-excited, so-called Rydberg, atoms has triggered great progress in the understanding of quantum mechanics (see [Gallagher, 1994; Stebbings and Dunning, 1983; Pillet and Gallagher, 2016]). The development of laser-cooling and consequently of the field of ultracold atomic gases, in combination with the extreme properties of Rydberg atoms, allowed to extend the research on Rydberg atoms to a broad range of topics [Löw *et al.*, 2012]: few- and many-body physics [Choi *et al.*, 2006; Comparat and Pillet, 2010; Hofmann *et al.*, 2014], quantum non-linear optics [Pritchard *et al.*, 2013; Firstenberg *et al.*, 2016; Murray and Pohl, 2016; Busche *et al.*, 2017], quantum simulation [Weimer *et al.*, 2008; Weimer *et al.*, 2010; Müller *et al.*, 2012; Labuhn *et al.*, 2016] and quantum computing [Saffman *et al.*, 2010; Saffman, 2016], strongly correlated plasmas [Killian *et al.*, 2007; Pohl *et al.*, 2011; Robert-de Saint-Vincent *et al.*, 2013] and ultracold chemistry [Bendkowsky *et al.*, 2009; Gaj *et al.*, 2014; Schlagmüller *et al.*, 2016]. The large separation between the Rydberg electron and its atomic core results in exaggerated dipole-dipole or van der Waals interactions, which can be several orders of magnitude larger than any other energy scale in ultracold Rydberg gases, rendering the system dominated by the quantum nature of such phenomena.

Here, some of the basic properties of Rydberg atoms are reviewed (Sec. 2.1). In particular, the nature of different types of interactions and the mapping onto spin Hamiltonians is presented (Sec. (2.2-2.3)). Then, the general experimental set-up (Sec. 2.4) and the microwave control of Rydberg-Rydberg transitions introduced in

the course of this thesis (Sec. 2.5) are discussed in detail.

2.1 Alkali Rydberg atoms: general properties

Rydberg atoms are atoms with at least one electron lying in a highly-excited atomic state. In such states, the electron experiences a $1/r$-potential as a consequence of the weak electronic bound, which renders the Rydberg atoms similar to hydrogen atoms. The behaviour of Rydberg atoms has been studied since the late 19th century, when Balmer described the spectral lines of hydrogen [Balmer, 1885], previously observed by Ångström [Angström, 1855]. The generalisation to other elements, realised by Rydberg [Rydberg, 1890], in combination with the theoretical framework provided by the Bohr model [Bohr, 1913], allowed to descriion of the hydrogen spectra and their binding energy.

The experiments presented in this thesis are performed with Rydberg states of Rubidium. As other alkali atoms, it has a single valence electron, which is excited to a Rydberg state and thus it is on average far away from the core. The other $Z-1$ electrons fill the low-lying electronic shells close to the core, reducing the physical description of the core potential to that of a single positive charge. For this reason, the wave functions of alkali atoms resemble those of the hydrogen atom. Nevertheless, the valence electron of alkali atoms can penetrate the low-lying shells and suffer from the effect of inner charges, leading to deviations of the real core potential to that of a single positive charge, which are relevant when the valence electron is in states with low angular momentum $\ell \leq 3$. Such effect results mainly in a phase shift of the wave function and a higher eigen-energies than those of hydrogen atom. This is quantified by means of quantum defect theory [Seaton, 1983], resulting in a generalisation of the Rydberg formula for the binding energy, as

$$E_n = -hc\frac{R_{Rb}}{(n-\delta_{n,\ell,j})^2} = -hc\frac{R_{Rb}}{(n^*)^2}\,. \tag{2.1}$$

Here, the Rydberg constant $R_\infty = \frac{m_e e^4}{8c\varepsilon_0^2 h^3}$ [Mohr *et al.*, 2016] is scaled by the effective mass of ^{87}Rb and, therefore, it is substituted by the effective Rydberg constant $R_{Rb} = \frac{R_\infty}{1+m_e/m_{Rb}} = 109736.62\,\mathrm{cm}^{-1}$. The hydrogenic quantum number n is replaced by an effective principal quantum number $n^* = n - \delta_{n,\ell,j}$ is an effective principal quantum number for the state $|n,l,j\rangle$. As a consequence of the significant quantum defect $\delta_{n,\ell,j}$ for $|nS\rangle$, $|nP\rangle$ and $|nD\rangle$ states, they are non-degenerate and thus spectroscopically distinguishable. For $\ell > 3$ the quantum defect $\delta_{n,l,j} \approx 0$, resulting in degenerate hydrogenic energy levels. The quantum defect of rubidium Rydberg

Property	Notation	(n^*)-scaling
Orbital radius	r	$(n^*)^2$
Electron binding energy	E_n	$(n^*)^{-2}$
Level spacing	$E_{n+1} - E_n$	$(n^*)^{-3}$
Ionisation field	$\mathcal{E}^{(\infty)}$	$(n^*)^{-4}$
Radiative lifetime	τ_0	$(n^*)^3$
Black-body lifetime	τ_{bb}	$(n^*)^2$
Polarizability	α	$(n^*)^7$
Rydberg transition dipole moment	$\langle nl \vert er \vert n(l+1)\rangle$	$(n^*)^2$
Excitation transition dipole moment	$\langle 5P \vert er \vert nl\rangle$	$(n^*)^{-3/2}$
Dipolar interaction strength	C_3	$(n^*)^4$
vdW interaction strength	C_6	$(n^*)^{11}$

Table 2.1: Scaling laws for Rydberg atom properties. Selected poperties of Rydberg atoms and their scalings with the effective principal quantum number $n^* = n - \delta_{n,l,j}$.

atoms has been studied spectroscopically [Li *et al.*, 2003; Han *et al.*, 2006]. It can be described by the Rydberg-Ritz formula $\delta_{n,\ell,j} = \delta_0 + \delta_2/(n-\delta_0)^2$ [Jastrow, 1948], with the following measured values

$$\delta_0 = 3.1311804 \qquad \text{and} \qquad \delta_2 = 0.1784 \tag{2.2}$$

for $|nS_{1/2}\rangle$ states and

$$\delta_0 = 2.6416737 \qquad \text{and} \qquad \delta_2 = 0.2950 \tag{2.3}$$

for $|nP_{3/2}\rangle$, broadly used in the course of this thesis.

As the physical properties of hydrogen Rydberg atoms still apply to alkali atoms with an effective principal quantum number n^* instead of n, some important properties widely used in this work and their scaling with n^* are given in Table 2.1 (see [Gallagher, 1994]), which can be used to infer the optimal range of n^* for a certain experiment. The orbital radius of the electron scales with $(n^*)^2$, leading to extremely large electronic wave functions for high n^* and thus, effective diameters of up to few µm. The scaling of the dipole matrix element preserves the same scaling than the orbital radius because it corresponds to the wave function overlap between the neighbouring states, which must increase with the same ratio than the individual wave functions. A direct consequence of this is the quadratic increase of Rabi frequency with n^* for Rydberg-Rydberg transitions.

Spontaneous and stimulated Rydberg atom decay

The lifetime of Rydberg states is an important quantity to account for in order to encode a spin-1/2 system onto Rydberg states. The spontaneous decay determines the loss of Rydberg atoms, whereas the stimulated black-body decay induces a redistribution within the Rydberg manifold.

The different decay terms can be quantified from the model developed by Gallager and Cooke [Gallagher and Cooke, 1979], where the individual transition rates are given by the Einstein A-coefficients of each transition. Thus, the global spontaneous decay rate is calculated as

$$\frac{1}{\tau_0} = \Gamma_0 = \sum_{i>f} A_{i\to f} = \sum_{i>f} \frac{4\omega_{if}^3}{3c^3} \frac{l_{max}}{2l+1} \mathcal{R}_{i\to f}^2 \,, \tag{2.4}$$

where $\mathcal{R}_{i\to f}$ is the transition matrix element from i to f states (see Appendix B) and ω_{if} is the frequency spacing of the transition. The radiative decay scales with the probability of the Rydberg electron to be close to the nucleus, since the overlap to the low-lying states is highest there.

Accounting for the Planck distribution of black-body photons for each transition $\bar{n}_{\omega_{if}} = \frac{1}{e^{\omega_{if}/k_B T}-1}$, the total black-body decay rate is expressed as

$$\frac{1}{\tau_{bb}} = \Gamma_{bb} = \sum_f A_{i\to f} \bar{n}_{\omega_{if}}. \tag{2.5}$$

Thus, the total lifetime of the Rydberg states consists of the contributions of spontaneous decay and stimulated black-body decay, resulting in the global rate

$$\frac{1}{\tau} = \Gamma_0 + \Gamma_{bb}. \tag{2.6}$$

The black-body redistribution is caused by the low transition frequencies amongst high-lying neighbouring states of the Rydberg manifold, which overlap with the black-body spectrum at typical room temperatures. Additionally, the large transition matrix elements between neighbouring Rydberg states enhances the coupling. The global scaling can be understood with the simple model $\Gamma_{bb} = \frac{4\alpha^3 k_B T}{3\hbar (n^*)^2}$. Precise calculations for $|nS\rangle$, $|nP\rangle$ and $|nD\rangle$ states may be consulted in [Beterov *et al.*, 2009]. In Figure 2.1, the resulting rates for the state $|48S_{1/2}\rangle$ are presented, which are relevant for experiments in Ch. (4-5).

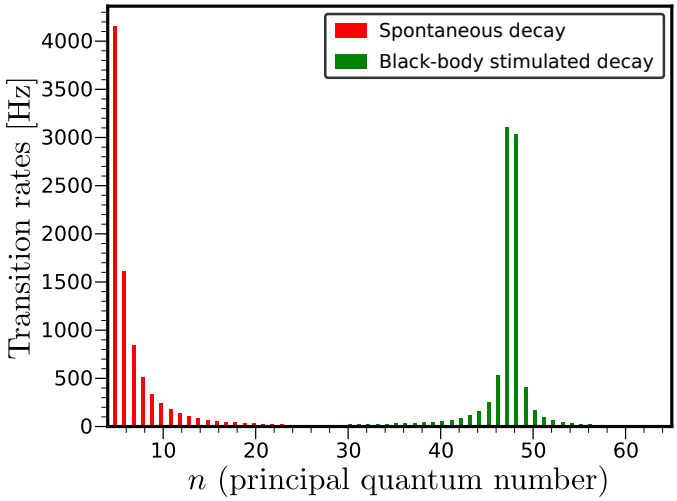

Figure 2.1: Transition rates of the $|48S_{1/2}\rangle$ state to other states. Radiative spontaneous decay (red) causes loss of population to the ground and close-by states. Stimulated emission due to black-body radiation at $T = 300\,\mathrm{K}$ (green) transfers some population to nearby Rydberg $|nP\rangle$ states. Calculations based on ARC [Sibalić *et al.*, 2017].

2.2 Rydberg-Rydberg interactions

Interactions amongst Rydberg atoms are well-described as the effect of the multipole expansion of the electric interaction between different atoms. Such interactions arise thanks to the huge transition dipole moments of Rydberg atoms. Here, a simple description of the origin of Rydberg-Rydberg interactions is reviewed and the quantum-mechanical mapping between the interaction matrix and the Heisenberg XX and XXZ Hamiltonians is summarised.

The main interaction mechanism is dipole-dipole interactions: a temporary fluctuation in the electronic distribution of one atom creates a dipole moment which subsequently induces a dipole moment in a neighbour atom, allowing for interactions to arise. Considering the two dipoles $\vec{\mu}_1$ and $\vec{\mu}_2$ separated by a distance $\vec{R}$, the classical dipole-dipole interaction is expressed as

$$H_{dd} = \frac{\vec{\mu_1} \cdot \vec{\mu_2}}{|\vec{R}|^3} - 3\frac{(\hat{R} \cdot \vec{\mu_1})(\hat{R} \cdot \vec{\mu_2})}{|\vec{R}|^3} \tag{2.7}$$

which can be developed in a series of angular dependent terms as detailed in [Reinhard *et al.*, 2007; Paris-Mandoki *et al.*, 2016].

2.2.1 Two-atom dipolar coupling

In the quantum mechanics the dipoles are described by dipole operators $\hat{\mu} = e\hat{r}$ with matrix elements $\mu = \langle\psi|\hat{\mu}|\psi'\rangle$. A detailed composition of the dipole operators can be consulted in Appendix B, including the effect of the angular distribution, which is neglected here for simplicity. Thus, the interaction energy V_{dd} for two atoms in the states $|\psi_1\rangle$ and $|\psi_2\rangle$ is build up as a combination of several terms such that

$$H^{dd}(R) \propto \frac{1}{R^3} \sum_{|\psi_1'\rangle,|\psi_2'\rangle} \langle\psi_1|\mu_1|\psi_1'\rangle \, \langle\psi_2|\mu_2|\psi_2'\rangle = \sum_{|\psi_1',\psi_2'\rangle} \langle\psi_1,\psi_2|\frac{\hat{\mu}_1 \, \hat{\mu}_2}{R^3}|\psi_1',\psi_2'\rangle \ , \quad (2.8)$$

accounting for the coupling to all possible states $|\psi_1'\rangle$ and $|\psi_2'\rangle$ that contribute to the interaction. Typically this is restricted to close-by states which present the strongest contribution. For example, considering the interaction between the states $|n_1S\rangle$ and $|n_2S\rangle$ as depicted in Figure 2.2, the strongest coupled states are $|n_1'P\rangle$ and $|n_2'P\rangle$.

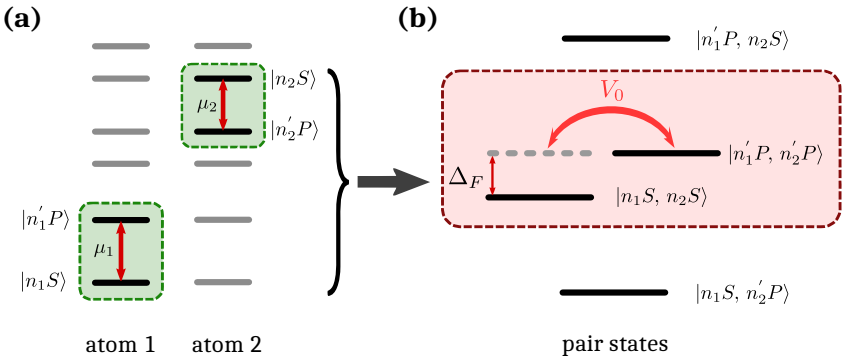

Figure 2.2: Illustration of strong Rydberg-Rydberg interactions. (a) Schematic of the bare states of two atoms. Interaction between $|n_1S\rangle$ and $|n_2S\rangle$ emerges due to coupling to their closest pair states $|n_1'P\rangle$ and $|n_2'P\rangle$, which constitute the main contribution to the interaction between the first pair. **(b)** Representation of the main interaction channels in the pair state basis. The coupling strength V_0 is determined by μ_1 and μ_2 and by the Förster defect Δ_F, which accounts for the the energy difference between coupled pairs. Taken from [Günter, 2014].

In order to calculate the interaction between two states, the pair state basis provides a more suitable description (Eq. (2.8)). The pair $|n_1S, n_2S\rangle$ is coupled to $|n_1'P, n_2'P\rangle$, as represented in Fig. 2.2(b). The complete Hamiltonian $\mathcal{H} = \mathcal{H}_1 \otimes \mathbf{1} + \mathbf{1} \otimes \mathcal{H}_2 + \mathcal{H}_{dd}$ describes the global system, which can be expressed as

$$\mathcal{H} = \begin{pmatrix} 0 & V_0/R^3 \\ V_0/R^3 & \Delta_F \end{pmatrix} , \quad (2.9)$$

with $V_0/R^3 = \langle n_1S,\, n_2S|\mathcal{H}_{dd}|n_1'P,\, n_2'P\rangle$ representing the strength of the dipole-dipole coupling and $\Delta_F = [E(|n_1'P\rangle) + E(|n_2'P\rangle)] - [E(|n_1S\rangle) + E(|n_2S\rangle)]$ is the so-called Förster defect which provides the energy difference between pairs. The eigenvalues of the coupled pair states deliver the energies of the coupled atoms

$$E_\pm = \frac{1}{2}\left(\Delta_F \pm \sqrt{\Delta_F^2 + 4(V_0/R^3)^2}\right). \tag{2.10}$$

As a function of the inter-atomic separation R and on the Förster defect Δ_F, two interaction regimes are possible:

- **resonant dipole-dipole interaction** ($V_0/R^3 \gg \Delta_F$): for small distances or when Δ_F is tuned to zero (e.g.: through the application of electric fields to reach a so-called Förster resonance [Gallagher *et al.*, 1982; Anderson *et al.*, 1998; Mourachko *et al.*, 1998]), the dipole-dipole coupling dominates, reducing the energy shift to

  $$E_\pm = \pm\frac{\mu_1\,\mu_2}{R^3} := \pm\frac{C_3}{R^3}. \tag{2.11}$$

  In this regime, the Rydberg atoms exhibit resonant dipole-dipole interactions with strength $C_3 = \mu_1\mu_2 \propto (n^*)^4$. A special case occurs when the two initial states are directly coupled to each other, e.g. a nearby $|nS, n'P\rangle$ pair. Then, the coupling dominantly produces exchange symmetric coupling to $|n'P, nS\rangle$ and the $1/R^3$ scaling is preserved at any distance.

- **van der Waals interaction** ($V_0/R^3 \ll \Delta_F$): for sufficiently large inter-atomic distance the perturbative expansion of the eigenenergies leads to

  $$E_+ \simeq \Delta_F + \frac{V_0^2/\Delta_F}{R^6} \quad \text{and} \quad E_- \simeq -\frac{V_0^2/\Delta_F}{R^6} := -\frac{C_6}{R^6}. \tag{2.12}$$

  In this van der Waals regime, the scaling of the Förster defect with the level spacing $\Delta_F \propto (n^*)^{-3}$ naturally leads to a strong scaling of the van der Waals coefficient $C_6 = C_3^2/\Delta_F \propto (n^*)^{4\times 2/(-3)} \propto (n^*)^{11}$. The sign of the interaction is determined by the Förster defect: $C_6 < 0$ corresponds to positive level shifts and repulsive interactions.

At an interaction energy close to the energy of the Förster defect, a transition between the two regimes takes place, resulting in a crossover distance $R_{cross} = \sqrt[6]{|C_6|/\Delta_F} \propto (n^*)^{7/3}$ [Walker and Saffman, 2008]. Whereas the $\propto 1/R^3$ regime is inherently long-range, the dynamics of a van der Waals dominated $\propto 1/R^6$ system is dominated by nearest neighbour interactions.

2.2.2 Mapping of Rydberg-Rydberg interactions onto spin Hamiltonians

Heisenberg XX Hamiltonian

We consider the case of two different Rydberg states that are directly coupled by a resonant dipole-dipole interaction term, e.g, $|nS\rangle$ and $|nP\rangle$. Since the interaction matrix (Eq. (2.9)) presents an off-diagonal form, the interaction can be mapped onto an exchange between two spin states. In terms of the spin operators $\hat{S}^{(x,y,z)} = \frac{\hbar}{2}\hat{\sigma}^{(x,y,z)}$, the interaction between two Rydberg spins in the states $|\downarrow\rangle = |nS\rangle$ and $|\uparrow\rangle = |nP\rangle$ can be expressed as the exchange Hamiltonian

$$\mathcal{H}_{int} = \frac{1}{2}\frac{C_3(\theta)}{R^3_{\downarrow\uparrow}}\left(\hat{S}^+_\downarrow \hat{S}^-_\uparrow + \hat{S}^-_\downarrow \hat{S}^+_\uparrow\right) = \frac{1}{2}\frac{C_3(\theta)}{R^3_{\downarrow\uparrow}}\left(\hat{S}^x_\downarrow \hat{S}^x_\uparrow + \hat{S}^y_\downarrow \hat{S}^y_\uparrow\right) , \tag{2.13}$$

where $\hat{S}^\pm = \hat{S}^x \pm i\hat{S}^y$. This constitutes a basic description of a long-range Heisenberg XX-type Hamiltonian [Bettelli *et al.*, 2013; Barredo *et al.*, 2015; Piñeiro Orioli *et al.*, 2017].

When the effect of a resonant driving field addressing the Rydberg-Rydberg transition is included, the generalised Hamiltonian which results for many Rydberg spins presents the general form $\mathcal{H}_{field} + \mathcal{H}_{int}$, expressed as

$$\mathcal{H} = \sum_i \Omega_i \left(\cos(\phi)\hat{S}^x_i + \sin(\phi)\hat{S}^y_i\right) + 2\Delta\sum_i\left(\hat{S}^z_i - 1\right) + \frac{1}{2}\sum_{i,j<i}\frac{C_3(\theta_{ij})}{R^3_{ij}}\left(\hat{S}^x_i \hat{S}^x_j + \hat{S}^y_i \hat{S}^y_j\right) , \tag{2.14}$$

where ϕ is the phase of the driving field and Δ is the detuning of the field from the resonance.

In a many-body disordered sample, the interaction term can be considered as $J_\perp = C_3/R^3_{ij}$. These states can be driven by a single-photon microwave transition in the GHz regime.

Heisenberg XXZ Hamiltonian

In a more general situation, two Rydberg states of the manifold can be considered, e.g. $|\downarrow\rangle = |nS\rangle$ and $|\uparrow\rangle = |n'S\rangle$ with equal magnetic quantum number. The principal contribution to the interaction is given by the coupling to nearby $|P\rangle$ states. In the pair basis, the pairs present a Förster defect Δ_F. Applying second order perturbation theory to derive the van der Waals operator [Reinhard *et al.*, 2007], an interaction

matrix arises such that

$$\hat{\mathcal{H}_{int}} = \frac{1}{R^6}\begin{pmatrix} C_{6_{\downarrow\downarrow}} & 0 & 0 & 0 \\ 0 & C_{6_{\downarrow\uparrow}} & \tilde{C}_{6_{\downarrow\uparrow}} & 0 \\ 0 & \tilde{C}_{6_{\uparrow\downarrow}} & C_{6_{\uparrow\downarrow}} & 0 \\ 0 & 0 & 0 & C_{6_{\uparrow\uparrow}} \end{pmatrix} \tag{2.15}$$

which presents off-diagonal exchange terms and diagonal terms contributing to an Ising shift.

Thus, in presence of a driving field the general Hamiltonian can be expressed as

$$\begin{aligned} \mathcal{H} \approx & \sum_i \Omega_i \left(\cos(\phi)\hat{S}_i^x + \sin(\phi)\hat{S}_i^y\right) + 2\Delta \sum_i \left(\hat{S}_i^z - 1\right) + \\ & \sum_{i,j<i} \left[J_z(R_{ij})\hat{S}_i^z\hat{S}_j^z + \frac{J_\perp(R_{ij})}{2}\left(\hat{S}_i^x\hat{S}_j^x + \hat{S}_i^y\hat{S}_j^y\right)\right], \end{aligned} \tag{2.16}$$

where $J_\perp = 2\tilde{C}_{6_{\downarrow\uparrow}}/R_{ij}^6$ represents the spin-exchange interaction energy and the term $J_z = \frac{1}{R_{ij}^6}\left(C_{6_{\uparrow\uparrow}} + C_{6_{\downarrow\downarrow}} - 2C_{6_{\downarrow\uparrow}}\right)$ is an Ising level shift. This case has been discussed in detail in the theoretical proposal by [Whitlock *et al.*, 2017].

2.3 Dipole blockade of the Rydberg excitation

The optical excitation of Rydberg atoms is strongly affected by Rydberg-Rydberg interactions. A prominent consequence of the strong Rydberg interactions is the emergence of so-called dipole blockade in the excitation from a ground to Rydberg states [Jaksch *et al.*, 2000; Lukin *et al.*, 2001]. To illustrate the phenomenon the simple case of a pair of atoms is considered, both of them initially in the ground state $|g\rangle$, and with laser excitation light resonant to the ground-to-Rydberg transition, as depicted in Figure 2.3(a). When one of the two gets excited to the Rydberg level $|r\rangle$, the energy of the second atom is shifted according to the inter-atomic distance. If this level shift is smaller than than the excitation bandwidth $\hbar\mathcal{W}$, the second atom can be still excited to the Rydberg state. However, if the energy shift is larger, the excitation process becomes off-resonant and greatly suppressed. In the pair basis, the states $|gr\rangle$ are almost unshifted due to the small polarisability of the ground state, but the transition $|gr\rangle \leftrightarrow |rr\rangle$ is rendered sensitive to the inter-particle separation R. The blockade condition can be expressed as the energy shift for which the condition $V(R)^{int} \geq \hbar\mathcal{W}$ is fulfilled. This introduces a natural length scale in the system: the critical distance below which double excitation $|rr\rangle$ is inhibited, so-called Rydberg

blockade radius R_{bl} (see Fig.2.3(b)). It can be generally defined as

$$R_{bl} = \sqrt[6]{\frac{C_6}{\hbar\mathcal{W}}} \qquad R_{bl} = \sqrt[3]{\frac{C_3}{\hbar\mathcal{W}}} \tag{2.17}$$

for van der Waals ($\propto 1/R^6$) and resonant dipole-dipole ($\propto 1/R^3$) interactions, respectively. It must be noted that the excitation bandwidth $\mathcal{W}$ depends on the Rabi frequency of the excitation process Ω and the dephasing of the excitation mechanism. Typical blockade radii correspond to distances on the order of few μm, which affect a spherical volume with radius R_{bl}. Whereas this blockade picture precisely describes the nature of the interactions amongst isotropic $|nS\rangle$ states, angular dependent anisotropic interactions (e.g. amongst $|nP\rangle$ or $|nD\rangle$ states) lead to complex ellipsoidal volumes or to no interaction for certain conditions [Saffman *et al.*, 2010]. Multiple experimental evidences of the dipole blockade have been revealed in the past years for different systems and configurations [Singer *et al.*, 2004; Tong *et al.*, 2004; Gaëtan *et al.*, 2009; Urban *et al.*, 2009; Viteau *et al.*, 2011; Hankin *et al.*, 2014], some of which are reviewed by Comparat *et al.* [Comparat and Pillet, 2010]. As a consequence, to excite Rydberg atoms in the blockaded regime, the laser frequency must be changed to match the energy shift of the atoms [Malossi *et al.*, 2014; Schempp *et al.*, 2014].

2.3.1 Collective Rydberg excitation

The emergence of Rydberg blockade also changes the dynamics of a gas of many atoms due to the reduction of accessible many-body states. Any individual blockade sphere is made up of $N-1$ ground state atoms and a single Rydberg excitation. This many-body state is symmetric under particle exchange, since the excitation cannot be assigned to a specific atom of the system, but is shared amongst all of them. This results in a collective quantum state of N atoms. Therefore, it can be expressed in a Dicke-state basis as

$$|R^{(1)}\rangle = \frac{1}{\sqrt{N}} \sum_{i=1}^{N} |g_1, ..., r_i, ..., g_N\rangle \,. \tag{2.18}$$

The excitation from the collective ground state $|g^{(0)}\rangle$ may be understood as the result of a collective $\sqrt{N}$ enhancement of the excitation Rabi frequency $\Omega_{col} = \sqrt{N}\Omega$. The increase of the excitation bandwidth also affects the blockade distance in this super-atom picture, such that

$$R_{bl} = \left(\frac{C_6}{\hbar\sqrt{N}\Omega}\right)^{1/6}. \tag{2.19}$$

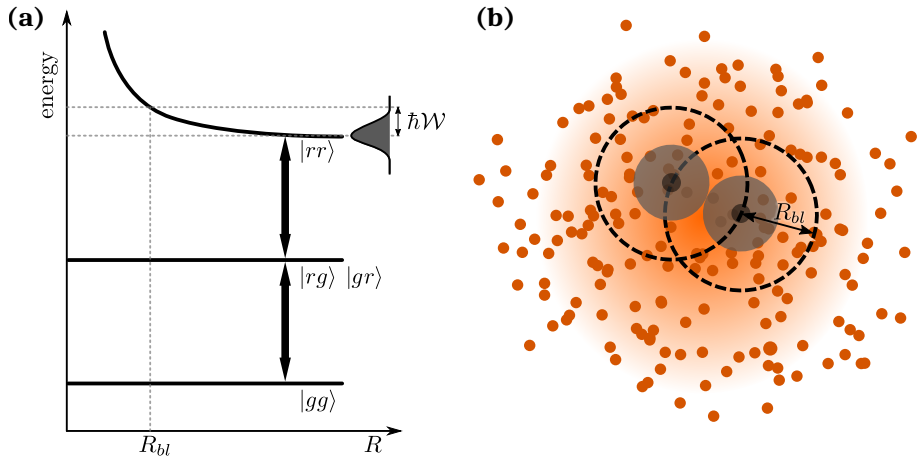

Figure 2.3: Rydberg excitation blockade effect. (a) Energy of an atomic pair as a function of inter-atomic distance R. Both atoms can be excited to the Rydberg state $|rr\rangle$ when the inter-atomic separation is large. However, for smaller separation, the pair-state interaction increasingly shifts the energy of the pair $|rr\rangle$. The blockade radius R_{bl} is defined at the inter-atomic distance at which the interaction energy equals the excitation bandwidth $\hbar\mathcal{W}$. At shorter distances, the formation of close Rydberg pair is inhibited and only a single excitation is allowed. **(b)** The blockade effect in a large atomic cloud generates blockade spheres (black dashed lines) in which a unique Rydberg excitation is allowed. Taken and adapted from [Hofmann, 2013; Günter, 2014; Gavryusev, 2016].

Despite the definition of a many-body blockade radius presents a higher complexity due to the specific positions of the atoms, this basic picture qualitatively explains the many-body theoretical calculations [Robicheaux, 2005] and experimentally accessible scaling of the blockade radius with the atomic density of a disordered sample [Heidemann *et al.*, 2007].

2.4 Experimental setup and methods

The experiments introduced in the course of this thesis are realised with the experimental setup described below, with the goal of preparing ultracold dense disordered atomic samples of ^{87}Rb in a tunable geometrical configuration and excite a fraction of the atoms to Rydberg states by means of optical laser beams to create Rydberg spins. The control and manipulation of the Rydberg atoms within the Rydberg manifold is discussed in Section 2.5. The main detection method for the spins, based on field ionisation detection is briefly discussed here, whereas its precise calibration is extensively discussed in Section 3.1.6.

The technical details and possibilities of the excitation are discussed within the

present section, whereas Chapter 3 provides results emerging from the experiments on Rydberg excitation of the spins. For a more detailed description of the general apparatus, the reader can find additional information in [Hofmann *et al.*, 2013; Hofmann, 2013] and the recent updates may be consulted in [Gavryusev, 2016].

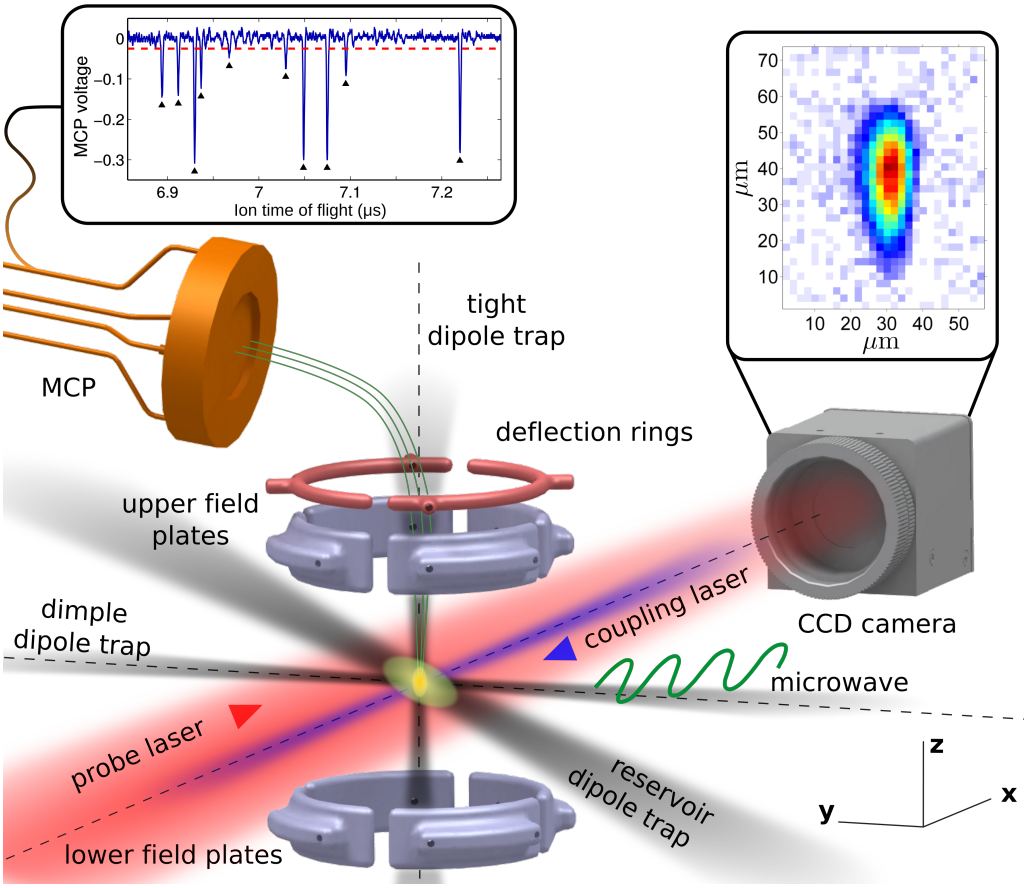

Figure 2.4: Setup for preparation and detection of Rydberg atoms in an ultracold $^{87}\mathrm{Rb}$ gas. Pre-cooled atoms are transferred from a magneto-optical trap into the reservoir optical dipole trap. An additional tight dipole trap in the vertical direction may be employed to create mesoscopic samples. After being released from the trap, the atoms are excited to Rydberg states by a combination of a $780\,\mathrm{nm}$ laser, a counter-propagating $480\,\mathrm{nm}$ coupling laser and microwave radiation at $\sim 2-67\,\mathrm{GHz}$. An electrode structure composed of 8 field plates is used for precise electric field control and for field ionisation of Rydberg atoms. Two deflection rings guide the ions (green trajectories) onto a micro-channel plate (MCP) detector. Spatial information on the distribution of ground state atoms is acquired in parallel by absorption imaging with a CCD camera. The inset shows the two-level absorption of the atoms in the tight trap. Adapted from [Gavryusev, 2016]

2.4.1 Preparation of ultracold atomic samples

In order to prepare ultracold and dense samples of ^{87}Rb, common laser cooling and trapping techniques are applied [Ketterle *et al.*, 1999]. A three step process is employed: **(i)** the atoms are pre-cooled in a 2D-MOT, **(ii)** then loaded into a 3D-MOT in the science chamber [Dieckmann *et al.*, 1998; Schoser *et al.*, 2002] **(iii)** and directly transferred into a "reservoir" optical dipole trap (ODT) [Grimm *et al.*, 2000]. The details of the MOT can be consulted in [Hofmann *et al.*, 2013]. Additionally, for a tighter confinement of the atoms, evaporative cooling and transfer into a smaller and denser ODT in the perpendicular (vertical) direction is available.

Optical dipole trap

This trap is composed of two weakly-focused laser beams crossing at a small angle and generated by a 50 W single frequency fiber amplifier laser at a wavelength of 1064 nm, resulting in an elongated cigar-shaped atomic cloud of width of $\sim 40\,\mu\text{m} \times 40\,\mu\text{m} \times 800\,\mu\text{m}$ at $1/e^2$, tilted from the x probing direction by 45° (Fig. 2.4). This geometry allows for efficient loading from the 3D-MOT, leading to large densities up to $5 \cdot 10^{11}\,\text{cm}^{-3}$ with typical temperatures of 40 μK. In order to control the atomic cloud geometry we can shape the beams or release the atoms from the trap during few milliseconds of time-of-flight to allow for the desired density distribution.

A second ODT, composed of a single focused "dimple" beam is oriented along y at 45° with respect to the "reservoir" trap. In order to achieve higher densities, the atoms are temporarily transferred from the reservoir trap to a "dimple" ODT aligned on the y direction. All-optical evaporative cooling is used to increase the phase-space density of the atoms whilst decreasing their temperature [Clément *et al.*, 2009]. The resulting atomic cloud resembles a cigar-shaped cloud of width $\sim 22\,\mu\text{m} \times 22\,\mu\text{m} \times 150\,\mu\text{m}$ at $1/e^2$. The temperature decreases to 1 μK and the ground state density increases up to a peak of $2 \cdot 10^{12}\,\text{cm}^{-3}$. An additional optimised ramp could be applied to reach Bose-Einstein condensation [Hofmann, 2013], which is not a subject of interest in the experiments of this thesis.

Tight optical dipole trap

Some experiments may require the use of much smaller atomic samples (see Ch 6). Experiments realized in the large ODT have shown the emergence of diffusive transport effects [Günter *et al.*, 2013] that may be undesired. To circumvent such effects, the atoms can be confined into a small region comparable to the typical

Rydberg blockade volume using an additional vertical tight ODT. In the experiment, a second intense and tightly focused dimple beam is oriented in the vertical direction z to trap the atoms at the intersection of all three traps. After performing evaporative cooling and transferring the atoms to the dimple ODT, the tight ODT is loaded by increasing its potential depth while reducing the one of the dimple trap. The final cloud contains up to 3000 atoms in a volume of $\sim 8\,\mu\text{m} \times 22\,\mu\text{m} \times 8\,\mu\text{m}$ (width at $1/e^2$), providing densities up to $1.5 \cdot 10^{12}\,\text{cm}^{-3}$ as well as low temperatures of $\sim 1\,\mu\text{K}$. Therefore only very few Rydberg atoms can be excited in this tight trap before reaching the fully-blockaded regime.

2.4.2 Excitation and detection techniques

Here, the technical capabilities of the experimental setup are explained, focusing on the tools which are used for different excitation schemes of Rydberg spins. The setup consists of the following components to manipulate the atomic state:

(i) Microwave synthesizer Windfreak SynthHD, for ground state preparation

(ii) 780 nm laser TOPTICA DL100 PRO, for imaging and Rydberg excitation.

(iii) 480 nm frequency doubled lasers TOPTICA TA-SHG and TOPTICA TA-SHG pro, for off-resonant and resonant coupling to the Rydberg state.

(iv) Microwave synthesizer Anritsu MG3697C , for transferring Rydberg atoms within the Rydberg manifold.

Ground state preparation

When the ultracold atomic sample is loaded into one of the dipole traps, a static magnetic field of up to 6 G is applied along the x direction to define the quantisation axis. Initially, the ground state atoms in $|5S_{1/2}\rangle$ are distributed amongst both the $F = 1$ and $F = 2$ manifolds. In order to prepare a clean ground state, the repumping light at the end of the MOT cooling stage is switched off, preventing the atoms from populating the $F = 2$ manifold. Thereafter, the population in the state $|5S_{1/2}, F = 1, m_F = 1\rangle$ is transferred to the desired ground state $|g\rangle = |5S_{1/2}, F = 2, m_F = 2\rangle$ by means of a microwave Landau-Zener adiabatic sweep of the magnetic field at a fixed frequency of 6.8 GHz, which addresses the central resonance of the $F = 1$ to $F = 2$ transition. Varying the duration of the sweep allows to control the ground-state atomic density of the sample.

780 nm probe beam: imaging light

In order to optically image the ultracold gas a 780 nm weak laser beam is coupled to the $|g\rangle \leftrightarrow |e\rangle = |5P_{3/2}, F = 3, m_F = 3\rangle$ transition with σ^+ polarisation, propagating along the x horizontal direction (parallel to the quantisation axis). The beam is collimated with a beam waist of 1.5 mm. The transmitted light is collected onto an Andor iXon Ultra 897 EM-CCD camera (Fig. 2.4) via a nearly diffraction limited imaging system with a resolution of 4.8 µm (Rayleigh criterion). Further details about the imaging setup can be found in [Helmrich, 2013]. This so-called "probe" laser beam is used at the transition resonance for two-level absorption imaging experiments (see Section 3.1.2) or for two-photon resonant excitation of the spins with an electromagnetically-induced transparency scheme (see: Section 3.2, Ch. 6).

780 nm off-resonant excitation beam

To allow for off-resonant excitation of spins, a vertical 780 nm beam propagating along the vertical direction is set up with linear polarisation perpendicular to the x quantisation axis. Thus, it is decomposed into two polarisation components σ^+ and σ^-. This beam is not shown in Fig. 2.4 for the sake of clarity of the picture. The beam addresses the transition $|g\rangle \leftrightarrow |e\rangle = |5P_{3/2}, F = 3, m_F = 3\rangle$ with the σ^+ component and is detuned from the transition by Δ_e. For most experiments, the σ^- component becomes irrelevant since it leads to off-resonant processes which can be reasonably neglected. This beam is used for two- (Sec. 3.1) and three-photon (Sec. 3.3) schemes, off-resonant from the intermediate state $|e\rangle$.

480 nm resonant coupling beam

An additional counter-propagating 480 nm strong coupling beam is focused on the center of the cloud to couple the transition from $|5P_{3/2}, F = 3, m_F = 3\rangle$ to a $|nS\rangle$ Rydberg state with σ^- polarisation. The transition is addressed resonantly and the beam size can be tuned by fine adjustment of the position of the beam relative to the collimating lens using a precise translation stage. This beam is employed in combination with the resonant 780 nm probe beam in experiments which require an EIT scheme (Section 3.2, Ch. 6) and in the de-excitation scheme for Rydberg atoms Sec. 3.4.

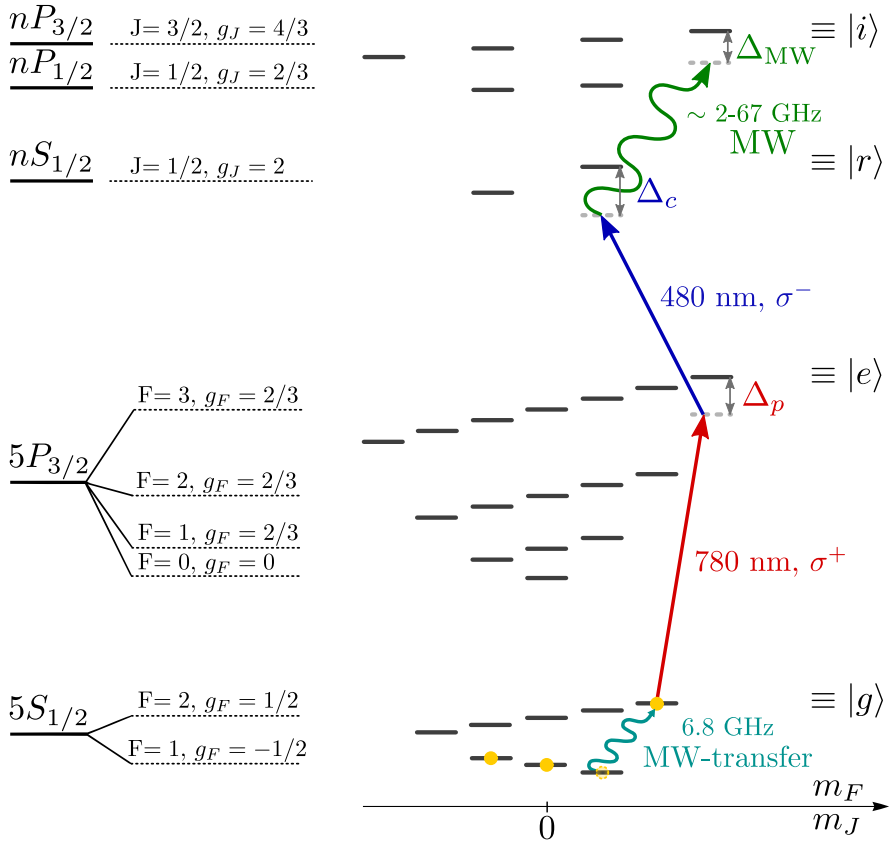

Figure 2.5: Relevant atomic levels of ^{87}Rb in presence of a magnetic field. The atoms distributed over the $F = 1$ manifold are transferred from $|5S_{1/2}, F = 1, m_F = 1\rangle$ to the selected ground state $|g\rangle \equiv |5S_{1/2}, F = 2, m_F = 2\rangle$. A 780 nm σ^+-polarized laser beam addresses the $|g\rangle \leftrightarrow |e\rangle \equiv |5P_{3/2}, F = 3, m_F = 3\rangle$ transition. A 480 nm σ^--polarised laser couples $|e\rangle$ to the Rydberg state $|r\rangle \equiv |nS\rangle$ or $|r\rangle \equiv |nD\rangle$ Rydberg states. The state $|i\rangle \equiv |nP_J, m_j\rangle$ may be excited in the desired Zeeman level by a microwave photon with a frequency between 2 and 67 GHz, depending on the chosen n. Two identical microwave photons allow to couple to $|i\rangle \equiv |nS\rangle$ or $|i\rangle \equiv |nD\rangle$. Taken from [Gavryusev, 2016]

480 nm off-resonant coupling beam

An additional 480 nm laser beam is available in the experimental setup, counter-propagating with σ^- polarisation in the same direction as the previously described resonant coupling beam. The size of the beam can be modified in a similar manner. However this laser beam is far detuned from the $|5P_{3/2}, F = 3, m_F = 3\rangle \leftrightarrow |nS\rangle$ transition. The detuning typically compensates for Δ_e such that the combination of both photons fulfils the two-photon resonance condition with $|nS\rangle$, which is relevant in Sec. 3.1.

Pound-Drever-Hall stabilisation

In order to minimise the dephasing rate on the Rydberg-state transition, the frequency fluctuations of the lasers which contribute to the dephasing rate γ_{gr} have to be minimised. For such purpose, the 780 nm and 480 nm lasers are frequency stabilised to a passive high finesse ultra-low-expansion glass Fabry-Pérot cavity [Gregory *et al.*, 2015; Aikawa *et al.*, 2011] via the Pound-Drever-Hall method (PDH) [Black, 2001]. The cavity mirrors are dual-wavelength coated, allowing for simultaneous stabilisation of both colours. We estimate the frequency stability of our lasers by measuring the root mean square instantaneous frequency deviation relative to a cavity mode of a reference active Fabry-Pérot cavity (Sirah Eagle Eye). For timescales longer than 3 µs, a linewidth below 10 kHz, considerably smaller than the typical Fourier width of the excitation pulses (µs-duration). A detailed characterisation may be consulted in [Gavryusev, 2016].

Microwave synthesizer

The Anritsu MG3697C microwave synthesizer provides a microwave field which allows to address transitions between Rydberg states, either with different angular momentum (e.g. $|nS\rangle \leftrightarrow |nP\rangle$ transitions), by means of a single photon, or with the same angular momentum (e.g. $|nS\rangle \leftrightarrow |(n+1)S\rangle$ transitions), by means of two identical photons. The frequencies generated range between 2 and 67 GHz. The microwave radiation is emitted into the science chamber by a microwave horn antenna which is tilted relative to the quantisation axis due to geometrical constraints of the accessibility to the science chamber. Thus, all polarisations are possible in the experiment. A refined control of the microwave field is discussed in the next section (Sec. 2.5).

Field ionisation

The experimental apparatus has an electrode structure which allows to apply and control the electric fields in the three dimensions. Moderate electric fields can be applied to DC-Stark shift the energy levels of the Rydberg atoms or to tune their Förster defect and therefore the strength of the interactions. The electrodes are used to ionise the Rydberg atoms after each experimental repetition and to guide them to a micro-channel-plate (MCP) particle detector, counting the number of impacts and the integrated signal, typically proportional to the atom number. This enables to detect the global the Rydberg atom number. A calibration of the detection efficiency

is presented in Sec. 3.1.6.

2.5 Microwave control of Rydberg transitions

As discussed in Chapter 1, the main goal of this thesis is to create a platform to investigate spin-1/2 dynamics with Rydberg atoms, where the spins are encoded onto two different Rydberg states. Thus, a remarkable fraction of the experiments requires control of atomic transitions within the Rydberg manifold [Goy *et al.*, 1982; Cheng *et al.*, 1994; Merkt and Schmutz, 1998; Li *et al.*, 2003]. To acquire such capability, different parameters must be controlled:

- The time t_{mw} of the microwave pulse.
- The frequency ν of the microwave field.
- The microwave power output, which determines the amplitude of the field.
- The phase of the field ϕ.

Transition (n) $nS_{1/2} \leftrightarrow nP_{3/2}$	ν_0 (GHz)	λ_0 (cm)
∼100	2.0	14.99
90	4.81	6.233
70	10.6	2.828
55	22.7	1.321
48	35.0	0.857
45	43.0	0.697
42	53.8	0.557
40	62.9	0.477
39	68.3	0.439

Table 2.2: Transition frequency between $nS_{1/2}$ and $nP_{3/2}$ Rydberg states in the range provided by the Anritsu MG3697C microwave synthesizer. The lowest addressable transitions of such type correspond to $|40S_{1/2}\rangle \leftrightarrow |40P_{3/2}\rangle$. Below $n = 40$, the required microwave frequency ν_0 exceeds the upper limit of the synthesizer In green, the transitions experimentally explored over the course of this thesis.

The microwave synthesis is performed by means of a commercial microwave synthesizer Anritsu MG3697C, which allows to address Rydberg transitions in the range between 2

to 67 GHz. A broad number of Rydberg-Rydberg transitions is accessible, as depicted in Table 2.2. However, due to slow modulation bandwidth ($\sim$ ms timescales), fast switching of the microwave phase and frequency are not possible on the timescales associated to the Rydberg atom dynamics (few µs). A new approach is required to efficiently implement and control complex pulse sequencies. We achieve this through frequency mixing of the microwave field with a modulating radio-frequency signal by means of a frequency up-conversion technique. The basic principles of frequency mixing may be consulted in [Hagen, 2000; Steer, 2009].

2.5.1 Frequency up-conversion in the GHz range

Frequency up-conversion is a technique which relies on the principles of frequency mixing, where the base signal and a control signal are manipulated to produce a third signal as an output. An ideal would output the multiplication of two oscillating signals: a local oscillator (LO) and an intermediate frequency (IF) [Marki and Marki, 2010]:

$$U_{RF} \approx \frac{U_{LO}U_{IF}}{2}\left[\cos(2\pi(\nu_{LO}+\nu_{IF})t)+\cos(2\pi(\nu_{LO}-\nu_{IF})t)\right] . \tag{2.20}$$

This signal consists of a two-peak spectrum shifted by the IF frequency ν_{IF} with respect to the LO carrier frequency ν_{LO}. A real mixer generates as well higher order harmonics of the input signals product, which often are undesired.

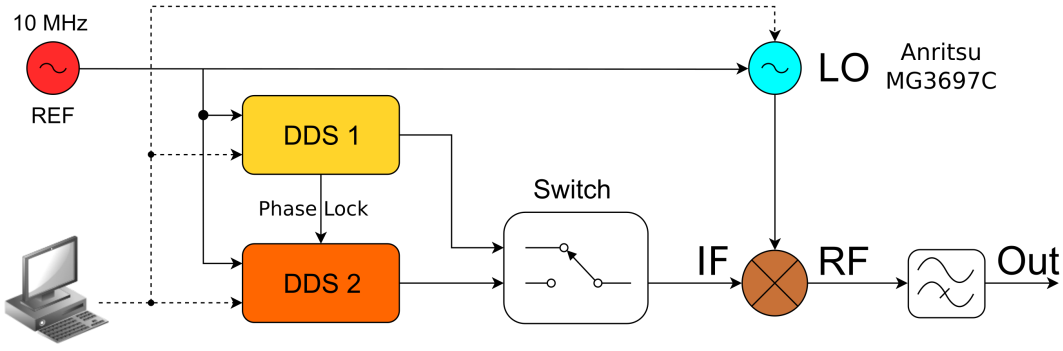

Figure 2.6: General frequency up-conversion setup for microwave control of Rydberg spins. The carrier microwave frequency from the Anritsu MG3697C microwave synthesizer (ν_{LO} = 2 to 67 GHz) is mixed up with another radio frequency signal provided by a DDS 1 (ν_{IF} = 400 MHz). A second DDS 2 is employed to realised complex sequences, switching between two sets of parameters $\{t_1, \Omega_1, \phi_1, \nu_1\}$ and $\{t_2, \Omega_2, \phi_2, \nu_2\}$.

Our setup for microwave synthesis consists of the following devices, as represented in Figure 2.6. A local oscillator, which our Anritsu 3697C synthesizes, provides a microwave field that can be tuned close to the Rydberg transition of interest. A digital-digital synthesizer (DDS 1) with a frequency range up to 1.2 GHz is used as intermediate frequency to modulate and control the amplitude and frequency of the desired output. A second DDS 2 is available in order to switch to a different configuration of frequency, amplitude or phase of the field. Both DDS are phase locked in order to accurately control the relative phase that can be implemented and all three synthesizers are locked to the same precise 10 MHz reference clock. A switch is used to select which DDS controls the mixing operation. After the output microwave field is produced, it is sent through a high-pass filter to remove the residual IF frequency. For the experiments performed in Chapter (4-5) are realised with a double balanced Marki M4-0165, which can cover the whole frequency range of the synthesizer ($1 - 65$ GHz). The principal source of error is given by the jitter of the DDSs, which is measured to be ≤ 10 ns. This makes a negligible impact on the measurements.

During an experimental run, the Anritsu 3697C LO signal is set to a fixed configuration and the synthesis of the microwave output field is controlled by the DDS. Since each DDS can be triggered to change its parameters once in each experimental run, a complex sequence of 2^N independent pulses can be generated, with N the number of DDS in parallel.

In Figure 2.7(a), a typical spectrum of the up-converted frequency output is presented. The observed peaks corresponds to the side-bands generated by the frequency mixing process around the carrier LO frequency, which is not completely suppressed. The "+1" side-band is used to address the atomic transition. Since the detuning between the driving side-band and the carrier (LO) is $\Delta/2\pi = 400$ MHz, the 18 dBc suppression of the LO with respect to the carrier leads to a reduction of off-resonantly excited population on the order of $\sim 10^5$ for typical Rabi frequencies of few MHz. In order to the eliminate the side-bands of one side of the spectrum, an IQ mixing process may be introduced, which relies on parallel mixing with two modulating branches and latter recombination of both outputs. A preliminary characterisation is presented in Appendix A.

An example of the up-conversion optimisation is depicted in Fig. 2.7(b) for a LO at 25 GHz and IF at 400 MHz. The up-conversion process is optimised at high IF powers, as in the present case $P_{IF} = 12$ dBm. At high LO and IF powers, the suppression of undesired side-bands and carrier frequency is maximized. The optimum working point is at the beginning of the saturation of the RF output power.

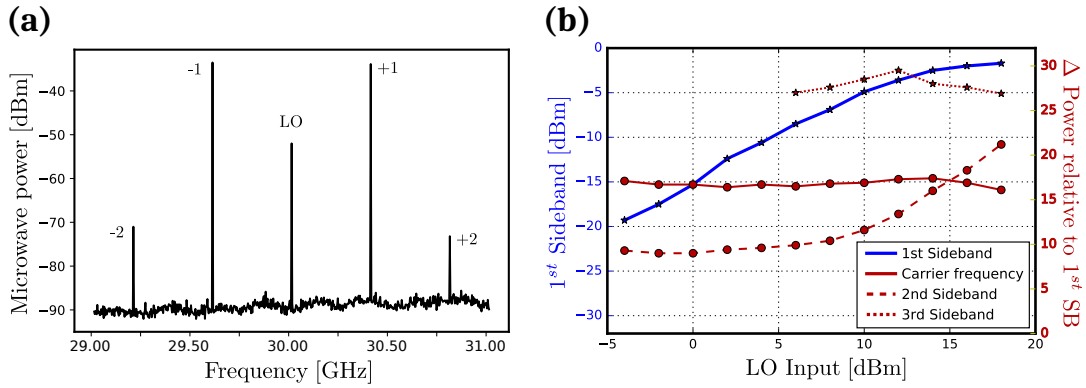

Figure 2.7: Optimisation of frequency up conversion with a Marki M4-0165 double balanced mixer. (a) Power spectral measurement for a carrier LO at $\nu_{LO} = 30.04\,\text{GHz}$ and input power $P_{LO} = 16\,\text{dBm}$. A DDS provides a modulating frequency $\nu_{IF} = 400\,\text{MHz}$. **(b)** Power output of the generated radio-frequency (RF) signal (blue) of the first side-band $(+1)$. The LO signal is provided by the microwave synthesizer at a frequency $\nu_{LO} = 25\,\text{GHz}$, and a $\nu_{IF} = 400\,\text{MHz}$ IF signal with power $P_{IF} = 12\,\text{dBm}$. The optimal suppression of the undesired signals occurs at the saturation point of the first side-band for high IF powers, where the power starts to redistribute to other components.

At higher powers, the excess of LO power in the mixer does not lead to an increase of the first side-band amplitude, but result in a stronger LO component. The poins at which the saturation reduces the RF output by 1 dB relative to the ideal linear increase is called the 1 dB compression point, which occurs at $P_{LO} \approx 13.5\,\text{dBm}$. Additional details of the characterisation may be consulted in [Geier, 2016].

Chapter 3

Preparation of Rydberg spins: excitation mechanisms and characterisation of the dynamics

Section 3.2 is based on parts of the following publication:

Density matrix reconstruction of three-level atoms via Rydberg electromagnetically induced transparency
V. Gavryusev, A. Signoles, M. Ferreira-Cao, G. Zürn, C. S. Hofmann, G. Günter, H. Schempp, M. Robert-de-Saint-Vincent, S. Whitlock and M. Weidemüller
J. Phys. B **49**, 16 (2016)

Section 3.3 is based on parts of the following publication:

Interaction-Enhanced Imaging of Rydberg P states
V. Gavryusev, M. Ferreira-Cao, A. Kekić, G. Zürn and A. Signoles
Eur. Phys. J. ST **225**, 15 (2016)

Investigations on Rydberg spin physics require an efficient preparation and precise detection of Rydberg atoms. For such purpose, $|nS\rangle$ or $|nD\rangle$ Rydberg states have been traditionally excited using two photon optical transitions, whereas direct excitation of $|nP\rangle$ states has been performed by means of an ultra-violet single-photon transition [Gallagher, 1994]. Alternative schemes relied on preliminary excitation of $|nS\rangle$ atoms and later transfer of population to $|nP\rangle$ by means of a microwave field, leading to undesired dipolar ($\propto \frac{1}{R^3}$) broadening of the spectrum [Anderson *et al.*,

2002; Afrousheh *et al.*, 2004; Afrousheh *et al.*, 2006b; Park *et al.*, 2011]. A three photon resonant scheme, but off-resonant from the intermediate levels, is implemented here to directly address such states with negligible population of additional Rydberg states.

The excitation dynamics of Rydberg states in dense atomic clouds presents strong deviations from the single-particle regime due to the increasing effect of Rydberg-Rydberg interactions, which strongly suppress the excitation in the blockaded regime [Singer *et al.*, 2004; Tong *et al.*, 2004] and may lead to collective dynamics [Reetz-Lamour *et al.*, 2008a; Dudin *et al.*, 2012; Gaëtan *et al.*, 2009; Urban *et al.*, 2009; Barredo *et al.*, 2014]. In order to locally characterise the Rydberg excitation processes, a new imaging technique, so-called Depletion Imaging, is introduced in this chapter. This method reveals the presence of Rydberg excitations by measuring the depletion of absorption when $|nS\rangle$ atoms are pre-excited, which allows to locally resolve the two-dimensional distribution of Rydberg atoms. Such spatial profile of Rydberg ensembles can be measured using a tomographic approach [Valado *et al.*, 2013] or by other imaging techniques previously applied to observe the two-dimensional excitation profile of a Rydberg cloud [Lochead *et al.*, 2013] or an ultracold plasma of Rydberg atoms [McQuillen *et al.*, 2013]. Nevertheless, here is reported the first direct observation of the local Rydberg fraction ρ_{Ry} and the spatial dependence of its profile in a many-body regime. This led to the first observation of the flat-top profile which emerges due to the strong interaction-induced van der Waals blockade over a large ensemble of up to $\sim 1.7 \cdot 10^4$ Rydberg atoms. Such phenomenon may result in the emergence of spatial order mediated by the dipole blockade, which has been previously observed [Schauß *et al.*, 2012]. Finally, characterisation of the excitation rates permits to discern several regimes of the driven dynamics in different regions of the Rydberg many-body ensemble [Heidemann *et al.*, 2007; Valado *et al.*, 2016], opening the path for local studies of universal excitation properties [Löw *et al.*, 2009; Helmrich *et al.*, 2016].

The chapter consists of the following structure. As a first step, two-photon excitation of $|nS\rangle$ is explained in Section 3.1 and locally characterised with an absorption imaging technique in order to measure the interacting dynamics of Rydberg atoms and calibrate the detection of spins. Then, in Section 3.2 a two-photon resonant scheme is implemented, based on the principles of electromagnetically-induced transparency, to reconstruct the Rydberg atom distribution and calibrate the local Rabi frequency of the excitation [Gavryusev *et al.*, 2016b]. In Section 3.3, a recently introduced three-photon excitation scheme of Rydberg $|nP\rangle$ states is presented [Gavryusev *et al.*, 2016a], reduced to an effective two-photon scheme

and applied for spectroscopic studies of Rydberg excitation dynamics and Rydberg interactions. Finally, a de-excitation protocol is introduced in Sec. 3.4 to selectively detect the Rydberg spin components.

3.1 Two-photon excitation of $|nS\rangle$ Rydberg states: global and local observation of the dynamics

In the present section, excitation of ^{87}Rb from the ground state to $|nS\rangle$ state by means of a two photon scheme is performed, off-resonant from the intermediate state $|e\rangle$. The two-photon scheme is resonant with the upper Rydberg level $|nS\rangle$ to avoid population transfer to undesired intermediate levels. Rydberg atom excitation has been object of multiple investigations due to the appearance of strong interaction blockade effects between Rydberg atoms, which modify the dynamics [Reetz-Lamour *et al.*, 2008a; Reetz-Lamour *et al.*, 2008b; Urban *et al.*, 2009; Gaëtan *et al.*, 2009], reviewed by [Comparat and Pillet, 2010]. The excitation dynamics is locally characterised by means of a new imaging technique based on absorption imaging and the profile of the excitations is revealed. The local and global sensitivity of the technique is characterised and this imaging tool is also used as a calibration protocol to quantify the detection efficiency η_{nS} of Rydberg atoms by field-ionisation detection. Thus, accurate numbers of Rydberg spins can be prepared and measured under a large variety of conditions.

3.1.1 Off-resonant excitation of $|nS\rangle$ states

The excitation of Rydberg $|nS\rangle$ atoms in this section is realised by the combination of a 780 nm infra-red and a 480 nm photons. The 780 nm vertical laser beam, homogeneously distributed at the position of the atoms, addresses the transition $|g\rangle \leftrightarrow |e\rangle$ with the relevant σ^+ component. As described in Fig. 3.1, the coupling is given by a Rabi frequency Ω_{eff} and it is detuned Δ_e from the transition resonance. In the experiments presented in this section, the states $|g\rangle = |5S_{1/2}, F = 2, m_F = 2\rangle$ and $|e\rangle = |5P_{3/2}, F = 3, m_F = 3\rangle$ are used, with a detuning $\Delta_e/2\pi = -97\,\text{MHz}$. The second excitation step is realised by means of a σ^- polarised $\sim 480\,\text{nm}$ laser beam with spatially-dependent Rabi frequency $\Omega_r(x, y)$. The Rabi frequency Ω_r of the beam addressing the $|e\rangle \leftrightarrow |r\rangle$ transition compensates for the detuning of the first photon. Thus, the two-photon process is resonant to the Rydberg energy level, $(\Delta_e + \Delta_r) = 0$. Hereafter, the described experiment considers the Rydberg

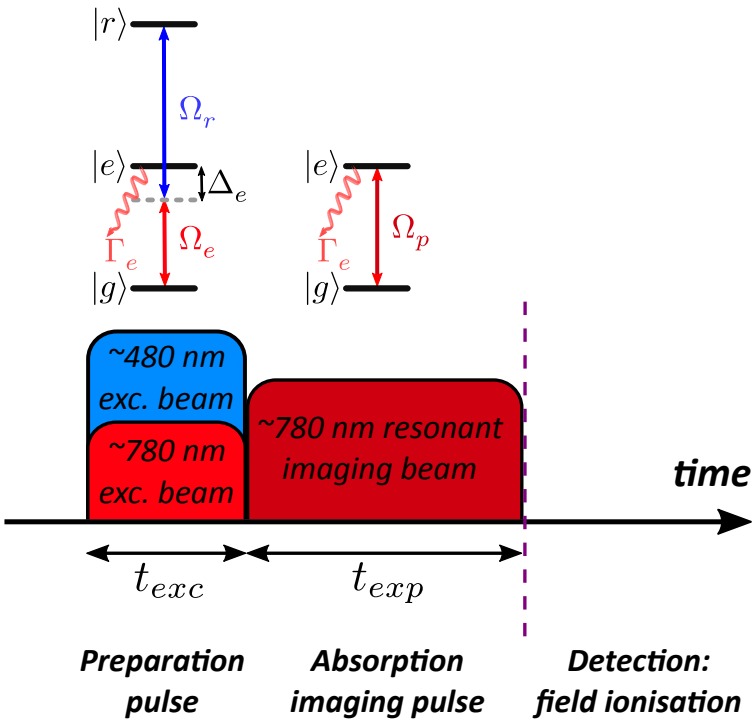

Figure 3.1: Excitation scheme and experimental sequence for two-photon off-resonant excitation, followed by a diagnosis absorption imaging pulse. The two-photon excitation pulse is applied during a variable time t_{exc}. In order to spatially resolve the excitation dynamics, an absorption imaging pulse is resonantly implemented during a fixed exposure time t_{exp} after the excitation. This is followed by a field-ionisation pulse to collect the ion signal from the Rydberg excitations in an MCP detector.

state $|r\rangle = |48S_{1/2}, m_j = 1/2\rangle$, for which the Zeeman sub-state is well-defined by a $B_z = 6.1\,\mathrm{G}$ magnetic field parallel to the imaging direction (see Sec. 2.4.1). It is important to note that $\Delta_e \gg \Omega_e,\ \Omega_r, \Gamma_e$, such that the population in the intermediate state is negligible in comparison to both $|g\rangle$ and $|r\rangle$ states. Therefore, the scheme may be considered as an effective two level transition between $|g\rangle$ and $|r\rangle$, with Rabi frequency $\Omega_{eff}(x,y) = \frac{\Omega_p \cdot \Omega_r(x,y)}{2\Delta_e}$ in the region of interest, adiabatically eliminating the population of the intermediate state $|e\rangle$ [Reiter and Sørensen, 2012].

The spatially-dependent Rabi frequency $\Omega_c(x,y)$ determines the maximum spatial extension of the excitation region of Rydberg atoms. Both laser beams are switched on and off simultaneously and the number of prepared Rydberg spins is controlled by varying the excitation time t_{exc}.

3.1.2 Spatially-resolved imaging of the excitation dynamics

In order to characterise the excitation process, we introduce an imaging technique which reveals the spatial distribution of Rydberg atoms in the cloud. It relies on the absorption imaging of the ground state $|g\rangle \equiv |5S_{1/2}, F = 2, m_F = 2\rangle$ atoms with a probe beam Ω_p addressing the intermediate state $|e\rangle \equiv |5P_{3/2}, F = 3, m_F = 3\rangle$ with σ^+ polarisation and the comparison of the absorption level with and without Rydberg atom excitation. Such Depletion Imaging method is simple to implement and nonetheless quite powerful because it allows to extract local information on the Rydberg atom distribution and excitation dynamics.

Description of the Depletion Imaging method

The optical response of an atomic gas of density n exposed to a probe light of intensity $I \propto \Omega_p^2$ can be well described through its first order susceptibility χ, defined for the general case as

$$\chi = \frac{\sigma_0 n \Gamma_e}{k \Omega_p} \rho_{eg} = \chi_0 \frac{\Gamma_e}{\Omega_p} \rho_{eg} \tag{3.1}$$

where $\sigma_0 = 3\lambda^2/2\pi$ is the resonant absorption cross-section, k the wavevector and ρ_{eg} the single-atom matrix element for the probe transition $|g\rangle \leftrightarrow |e\rangle$. In our experiments, the density is a function of position $n(\mathbf{r})$ due to the Gaussian profile of the atomic cloud, while ρ_{eg} depends in particular on the probe intensity I.

For a simple two-level system, the resonant scaled susceptibility $\tilde{\chi}_{2l}$ is given by

$$\tilde{\chi}_{2l} = \frac{\chi_{2l}}{\chi_0} = \frac{i\Gamma_e^2}{\Gamma_e^2 + 2\Omega_p^2}. \tag{3.2}$$

To detect the distribution of Rydberg atoms, two sets of images, with and without Rydberg state excitation, are acquired on a CCD camera. Assuming constant light intensity at the atom position, non-linear effects of the light propagation can be neglected. Experimentally, the total absorption $A = (I_{in} - I_{trans})/I_{in}$ is accessed, given by

$$A = 1 - e^{-OD} \quad \text{with} \quad OD = \int_{-\infty}^{+\infty} k \cdot \mathrm{Im}[\chi] dx = \sigma_0 \mathrm{Im}[\tilde{\chi}] n_{2d} \tag{3.3}$$

where OD is the optical density and I refers to the light intensity collected on the CCD camera for each specific case and n_{2d} is the atomic density integrated along the propagation direction. To collect only information about the Rydberg atoms pre-excited in the atomic gas, the collected light under presence of Rydberg

atoms I_{Ry} and without them I_{2l} is to be compared through the depleted absorption $\Delta A = (I_{Ry} - I_{2l})/I_{Ry}$

$$\Delta A = 1 - e^{-\Delta OD} \quad \text{with} \quad \Delta OD = OD_{2l} - OD_{Ry} \tag{3.4}$$

that can be experimentally accessed. This missing absorption represents the signal emerging from the excited spins, varying from 0 to A_{2l}.

The effective number ΔN of depleted ground-state atoms due to the presence of pre-excited Rydberg atoms is calculated with up to pixel resolution (pixel area $a_{px} = 4.29\,\mu\text{m}^2$ in the object plane) as

$$\Delta N = \frac{a_{px}(1+s_0)}{\sigma_0}\Delta OD = \frac{a_{px}(1+s_0)}{\sigma_0}\ln\left[(1-\Delta A)^{-1})\right] = \frac{a_{px}(1+s_0)}{\sigma_0}\ln\left[\frac{I_{Ry}}{I_{2l}}\right], \tag{3.5}$$

where $s_0 = 2\Omega_p^2/\Gamma_e^2$ accounts for intensity saturation effects of the addressed transition.

Experimental realisation

The experiments presented in this section are realised under the following conditions. In a first repetition, the ground state atomic cloud is probed by a resonant imaging beam in the $|g\rangle \leftrightarrow |e\rangle$, as described in Sec. 3.1.1. At $T \approx 40\,\mu\text{K}$, the average displacement of ^{87}Rb atoms is $\sim 1\,\mu\text{m}/\mu\text{s}$. Therefore, a reduced exposure time $t_{exp} = 5\,\mu\text{s}$ and a strong Rabi frequency $\Omega_p = 2\pi \times 1.57\,\text{MHz}$ are selected to minimize the cloud expansion during imaging, while preserving a good SNR. We measure a Gaussian-shaped atomic cloud with $\langle N\rangle \approx 1.27 \cdot 10^5$ atoms with waists $\sigma_x = 233\,\mu\text{m}$, $\sigma_y = \sigma_z = 57\,\mu\text{m}$ $(1/e^2)$. In a second repetition, Rydberg atoms are pre-excited to the state $|r\rangle = |48S_{1/2}, m_j = 1/2\rangle$, as described in Section 3.1.1. The effective Rabi frequency is estimated to present a Gaussian spatial profile with $\Omega_{eff_0} = 143\,\text{kHz}$, with waist $\sigma = 125\,\mu\text{m}$ $(1/e^2)$. Afterwards, an imaging pulse is performed in the same conditions of the first run. The collected transmitted light is processed as in Eq. 3.5 to reconstruct the two-dimensional profile of the atoms, integrated along the propagation direction $(\hat{z})$. The experiment is repeated for different excitation times ranging from $t_{exc} = 0.1\,\mu\text{s}$ up to $t_{exc} = 3\,\mu\text{s}$, in order to map the local excitation dynamics in several interaction regimes and be able to neglect dissipative effects taking place at longer times. Since the 780 nm excitation is activated during short time, the additional heating of the atomic cloud during the excitation makes a negligible impact.

In Figure 3.2, the spatial profile of the depleted absorbers $\langle \Delta N(x,y)\rangle = \langle N_{Ry}(x,y)\rangle$ is presented after an excitation time $t_{exc} = 2.03\,\mu\text{s}$, averaged over 50 repetitions of

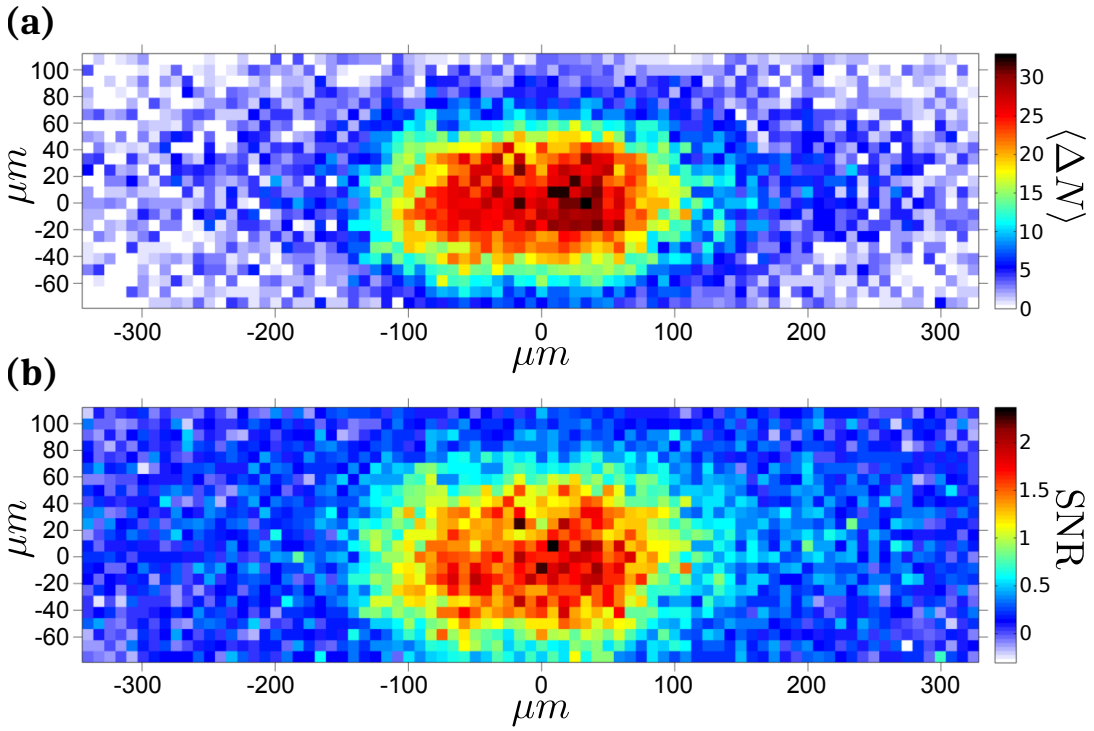

Figure 3.2: Spatial distribution of $|48S_{1/2}, m_j = 1/2\rangle$ Rydberg atoms. (a) Two-dimensional distribution of the missing number of absorbers $\Delta N(x, y)$, comparing absorption imaging of ground state atoms for two experimental realisations: with and without pre-excitation of Rydberg atoms. The difference in atom number between is attributed to the presence of Rydberg atoms $\Delta N \equiv N_{Ry}$. **(b)** Local signal-to-noise ratio (SNR). The image is the average over 50 repetitions, with exposure time $t_{exp} = 5\,\mu s$ and $\Omega_p = 2\pi \times 1.57\,\mathrm{MHz}$. The excitation time is $t_{exc} = 2.03\,\mu s$. Each image bin (4x4 pixels) is equivalent to $\sim 8.28 \times 8.28\,\mu m^2$ on the object plane at the atoms' position.

the experiment, with $8.28 \times 8.28\,\mu m$ resolution due to the use of software binning on a region of 4×4 pixels. The Rydberg ensemble emerges in a region determined by the extension of the Gaussian coupling laser beam $\Omega_c(x, y)$, with its maximum at the center, where the signal-to-noise ratio (SNR) is maximum and leads to reliable observations.

3.1.3 Observation of strong blockade in the excitation profile

By comparing the local number of ground state atoms $N(x, y)$ to the depleted number of atoms $N_{Ry}(x, y)$, this technique allows to reconstruct the population

density-matrix elements of the effective two-level system, ρ_g and ρ_{Ry}, such that

$$\rho_{Ry}(x,y) = \frac{N_{Ry}(x,y)}{N(x,y)} \qquad \text{and} \qquad \rho_{g(x,y)} = 1 - \rho_{Ry}(x,y). \tag{3.6}$$

The experimentally observed Rydberg fraction profile ρ_{Ry} is shown in Figure 3.3. At increasing driven excitation time, the initially quasi-Gaussian distribution of excitations progressively reaches a spatially-homogeneous saturation at an observed maximum $\rho_{Ry} \approx 0.28$. Fig. 3.3(b) shows a horizontal cut of the distribution at the vertical center, in which the emergence of an extended flat-top distribution of Rydberg excitations is revealed. As a consequence, the volume of the excitation region presents an increase far beyond the maximum expectations for thermal expansion.

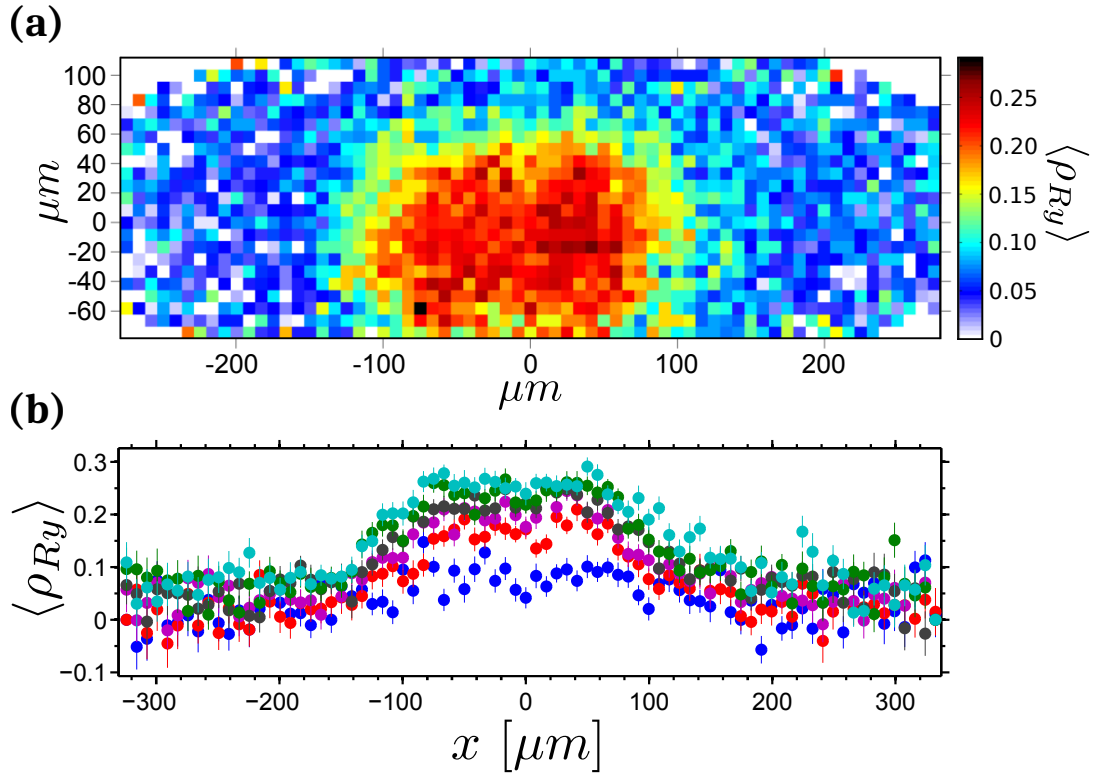

Figure 3.3: Emergence of a flat-top profile on the Rydberg distribution $\langle\rho_{Ry}\rangle$ at the center of the ensemble. (a) Rydberg fraction distribution $\langle\rho_{Ry}\rangle$ at the excitation time $t_{exc} = 2.03\,\mu s$. **(b)** Horizontal profile at the center of the Rydberg cloud ($y = 0\,\mu m$). The different data points correspond to various excitation times: $0.58\,\mu s$ (navy blue), $1.07\,\mu s$ (red), $1.55\,\mu s$ (violet), $2.03\,\mu s$ (brown), $2.52\,\mu s$ (green), $3.00\,\mu s$ (sky blue). The saturation towards a flat-top profile at higher excitation times is caused by the increasing blockade amongst Rydberg atoms. Each image bin (4x4 pixels) is equivalent to $\sim 8.28 \times 8.28\,\mu m^2$ on the object plane at the atoms' position.

The observation of saturation is interpreted as a direct effect of repulsive van der Waals interaction amongst Rydberg atoms, leading to a Rydberg blockade effect with a critical distance, estimated to be $R_{bl} = (C_6/\hbar\Delta\nu)^{1/6} \approx 4.7\,\mu$m, where $\Delta\nu$ is the spectral width of the Rydberg excitation ($\Delta\nu \gg \Omega_{eff}$). Within this distance, only a single Rydberg atom is likely to be excited. This constitutes the first direct observation of an homogeneous blockaded profile over a large ensemble of Rydberg excitations, which confirms previous observations of the emergent spatial order in Rydberg gases [Schauß *et al.*, 2012].

3.1.4 Local excitation dynamics

Further insight into the excitation dynamics can be obtained by following the temporal evolution of sub-samples of the ensemble. Previous experiments demonstrated collective Rabi oscillations amongst Rydberg atoms in a mesoscopic ensemble [Reetz-Lamour *et al.*, 2008a; Dudin *et al.*, 2012] and even at the few atom level [Gaëtan *et al.*, 2009; Urban *et al.*, 2009; Barredo *et al.*, 2014].

However, in the weakly driven regime of these experiments, the dynamics is dominated by contributions from many dephased superatoms. This results in an incoherent excitation of the Rydberg atoms, leading to saturation in the blockaded regime, previously explored in experiments performed in a large magnetic trap with homogeneous Rabi coupling [Heidemann *et al.*, 2007].

In order to quantify the excitation rates and the blockaded fraction, our data is fitted to an exponential saturation function

$$\rho_{Ry}(t) = \rho_{sat}\left(1 - e^{\frac{-R_{exc}\cdot t}{\rho_{sat}}}\right). \tag{3.7}$$

In Figure 3.4, the evolution of the excitation process in different parts of the sample is presented, revealing different regimes of evolution: fast dynamics at the center of the cloud, where the coupling is strongest, is followed by saturation as observed in Fig. 3.3, and a linear increase at the outer regions around the edge of the excitation volume (sky blue curve). The two regimes are discriminated by the ratio between the effective Rabi frequency and the interaction strength. The suppression of Rabi oscillations, leading to an initial quasi-linear increase of the excitation probability, has been predicted by many-atom wave function calculations [Robicheaux, 2005], where the effective dephasing between superatoms dominates the dynamics.

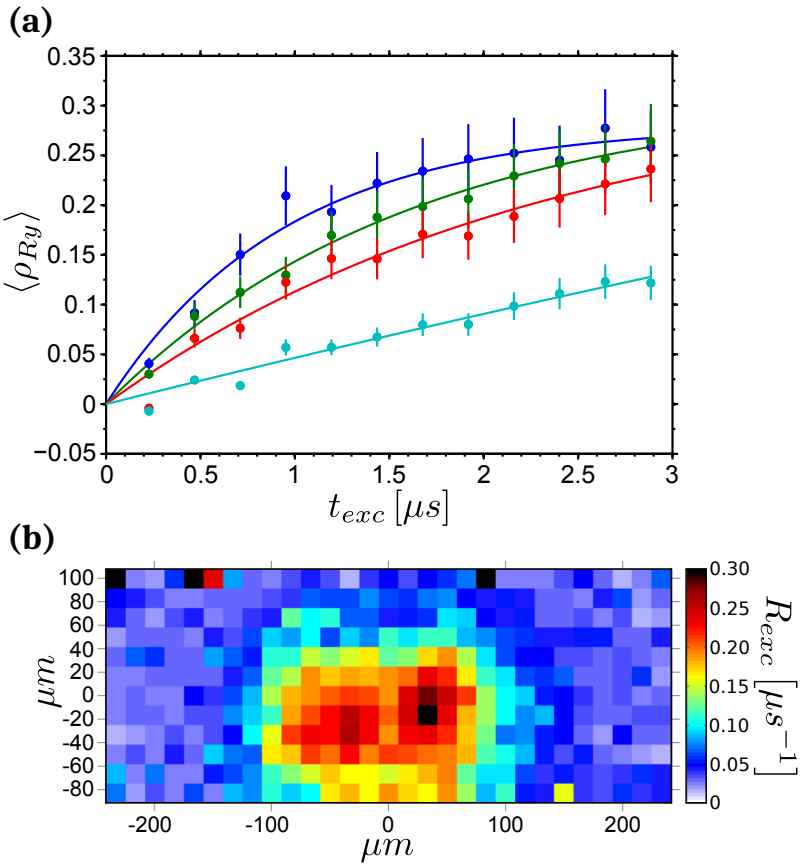

Figure 3.4: **(a)** Local excitation dynamics at different cloud positions. The lines are represent the corresponding fits to an exponentially saturating function (Eq. (3.7)). The dynamics presents a faster excitation dynamics closer to the center of the excitation region (blue, $R_{exc} = 0.298\,\mu s^{-1}$) than in outer regions (green, $R_{exc} = 0.192\,\mu s^{-1}$; red, $R_{exc} = 0.139\,\mu s^{-1}$) or at the tails (turquoise, $R_{exc} = 0.045\,\mu s^{-1}$). The fits reveal saturation due to van der Waals interaction at the following Rydberg fraction: 0.28 (blue), 0.31 (green), 0.32 (red). The dynamics saturates due to Rydberg interaction effects. Regions at the edge of the excitation area follow a slower dynamics (e.g. sky blue curve). A temporal offset $t_0 = 0.11\,\mu s$ is subtracted. **(b)** Local excitation rate R_{exc} extracted from the local fits of the excitation dynamics. Each data point (in **(a)**) or image bin (in **(b)**) corresponds to a $16.57 \times 16.57\,\mu m^2$ region at the cloud position, integrated along the imaging direction (8x8 pixels).

3.1.5 Sensitivity of the optical detection

In order to characterise the resolution of this imaging technique and determine the precision in the measurement of a local number of Rydberg atoms N_{Ry}, the local sensitivity has to be calculated. The simplest procedure consists in the determination of the signal-to-noise ratio (SNR) of the average measurements, defined as the ratio

between the mean quantity of a distribution of measurements and the standard deviation from the mean. In this specific case, the SNR of the local Rydberg atom number is given as

$$\mathrm{SNR}_{\langle N_{Ry}(x,y)\rangle} = \frac{\langle N_{Ry}(x,y)\rangle}{\sigma_{N_{Ry}(x,y)}} \tag{3.8}$$

This estimator depends on the imaging noise introduced by the optical detection and the shot-to-shot fluctuations of the ground-state density. The minimum number of atoms that generate an accurately quantifiable change in the absorption image is identified as the sensitivity threshold $\mathcal{S}$, which corresponds to the average number of atoms detected with SNR = 1, quantity directly influenced by the size of the local detection area of our CCD camera.

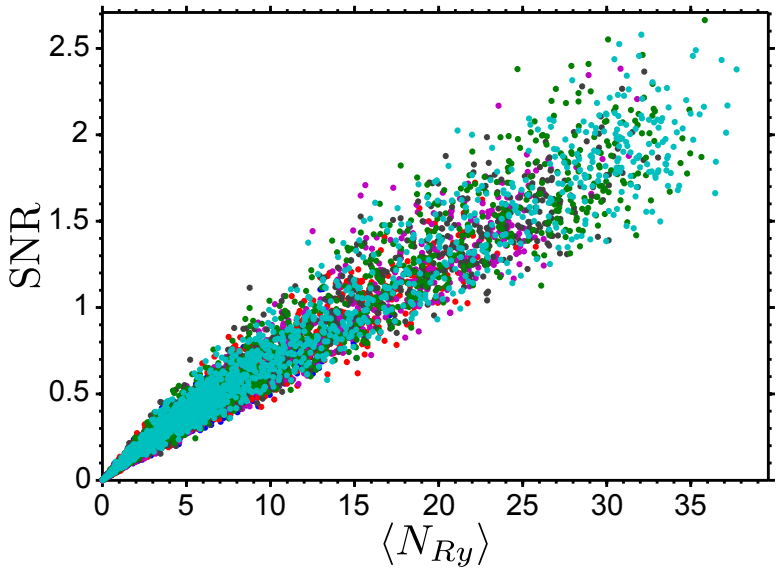

Figure 3.5: Sensitivity of the imaging technique. Signal-to-noise ratio (SNR) as a function of the mean number of Rydberg atoms $\langle N_{Ry}\rangle$ in an integrated area of $16.57 \times 16.57\,\mu\mathrm{m}^2$ (4x4 pixels). The different colours represent data from various excitation times t_{exc}, showing that the sensitivity only depends on the size of the analysed region and the imaging properties. The measured sensitivity is $\mathcal{S} \sim 15$ Rydberg atoms.

In Figure 3.2(b), the SNR corresponding to the local Rydberg atoms $\langle N_{Ry}\rangle$ from Fig. 3.2(a) is presented. The measurement reveals a fine signal-to-noise SNR > 2 towards the center of the excitation region, whereas it drops below 1 around the tails of the distribution, for each region of 16 pixels. Hence, this bin size can be preserved to spatially resolve the Rydberg excitation properties. The local sensitivity is estimated from Fig. 3.5. Each point of the graph represents the SNR of an individual $8.28 \times 8.28\,\mu\mathrm{m}^2$ integrated region. Different colours show measurements

from various t_{exc}, which present a very similar spread in $\langle N_{Ry} \rangle$ and SNR. This can be understood as an indication that the dominating noise sources are not related to the Rydberg excitation dynamics but to the experimental shot-to-shot fluctuations of light intensity. The sensitivity is estimated to be $S \simeq 15$ Rydberg atoms with a Poissonian spread, which scales quadratically with the bin surface. Therefore, in a $4.14 \times 4.14\,\mu m^2$, below R_{bl}, the depleted absorption of approximately 7.5 Rydberg atoms is required for sensitive observations, impeding to achieve enough local sensitivity to map Rydberg correlations from the intensity pattern of the image.

Global single-shot sensitivity

To quantify the accuracy of measuring a certain number of Rydberg atoms in a single realisation, a different procedure has to be introduced. We employ the threshold method to calculate the probability of having $\langle N_{Ry} \rangle$ Rydberg atoms present in the cloud or, alternatively, the presence of none of them. Then, two distributions arise from our experiment: the background distribution, where only ground-state atoms are present and therefore, it is centered around $\langle N_{Ry} \rangle \approx 0$, and the distribution with Rydberg atoms pre-excited. The later represents the "null" hypothesis H_0 that Rydberg atoms are present in the cloud, which has to be verified. The detection fidelity $\mathcal{F}$ [Bochmann *et al.*, 2010], answers this question, since it quantifies the probability for the hypothesis to be true in any single experiment, expressed as

$$\mathcal{F} = 1 - \epsilon_{max} \tag{3.9}$$

where ϵ_{max} is the maximum probability of incorrectly rejecting the H_0 hypothesis due to imperfections in the detection and/or the state preparation. Initially, an arbitrary threshold is set such that the hypothesis is accepted when $N_{Ry} < N_{thr}$. This threshold is iteratively varied until the probability of incorrect assignment is minimal and, therefore, the fidelity is maximised. In this case, this sensitivity gives a bound for detection in a single shot of the experiment. This concept is applied here to describe the single-shot measurement of the global quantities, instead of the local averaged measurements. The information extracted is complementary to the local SNR calculations.

From the fidelity $\mathcal{F}$, the single-shot sensitivity $\mathcal{S}$ can be extracted. As in the previous section, given the large number of Rydberg atoms and knowing that they follow a Gaussian distribution, we define the sensitivity threshold for single shot detection to correspond to an SNR equal to 1, which corresponds to a fidelity of $\mathcal{F} = 0.8413$. Figure 3.6 shows the fidelity calculated with the threshold method, and

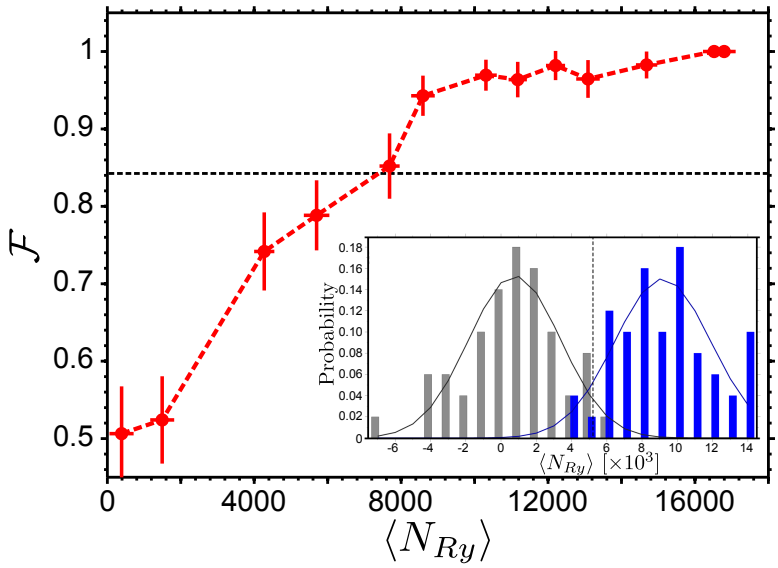

Figure 3.6: Single-shot detection fidelity for an increasing average number of Rydberg atoms $\langle N_{Ry} \rangle$. For different excitation times the sensitivity threshold $\mathcal{F} = 0.8413$ (black dashed line) is crossed at $\langle N_{Ry} \rangle \sim 7300$ Rydberg atoms. Errorbars correspond to the statistical error from the bootstrap method. **Inset:** Distributions of the background (grey), where no Rydberg spins are pre-excited, and the Rydberg atom number (blue) for the case of $\langle N_{Ry} \rangle = 8595$, revealing a fidelity $\mathcal{F} = 0.943 \pm 0.029$ per single shot.

we observe that the threshold of $\mathcal{F} = 0.8413$ is crossed at $\langle N_{Ry} \rangle \sim 7300$ Rydberg atoms, establishing that the global single-shot sensitivity of our imaging technique in the current conditions is $S \sim 7300$ Rydberg atoms in the state $|48S\rangle$.

Whereas Depletion Imaging of Rydberg atoms constitutes a precise tool to study the excitation dynamics of Rydberg atoms locally and to potentially investigate the scaling of the Rydberg spin driven dynamics [Heidemann *et al.*, 2007; Löw *et al.*, 2009; Valado *et al.*, 2016; Helmrich *et al.*, 2016], this technique is not suitable to observe the dynamical evolution of few Rydberg spins due to the insufficient sensitivity and the lack of state selectivity. In order to study the evolution of few Rydberg spins with high resolution, a sophisticated imaging technique called Interaction Enhanced Imaging has been developed and is presented in Chapter 6.

3.1.6 Detection of spins via field ionisation

As discussed in Section 2.4.2, electric fields may be applied in the experiments to bring the Rydberg atom energy above the ionisation threshold due to the Stark effect and, thus, generate Rydberg ions and guide them to an MCP detector. Due to

the lack of selectivity and the small sensitivity of the Depletion Imaging technique which has been introduced along this section, Rydberg spin detection based on the field ionisation mechanism is used in the present work as the main detection method to measure smaller number of Rydberg spins with high accuracy and when no spatial information is required, providing a global observable. Here, the detection of Rydberg atoms via field ionisation is characterised over three orders of magnitude in the Rydberg atom number. The method is compared to the global Rydberg spin measurements via Depletion Imaging, allowing to calibrate the detection efficiency η. The experiments discussed in this section are performed on the Rydberg state $|48S_{1/2}, m_j = 1/2\rangle$.

In order to calibrate the atomic detection, the global number of optically measured atoms $\langle N_{Ry}\rangle$ displayed in Figure 3.7(a) is considered as a reliable measurement. There, the initially linear increase starts to slightly saturate, due to the van der Waals blockade between Rydberg atoms. However, the global measurement does not show such strong saturation (see Fig. 3.3) since Rydberg atoms can still be excited in the tails of the distribution. In contrast, the dynamics measured by field ionisation (Fig. 3.7(b)) reveals a big saturation effect, starting at ~ 1270 (a.u.). At this turning point the Rydberg atom densities are $\geq 1.5 \times 10^9\,\mathrm{cm}^{-3}$, leading to an estimated Wigner-Seitz radius $\leq 5.3\,\mu\mathrm{m}$. This could arise due to the increasing Coulomb repulsion amongst the created ions during the time-of-flight towards the MCP, such that a fraction of ions is unable to hit the detector. As a consequence, initially constant detection efficiency $\eta_{48S} = 0.227$ can be accurately inferred from the comparison of both methods in the linear regime, where all the experiments explained in the scope of this thesis occur. As observed in Fig. 3.7(c), the efficiency progressively decreases at high atom numbers.

Hence, combined optical and atomic detection of Rydberg atoms establishes an accurate and consistent calibration protocol which is used to measure the detection efficiency of the MCP detector across few orders of magnitude in the Rydberg density. In the following spin experiments from Chs. (4, 5), all measurements are performed in the linear regime for low and intermediate Rydberg densities. In spite of the increasing systematic error introduced at higher densities, field ionisation detection is a very sensitive technique (SNR $\gg 1$) to measure global Rydberg spin numbers in different regimes and the bias of the signal can be corrected by accounting for the quasi-linear reduction of detection efficiency.

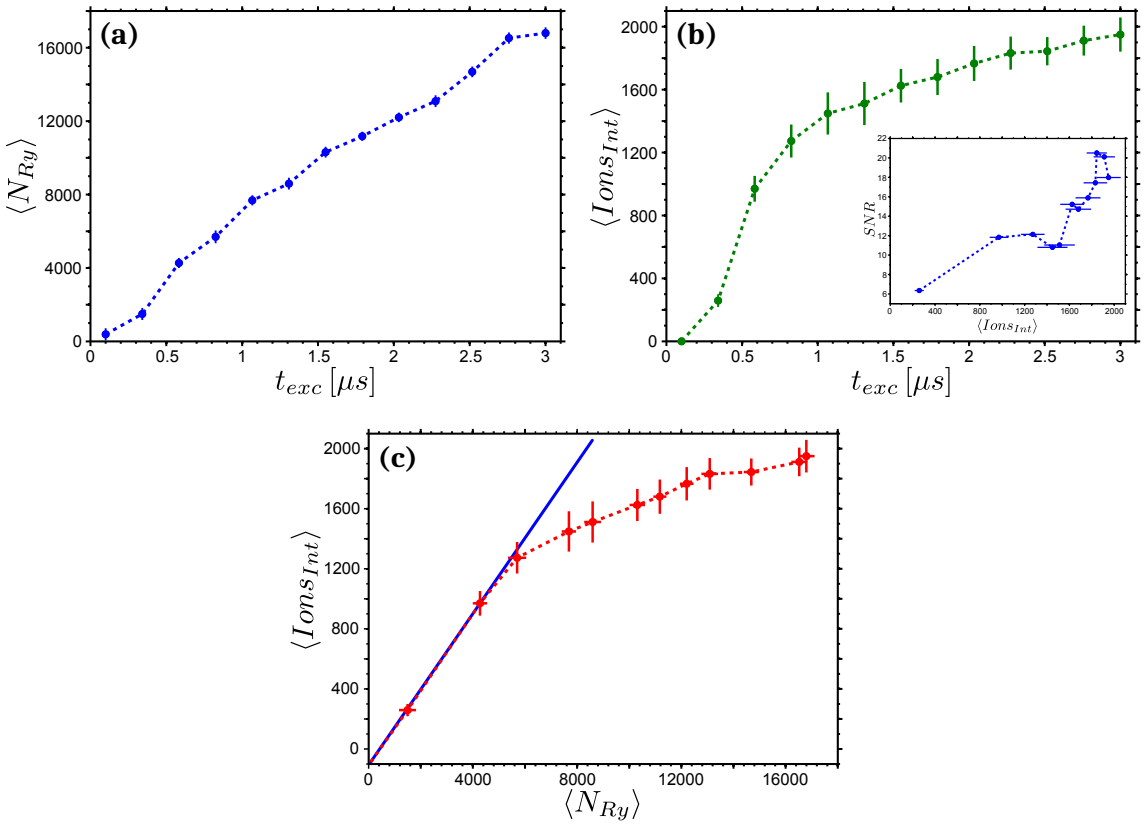

Figure 3.7: Global measurements of $|48S_{1/2}, m_j = 1/2\rangle$ Rydberg atom signal. **(a)** Total average number of Rydberg atoms in the excitation time as a function of the excitation time t_{exc}. The optically measured number of Rydberg atoms $\langle N_{Ry} \rangle$ is extracted from the mean depletion of the ground state, averaging over 50 repetitions. **(b)** Integrated ion signal on the MCP detector . At high number of ions, the signal $\langle Ions_{Int} \rangle$ collected on the MCP saturates. Inset: SNR of the field-ionised integrated ion signal. SNR $\gg 1$. The signal $\langle Ions_{Int} \rangle$ is the average over 50 repetitions. Errorbars correspond to the standard deviation. **(c)** Comparison between the optically detected number of Rydberg atoms $\langle N_{Ry} \rangle$ and the measured integrated ion signal $\langle Ions_{Int} \rangle$. The detection efficiency in the typical regime is extracted from a fit of the first two points, giving $\eta_{48S} \approx 0.227$.

3.2 Two-photon resonant excitation: spatial characterisation

In this section, a two-photon resonant scheme is applied, based on the principles of electromagnetically-induced transparency (EIT), to excite a fraction of the ground state atoms to the Rydberg state. Unlike for the two-photon off-resonant scheme implemented in Section 3.1, we do not require an additional Depletion Imaging

method to characterise the subsequent spin distribution in the resonant case, but can be fully described by combining the theoretical knowledge of EIT with measurements of the EIT absorption spectra and applying parallel optical spectroscopy analysis of multiple pixels in a single experiment to resolve the spatial distribution. This is combined with additional information obtained by atomic spectroscopy of the Rydberg population spectrum. The coupling Rabi frequency profile $\Omega_c(x, y)$ as well as spatially resolved optical susceptibility χ and Rydberg fraction ρ_{rr} are successfully reconstructed [Gavryusev *et al.*, 2016b]. Such scheme has been previously used to create Rydberg spins to the state $|\downarrow\rangle = |48S_{1/2}, m_j = 1/2\rangle$ and measure the interaction-induced dephasing on Rabi oscillations to the spin state $|\uparrow\rangle$ [Schempp, 2014, Ch. 7; Piñeiro Orioli *et al.*, 2017]. In addition, the characterisation presented here constitutes the basis to apply Interaction Enhanced Imaging to observe of Rydberg spins, as explained in Chapter 6.

3.2.1 Three-level Optical Bloch Equations and weak probe solution

Electromagnetically-induced transparency is a quantum interference effect which emerges in a three-level system when two long-lived states are coherently and resonantly coupled to a short-lived state [Harris, 1997; Marangos, 1998; Fleischhauer *et al.*, 2005]. Hereafter, a ladder scheme described by the atomic ground state $|g\rangle = |5S_{1/2}\rangle$, the fast decaying intermediate state $|e\rangle = |5P_{3/2}\rangle$ and a long-lived Rydberg state $|nS_{1/2}\rangle$ is considered, as described in Fig. 3.8. The optical control field Ω_c which couples the $|e\rangle \leftrightarrow |r\rangle$ branch renders an otherwise absorptive gas transparent to the weak probe beam Ω_p. Strong coupling produces an Autler-Townes doublet of dressed states and, subsequently, destructive interference on the transition probability [Fano, 1961] for the probe laser addressing the transition $|g\rangle \leftrightarrow |e\rangle$. Therefore, the transparency resonance is sensitive to the Rydberg-state properties [Mohapatra *et al.*, 2007].

In the low density regime, the system can be well-described by the analytic solution of the steady-state optical Bloch equations (OBE) for the single-atom density matrix. The three-level non-interacting Hamiltonian of the atom-light coupled system in the rotating wave approximation is described as

$$\hat{\mathcal{H}} = \frac{\hbar}{2} \begin{pmatrix} 0 & \Omega_p & 0 \\ \Omega_p & -2\Delta_p & \Omega_c \\ 0 & \Omega_c & -2\left(\Delta_p + \Delta_c\right) \end{pmatrix} \tag{3.10}$$

where $\Omega_{p,c}$ are the Rabi frequencies of the probe and coupling lasers, and $\Delta_{p,c}$ are the detunings from the probe and coupling transitions. The intermediate state decays with decoherence rate Γ_e to the ground state, whereas decay from the long-lived Rydberg state can be neglected ($\Gamma_r \ll \Gamma_e\,\Omega_{p,c}$). In order to account for incoherent effects like decay and laser dephasing [Pritchard *et al.*, 2010; Gärttner and Evers, 2013], the master equation for the single-atom density matrix ρ is derived

$$\dot{\rho} = -\frac{\mathrm{i}}{\hbar}[\hat{\mathcal{H}}, \rho] + \mathcal{L}_{\mathrm{dec}}(\rho) + \mathcal{L}_{\mathrm{deph}}(\rho). \tag{3.11}$$

The Lindblad superoperator terms [Lindblad, 1976] read as

$$\mathcal{L}_{\mathrm{dec}}(\rho) = -\frac{1}{2}\sum_k (C_k^\dagger C_k \rho + \rho C_k^\dagger C_k) + \sum_k C_k \rho C_k^\dagger \tag{3.12a}$$

$$\mathcal{L}_{\mathrm{deph}}(\rho) = -\frac{1}{2}\begin{pmatrix} 0 & \gamma_p\rho_{ge} & \gamma_{gr}\rho_{gr} \\ \gamma_p\rho_{eg} & 0 & \gamma_c\rho_{er} \\ \gamma_{gr}\rho_{rg} & \gamma_c\rho_{re} & 0 \end{pmatrix}, \tag{3.12b}$$

where $C_{ge} = \sqrt{\Gamma_e}\,|g\rangle\langle e|$ and $\sqrt{\Gamma_r}\,|e\rangle\langle r|$ describe the quantum jumps amongst the involved states.

As a result, the system is fully described by the following set of coupled equations

$$\begin{aligned}
\dot{\rho}_{gg} &= -\Omega_p \mathrm{Im}[\rho_{ge}] + \Gamma_e \rho_{ee} \\
\dot{\rho}_{ee} &= +\Omega_p \mathrm{Im}[\rho_{ge}] - \Omega_c \mathrm{Im}[\rho_{er}] - \Gamma_e \rho_{ee} + \Gamma_r \rho_{rr} \\
\dot{\rho}_{rr} &= +\Omega_c \mathrm{Im}[\rho_{er}] - \Gamma_r \rho_{rr} \\
\dot{\rho}_{ge} &= -\Gamma_{ge}\rho_{ge}/2 + \mathrm{i}\Omega_c \rho_{gr}/2 + \mathrm{i}\Omega_p(\rho_{gg} - \rho_{ee})/2 \\
\dot{\rho}_{gr} &= -\Gamma_{gr}\rho_{gr}/2 - \mathrm{i}(\Omega_p \rho_{er} - \Omega_c \rho_{ge})/2 \\
\dot{\rho}_{er} &= -\Gamma_{er}\rho_{er}/2 - \mathrm{i}(\Omega_c \rho_{rr} + \Omega_p \rho_{gr} - \Omega_c \rho_{ee})/2\,,
\end{aligned} \tag{3.13}$$

with $\rho_{jk} = \rho_{kj}^*$. The equations rely on the rates $\Gamma_{ge} = \Gamma_{ge}^0 + 2\mathrm{i}\Delta_p$, $\Gamma_{er} = \Gamma_{er}^0 + \gamma_c + 2\mathrm{i}\Delta_c$ and $\Gamma_{gr} = \Gamma_{gr}^0 + 2\mathrm{i}(\Delta_p + \Delta_c)$ with $\Gamma_{ge}^0 = \Gamma_e + \gamma_p$, $\Gamma_{er}^0 = \Gamma_e + \Gamma_r + \gamma_c$, $\Gamma_{gr}^0 = \Gamma_r + \gamma_{gr}$.

Steady-state weak-probe solution

After transient evolution, the system reaches stationary equilibrium. Such steady state is described at $\dot{\rho_{jk}} = 0$ by the following relations

$$\rho_{ee} = \frac{\Omega_p \mathrm{Im}[\rho_{ge}]}{\Gamma_e}, \quad \rho_{er} = \frac{\Omega_p \mathrm{Im}[\rho_{gr}]}{\mathrm{Re}[\Gamma_{er}]}, \quad \rho_{rr} = \frac{\mathrm{i}\Gamma_{er}\rho_{er} + \Omega_c \rho_{ee} - \Omega_p \rho_{gr}}{\Omega_c}. \tag{3.14}$$

Assuming a weak probe approximation ($\Omega_p \ll \Omega_c, \Gamma_e$), the coherences are analytically approximated as

$$\rho_{ge} \approx \frac{\mathrm{i}\Gamma_{gr}\Omega_p}{\Gamma_{ge}\Gamma_{gr} + \Omega_c^2}, \quad \rho_{gr} \approx \frac{-\Omega_c\Omega_p}{\Gamma_{ge}\Gamma_{gr} + \Omega_c^2}. \tag{3.15}$$

When both transitions are resonantly addressed and Ω_c is higher than the dephasing terms, then, due to destructive interference, the probability to populate the intermediate state drops to zero, opening a transparency window with FWHM as $\sigma_{eit} = \Gamma_{gr}^0 + \frac{\Omega_c^2}{\Gamma_e}$ for $\Omega_c < \Gamma_e$ and $\sigma_{eit} = \Omega_c$ when $\Omega_c \geq \Gamma_e$.

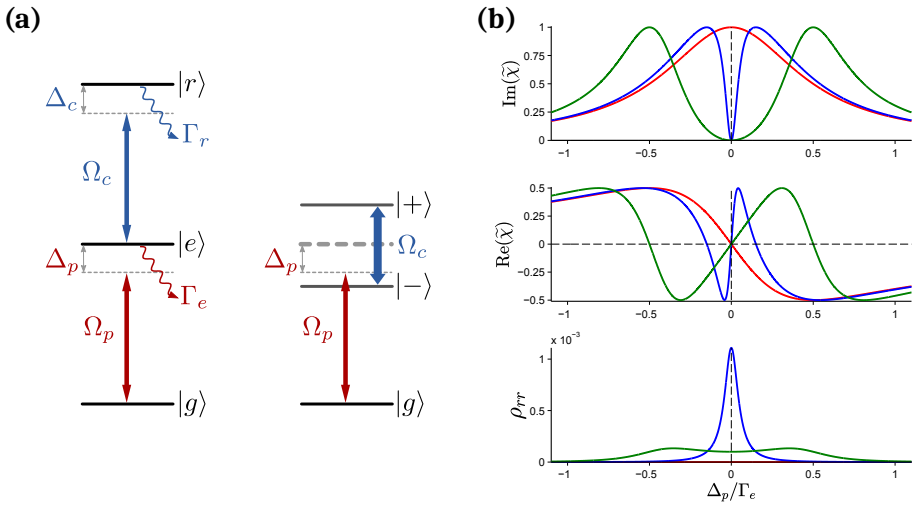

Figure 3.8: **(a)** Three-level ladder scheme for Rydberg EIT. The atomic ground state $|g\rangle$, the fast-decaying intermediate state $|e\rangle$ and the selected Rydberg state $|r\rangle$ are simultaneously coupled by two laser fields with probe and coupling Rabi frequencies $\Omega_{p,c}$ and $\Delta_{p,c}$ detuned from the single photon resonances. The excited and Rydberg states decay with rates $\Gamma_{e,r}$, where $\Gamma_r \lll \Gamma_e$. Under strong coupling ($\Omega_c \geq \Gamma_e$), the eigenstates are well-defined in the dressed-state basis as the split Autler-Townes doublet $|\pm\rangle = \frac{1}{\sqrt{2}}(|r\rangle \pm |e\rangle)$. Scheme adapted from [Günter, 2014]. **(b)** Analytical weak-probe response of the imaginary and real part of the scaled optical susceptibility and Rydberg population fraction (Eqs.(3.14,3.15)) as a function of the probe detuning, given $\Gamma_r, \Delta_c = 0$ and negligible laser-induced dephasing. Three cases are presented: $\Omega_c = 0$ (red) describes the two-level response; $\Omega_c = 0.3\Gamma_e$ shows a narrow EIT resonance with Lorentzian ρ_{rr} distribution; $\Omega_c = \Gamma_e$ presents the strong coupling regime, where the Autler-Townes peaks are highly separated ($\sigma_{eit} \approx \Omega_c$) and the Rydberg population is suppressed.

Experimentally accessible variables

The density matrix element ρ_{ge} can be immediately determined by accessing the scaled susceptibility (Eq. 3.1). Simulated weak-probe steady-state scaled susceptibility can be found in Fig. 3.8(b). Additional laser dephasing mechanisms would lead to finite absorption, reducing the depth of the EIT resonance, as described in [Pritchard, 2011; Günter, 2014; Gavryusev, 2016]. This quantity determines the transmission of the probe field through the atomic cloud,

$$T \approx= \exp\left(-\sigma_0 \mathrm{Im}[\tilde{\chi}] n_{2d}\right) = \exp(-\mathrm{OD})\,. \tag{3.16}$$

Additionally, the Rydberg population $N_r = \int \rho_{rr}(r) n(r) dr$ can be measured by field ionisation.

Three-level optical susceptibility

Based on an analytical calculation of ρ_{ge} (Eq. 3.15), the specific case of the resonant EIT susceptibility χ^0_{eit} results in

$$\chi^0_{eit} = \frac{\sigma_0 n}{k} \frac{i\Gamma_e^2}{\Gamma_e^2 + \Omega_c^2 \Gamma_e/\gamma_{gr} + 2\Omega_p^2}\,. \tag{3.17}$$

χ^0_{eit} depends on the effective dephasing rate $\gamma_{gr}/2$ of the matrix element ρ_{gr} (Eq. 3.15), with contributions of the decay rate of $|r\rangle$ and any additional dephasing effect. However, the sources of dephasing acting on the intermediate level $|e\rangle$ are negligible compared to Γ_e. Equation (3.17) shows that $\chi^0_{eit} \ll \sigma_0 n/k$ as soon as $\Omega_c^2 \gg \Gamma_e \gamma_{gr}$, which is satisfied for coupling Rabi frequencies Ω_c on the order of few MHz.

3.2.2 Experimental reconstruction of spatial properties: non-interacting density matrix

Here, we show measurements of EIT optical and atomic spectra as function of the probe laser detuning Δ_p for the case of a spatially inhomogeneous coupling beam $\Omega_c(x, y)$ [Gavryusev *et al.*, 2016b]. The observations from Figs. (3.9, 3.10) are performed under identical experimental conditions. Prior knowledge given by the analytic weak-probe solution of the OBEs is used to identify the two observables allow to fully characterise the system by determining its non-interacting density matrix: Rydberg population N_r and probe-beam transmission through the cloud T (Eq. (3.16)). All experimental parameters $(\Omega_{p,c}\,, \Delta_{p,c}\,, \Gamma_{ge,gr})$ and density matrix elements of interest $(\rho_{ge}\, \rho_{rr})$ can be obtained by accurate analysis of both variables.

For the sake of simplicity, the few kHz Rydberg decay rate can be neglected, since it is three orders of magnitude smaller than the other decays and Rabi frequencies. Laser-induced dephasing on the probe transition is also neglected, since $\gamma_p \ll \Gamma_e$, whereas γ_{deph} must be still considered in the Rydberg state.

Experimental procedure: local resolution

In the experiments presented here, a three-level ladder scheme (Fig. 3.8(a)) couples the states $|g\rangle = |5S_{1/2}, F = 2, m_F = 2\rangle$, $|e\rangle = |5P_{3/2}, F = 3, m_F = 3\rangle$ and $|g\rangle = |42S_{1/2}, m_j = 1/2\rangle$, as described in Section 2.4.1. A homogeneous 3 G magnetic field along the probe beam direction defines the quantisation axis. Our probe Rabi frequency is measured by saturated absorption imaging, such that $\Omega_p/2\pi = (1.03 \pm 0.05)$ MHz [Reinaudi *et al.*, 2007]. The coupling laser is focused into the center of the cloud with a waist of $\sim 15\,\mu$m and an intensity of $\sim 0.9\,\frac{\text{kW}}{\text{cm}^2}$. Approximately $3 \cdot 10^6$ ground state atoms are prepared in the ODT, resulting in an elliptical Gaussian-shaped cloud with width $\sigma_{\text{radial}} = 90 \pm 7\,\mu$m, $\sigma_{\text{axial}} = 380 \pm 13\,\mu$m ($1/e^2$) and a peak atomic density of $n_0 = 7 \cdot 10^9\,\text{cm}^{-3}$. The peak Rydberg density is expected to be $\rho_{rr} n_0 \leq 2 \cdot 10^9\,\text{cm}^{-3}$, corresponding to a Wigner-Seitz radius of $4.9\,\mu$m, much larger than the predicted blockade radius of $\approx 2.3\,\mu$m. Under these conditions, interactions effects are assumed to be negligible [Pritchard *et al.*, 2010; Schempp *et al.*, 2010; Sevinçli *et al.*, 2011; Ates *et al.*, 2011].

To measure the optical response we record 93 averaged absorption images for different probe detunings $\Delta_p/2\pi$ ranging from -8.1 MHz to 8.1 MHz. Since the coupling beam does not cover the whole cloud, the measured transmission in the regions where the coupling Rabi frequency is negligible ($\Omega_c \to 0$) provides information on the susceptibility of the two-level system composed by the states $|g\rangle$ and $|e\rangle$. Pixels illuminated by the coupling beam are excluded in order to fit each image to a 2D Gaussian distribution. This fit is interpolated into the excluded area to infer the two-level absorption and the local atomic 2D density n_{2d} of the atom cloud at the position of the coupling beam. Then, the scaled optical susceptibility $\tilde{\chi}(\Delta_p)$ is extracted for each pixel as in Eq. 3.16. In addition, the Rydberg-state population is detected at the end of the sequence, with the signal integrated and calibrated as described in Ch. 2.4.1 to quantify the number of detected ions.

In Figure 3.9(a), the imaginary part of $\tilde{\chi}(\Delta_p)$ is presented, for a region measured at the center of the coupling laser beam (red diamonds). This is compared with the two-level susceptibility (blue circles) and the corresponding Rydberg population spectrum (green squares). On two-photon resonance, we observe a complete suppression of

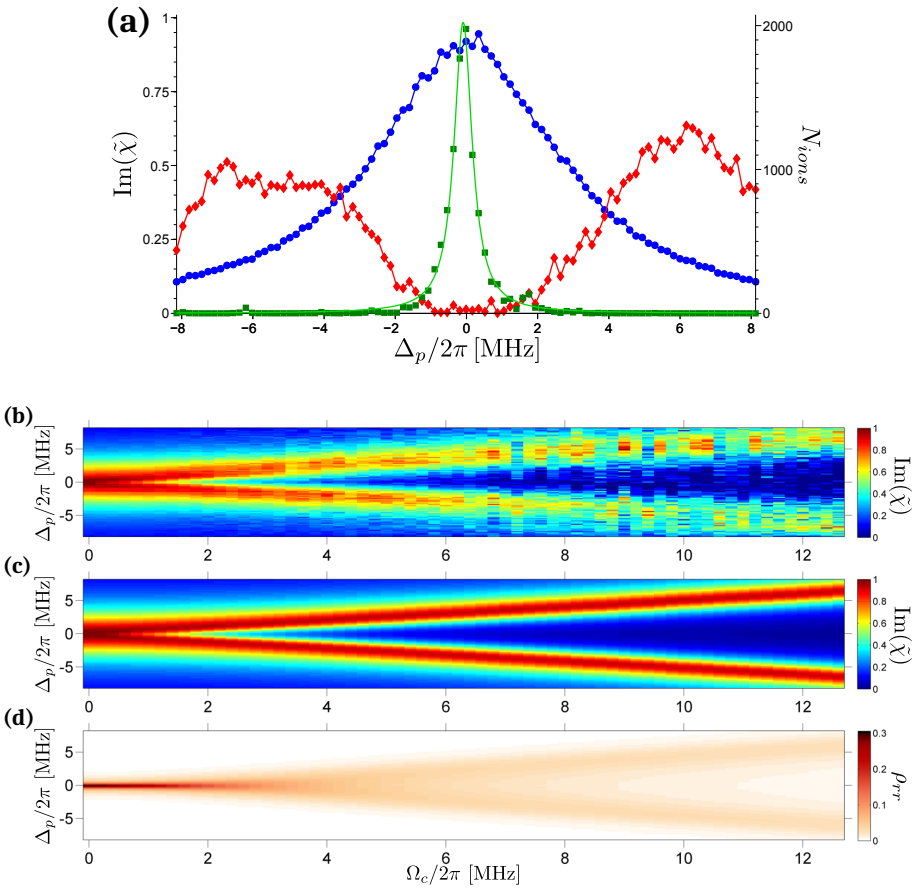

Figure 3.9: **(a)** Local scaled optical susceptibility and population spectrum as a function of the probe laser detuning. The three curves show: three-level optical response averaged over the center of the coupling laser beam (red diamonds), two-level optical response (blue circles) and integrated Rydberg population (green squares, right axis). The green solid line represents the Rydberg population spectrum estimated by numerically solving the OBEs. The asymmetry of the absorption spectrum is attributed to residual lensing effects [Han *et al.*, 2015]. **(b)** Locally measured three-level absorption spectra, sorted according to the fitted coupling Rabi frequencies with $0.2\,\mathrm{MHz}$ binning. The transition from the EIT towards the Autler-Townes regime is observed. **(c)** Fitted absorption spectra using Eqs. (3.15-3.2). **(d)** Rydberg population spectrum inferred analytically (Eq. (3.14)).

absorption ($> 99\%$). The Rydberg population spectrum is much narrower and shows no evidence for the Autler-Townes doublet structure.

A two-step fitting algorithm is applied to allow pixel-by-pixel resolution. In the first step, the two level absorption is fitted to a Lorentzian lineshape and used to calibrate the two-level optical response. The resonance width is observed to be $(6.21 \pm 0.03)\,\mathrm{MHz}$, in good agreement with the power broadened natural decay rate $\Gamma_e/2\pi \cdot \sqrt{1 + 2(\Omega_p/\Gamma_e)^2} = 6.23\,\mathrm{MHz}$. This confirms that the dephasing

plays a limited role on the $|g\rangle \leftrightarrow |e\rangle$ transition. Analogously, a Lorentzian fit is employed on the detected Rydberg population to determine the laser detuning $\Delta_c/2\pi = (0.10 \pm 0.01)\,\mathrm{MHz}$ and the resonance width $W/2\pi = (0.63 \pm 0.01)\,\mathrm{MHz}$, which is attributed to dephasing of the Rydberg state ($\gamma_{\mathrm{deph}} = W$). Now, all global parameters are determined and only the locally varying $\Omega_c(x, y)$ remains unknown. Using the fitted local two-level optical susceptibility and Eqs. (3.2, 3.16), $\tilde{\chi}(\Delta_p)$ is extracted. The local measurement is shown in Fig. 3.9(b). In order to efficiently estimate $\Omega_c(x, y)$ (Fig. 3.9(c)), the least-squares difference amongst each-pixel spectrum and the theoretical model is minimised. The measurements yield coupling Rabi frequencies up to 12.8 MHz.

Reconstruction of Ω_c, ρ_{33} and $\tilde{\chi}$

Figure 3.10(a) shows the spatial distribution of coupling beam Rabi frequencies as extracted from the fits to the single-pixel optical spectra. The distribution reflects the elliptical shape of the coupling beam, independently confirmed using a beam profiler. The measured coupling profile approaches a Gaussian with peak Rabi frequency $\Omega_c/2\pi = (12.8 \pm 0.5)\,\mathrm{MHz}$, close to the theoretical expectation of $\Omega_c/2\pi = 10.7\,\mathrm{MHz}$ which considers the coupling laser intensity, the dipole matrix element for the $|5P_{3/2}\rangle$ to $|42S_{1/2}\rangle$ transition and the extension of the excitation region. The fitted sigma radii of the axes present are 11.8 µm (semi-minor) and 15.4 µm (semi-major).

Combining the spatially-resolved distribution of Rabi frequencies (Fig. 3.10(a)) and the global parameters constrained by the two-level absorption and of the total Rydberg population spectrum, we can reconstruct the full density matrix of the system at each position using the analytical solution derived in equations (3.14) and (3.15). As practical demonstrations, we show the spatial distribution of $\tilde{\chi}$ and the Rydberg population ρ_{rr} (Fig. 3.10(b-d)). Using the results of this reconstruction procedure, we also present the Rydberg population as a function of Ω_c and Δ_p in Fig. 3.9(d). For large coupling strengths ($\Omega_c > \Gamma_e$) the Rydberg population resembles the Autler-Townes doublet resonance structure with two maxima at $\Delta_p = \pm\Omega_c/2$, while in the limit of weak coupling $\Omega_c \ll \Gamma_e$ the population is concentrated in a narrow peak with maximum at resonance. The small population is consistent with the expression $\rho_{rr} \approx \Omega_p^2/(\Omega_p^2 + \Omega_c^2)$ for two-photon resonant with negligible dephasing.

At the edges of the coupling beam region, the validity of the analytic solution breaks down, since the condition $\Omega_p \ll \Omega_c$ is not fulfilled, which becomes visible in Fig. 3.10(b). This is compared to the time-dependent numerical solution of the OBEs, finding a mismatch smaller than 25% for coupling Rabi frequencies $\Omega_c \geq \Omega_p$,

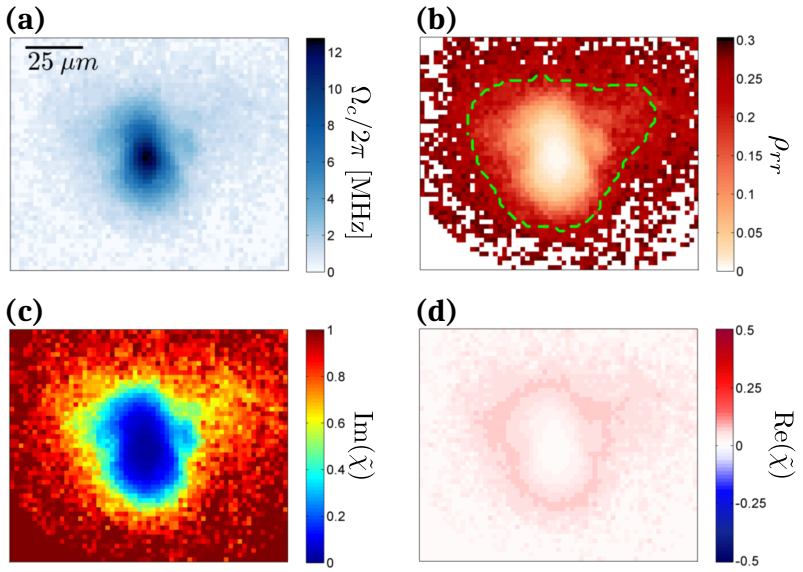

Figure 3.10: Reconstructed spatial distribution of **(a)** the coupling Rabi frequency $\Omega_c(x, y)$, **(b)** the Rydberg population distribution and **(c-d)** the imaginary and real parts of the scaled optical susceptibility $\tilde{\chi}$. For (b-d) we use analytic solutions of the OBE (Eqs. (3.14-3.2)) for $\Delta_p = 0$. The green dashed line in (b) marks the limit of validity of the analytic reconstruction of ρ_{33} using Eq. (3.14). Outside the coupling region defined by **(a)** $\mathrm{Im}[\tilde{\chi}]$ tends to reach the two-level response. $\mathrm{Re}[\tilde{\chi}] \approx 0$, with slightly increasing towards the edge of the region of interest due to the effect of a small detuning $\Delta_c/2\pi = 0.1\,\mathrm{MHz}$.

which is set as a criteria for validity of the analytic reconstruction and is indicated by the green dashed line in Fig. 3.10(b). The numerical simulation is also employed to reproduce the measured population spectrum (solid green line in Fig. 3.9(a)) by spatially integrating $\rho_{rr}(x, y)$. Best agreement is achieved fort $\gamma_{\mathrm{deph}}/2\pi$ to the value $(0.20 \pm 0.02)\,\mathrm{MHz}$. Therefore, additional broadening seen in Fig. 3.9(a) may be attributed to a combination of power broadening of the $|g\rangle \leftrightarrow |e\rangle$ transition and spatial averaging over the excitation volume, atomic motion and residual Rydberg-Rydberg interactions [Pritchard *et al.*, 2010; Gärttner and Evers, 2013; Zhang *et al.*, 2014a]. Further details can be consulted in [Gavryusev *et al.*, 2016a].

The reconstructed imaginary and real parts of the scaled optical susceptibility $\tilde{\chi}$ using the analytical formulas in Sec. 3.2 are shown for $\Delta_p = 0$ (for $\gamma_{\mathrm{deph}}/2\pi = 0.63\,\mathrm{MHz}$) in Fig. 3.10(c-d). As expected, $\mathrm{Im}[\tilde{\chi}]$ shows almost full transparency $\mathrm{Im}[\tilde{\chi}] \approx 0$ at the center of the coupling beam, whereas it approaches the two-level response in the outer region. In contrast, $\mathrm{Re}[\tilde{\chi}]$, which is responsible for light dispersion, is nearly zero across the whole spatial profile for $\Delta_p = 0$. The small

observed deviation at the edges of the coupling beam region is due to the relatively steep dispersion for $\Omega_c \ll \Gamma_e$, combined with the slight detuning of the coupling beam $\Delta_c/2\pi = 0.1\,\mathrm{MHz}$. For larger detunings $\Delta_p \approx \Omega_c/2$ the amplitude of $\mathrm{Re}[\tilde{\chi}]$ can increase significantly. Similar effects have been studied in [Han *et al.*, 2015].

Application as a spin preparation method

Combined field ionisation atomic detection and optical absorption spectroscopy allowed us to spatially reconstruct relevant terms of the density matrix of a non-interacting Rydberg ultracold gas under EIT conditions. Specially useful is the usage of the technique to characterise $\Omega_c(x, y)$ in a spatially-resolved manner, which is used for all excitation schemes described in this thesis. The spatial distribution of Rydberg spins is successfully inferred, demonstrating that the spin distribution is suppressed at the center of the coupling laser beam, where the transparency is stronger. Such scheme is also used in Ch. 6 as a method to prepare an appropriate medium to image Rydberg atoms.

3.3 Three-photon excitation of $|nP\rangle$ Rydberg states

To prepare $|nP\rangle$ Rydberg states, a two-photon excitation is prohibited by the selection rules. Instead we use a three-photon excitation, making use of two optical photons and an additional microwave photon. This procedure aims to create $|nP\rangle$ Rydberg spins directly, with no need to excite $|nS\rangle$ states beforehand. The excitation mechanism relies on a three-photon excitation scheme, off-resonant from the intermediate $|e\rangle$ and $|nS\rangle$ states, to directly transfer the population to the addressed $|nP\rangle$ with negligible population of the intermediate levels. This approach allows us to independently excite $|nP\rangle$ states or $|nS\rangle$, both required for the experiments presented in this thesis. Here, the theoretical approach to describe a four level system and its approximation as an effective two level system is explained before presenting a spectroscopic characterisation of the excitation dynamics, including the underlying atomic physics and observable effects of Rydberg-Rydberg interactions.

3.3.1 Off-resonant excitation of $|nP\rangle$ states: theoretical description

The three-photon excitation scheme is presented in Figure 3.11. The first stage of the excitation is done using a 780 nm laser beam propagating along the vertical

direction and linearly polarized perpendicular to the quantisation axis (defined by B_x), such that it generates both σ^+ and σ^- polarisation. The σ^+-polarisation couples the ground state $|g\rangle$ to the intermediate state $|e\rangle$. The σ^--polarised light leads to off-resonant processes that can be neglected in good approximation. Hence, a 480 nm σ^--polarised laser, parallel to the quantisation axis, couples $|e\rangle$ to the Rydberg state $|r\rangle = |nS_{1/2}, m_j = 1/2\rangle$. The third stage of the excitation to the state $|i\rangle = |nP_{3/2}, m_j\rangle$ is done using a microwave photon from the Anritsu MG3697C microwave synthesizer with a frequency between 2 and 67 GHz, depending on the chosen n. The selection of m_j sub-state of $|i\rangle$ is performed by the polarisation of the microwave field. This four-level system is then described by the Hamiltonian

$$\hat{\mathcal{H}} = \frac{\hbar}{2}\begin{pmatrix} 0 & \Omega_e & 0 & 0 \\ \Omega_e & -2\Delta_e & \Omega_r & 0 \\ 0 & \Omega_r & -2\Delta_r & \Omega_{mw} \\ 0 & 0 & \Omega_{mw} & -2\Delta_{mw} \end{pmatrix} \tag{3.18}$$

in the basis $\{g, e, r, i\}$. The accumulated one-photon, two-photon and three-photon detunings are given by Δ_e, Δ_r, Δ_{mw}, respectively, whereas Ω_e, Ω_r, Ω_{mw} refer to the Rabi frequencies of each transition.

Effective two-level approximation of a four-level system

To avoid populating the two intermediate states $|e\rangle$ and $|r\rangle$, we use large intermediate detunings Δ_e and Δ_r compared to the Rabi frequencies Ω_e, Ω_r and Ω_{mw}. In this regime, the four-level excitation can be described by an effective two-level system that we theoretically develop in this section. The model helps to derive the best strategy to efficiently excite Rydberg $|nP\rangle$ states without any undesired additional effects.

To simulate the three-photon excitation one can use the optical Bloch equations in the four-level basis and numerically solve them for a set of the six experimental parameters given by Eq. (3.18). However, the numerical simulations do not give insight into the excitation process to find the optimal settings for efficient state preparation. Since the excitation is done in the off-resonant regime $\Delta_e, \Delta_r \gg \Omega_e, \Omega_r, \Omega_{mw}$, the evolution of the intermediate state populations exhibit two very different timescales, leading to a rapidly oscillating term at a frequency $\Delta_{e,r}$ and a slow-varying envelope that evolves together with the states $|g\rangle$ and $|i\rangle$. After a short-time, the fast oscillations average to zero due to the decay of the short-lived intermediate state $|e\rangle$. The time derivative of the $|e\rangle$ and $|r\rangle$ populations can then be set to zero as they are dominated by the fast-oscillating terms. By introducing the steady state solutions in

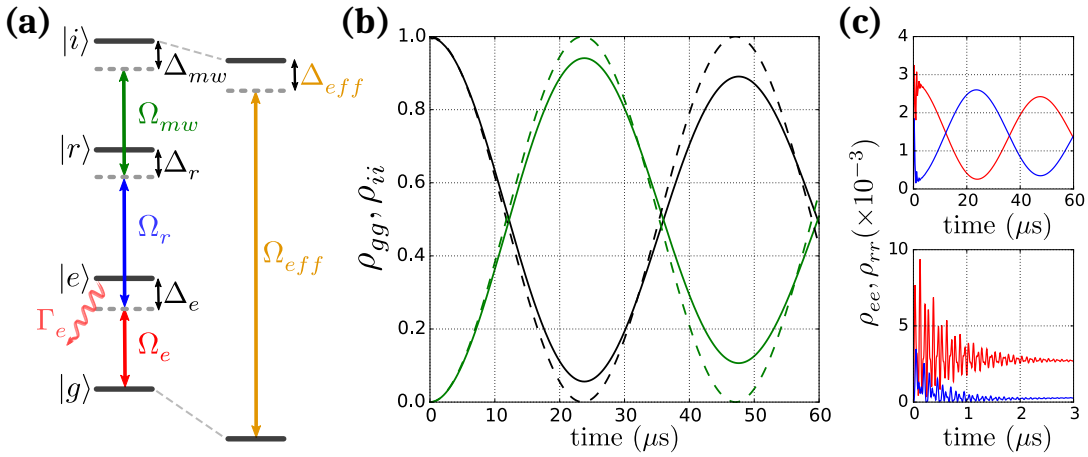

Figure 3.11: Excitation scheme of Rydberg P states. (a) Three-photon excitation scheme. The ground state $|g\rangle$ is off-resonantly coupled to the Rydberg state $|i\rangle$ by two optical fields and one microwave field with Rabi frequencies Ω_e, Ω_r and Ω_{mw}, respectively. Large intermediate detunings Δ_e and Δ_r prevent extensive populations of the two intermediate states $|e\rangle$ and $|r\rangle$. **(b)** Simulation of the time-evolution of the state populations ρ_{gg} and ρ_{ii} (resp. black and green lines), assuming the initial population in the ground state, with $\Delta_e = \Delta_r = -2\pi \cdot 100\,\mathrm{MHz}$, $\Omega_e = \Omega_{mw} = 2\pi \cdot 2.4\,\mathrm{MHz}$ and $\Omega_r = 2\pi \cdot 25\,\mathrm{MHz}$. The exact calculation is compared to the effective two-level model (dashed lines). The observed deviation is due to the absence of the decay Γ_e in the latter. **(c)** Populations ρ_{ee} (red) and ρ_{rr} (blue) simulated in the same regime. With a maximum fraction of $3 \cdot 10^{-3}$ these states are weakly populated. On short timescales, very fast transient oscillations are damped after 2 µs, justifying the adiabatic elimination, then the populations follow a similar evolution to $|g\rangle$ and $|r\rangle$.

the optical Bloch equations, one can eliminate all the terms involving $|e\rangle$ and $|r\rangle$ in order to write an effective equation valid in the limit of long timescales, which directly couples $|g\rangle$ to $|i\rangle$. This approximation is known as adiabatic elimination [Linskens *et al.*, 1996; Brion *et al.*, 2007]. With c_x the projection of the wavefunction to the state $|x\rangle$ $(x = g, e, r, i)$, one obtains the following coupled equations

$$\dot{c}_g = -iS_g c_g + i\frac{\Omega_{eff}}{2} c_i \tag{3.19}$$

$$\dot{c}_i = -i(\Delta_{mw} - S_i)c_i + i\frac{\Omega_{eff}}{2} c_g \tag{3.20}$$

where S_g and S_i are the AC-Stark shifts of the states $|g\rangle$ and $|i\rangle$ defined by

$$S_g = \frac{\Omega_e^2}{4\Delta_e - \frac{\Omega_r^2}{\Delta_r}} \qquad S_i = \frac{\Omega_{mw}^2}{4\Delta_r - \frac{\Omega_r^2}{\Delta_e}} \tag{3.21}$$

and Ω_{eff} is the effective Rabi frequency of the four-level system defined by

$$\Omega_{eff} = \frac{\Omega_e \Omega_r \Omega_{mw}}{4\Delta_e \Delta_r - \Omega_r^2}. \tag{3.22}$$

Equations (3.21, 3.22) simply show that one can reduce the effect of the three off-resonant fields to AC-Stark shifts of the two outer states $|g\rangle$ and $|i\rangle$ and to an effective Rabi frequency Ω_{eff} coupling these states. The AC-Stark shifts may be calculated in a perturbative approach. By setting the ground-state energy to zero via a rotation in the rotating frame, the differential equations can be rewritten as

$$\dot{c}_g = i\frac{\Omega_{eff}}{2} c_p \tag{3.23}$$

$$\dot{c}_i = -i\Delta_{eff} c_i + i\frac{\Omega_{eff}}{2} c_g. \tag{3.24}$$

with $\Delta_{eff} = \Delta_i + S_g - S_i$ the effective detuning. At this stage one can identify the Schrödinger equation of a two-level system with Rabi frequency Ω_{eff} and detuning Δ_{eff}. Therefore the whole system can be considered as an effective two-level system where conditions for the inversion of state populations are known.

This effective description is illustrated in Fig. 3.11(b), where the populations of the four levels are plotted as a function of the excitation time (black and green dashed lines) and compared to full numerical solutions of the optical Bloch equations. The simulations clearly show that the two intermediate states are negligibly populated and that the two outer states $|g\rangle$ and $|i\rangle$ behave like a two-level system, exhibiting an evolution similar to two-level Rabi oscillations. It is worth noticing that the effective model does not predict the decay of the oscillations which would be a consequence of the decay of the intermediate state $\Gamma_e/2\pi = 6.067\,\mathrm{MHz}$, not considered in the current effective model. To take it into account an effective operator formalism for open quantum systems is used to derive an effective master equation [Reiter and Sørensen, 2012]. The decay of the Rydberg states is neglected, since Γ_r, $\Gamma_i \ll \Gamma_e$. It results that the decay Γ_e effectively leads to various terms in the two-level model which can, on long timescales, either kill or enhance coherences. The typical experimental times are limited to $t_{exc} \leq 15$ µs, where both models give very similar results. In the following discussion this decay is neglected, since it has no crucial impact on the regime of exploration.

Using this approach, an optimized excitation scheme of the Rydberg state $|i\rangle$ is derived. Due to the AC-Stark shifts, the intuitive resonance condition with $\Delta_{mw} = 0$ is not valid. From the effective two-level model, a modified resonance condition is

derived, which must be fulfilled to efficiently transfer an atom from $|g\rangle$ to $|i\rangle$

$$\Delta_{eff} = \Delta_i + \frac{\Omega_e^2}{4\Delta_e - \frac{\Omega_r^2}{\Delta_r}} - \frac{\Omega_{mw}^2}{4\Delta_r - \frac{\Omega_r^2}{\Delta_e}} = 0. \tag{3.25}$$

Experimentally, this can be spectroscopically measured and compensated.

In addition, two other constraints must be considered before performing the experiment. On the one hand, excitation of the $|nP\rangle$ state on a timescale shorter than its lifetime is required, leading to the condition

$$\Omega_{eff} \leq \tau_i^{-1}. \tag{3.26}$$

On the other hand, avoiding population in both intermediate states is aimed. Populations in the Rydberg state $|r\rangle$ cannot be directly resolved by our field ionisation protocol and would be mistaken for the desired state, while population in $|e\rangle$ could lead to scattering and heating of the cloud. In Section 3.4, an optical approach to distinguish both Rydberg populations is introduced. In the far-detuned regime, which satisfies the condition $\Omega_r \ll \Delta_e, \Delta_r$, the atomic-state coefficients c_e and c_r are accurately approximated by $\Omega_e/\Delta_e \cdot c_g$ and $\Omega_{mw}/\Delta_{mw} \cdot c_i$, respectively. To satisfy both conditions, it is favourable to keep Ω_e and Ω_{mw} relatively small, while Ω_r can remain large as long as the far-detuned condition is still fulfilled.

Experiments presented in Ch. 6.3.1, aimed at optically revealing the presence of $|nP\rangle$ states, require a two-photon resonant EIT coupling to $|nS\rangle$ states. In the following sub-sections and the mentiond Ch. 6.3.1, the same principal quantum number n is chosen for both the $|r\rangle$ and $|i\rangle$ states, such that the same 480 nm laser field is shared between the second step of the off-resonant excitation scheme and the electromagnetically-induced transparency (EIT) coupling. Hence $\Delta_r = 0$ and the detunings must fulfil $\Delta_e = \Delta_r$. In all experiments presented in this section, these detunings are set to $\sim 2\pi \cdot 100\,\text{MHz}$. In such conditions, the red beam heating effect is negligible if the Rabi frequency Ω_e is below a critical value of typically $2\pi \cdot 2.5\,\text{MHz}$. Hence, Ω_r and Ω_{mw} can be adjusted to respect the above-mentioned conditions. The simulations in Fig. 3.11(b),(c) show an example of efficient excitation with populations in the intermediate states smaller than 3 %.

3.3.2 Three-photon spectroscopy of $|42P\rangle$ Rydberg states

Here, demonstration of three-photon off-resonant excitation of $|nP\rangle$ Rydberg atoms is demonstrated, as a powerful method to prepare $|nP\rangle$ as a spin state avoiding populating $|nS\rangle$ during the process. According to the scheme proposed in Sec. 3.3.1

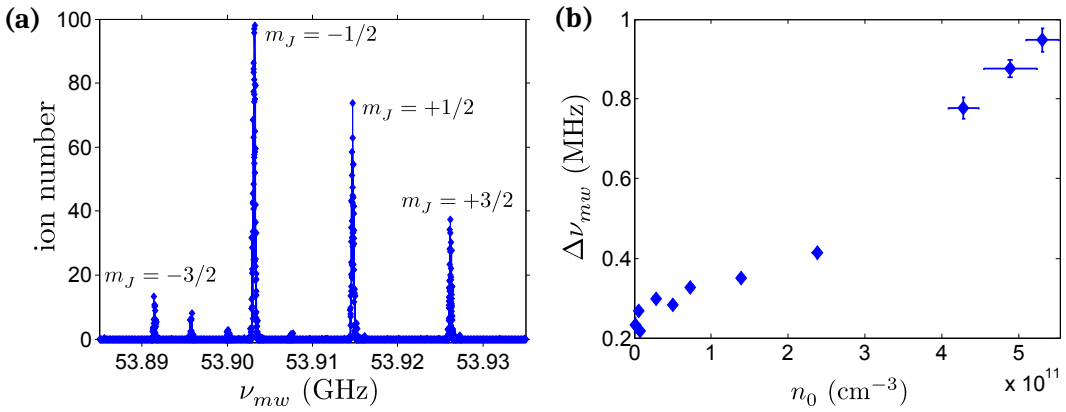

Figure 3.12: Three-photon spectroscopy of the $|42P_{3/2}\rangle$ states. (a) Microwave frequency scan around the three-photon resonance, at a peak density $n_0 = (3.30 \pm 0.18) \cdot 10^9\,\mathrm{cm}^{-3}$ where interaction effects do not play a significant role. The atoms, initially prepared in $|g\rangle$, are off-resonantly driven to $|e\rangle$ and $|r\rangle = |42S_{1/2}, m_j = 1/2\rangle$. A detuned microwave radiation finally excites the state $|i\rangle$ by compensating the energy mismatch. Only the Zeeman substates $m_j = \{3/2, 1/2, -1/2\}$ are addressed with $\{\sigma^+, \pi, \sigma^-\}$ polarization components, respectively. The Rabi frequencies are calibrated to be $\Omega_e = 2\pi \cdot 9.7\,\mathrm{MHz}$, $\Omega_r = 2\pi \cdot 25\,\mathrm{MHz}$, $\Omega_{mw} = 2\pi \cdot 12\,\mathrm{MHz}$. The spectrum shows a significant population of $|42P_{3/2}, m_j = -3/2\rangle$, coming from a residual π polarization component of Ω_e. The additional residual peaks come from a cycling process that populates different m_F sub-states of $|5S_{1/2}, F = 2\rangle$. A magnetic field $B_x = 6.43\,\mathrm{G}$ is estimated from the fine splitting observed between the m_j peaks. **(b)** Density dependent width of the $|42P_{3/2}, m_j = 3/2\rangle$ resonance, extracted from Lorentzian fits. In contrast to (a), interaction effects play a major role on the lineshape at higher densities. The spectrum is acquired with $\Omega_e = 2\pi \cdot 5.6\,\mathrm{MHz}$, $\Omega_r = 2\pi \cdot 25\,\mathrm{MHz}$, $\Omega_{mw} = 2\pi \cdot 12\,\mathrm{MHz}$.

and after theoretically understanding the excitation process, the resonance of different m_j sub-states of $|i\rangle = |42P_{3/2}\rangle$ is found and Rydberg-Rydberg interaction effects are spectroscopically measured. This states can be used in later experiments to prepare Rydberg spins or to image the evolution of coupled Rydberg atoms. The theoretical predictions on the AC-Stark shift allow us to calibrate the coupling Rabi frequencies Ω_e and Ω_{mw}, leaving Ω_r as the only experimental parameter that is not calibrated by spectroscopic methods. In Chapter 3.2.2, a method to spatially reconstruct the two-dimensional Gaussian profile of Ω_r is presented.

The two optical photons ($\sim 780\,\mathrm{nm}$ and $\sim 480\,\mathrm{nm}$) off-resonantly address the Zeeman sub-state $|42S_{1/2}, m_j = 1/2\rangle$. The target state $|42P_{3/2}\rangle$ is addressed by a microwave field with different polarisation components $\{\sigma^+, \pi, \sigma^-\}$, as discussed in Section 2.4.1, allowing for excitation of the $m_j = \{-1/2, 1/2, 3/2\}$ states. The

magnetic field induces a Zeeman shift that lifts the degeneracy between the m_j components and allows for independent addressing of such sub-states. Scanning the microwave frequency ν_{mw}, the spectrum shown in Figure 3.12(a) is recorded by means of field-ionisation detection after the excitation pulse. Large numbers of ions are measured at three expected equally-spaced frequencies. In addition a fourth, smaller peak appears at the expected position of the $m_j = -3/2$ Zeeman sub-state, which can be explained by misalignment of the polarisation of the 780 nm excitation beam with the perpendicular direction to the quantisation axis, resulting in a residual π-polarized component for which two additional σ^- photons allow to address the $m_j = -3/2$ state. Small additional peaks with frequency separations exactly corresponding to the ground state Zeeman splitting are also observed. Such resonances are signature of transitions from the other hyperfine levels of the ground state $|5S_{1/2}, F = 2\rangle$ to the $|42P_{3/2}\rangle$ state. Population in these states cannot be explained by imperfections of the state preparation, since the pure $m_F = 2$ hyperfine state is initially excited with high-efficiency. However, they could arise from coupling to the Rydberg state, for which the purity of the m_F quantum number is not preserved.

The spectrum in Fig. 3.12 (a) was taken under low-density conditions to minimize multi-particle interaction effects, which have been reported to strongly modify the width of the observed transitions [Anderson *et al.*, 2002; Park *et al.*, 2011; Afrousheh *et al.*, 2004; Afrousheh *et al.*, 2006a; Goldschmidt *et al.*, 2016]. In these experiments, excitation of the $|42P_{3/2}, m_j = 3/2\rangle$ is realised at various densities of ground state atoms and, as shown in Fig. 3.12(b), an increase of the width of the spectral line at higher densities is observed, which constitutes a signature of van der Waals Rydberg-Rydberg interactions [Singer *et al.*, 2004].

Calibration of three-photon excitation experimental parameters

Three-photon spectroscopy provides a powerful tool to calibrate the Rabi frequencies and the detunings of the fields involved in the excitation process because the resonance condition depends on all these parameters according to Eq. (3.25). Only the measurement of the coupling Rabi frequency $\Omega_r = \Omega_c$ is independently realized using a method based on a local fitting of the electromagnetically-induced transparency profile [Gavryusev *et al.*, 2016b], described in Ch. 3.2.2. By performing three-photon spectroscopy at different Ω_e (see Fig. 3.13(a)) while keeping the other settings constant, we observe that the resonance frequency exhibits a linear behavior with the laser power $P_e \propto \Omega_e^2$ (measured independently), in perfect agreement with Eq. (3.25). The unshifted resonance frequency is determined from a linear

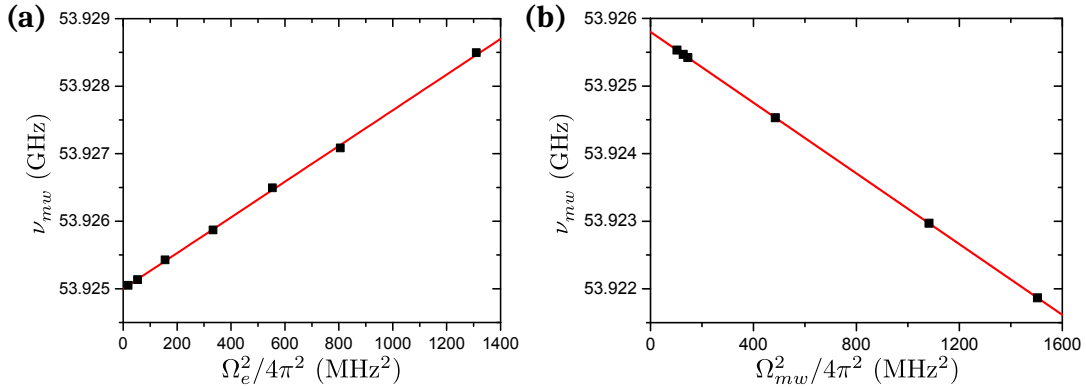

Figure 3.13: Calibration of Ω_e and Ω_{mw} from the light shift of the resonance. **(a)** For a given coupling of Ω_r and Ω_{mw} the intensity of the red beam Ω_e is varied. The resonant position of the peak $|42P_{3/2}, m_j = 3/2\rangle$ undergoes a quadratic light shift following Eq. (3.21). **(b)** Analogously, for given Ω_e and Ω_r, the same procedure can be applied to calibrate Ω_{mw}. We must rely on the fact that the AC-Stark Shift is linear with the power and therefore find the unperturbed central peak frequency.

extrapolation to zero intensity and afterwards the measured resonance frequencies are expressed in terms of light shifts S_g of the ground state, enabling to use equation (3.21) to calculate the Rabi frequency Ω_e. The calibration between P_e and Ω_e^2 is then employed in Figure 3.13(a), revealing a linear relation as would have been expected from the two-level model, thus validating its use.

A similar unbiased procedure cannot be applied to calibrate the microwave Rabi frequency Ω_{mw} since the intensity of the microwave source at the position of the atoms is unknown. Therefore we rely on the same theoretical predictions for the AC-Stark shift, assuming a linear dependence with Ω_{mw}^2. From the variation of the spectral peak position for different microwave intensities, the non-shifted three-photon resonance that leads to a linear relation of the resonance frequency with Ω_{mw}^2 is inferred (Fig. 3.13(b)). From it, the AC-Stark shifts are calculated and therefore an accurate calibration of Ω_{mw} is deduced. Measuring the non-shifted transition, where $\Omega_e = \Omega_{mw}$ demonstrates the consistency of these measurements, obtaining a resonance shifted by $-96\,\mathrm{MHz}$, in agreement with the experimental calibration of the detuning within $0.5\,\mathrm{MHz}$ uncertainty. In this way all the required parameters to perform an efficient and controllable excitation of Rydberg $|nP\rangle$-states are determined.

3.3.3 Incoherent excitation of $|42P\rangle$ Rydberg states

In order to precisely control the number of Rydberg atoms excited to $|i\rangle = |42P_{3/2}, m_j = 3/2\rangle$, it is necessary to characterise and control the number of excited atoms given by the evolution of the population in $|i\rangle$ with the excitation time t_{exc}. The theoretical model predicts coherent Rabi oscillations between the ground and the P-states with an effective Rabi frequency Ω_{eff} given by Eq. (3.22). Yet the measurements show the emergence of a saturation effect after typically 6 µs (see Fig. 3.14(a)), that is attributed to incoherent excitation of the $|42P_{3/2}, m_j = 3/2\rangle$ Rydberg state. This is understood to be a consequence of a large degree of dephasing introduced by the strong inhomogeneity of the effective Rabi frequency Ω_{eff}, due to the Gaussian profile of the coupling beam [Heidemann *et al.*, 2007].

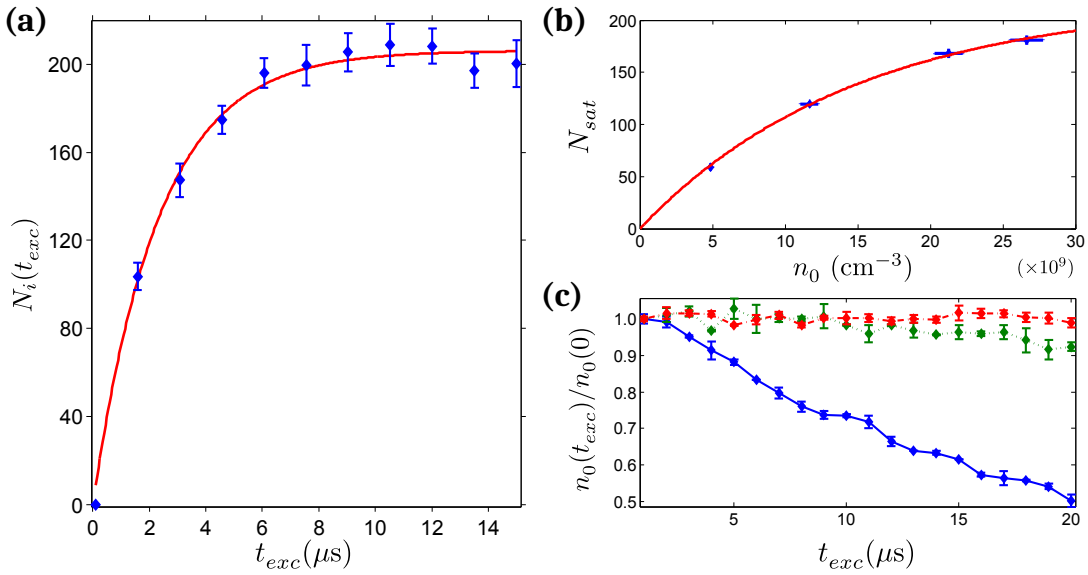

Figure 3.14: Excitation of $|42P_{3/2}, m_j = 3/2\rangle$ Rydberg atoms. **(a)** Excitation dynamics as a function of the excitation time t_{exc}. The measurement is done after a fixed time-of-flight of 1 ms, at a peak ground-state density $n_0 = (7.26 \pm 0.21) \cdot 10^9\,\mathrm{cm}^{-3}$, with $\Omega_e = \Omega_{mw} = 2\pi \cdot 10\,\mathrm{MHz}$, $\Omega_r = 2\pi \cdot 25\,\mathrm{MHz}$. The data shows a saturation of the number of excitations N_i. A fit with the function $N_i(t_{exc}) = N_{sat}(1 - e^{-t_{exc}/\tau})$ gives $N_{sat} = 206.2 \pm 2.6$ and $\tau = (2.34 \pm 0.11)$ µs. **(b)** Blockade effect on the excited states. Repeating the same experiment, we observe a saturation of N_{sat} while increasing the ground-state density. To reach high enough densities, the time-of-flight is reduced to 0.5 ms. **(c)** Heating induced by scattering on the $|g\rangle \leftrightarrow |e\rangle$ transition. The density is plotted at different excitation times for $\Omega_e = 2\pi \cdot [2.4,\ 7.1,\ 21]\,\mathrm{MHz}$ (resp. dash-dotted red, dotted green and solid blue lines). The microwave is switched off to avoid density reduction due to Rydberg excitation. Error bars represent the standard deviation.

Repeating the experiment for increasing ground-state atomic densities, we observe a similar behavior of the excitation dynamics on the same timescale, but with different saturated number of excitations N_{sat}. In Figure 3.14(b) this number is plotted versus the ground-state density n_0. As can be seen from the plot, a second saturation effect is observed. This can be attributed to the Rydberg blockade between P-states: due to their van der Waals interactions, the total number of Rydberg atoms in the finite volume of the cloud is limited. The value $N_{bl} = 218 \pm 6$ is extracted from the exponential fit is consistent with a geometrical estimation based on the van der Waals $P - P$ blockade radius $R_{ii} = (C_6^{ii}/\hbar\Delta\nu_{mw})^{1/6} \sim 4\,\mu\text{m}$, which would lead to ~ 230 Rydberg atoms in the excitation volume. Here, $\Delta\nu_{mw}$ is the width of the resonance at low density, estimated from Fig. 3.12(b)).

The final step to optimize the excitation of $|42P_{3/2}, m_j = 3/2\rangle$ Rydberg states consists in minimizing any heating effects due to large excitation Rabi frequency Ω_e, which lead to loss of atoms from the atomic cloud (see Fig. 3.14(c)). In order to avoid such an effect, the power of the 780 nm laser beam is reduced to $\Omega_e = 2\pi \cdot 2.4\,\text{MHz}$ and compensated by increasing the microwave Rabi frequency Ω_{mw} to $2\pi \cdot 14\,\text{MHz}$, such that the effective coupling is not significantly affected. Thus, a well-controlled method to excite Rydberg spins directly to Rydberg $|P\rangle$ states has been demonstrated, including high degree of control over all experimental parameters.

3.4 Distinguishability of spin components via selective optical de-excitation

In the previous sections, excitation mechanisms for the creation of $|nS\rangle$ and $|nP\rangle$ Rydberg spins have been provided. They can be potentially used as two interacting spin states, coupled by dipole-dipole interactions, as will be explained in Ch. 4. Experiments exploring the dynamics of such spin system requires independent measurements of both spin states $|\uparrow\rangle$ and $|\downarrow\rangle$. As described in Sec. 3.1.6, field ionisation allows to count the total number of Rydberg spins (see Sec. 3.1) and the electric fields are set to ionise Rydberg atoms with energies above a certain threshold, which is selected below the Rydberg state $|r\rangle \equiv |\downarrow\rangle$.

To study the dynamics of two coupled Rydberg spins, distinction of each spin component is essential. For such purpose, here is developed a method which combines optical de-excitation of one spin state, e.g. $|\downarrow\rangle = |nS\rangle$, with the global ionisation of the remaining higher-lying Rydberg states (originally introduced in [Schempp, 2014, Ch. 7]). A resonant 480 nm laser beam, Ω_{dp} (see Fig. 3.15), is used to de-

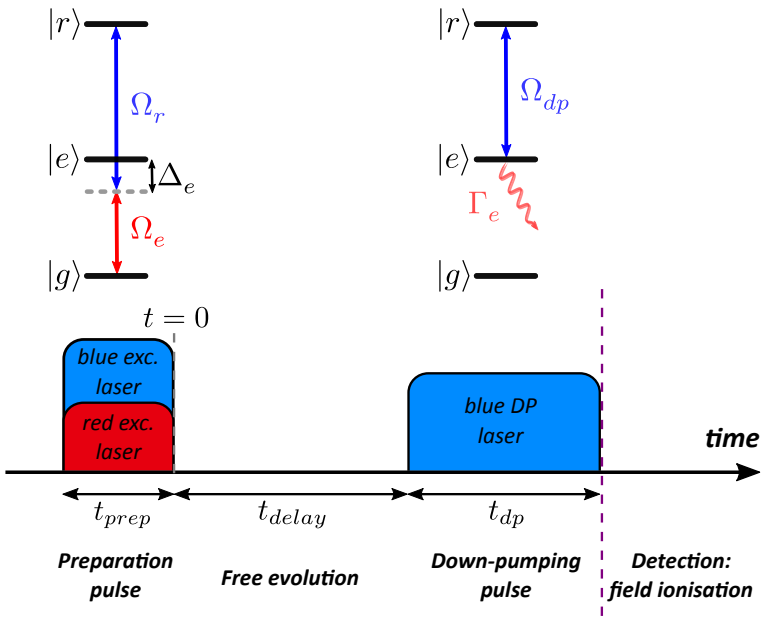

Figure 3.15: Scheme for preparation and down-pumping of the spin states. The spins are prepared in the Rydberg state $|r\rangle$ by means of a two-photon off-resonant process. After preparation, the spin state evolves during a time t_{delay}. The fraction of spins in the state $|r\rangle$ is projected down to the ground state $|g\rangle$ by means of a down-pumping resonant laser beam towards the rapidly-decaying intermediate state $|e\rangle \equiv |5P_{3/2}\rangle$.

excite the spin down state into the intermediate state $|e\rangle \equiv |5P_{3/2}\rangle$ which rapidly decays into the ground state, potentially allowing to transfer the whole of the system $|g\rangle$, potentially allowing to transfer the whole ρ_{rr} population into ρ_{gg}. The beam covers a significantly larger region than the excitation beam Ω_r, so the depletion of population is efficient in all regions of the cloud. Whereas other experiments rely on this scheme to measure the Rydberg population on a single spin state by measuring the fluorescence from $|e\rangle$ generated by the de-excitation procedure [Schauß *et al.*, 2012], our experiments use of it to distinguish different Rydberg components.

As can be observed in Fig. 3.16(a), the population in the Rydberg state (ρ_{rr}) quickly evolves towards the ground state (ρ_{gg}). The intermediate state (ρ_{ee}) decays to the ground state in a time-scale $\tau_e \sim \frac{1}{\Gamma_e}$. The simulations in Fig. 3.16(b) show an optimal depletion of the Rydberg atoms at $\Omega_{dp} \sim \Gamma_e$. This process is considerably slower if $\Omega_{dp} \ll \Gamma_e$, whereas the efficiency does not increase when $\Omega_{dp} \gg \Gamma_e$, since the fastest time-scale is set by the spontaneous decay Γ_e^{-1}. Damped Rabi oscillations may appear during this transient time. In Fig. 3.16(c), a de-excitation experiment reveals the predicted behaviour for $\Omega_{dp} \leq \Gamma_e$. Nevertheless, deviations arise in the efficiency of the process: a residual fraction of atoms $\sim 4.1\,\%$ remains at the steady-state,

whereas simulations predict complete depletion of the spin state.

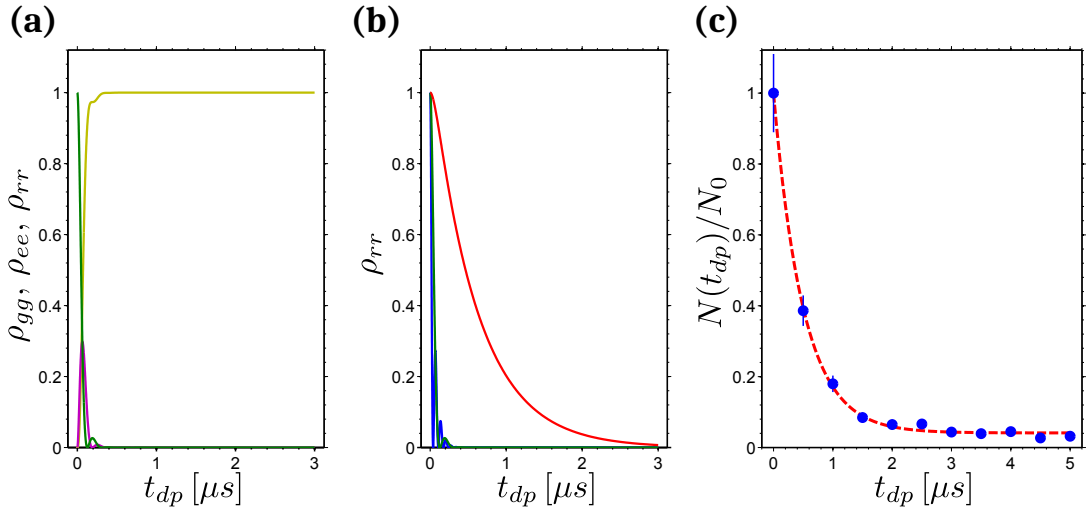

Figure 3.16: **(a)** OBE simulation of the evolution of populations ρ_{gg} (golden), ρ_{ee} (violet), ρ_{rr} (green) according to the couplings described in Fig. 3.15(c). $\Omega_{dp}/2\pi = \Gamma_e/2\pi = 6.067\,\mathrm{MHz}$. **(b)** Fraction of Rydberg atoms ρ_{rr} as a function of coupling time to the resonant down-pumping beam at $\Omega_{dp}/2\pi = 15\,\mathrm{MHz}$ (blue), $\Omega_{dp}/2\pi = \Gamma_e/2\pi = 6.067\,\mathrm{MHz}$ (green) and $\Omega_{dp}/2\pi = 1.25\,\mathrm{MHz}$ (red). **(c)** Fraction of atoms in the prepared $|42S_{1/2}, m_j = 1/2\rangle$ state with respect to the down-pumping time t_{dp}. The residual number of background atoms saturates to $N_{res}/N_0 \sim 4.1\,\%$. The exponential fit shows a down-pumping rate $\Gamma_{dp} = 2\,\mathrm{MHz}$.

In order to understand the limitations described in Fig. 3.16(c), the time-dependence of the down-pumping efficiency is explored. Rydberg atoms are excited to $|r\rangle \equiv |42S_{1/2}\rangle$ during a $t_{exc} = 5\,\mu\mathrm{s}$ excitation process, as described in Fig. 3.15(a). After the excitation, a certain number of Rydberg atoms N_0 is detected via field-ionisation. The experiment is repeated with different delay times t_{delay} between the excitation and a $t_{dp} = 3\,\mu\mathrm{s}$ down-pumping pulse, obtaining the residual population $N(t_{delay})$. The efficiency of the process is given by

$$\eta_{dp}(t_{delay}) = \frac{N(t_{delay})}{N_0}, \tag{3.27}$$

which represents the fraction of de-excited atoms.

As observed in Fig. 3.17, the down-pumping efficiency decreases with time, with a rate $\Gamma_\eta = 7.701\,\mathrm{kHz}$, which can be attributed to population of additional Rydberg states, not addressed by the down-pumping laser, due to black-body radiation induced decay. According to the calculations explained in Sec. 2.1 (see Fig. 2.1), the global black-body transition rate from $|r\rangle \equiv |42S_{1/2}\rangle$ is $\Gamma_{bb_{42S}} = 13.244\,\mathrm{kHz}$, given a room

temperature $T \approx 295\,\mathrm{K}$. The discrepancy between the theoretical and the measured rates, $\Gamma_{bb_{42S}} = 1.719 \times \Gamma_\eta$, comes from the selection of our ionisation threshold. Thus, the residual population corresponds to the fraction of atoms above $n \geq 42$, including a fraction of atoms decaying to $|42P\rangle$ due to the proximity of its binding energy to the ionization threshold.

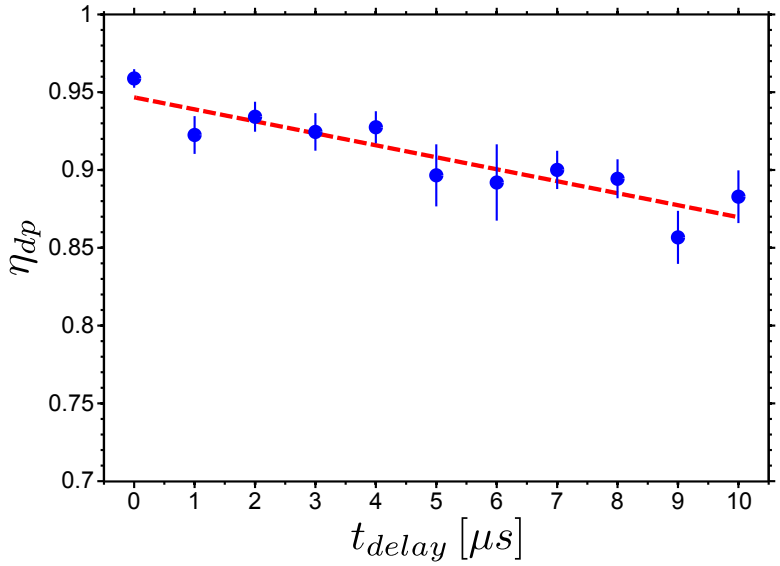

Figure 3.17: Down-pumping efficiency η_{dp} for various delay times t_{delay} between the preparation of the Rydberg spins in the $|42S_{1/2}, m_j = 1/2\rangle$ state ($t_{exc} = 5\,\mu\mathrm{s}$) and the down-pumping pulse ($t_{dp} = 3\,\mu\mathrm{s}$). The fraction of down-pumped atoms decreases over time with a rate $\Gamma_\eta = 7.701\,\mathrm{kHz}$.

Additionally, the first order decay rates to individual Rydberg states are calculating, using Eqs. (2.4, 2.5). For states above the original $|42S\rangle$, a total rate of 5.328 kHz is predicted. A simple model with this rate predicts a residual fraction of atoms in higher black-body states of 4.26 %, slightly smaller than the 5.39 % observed. However, the experimental observation $\Gamma_\eta = 7.701\,\mathrm{kHz}$ can be understood by including 57.4 % of the decay to $|41P\rangle$ state. Therefore, this experiment can be used to calibrate the ionisation threshold. The time origin of the linear fit from Fig. 3.17(a) suggest that the redistribution of Rydberg atoms starts $\sim 6.922\,\mu\mathrm{s}$ before the down-pumping experiment is complete. This is consistent with a redistribution process during the excitation (5 µs) and down-pumping (3 µs) time.

3.4.1 Optimal conditions

Black-body redistribution of Rydberg states plays an important role because it affects spin experiments in several ways (see Ch. 4). On one hand, it reduces the lifetime of the Rydberg spin states and constrains the time scale to explore the driven dynamics of the Rydberg spins. On the other hand, it creates additional Rydberg atoms that distort the precision on the detection of different spin components, since it is not possible to directly detect to which Rydberg states the atoms have been transferred by stimulated emission. The first limitation is overcome by driving the dynamics on a much shorter timescale than the decay time of the Rydberg spins. A third potential limitation of black-body redistribution concerns the introduction of undesired interaction effects on the spin dynamics. Whereas the interaction between atoms in well-defined spin states $|nS\rangle \leftrightarrow |nP\rangle$ or $|nS\rangle \leftrightarrow |n'S\rangle$ can be easily described in terms of spin operators (Sec. 2.2), this reservoir of Rydberg atoms in various states contributes to additional interaction effects, acting a strong local perturbations despite the total fraction of atoms in black-body redistributed states is one order of magnitude smaller than the actual spin fraction. In order to reduce the black-body decay fraction, a fast excitation of the spins and an efficient and quick down-pumping are beneficial. Therefore, for the experiments presented in the following chapter, we use a focused excitation beam with high coupling Rabi frequency Ω_c and a slightly broader but intense down-pumping beam with $\Omega_{dp} \geq \Gamma_e$.

3.5 Prospects

In this chapter, three excitation schemes have been described, implemented and characterised to potentially create Rydberg spins in two-different principal quantum numbers (Sec 3.3 and Sec. (3.1, 3.2), respectively) and an efficient de-excitation procedure is proposed to selectively discern the spin-state evolution (Sec. 3.4). This is applied in spin experiments to characterise the magnetisation of the spin ensemble, as described in Chapter 4. Schemes off-resonant from the intermediate states have been demonstrated to be more convenient for the preparation of spins due to the well defined distribution of Rydberg excitations, whereas the two-photon resonant scheme (used in [Piñeiro Orioli *et al.*, 2017]) generates an inhomogeneous toroidal distribution, with suppression of population (and therefore, of the spin-spin interaction) in the center of the excitation region, where the EIT is strong. Excitation mechanisms based on the stimulated Raman adiabatic passage (STIRAP) from ground to a Rydberg state may be implemented to achieve high transfer efficiency in a low

density regime [Cubel *et al.*, 2005; Deiglmayr *et al.*, 2006].

In addition, an imaging technique has been demonstrated to characterise the local excitation dynamics, revealing the emergence of an extended flat-top distribution in the Rydberg atom two-dimensional profile as a consequence of the strong van der Waals blockade in the many-body regime. This imaging tool constitutes an excellent diagnostic probe tool for future local studies of scaling dynamics of the Rydberg excitation [Heidemann *et al.*, 2007; Löw *et al.*, 2007], dependent on the local ground state atom number $N(x, y)$ and Rabi frequency $\Omega_{eff}(x, y)$, allowing to investigate a large parameter space where many different regimes are expected [Valado *et al.*, 2013; Helmrich *et al.*, 2016]. Further applications of this technique may reveal the local seeding dynamics of the creation of Rydberg aggregates [Schempp *et al.*, 2014; Malossi *et al.*, 2014].

Finally calibrating detection efficiency of the ion signal collected on the MCP detector by means of this imaging technique permits us to obtain accurate Rydberg atom numbers in different density regimes, which constitutes an important observable to understand the properties of the spin dynamics, presented in the next chapter (see Ch. 4).

Chapter 4

Dynamics of a non-interacting Rydberg spin-1/2 system

Rydberg atoms are well known to possess extreme properties like huge transition dipole moments ($\propto n^{*2}$) and enhanced lifetimes ($\propto n^{*3}$) [Gallagher, 1994]. Intensive studies have been realised in the last decades in order to understand the effects of van der Waals ($\propto \frac{1}{R^6}$) [Singer *et al.*, 2004; Tong *et al.*, 2004] and dipolar ($\propto \frac{1}{R^3}$) [Mourachko *et al.*, 1998; Anderson *et al.*, 1998] interactions. The possibility of controlling such interaction effects opened the path to perform quantum computation and quantum information processing with Rydberg atoms [Jaksch *et al.*, 2000; Lukin *et al.*, 2001; Saffman *et al.*, 2010] and the implementation of dipole-blockade mediated quantum gate [Isenhower *et al.*, 2010]. The observation of collective Rydberg excitation dynamics [Heidemann *et al.*, 2007; Reetz-Lamour *et al.*, 2008a] triggered investigations on many-body physics with Rydberg atoms [Gallagher and Pillet, 2008; Browaeys *et al.*, 2016].

The strong tunability of the interactions, through inter-atomic distance and quantum numbers, has been used to vary the energy range of the interactions from a negligible strength to few kHz, MHz or even up to several GHz. In recent years, cold Rydberg gases were demonstrated to constitute a versatile platform to perform quantum simulation of Ising quantum magnets [Löw *et al.*, 2009; Schauß *et al.*, 2015] using ground and Rydberg states as spins. Several proposals have been realised in order to establish Rydberg atoms as a broader platform for quantum simulation of Ising, Heisenberg XX and Heisenberg XXZ Hamiltonians [Bettelli *et al.*, 2013; van Bijnen and Pohl, 2015; Whitlock *et al.*, 2017] with different long-range scaling ($\propto \frac{1}{R^3}, \frac{1}{R^6}$), as discussed in Chapter 2. This requires control of different spin states within the Rydberg manifold. Achieving fast driving Rabi frequencies of few MHz

is not a complex task in the Rydberg manifold due to the huge dipole matrix elements. Thus, encoding a spin on a Rydberg quantum state can reveal a fast dynamical evolution of several Rabi cycles on typical timescales of few µs, dominated by microwave-induced couplings instead of Rydberg-Rydberg interactions. These timescales are much faster than those dominating the dynamics of ground state cold atoms ($\sim 100\,\mathrm{kHz}$) [Matthews *et al.*, 1998; Windpassinger *et al.*, 2008], trapped ions ($\sim 100\,\mathrm{kHz}$) [Schmidt *et al.*, 2005] or polar molecules ($\sim 1\,\mathrm{kHz}$) [Ospelkaus *et al.*, 2010] and similar to those driving electronic spins in vacancy centers [Golter and Wang, 2014]. Whereas efficient manipulation of two and three spins and observation of their dynamics have already been proved [Ravets *et al.*, 2014; Barredo *et al.*, 2014; Ravets *et al.*, 2015; Barredo *et al.*, 2015; Labuhn *et al.*, 2016], much is still to be investigated in the many-body regime.

In the present chapter, efficient control of the quantum state of hundreds of spins driven between two Rydberg states by a microwave field in a cold atom set-up is demonstrated. Transitions between Rydberg states $|nS\rangle \leftrightarrow |nP\rangle$ and $|nS\rangle \leftrightarrow |(n+1)S\rangle$ have been considered, driven by one and two microwave photons, respectively [Ryabtsev *et al.*, 2005]. The impact of imperfect spin preparation, field fluctuations and spin-state redistribution is characterised. Additionally, Ramsey interferometry [Ramsey, 1950] and rotary echo [Solomon, 1959; Rhim *et al.*, 1971] sequences are implemented to measure the visibility, coherence T_2^* time and phase shifts of the Rydberg spins. This work aims to provide a well-controlled platform to investigate interaction-induced Rydberg dynamics with negligible single particle limiting effects. Additionally, by mapping the microwave field on the atom dynamics, we establish an alternative approach to microwave electrometry [Sedlacek *et al.*, 2012; Anderson *et al.*, 2014; Anderson *et al.*, 2016; Oelsner *et al.*, 2017].

This chapter is structured in the following way. First, efficient microwave control of Rydberg-Rydberg transitions is demonstrated in section 4.1, for both single-photon and two-photon transitions within the Rydberg manifold. Additionally, experimental limitations on the observation of coherence are discussed in section 4.2. Subsequently, a theoretical mapping of the Rydberg atoms as a Rydberg spin-1/2 system is presented in section 4.3. Special emphasis is given to the description of the time evolution and the magnetisation reconstruction of the spin ensemble. Section 4.5 shows a tomographic approach to Rydberg spin interferometry. Finally, section 4.6 reveals the observation of coherence amongst the spins, quantifying the visibility and T_2^* coherence time of the spin ensemble by means of Ramsey interference experiments.

4.1 Microwave driving of Rydberg transitions

Accurate microwave driving of Rydberg atoms is essential to control the quantum state of Rydberg spins. Here, we present investigations on the driving of one- and two-photon Rydberg-Rydberg transitions for a three-dimensional disordered sample of ultracold atoms. The experiments introduced along this section are limited to the low Rydberg density regime, where the interactions between the atoms play a negligible role, whereas additional phenomenology due to dipolar effects can be observed in Chapter 5 (Sec. 5.1). The schemes for driving the desired transitions and the characterisation of the experimental results in terms of effective two-level systems are discussed.

4.1.1 Experimental procedure for one- and two-photon Rydberg-Rydberg transitions

In order to experimentally observe Rydberg-Rydberg transitions, we apply the experimental sequence sketched in Figure 4.1(a). Rydberg states are excited by means of a two-photon pulse of length t_{exc} from the ground state of ^{87}Rb to a Rydberg state $|nS, m_j\rangle$, as previously detailed in Sections (2.4,3.1). A microwave field oscillating in the few-GHz regime addresses the desired transition between Zeeman substates with the allowed polarisation. The transition is probed during a time t_{ev}. Transitions between $|nS_{1/2}, m_j\rangle \leftrightarrow |nP_J, m'_j\rangle$ are driven with a single microwave photon. Successful observation of Rabi oscillation with no significant effect of additional m_j transitions has already been reported in [Piñeiro Orioli *et al.*, 2017], for $|48S_{1/2}, m_j = 1/2\rangle \leftrightarrow |48P_{3/2}, m_j = 3/2\rangle$ transitions. In addition, transitions amongst $|nS_{1/2}, m_j\rangle \leftrightarrow |n'S_{1/2}, m'_j\rangle$ are accessible with two isochromatic photons. The later condition implies that the individual photons are detuned from the intermediate $|nP\rangle$ states. As a result, the Rydberg states are coupled with a Rabi frequency Ω. A complete scheme of the transitions is provided in Figure 4.3(a.1),(b.1). A magnetic field $B_z = 6.1\,\mathrm{G}$ is set in the direction of the laser fields during the experimental sequence to set our quantisation axis and split the Zeeman sub-levels of $|nS\rangle$,$|nP_{1/2}\rangle$, and $|nP_{3/2}\rangle$ by ~ 17.1, ~ 5.7 and $\sim 11.4\,\mathrm{MHz}$, respectively. Two reasons motivate the removal of the m_j degeneracy:

- Suppress the effect of quantum beats due to driving of additional transitions with different polarisation of the microwave field [Ryabtsev and Tretyakov, 2001]. Therefore, $\Delta_{g_j} \gg \Omega$ of the effective transition.

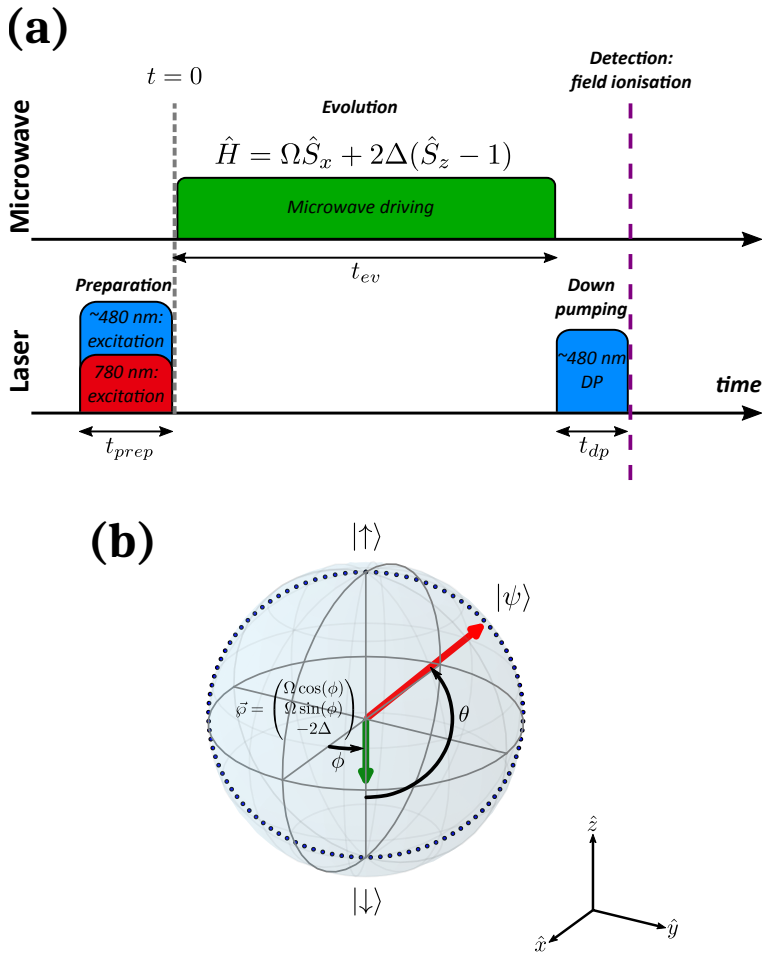

Figure 4.1: (a) General technique for manipulation and detection of Rydberg spins. During the initialization, the atoms are excited to the Rydberg $|\downarrow\rangle$ (red and blue excitation pulses). The spin dynamics evolves under the effect of the Hamiltonian $\hat{H}$. $|\downarrow\rangle$ is eliminated by a down-pumping (blue pulse). By means of an electric field pulse, the remaining Rydberg atoms above the ionisation threshold are ionised and read out. **(b) Control of the quantum state of the spins.** The field vector $\vec{\wp}$ (green) and the spin-state vector (red) are represented. The spins evolve on the plane orthogonal to $\vec{\wp}$. The global spin state $|\Psi\rangle = \cos\left(\frac{\theta}{2}\right)|\downarrow\rangle + e^{i\left(\phi+\frac{\pi}{2}\right)}\sin\left(\frac{\theta}{2}\right)|\uparrow\rangle$ can be rotated to any arbitrary point of the Bloch-Poincaré sphere.

- Reduce dipole-induced coupling of the Zeeman sub-levels in future studies of interaction-driven dynamics [Tresp *et al.*, 2015; Vermersch *et al.*, 2016]. For such reason, $\Delta_{g_j} \gg V_{int}$.

Finally, a 480 nm laser beam, resonantly coupling $|nS, m_j\rangle$ and $|5P_{3/2}, F = 3, m_F = 3\rangle$ during t_{dp}, pumps the population in such Rydberg state outside the Rydberg manifold

and allows to distinguish the different spin components (further details may be consulted in Section 3.4). Immediately afterwards, an electric field is ramped to ionise the remaining Rydberg atoms and to guide them to our MCP detector.

These experiments can be understood in terms of the Bloch-Poincaré picture as the coupling of two quantum states $|\downarrow\rangle$ and $|\uparrow\rangle$. As presented in Figure 4.1(b), rotations of the spin state of the driven system are characterised by two-coordinates, θ and ϕ. The length t_{ev} and strength Ω of the microwave pulses determine the rotation of the state between the poles, with the angle $\theta = \theta = \Omega \cdot t_{ev}$, which establishes the degree of superposition of both states, where $\Omega_{ef} = \sqrt{\Omega^2 + 4\Delta^2}$, whereas $\phi = \phi_0 + 2\Delta \cdot t$ determines the position of the field vector $\vec{\wp} = \Omega\left(\cos(\phi)\hat{x} + \sin(\phi)\hat{y}\right) - 2\Delta\hat{z}$ on the xy-plane. Hereafter, we consider ϕ_0 as the phase of the microwave field. For a single microwave pulse, the phase may be arbitrarily considered to be $\phi = 0$. Under the effect of the driving field, the spin vector $\vec{R}_\psi$ can precess about $\vec{\wp}$ [Riehle, 2004; Steck, 2007], as

$$\frac{d\vec{R}_\psi(t)}{dt} = -\vec{\wp} \times \vec{R}_\psi(t). \tag{4.1}$$

Thus, the system can be described as the evolution of a general state $\psi(t_{ev})$ under coherent evolution given by the Hamiltonian

$$\hat{\mathcal{H}} = \Omega \cdot (\cos(\phi) \cdot \hat{S}_x + \sin(\phi) \cdot \hat{S}_y) + 2\Delta(\hat{S}_z - 1). \tag{4.2}$$

In the resonant case, given $\Delta = 0$, the spin evolution can be simplified to

$$|\Psi(t_{ev})\rangle = \cos\left(\frac{\theta}{2}\right)|\downarrow\rangle + e^{i\left(\phi + \frac{\pi}{2}\right)} \sin\left(\frac{\theta}{2}\right)|\uparrow\rangle\,. \tag{4.3}$$

4.1.2 Microwave spectroscopy of Rydberg-Rydberg transitions

In order to explore the quality of our experimental procedure, we perform spectral measurements of both $|nS\rangle \leftrightarrow |nP\rangle$ and $|nS\rangle \leftrightarrow |(n+1)S\rangle$ and observe the atoms transferred to the spin-up state $|\uparrow\rangle$. In the low-density limit, without interaction-induced broadening and with negligible decoherence sources, the driven transitions are expected to follow the behaviour described by the Rabi-Breit model [Breit and Rabi, 1931]. For two and three levels, the formulas that describe the spectrum are expressed as

$$\rho_{\uparrow\uparrow_{1-\gamma}} = \frac{\Omega^2}{4\Delta^2 + \Omega^2} \sin^2\left(\frac{t}{2}\sqrt{4\Delta^2 + \Omega^2}\right) \tag{4.4a}$$

$$\rho_{\uparrow\uparrow_{2-\gamma}} = \frac{\Omega^2}{4(\Delta - \Delta_{LS})^2 + \Omega^2} \sin^2\left(t\sqrt{4(\Delta - \Delta_{LS})^2 + \Omega^2}\right), \tag{4.4b}$$

where $\rho_{\uparrow\uparrow}$ refers to the transition probability from $|\downarrow\rangle$ to $|\uparrow\rangle$, as defined in [Ryabtsev *et al.*, 2005]. Δ_{LS} is the power line shift contribution to the total detuning, which will be characterised in Sec. 4.1.3.

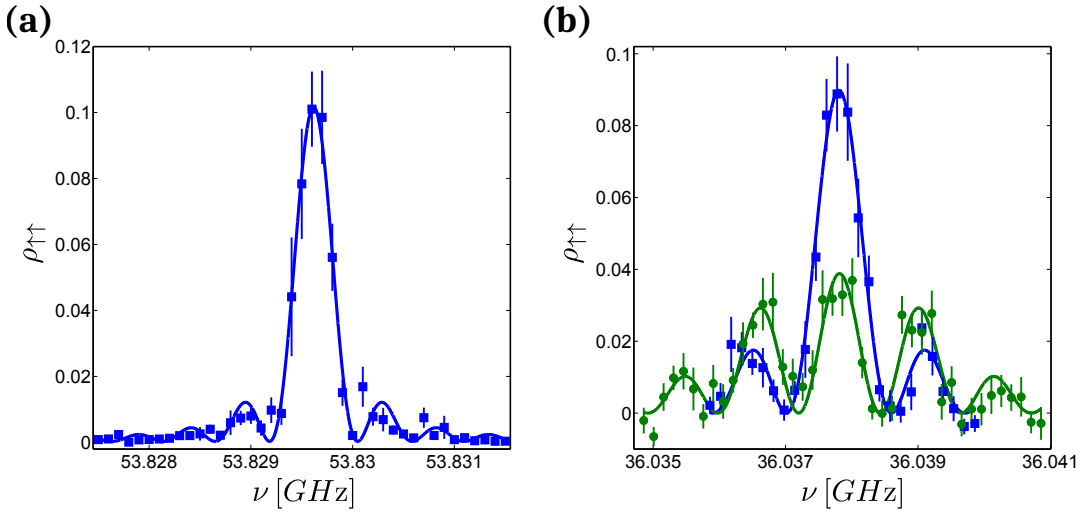

Figure 4.2: Spectral profile of spin-up population fraction $\rho_{\uparrow\uparrow}$ for one- ((a)) and two-photon ((b)) microwave transitions between Rydberg states. (a) Single-photon transition $|42S_{1/2}, m_j = 1/2\rangle \leftrightarrow |42P_{3/2}, m_j = 3/2\rangle$. The microwave driving time is set to $2\,\mu s$. Line corresponds to a fit to the Rabi-Breit formula from Eq. (4.4a). The population of atoms driven to external Rydberg states is observed to be negligible. $\Omega = 2\pi \times 0.50 \pm 0.01\,\mathrm{MHz}$, $N = 262 \pm 7$ spins, $\nu_0 = 53.830\,\mathrm{GHz}$. **(b)** Two-photon transition $|48S_{1/2}, m_j = 1/2\rangle \leftrightarrow |49S_{1/2}, m_j = 3/2\rangle$ for a $0.5\,\mu s$ microwave pulse at two different effective Rabi frequencies: $\Omega = 2\pi \times 1.22 \pm 0.04\,\mathrm{MHz}$ (blue squares) and $\Omega = 2\pi \times 1.58 \pm 0.02\,\mathrm{MHz}$ (green circles). The fitted offset reveals that $1.85\,\%$ of the atoms are driven outside the spin-state transition. $N = 566 \pm 37$ spins, $\nu_0 = 36.037\,\mathrm{GHz}$ (blue); $N = 591 \pm 45$ spins, $\nu_0 = 36.037\,\mathrm{GHz}$ (green) Lines correspond to a fit to the Rabi-Breit formula for three-levels (see. Eq. (4.4b)). Error bars are given by one standard error. Data are the average of 10 repetitions.

In Figure 4.2, the frequency-dependent profile of $|\downarrow\rangle = |42S_{1/2}, m_j = -1/2\rangle \leftrightarrow |\uparrow\rangle = |42P_{3/2}, m_j = -3/2\rangle$ and $|\downarrow\rangle = |48S_{1/2}, m_j = 1/2\rangle \leftrightarrow |\uparrow\rangle = |48S_{1/2}, m_j = 1/2\rangle$ is shown. The measurements are fitted to the equations (4.4a,4.4b), showing good agreement. The width of the spectral peaks corresponds to the Fourier limited given by the Fourier Transform of the pulse temporal width. Such good agreement to the theoretical limiting predictions demonstrates the small effect of dephasing sources on the short timescales of the pulses. Additional analysis of the experimental limitations of the driving will be presented in Section 4.2. By splitting the Zeeman sub-levels with a magnetic field $B_z = 6.1\,\mathrm{G}$, a complete isolation of the one photon transition

is achieved, with a negligible fraction of atoms driven to neighbouring sub-states (Fig. 4.2(a)). Analogously, we can observe a less efficient isolation in two-photon excitation, where a significant percentage ($\sim 1.85\,\%$ in Fig. 4.2(b)) of the atoms evolve outside the desired transition.

4.1.3 Microwave field dependency of Rydberg-Rydberg transitions

The Zeeman splitting of the Rydberg spin sub-states allows us to assume an effective two-level approximation to drive the transition between two specific sub-states. In order to confirm such approximation, we characterise the relation between the microwave power and the observed Rabi frequency of either one- and two-photon transitions.

In Section 4.1.2, the transition probability has been measured spectroscopically, by resonantly probing the transition for a variable driving time t_{ev}, allowing for the observation of coherent Rabi oscillations. The Rabi frequency Ω can be precisely calibrated from a fit to $\rho_{\uparrow\uparrow} = \frac{1}{2}[1 - \cos(\Omega \cdot t) \cdot \exp(-t^2/\sigma_\tau^2)]$. A more extensive analysis of this phenomenon is presented in Section 4.2. For $|nS\rangle - |nP\rangle$ transitions the Rabi frequency is expected to scale linearly with the electric field, whereas for $|nS\rangle - |(n+1)S\rangle$ transitions, the relation is proportional to the product of both Rabi frequencies and, therefore, quadratic with the microwave field. Ideally, for ultracold atoms, the Rabi frequency is given as

$$\Omega_{(1-\gamma)} = \frac{\mu|E|}{\hbar} \tag{4.5a}$$

$$\Omega_{(2-\gamma)} = \frac{\mu_1\mu_2|E|^2}{8\hbar^2\Delta} \tag{4.5b}$$

Independent measurements of the electric field involved in the coupling are not accessible due to the extended intensity profile emitted by the microwave antenna, which makes it impossible to map the field amplitude at the position of the atoms. However, the scaling relation can be still characterised, as microwave power output is proportional to the square of the field amplitude, $P \propto |E|^2$. In Figure 4.3, the calibration of the scaling behaviour is presented. We show results for the transitions $|42S_{1/2}, m_j = -1/2\rangle \leftrightarrow |42P_{3/2}, m_j = -3/2\rangle$ and $|48S_{1/2}, m_j = 1/2\rangle \leftrightarrow |49S_{1/2}, m_j = 1/2\rangle$, respectively. The observations confirmed that single-photon transitions amongst well-separated m_j sub-states follow the expected proportionality with the electric field (Fig. 4.3(a.2)) and the two-photon processes scale quadratically

(Fig. 4.3(b.2)), despite possible interference effects of the multiple paths, represented in Fig. 4.3(b.1).

Another important evidence of the validity of the effective two-level approximation is demonstrated by the measurement of the spectral light shift Δ_{LS}. At increasing Rabi frequencies, a shift in the resonant position is measured. Compared to the measured Rabi frequency of the $|48S_{1/2}, m_j = 1/2\rangle \leftrightarrow |49S_{1/2}, m_j = 1/2\rangle$ two-photon transition, a linear scaling is observed, with a fitted slope $\sim 0.051 \pm 0.001$. Theoretical analysis of two-photon light shift [Ryabtsev *et al.*, 2005] leads to the following behaviour

$$\Delta_{LS} = \frac{(\mu_1^2 - \mu_2^2)|E|^2}{16\hbar^2\Delta} = \frac{\mu_1^2 - \mu_2^2}{2\mu_2 \cdot \mu_2} \cdot \Omega, \tag{4.6}$$

thus, predicting a slope ≈ 0.025.

In addition, we can rely on the precise knowledge of the dipole matrix elements (see Appendix B) to perform local measurements of the microwave field, using the atoms as a sensor. We are sensitive to microwave fields smaller than $|E| \sim 1 \frac{\mu V}{cm}$ in the present conditions, which can be further enhanced with a tailored selection of states. This constitutes a precise and highly sensitive technique to perform microwave electrometry in a cold gas of Rydberg atoms with reduced amplitude uncertainty, as an alternative to other methods based on microwave Autler-Townes splitting of Rydberg-EIT spectra in thermal vapour cells [Sedlacek *et al.*, 2012; Anderson *et al.*, 2014; Anderson *et al.*, 2016]. Sensitivities of $|E| \sim 8 \frac{\mu V}{cm}$ have been reported in [Anderson *et al.*, 2014] for the degenerate transition $|62S_{1/2}\rangle \leftrightarrow |62P_{3/2}\rangle$, for which we expect a factor of ~ 2.2 sensitivity enhancement due to the $\propto n^*$ scaling of the transition matrix elements. Our atomic detection via calibration of Rabi oscillations surpasses the to-date reported level of sensitivity and presents polarisation selectivity. As a counterpart, this requires the implementation of a more complex cold-atom and detection scheme, with less perspective for future miniaturisation and commercial development of microwave sensors [Holloway *et al.*, 2014].

In conclusion, our investigations reveal a precise control of one- and two-photon microwave driven transitions and prove the validity of the effective two-level approximation in the explored range. Nevertheless, enhancement or suppression of the effective coupling $\Omega_{(2-\gamma)}$ could happen due to interference of multiple pathways in the two-photon case, as sketched in Fig. 4.3(b.1).

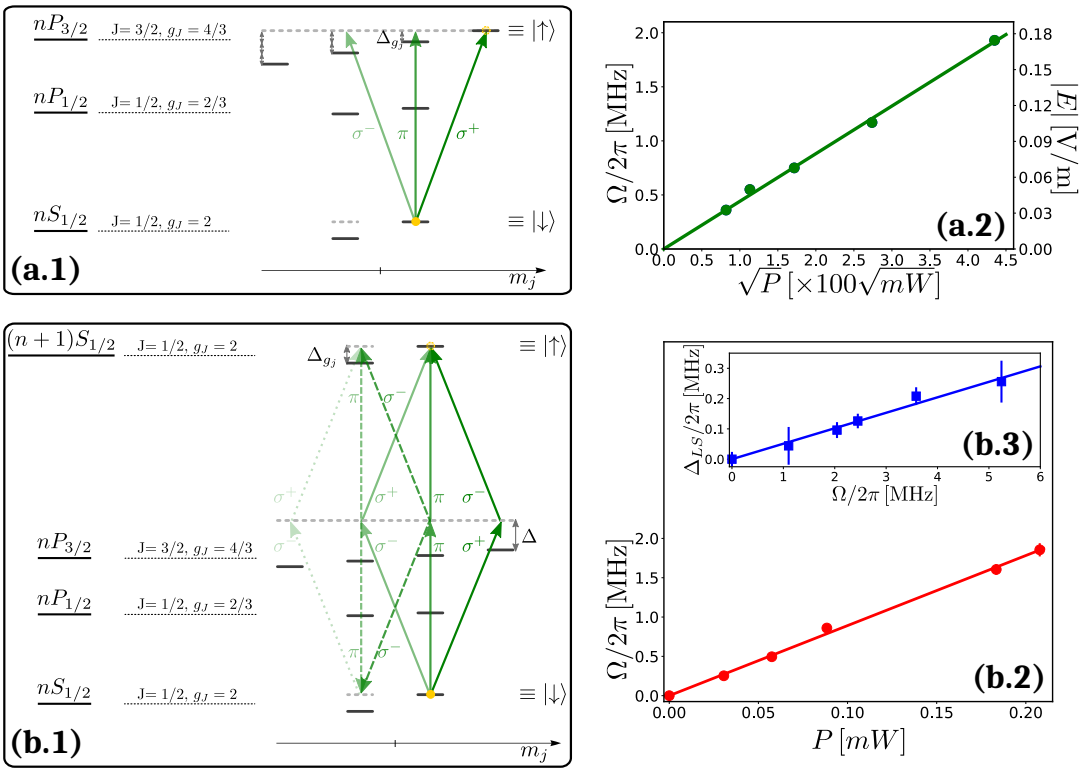

Figure 4.3: Experimental preparation of a Rydberg spin-$1/2$ system addressed by one- ((a)) and two-photon transitions ((b)). **(a.1)** Level scheme for nS-nP transitions separated by Zeeman shift. Rydberg atoms prepared in the selected spin state, e.g. $|\downarrow\rangle = |nS_{1/2}, m_j = 1/2\rangle$, are coupled to the spin-up state, e.g. $|\uparrow\rangle = |nP_{3/2}, m_j = 3/2\rangle$, by means of a microwave field with three polarisation components. The Zeeman m_j sub-states are split by a magnetic field $B_z \approx 6.1\,\mathrm{G}$ that strongly suppresses population transfer to neighbouring sub-states. (Zeeman splitting to scale.) **(a.2)** Measured Rabi oscillations reveal a linear relation between the Rabi frequency Ω and the generated output field $\sqrt{P}$ (measurements taken for $|42S_{1/2}, m_j = -1/2\rangle \leftrightarrow |42P_{3/2}, m_j = -3/2\rangle$). The amplitude $|E|$ of significantly weak microwave fields is accurately inferred. **(b.1)** Level scheme for nS-$(n+1)S$ transitions. Rydberg atoms initially prepared in an nS Zeeman sub-state, e.g. $|\downarrow\rangle = |nS_{1/2}, m_j = 1/2\rangle$, are coupled to a Zeeman sub-state of $(n+1)S$ by means of two photons of equal frequency, addressing the intermediate $nP_{3/2}$ state with a large detuning Δ from the reference $m_j = 3/2$, which suppresses single-photon processes. A residual fraction of population can be driven to the neighbouring Zeeman $S_{1/2}$ sub-states. **(b.2)** Consequently, driving of spins results in an effective two-photon transition with Rabi frequency $\Omega \propto |E|^2$, observed in the linear relation of Ω to the microwave power P (for $|48S_{1/2}, m_j = 1/2\rangle \leftrightarrow |49S_{1/2}, m_j = 1/2\rangle$). **(b.3)** Linearity of spectral AC-Stark shift Δ_{LS} with the effective Rabi frequency Ω.

4.2 Limitations to the observation of coherent Rabi oscillations

In order to explore the dynamical properties of Rydberg spins under different conditions, we aim to comprehend on which timescales we can observe coherent Rabi oscillations. The dephasing due to frequency fluctuations of the microwave field is negligible in comparison to any other timescales of the system, whereas the loss of spins is small on timescales of few microseconds due to the large lifetimes of Rydberg atoms (see Section 2.1). The wavelength of the microwave field that can be generated by our Anritsu MG3697C microwave synthesizer ranges from $\sim 4.5\,\mathrm{mm}$ to $\sim 150\,\mathrm{mm}$, as discussed in Section 2.5. Therefore, it is reasonable to assume a spatially homogeneous microwave field over the whole region of the Rydberg atoms ($\sim 60\,\mu\mathrm{m}$). Such synthesizers also provide remarkable power stability, so the intrinsic temporal power fluctuations should make a negligible impact on the experimental observations. Taking all these factors into account, observation of full contrast in resonant Rabi oscillations should be possible over $\sim 10\,\mu\mathrm{s}$. Nevertheless, fluctuations in the microwave intensity were measured by collecting the radiation from the emitting microwave antenna with a second antenna after the experimental chamber. Such fluctuations play an important role on the damping of the Rabi cycles. The underlying process leading to intensity fluctuations of the field at the cloud position may be related to interference effects of the field within the experimental apparatus. As our experimental chamber presents metallic surfaces, the emission pattern of the microwave field can be strongly reflected. Thus, the atoms could be affected by an intensity pattern emerging from the interference of different contributions. Any small variation of the optical path can generate a local variation of the relative phase of the interfering fields and, thus, a temporal fluctuation in the intensity pattern. Such random phase fluctuations would lead to temporal Gaussian fluctuation of the local intensity at the position of the Rydberg atoms. Hence, this process can be modelled by assuming a Gaussian distribution of intensity over time.

Considering a two-photon transition, $|nS\rangle \leftrightarrow |(n+1)S\rangle$, the transition Rabi frequency Ω has been demonstrated to scale linearly with the microwave power (Section 4.1). Therefore, Gaussian fluctuations of the microwave intensity may be modelled as a Gaussian probability distribution of Rabi frequencies

$$\frac{d\mathcal{P}_\Omega}{d\Omega}(\Omega) = \frac{1}{\sigma_\Omega\sqrt{2\pi}} e^{\frac{-\Omega^2}{2\sigma_\Omega^2}}. \tag{4.7}$$

In this case, the dynamical evolution can be solved analytically. For a single Rabi

oscillation, the time evolution of the spin population in the $|\uparrow\rangle$ state, $\rho_{\uparrow\uparrow}$, is commonly described as be

$$\rho_{\uparrow\uparrow}(t,\Omega_0) = \sin^2\left(\frac{\Omega_0 t}{2}\right) = \frac{1-\cos(\Omega_0 t)}{2}. \tag{4.8}$$

In order to include the effect of Gaussian fluctuations on the Rabi frequency, the Fourier transform of both frequency-dependent functions must be integrated in the time domain thus leading to the following general expression for the spin-up population

$$\bar{\rho}_{\uparrow\uparrow}(t) = \frac{1-\cos(\Omega_0 t)\cdot e^{\frac{-\sigma_\Omega^2 t^2}{2}}}{2}. \tag{4.9}$$

The simplicity of the analytical solution from Eq. (4.9) allows for precise experimental inference of the microwave intensity noise. As can be observed in Fig. 4.4(a), our normalised Rabi oscillations present a significant dephasing. In order to account for the dephasing rate, damped oscillations are fitted to the function

$$\rho_{\uparrow\uparrow}(t) = \frac{A}{2}\left(1-\cos(\Omega_0 t)\cdot e^{-\frac{t^2}{\sigma_\tau^2}}\right). \tag{4.10}$$

A linear correlation between the dephasing rate σ_τ^{-1} and the Rabi frequency $\Omega_0/2\pi$ is directly inferred (Fig. 4.4(b)), which implies the observation of a constant number of Rabi cycles, $\sigma_\tau \cdot \Omega_0/2\pi$ independently of the driving Rabi frequency. Given that the noise distribution is assumed to be Gaussian (Eq. (4.7)), the fraction of intensity fluctuations C is defined as the quotient between the distribution frequency width σ_Ω and its maximum Ω_0. As a consequence, σ_Ω and its associated intensity noise are predicted by comparing this correlation to the experimental dephasing rate of the Rabi oscillations σ_τ^{-1}. This is described by the simple expression

$$C = \frac{\sigma_\Omega}{\Omega_0} = \frac{\sqrt{2}}{\sigma_\tau \cdot \Omega_0}. \tag{4.11}$$

Thus, the microwave intensity fluctuation C is directly proportional to the slope of Figure 4.9(b), $s = \frac{C\cdot 2\pi}{\sqrt{2}}$, proving that only a fixed limited number of Rabi cycles can be distinguished. The experiments show evidence of an initial $7.3 \pm 0.5\,\%$ relative variation of Rabi frequency (red curve), which corresponds to 3.1 ± 0.1 coherent Rabi cycles. To reduce this dephasing source, the microwave intensity stability could be considerably improved by using metallic materials to guide the field between the microwave antenna and the experimental chamber. Limiting the reflections and interference effects of the microwave field with different parts of the set-up reduced

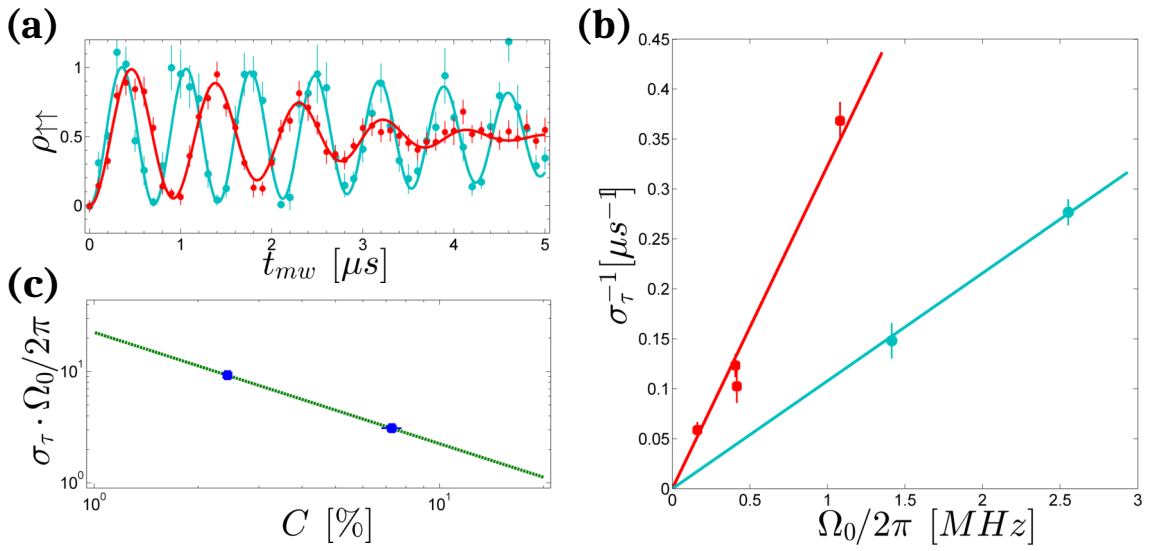

Figure 4.4: Normalised two-photon Rabi oscillations between $|48S_{1/2}, m_j = 1/2\rangle$ and $|49S_{1/2}, m_j = 1/2\rangle$. **(a)** Comparison between Rabi oscillations without (red, $\Omega_0/2\pi = 1.081 \pm 0.004\,\mathrm{MHz}$) and with intensity stabilisation (turquoise, $\Omega_0/2\pi = 1.414 \pm 0.003\,\mathrm{MHz}$). A significant increase of the number of observed oscillations can be appreciated after reducing the microwave intensity noise. Lines correspond to fit with Gaussian envelope as described in Eq. (4.10). **(b)** Dependence of the dephasing rate σ_τ^{-1} on the Rabi frequency for experiments performed with (turquoise) and without intensity stabilisation (red). The slopes reveal power fluctuations of $C = 7.3 \pm 0.5\,\%$ and $C = 2.4 \pm 0.2\,\%$, respectively, that correlate dephasing time σ_τ^{-1} and Rabi frequency Ω_0 for each set-up. **(c)** Measured (blue) and predicted (green line) number of Rabi cycles within the dephasing rate σ_τ, given by $\sigma_\tau \cdot \Omega_0/2\pi$, as a function of the percentage of fluctuations C. The number of cycles is independent of the measured Rabi frequency Ω_0. Data are the average over 10 (turquoise) and 20 (red) realisations. Error bars are given by one standard error.

the relative fluctuation to $2.4 \pm 0.2\,\%$ (turquoise curve) and allowed to observe an increased number of 9.3 ± 0.2 Rabi cycles within the dephasing time σ_τ $(1/e)$. Whereas the intensity fluctuations produce damping of the Rabi oscillations, they would lead to Gaussian broadening of the spectrum for long driving times, when the spectral width can no longer be reproduced by the Fourier limited Rabi-Breit formula (see Section 4.1).

For the case of a single-photon transition, $|nS\rangle \leftrightarrow |nP\rangle$, the Gaussian probability distribution of power leads to a non-Gaussian Rabi frequency probability distribution such as

$$\frac{d\mathcal{P}_P}{dP}(P) = \frac{1}{\sigma_P\sqrt{2\pi}} e^{\frac{-P^2}{2\sigma_P^2}} \Longrightarrow \frac{d\mathcal{P}_\Omega}{d\Omega}(\Omega) = \frac{2\Omega}{\sigma_P\sqrt{2\pi}} e^{\frac{-\Omega^4}{2\sigma_P^2}}. \tag{4.12}$$

The Fourier transform of such distribution, which describes the envelope of the temporal evolution is a more complex function, inappropriate to analytically describe the field fluctuations. Nevertheless, the resultant distribution of Rabi frequencies presents a shape that can still be approximated by a Gaussian. Thus, an oscillating function with a Rabi frequency dependent Gaussian envelope can still constitute a good model to describe $|nS\rangle \leftrightarrow |nP\rangle$ oscillations.

The experiments discussed in this section revealed that power instability of the driving field constitutes the principal limitation to the observation of coherence in Rabi oscillations. Further improvement of the power stability would be beneficial, in order to exclude dephasing effects from the driving field to play a role on more refined experimental sequences. The effect of our field fluctuations on specific pulse sequences will be quantified in Section 4.5. In addition, implementation of BB1 control sequences allows to perform oscillations between the spin states with reduced effect of field intensity fluctuations [Morton *et al.*, 2005].

4.3 Modelling the dynamics of non-interacting Rydberg spins

In Section 4.1, the experimental approach to drive Rydberg-Rydberg transitions has been presented. However, the fundamental limitations on the coherence of Rydberg spins must be discussed. In this section, the behaviour of the spin system is described with a simple model of two-level spins plus a third level which accounts for the decay of the spin populations, acting as a container of additional states. The coherent evolution is described by its Hamiltonian in the rotating frame (details can be consulted in [Steck, 2007]) and the decoherence processes are considered by a Lindblad superoperator. The evolution of the system is described in terms of its density matrix [Blum, 2012].

The spin states $|\downarrow\rangle$ and $|\uparrow\rangle$, are coupled by means of a microwave field, with Rabi frequency Ω. A third state $|c\rangle$ includes the population of any other additional states. The basis $\{\downarrow, \uparrow, c\}$ forms the Hilbert space of our model.

Two loss mechanisms are considered:

(i) Spontaneous decay from the spin states towards allowed dipole transitions. This process presents negligible rates to nearby Rydberg states and high rates to low-lying quantum states.

(ii) Stimulated black-body decay from the spin states. This phenomenon redistri-

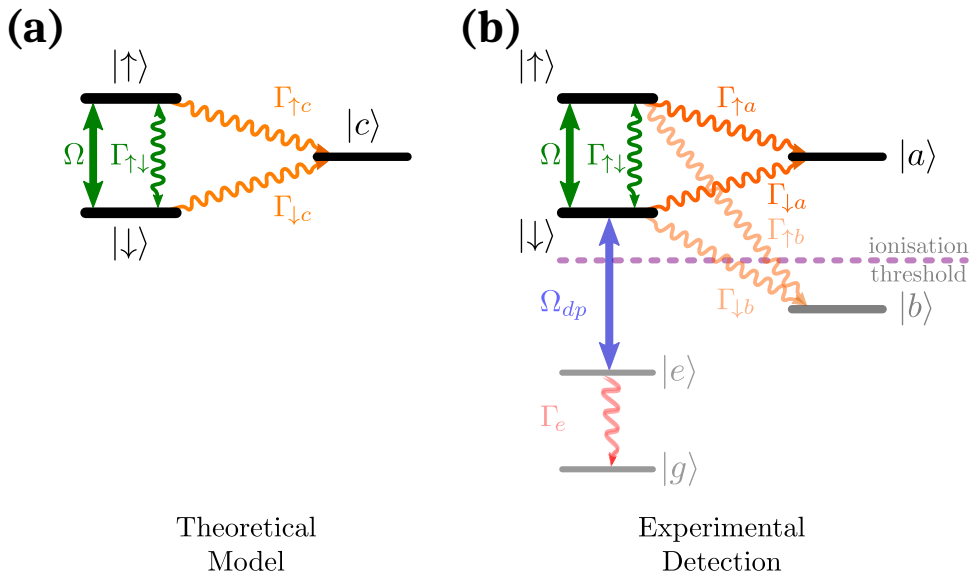

Figure 4.5: General level scheme to model the dynamics of Rydberg spins. (a) Two Rydberg spin states $|\downarrow\rangle$ and $|\uparrow\rangle$ are coupled through a microwave field with Rabi frequency Ω. The population on the spin states is reduced due to loss of population towards a container of additional states $|c\rangle$ and their coherence is limited by the interstate decay $\Gamma_{\uparrow\downarrow}$ (given $\Gamma_{\downarrow\uparrow} \cong \Gamma_{\uparrow\downarrow}$). **(b)** Experimentally, all states above the ionisation threshold are detected. The redistribution of $|\downarrow\rangle$ and $|\uparrow\rangle$ spin states causes that a fraction of the population decays to states above the ionisation threshold, $|a\rangle$, with rates $\Gamma_{\downarrow a}$, $\Gamma_{\uparrow a}$, whereas the rest is lost to non-detected states below, $|b\rangle$, with rates $\Gamma_{\downarrow b}$, $\Gamma_{\uparrow b}$. The detection of $|\downarrow\rangle$ is discriminated by means of a rapid down-pumping pulse Ω_{dp}, which depletes the $|\downarrow\rangle$ population before detection. Independent experiments are required to measure the decay rates towards $|a\rangle$ and $|b\rangle$.

butes spin populations towards dipole-allowed nearby states. A fraction of this decay evolves bidirectionally between both spin states, incoherently exchanging population.

The spin decay is quantified by the decay rates $\Gamma_{\downarrow c}, \Gamma_{\uparrow c}$ from the spin states to the container state $|c\rangle$. Such rates include the effect of spontaneous emission and the fraction of black-body stimulated emission which evolves outside the two spin-state sub-space $\{\downarrow, \uparrow\}$. Furthermore, the decay rates $\Gamma_{\uparrow\downarrow}, \Gamma_{\downarrow\uparrow}$ account for the internal decay between the spins. For Rydberg-Rydberg transitions, such rates are congruent $\Gamma_{\uparrow\downarrow} \cong \Gamma_{\downarrow\uparrow}$. The details of out schematic model can be consulted in Figure 4.5(a).

4.3.1 Optical Bloch equations' solution

To describe the coupled atom-light system, we consider the spins in the low density regime, such that spin-spin interaction effects can be neglected. In the dipole and rotating wave approximations, the system is described by the Hamiltonian

$$\hat{\mathcal{H}} = \frac{\hbar}{2}\begin{pmatrix} 0 & \Omega & 0 \\ \Omega & -2\Delta & 0 \\ 0 & 0 & 0 \end{pmatrix}, \tag{4.13}$$

in the basis $\{\downarrow, \uparrow, c\}$.

The complete evolution of the dynamics and what limits the coherence time we use the density matrix formalism and derive the master equation for the single atom density matrix ρ

$$\dot{\rho} = -\frac{i}{\hbar}[\hat{\mathcal{H}}, \rho] + \mathcal{L}_{dec} + \mathcal{L}_{deph} \tag{4.14}$$

where $\rho_{ij} = \rho^*_{jk}$ and $\mathcal{L}_{dec}$ is the Lindblad superoperator, accounting for the loss of coherence due to population decay amongst the involved states

$$\mathcal{L}_{dec} = -\frac{1}{2}\sum_k (C_k^\dagger C_k \rho + \rho C_k^\dagger C_k) + \sum_k C_k \rho C_k^\dagger \tag{4.15}$$

with the decay stength of the $k-th$ decay channel defined by the collapse operators C_k. In our model, the decay channels involved are the following

$$\begin{aligned} C_{\downarrow c} &= \sqrt{\Gamma_{\downarrow c}}\,|c\rangle\langle\downarrow|\,, \qquad C_{\uparrow c} = \sqrt{\Gamma_{\uparrow c}}\,|c\rangle\langle\uparrow|\,, \\ C_{\downarrow\uparrow} &= \sqrt{\Gamma_{\downarrow\uparrow}}\,|\uparrow\rangle\langle\downarrow|\,, \qquad C_{\uparrow\downarrow} = \sqrt{\Gamma_{\uparrow\downarrow}}\,|\downarrow\rangle\langle\uparrow|\,. \end{aligned} \tag{4.16}$$

The terms $C_{\downarrow c}$ and $C_{\uparrow c}$ correspond to the decay from the states $|\downarrow\rangle$ or $|\uparrow\rangle$, respectively, to the reservoir state $|c\rangle$, whereas $C_{\downarrow\uparrow}$ and $C_{\uparrow\downarrow}$ account for the rate of black-body induced decay from $|\downarrow\rangle$ to $|\uparrow\rangle$ and vice versa.

Since the driving microwave signal presents few hertz stability, we can ignore the Lindblad term $\mathcal{L}_{deph}$ related to dephasing. Hence, the matrix elements ρ_{ij} are described by a set of time-dependent coupled equations, so called Optical-Bloch

equations (OBEs):

$$\dot{\rho}_{\downarrow\downarrow} = -\big(\Gamma_{\downarrow\uparrow} + \Gamma_{\downarrow c}\big)\rho_{\downarrow\downarrow} + \Gamma_{\uparrow\downarrow}\rho_{\uparrow\uparrow} - \tfrac{i}{\hbar}\tfrac{\Omega}{2}\big(\rho_{\uparrow\downarrow} - \rho_{\downarrow\uparrow}\big) \tag{4.17a}$$

$$\dot{\rho}_{\uparrow\uparrow} = -\big(\Gamma_{\uparrow\downarrow} + \Gamma_{\uparrow c}\big)\rho_{\uparrow\uparrow} + \Gamma_{\downarrow\uparrow}\rho_{\downarrow\downarrow} + \tfrac{i}{\hbar}\tfrac{\Omega}{2}\big(\rho_{\uparrow\downarrow} - \rho_{\downarrow\uparrow}\big) \tag{4.17b}$$

$$\dot{\rho}_{cc} = \Gamma_{\downarrow c}\rho_{\downarrow\downarrow} + \Gamma_{\uparrow c}\rho_{\uparrow\uparrow} \tag{4.17c}$$

$$\dot{\rho}_{\downarrow\uparrow} = -\tfrac{1}{2}\big(\Gamma_{\downarrow\uparrow} + \Gamma_{\uparrow\downarrow} + \Gamma_{\downarrow c} + \Gamma_{\uparrow r}\big)\rho_{\downarrow\uparrow} - \tfrac{i}{\hbar}\tfrac{\Omega}{2}\big(\rho_{\uparrow\uparrow} - \rho_{\downarrow\downarrow}\big) - \tfrac{i}{\hbar}\Delta\rho_{\downarrow\uparrow} \tag{4.17d}$$

$$\dot{\rho}_{\downarrow c} = -\tfrac{1}{2}\big(\Gamma_{\downarrow\uparrow} + \Gamma_{\downarrow c}\big)\rho_{\downarrow c} - \tfrac{i}{\hbar}\tfrac{\Omega}{2}\rho_{\uparrow c} \tag{4.17e}$$

$$\dot{\rho}_{\uparrow c} = -\tfrac{1}{2}\big(\Gamma_{\uparrow\downarrow} + \Gamma_{\uparrow c}\big)\rho_{\downarrow c} - \tfrac{i}{\hbar}\tfrac{\Omega}{2}\rho_{\downarrow c} - \tfrac{i}{\hbar}\Delta\rho_{\uparrow c} \tag{4.17f}$$

$$\dot{\rho}_{\uparrow\downarrow} = (\dot{\rho}_{\downarrow\uparrow})^* \tag{4.17g}$$

$$\dot{\rho}_{c\downarrow} = (\dot{\rho}_{\downarrow c})^* \tag{4.17h}$$

$$\dot{\rho}_{c\uparrow} = (\dot{\rho}_{\uparrow c})^*. \tag{4.17i}$$

The numerical integration of equations (4.17) describes the general evolution of the spin system. To fully understand the dynamics of the non-interacting spins, the evolution of the spin projections under driving conditions has to be understood. For such purpose, the evolution of the expectation values of the spin operators $\langle \hat{S}_\alpha \rangle$ has to be described. For a spin-$\frac{1}{2}$ system with loss of particles to a non-involved reservoir, the components of the spin vector can be defined as

$$\hat{S}_x = \frac{\hbar}{2}\begin{pmatrix} 0 & 1 & 0 \\ 1 & 0 & 0 \\ 0 & 0 & 0 \end{pmatrix}, \qquad \hat{S}_y = \frac{\hbar}{2}\begin{pmatrix} 0 & -i & 0 \\ i & 0 & 0 \\ 0 & 0 & 0 \end{pmatrix}, \qquad \hat{S}_z = \frac{\hbar}{2}\begin{pmatrix} 1 & 0 & 0 \\ 0 & -1 & 0 \\ 0 & 0 & 0 \end{pmatrix}. \tag{4.18}$$

Since the subspace of interest is composed by the two spin states $|\downarrow\rangle$ and $|\uparrow\rangle$, the evolution of the system is re-normalised over time by the remaining fraction of atoms in the spin states. By performing this re-normalisation, we can define the $\alpha-$magnetisation of the spin states as

$$M_x(t) = \frac{\rho_{\uparrow\downarrow}(t) + \rho_{\downarrow\uparrow}(t)}{2 \cdot \big(\rho_{\uparrow\uparrow}(t) + \rho_{\downarrow\downarrow}(t)\big)} \tag{4.19a}$$

$$M_y(t) = -i\frac{\rho_{\uparrow\downarrow}(t) - \rho_{\downarrow\uparrow}(t)}{2 \cdot \big(\rho_{\uparrow\uparrow}(t) + \rho_{\downarrow\downarrow}(t)\big)} \tag{4.19b}$$

$$M_z(t) = \frac{\rho_{\uparrow\uparrow}(t) - \rho_{\downarrow\downarrow}(t)}{2 \cdot \big(\rho_{\uparrow\uparrow}(t) + \rho_{\downarrow\downarrow}(t)\big)} \tag{4.19c}$$

In Figure 4.6, the evolution of populations ρ_{ii}, spin operators $\langle \hat{S}_\alpha \rangle$ and M_z magnetisation is numerically simulated (Eq. (4.17)). On the one hand, decay of the spins between $|\downarrow\rangle$ and $|\uparrow\rangle$ results in a symmetric decoherence, which exponentially

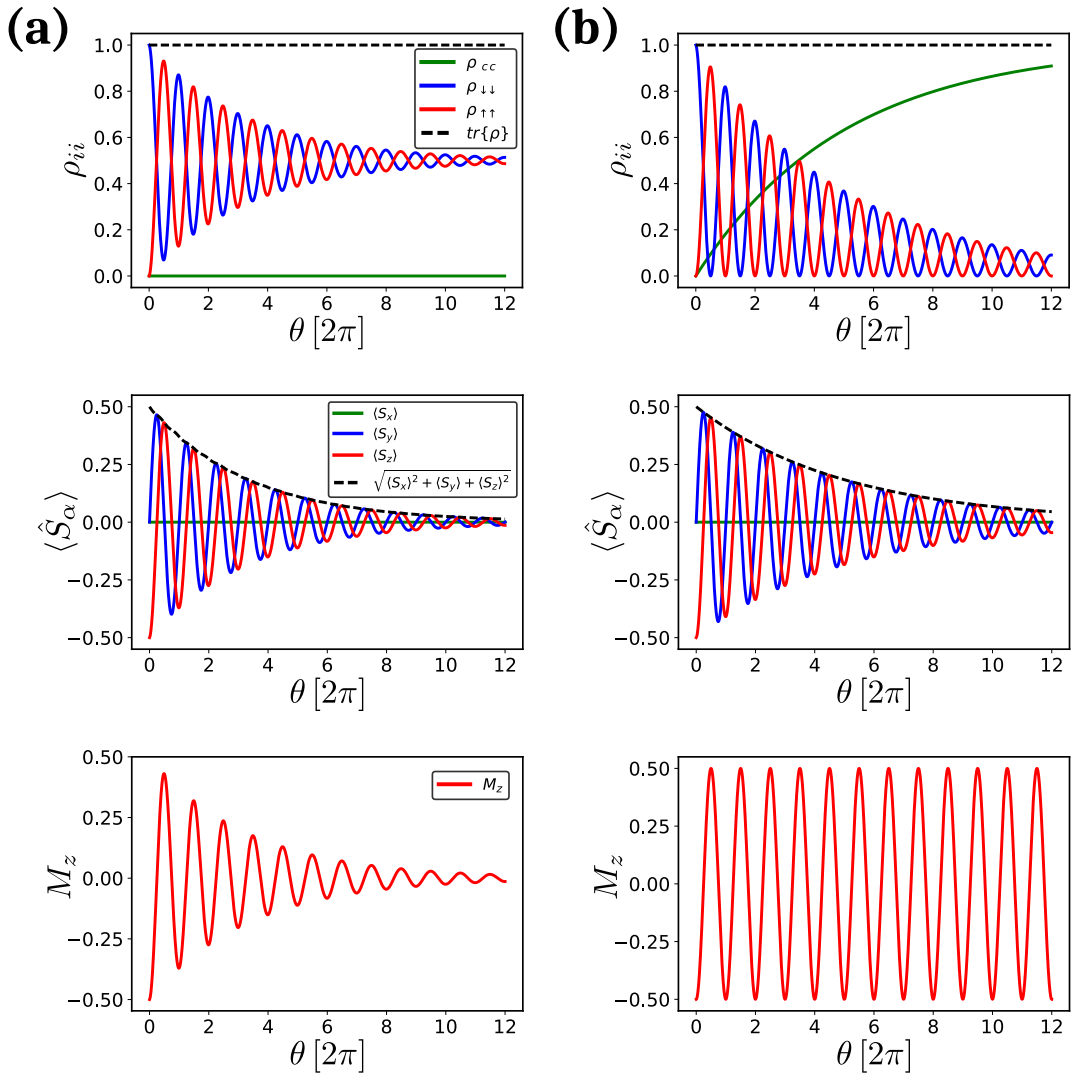

Figure 4.6: Simulations of the microwave-driven Rydberg spin dynamics. The initial state is prepared as $|\psi_0\rangle \equiv |\downarrow\rangle$ and resonantly driven with Rabi frequency Ω, allowing for evolution during a certain number of Rabi cycles θ. **(a)** The internal decay between the desired spin states leads to decoherence, observed as an exponential decay of contrast in population (ρ_{ii}), the expectation value of spin operators ($\langle \hat{S}_\alpha \rangle$) and the magnetsation ($M_z$) of the spin ensemble, with rate $\Gamma_{dec} = \frac{\Gamma_{\downarrow\uparrow}+\Gamma_{\uparrow\downarrow}}{4/3}$. $\Gamma_{\downarrow\uparrow} = \Gamma_{\uparrow\downarrow} = 0.2 \cdot \Omega/2\pi$, $\Gamma_{\downarrow c} = \Gamma_{\uparrow c} = 0$. **(b)** Loss of spins during the evolution time leads to an exponential decrease of the spin populations with rate $\Gamma_c = \frac{\Gamma_{\downarrow c}+\Gamma_{\uparrow c}}{2}$. This causes reduction of contrast in $\langle \hat{S}_\alpha \rangle$ but the magnetisation M_z remains unaffected by the loss of spin population. Hence, M_z is a robust observable to characterise decoherence effects in the spin dynamics (Eq. (4.23)). $\Gamma_{\downarrow\uparrow} = \Gamma_{\uparrow\downarrow} = 0$, $\Gamma_{\downarrow c} = \Gamma_{\uparrow c} = 0.2 \cdot \Omega/2\pi$. For realistic Rydberg spins, all rates are an order of magnitude smaller, depending on the selection of quantum numbers.

reduces the contrast of the three quantities towards half of their maximum amplitude with rate $\Gamma_{dec} = \frac{\Gamma_{\downarrow\uparrow}+\Gamma_{\uparrow\downarrow}}{4/3}$. On the other hand, the effect of spin loss generates a decrease of amplitude in the oscillations, transferring part of the population to the container $|c\rangle$, which exponentially increases with the rate $\Gamma_c \approx \frac{\Gamma_{\downarrow c}+\Gamma_{\uparrow c}}{2}$. This spin loss affects $\langle \hat{S}_\alpha \rangle$ as well, symmetrically decaying according to Γ_c. However, the magnetisations M_α of the spin ensemble are insensitive to the loss of spins, constituting a reliable platform to study the effect of the inter-spin decay, disentangled from the influence of Γ_c. Thus, under continuous resonant driving, the numerical solution of the temporal evolution is well described by the set of equations

$$\rho_{\uparrow\uparrow}(t) = \frac{1-\cos(\Omega t)\cdot e^{-\frac{\Gamma_{\uparrow\downarrow}+\Gamma_{\downarrow\uparrow}}{4/3}t}}{2}\cdot e^{-\frac{\Gamma_{\uparrow c}+\Gamma_{\downarrow c}}{2}t} \tag{4.20a}$$

$$\langle \hat{S}_z \rangle (t) = -\frac{\cos(\Omega t)}{2}\cdot e^{-\frac{\Gamma_{\uparrow\downarrow}+\Gamma_{\downarrow\uparrow}}{4/3}t}\cdot e^{-\frac{\Gamma_{\uparrow c}+\Gamma_{\downarrow c}}{2}t} \tag{4.20b}$$

$$M_z(t) = -\frac{\cos(\Omega t)}{2}\cdot e^{-\frac{\Gamma_{\uparrow\downarrow}+\Gamma_{\downarrow\uparrow}}{4/3}t} \tag{4.20c}$$

in the limit where $\Gamma_{\uparrow\downarrow} \sim \Gamma_{\downarrow\uparrow}$ and $\Gamma_{\uparrow c} \sim \Gamma_{\downarrow c}$. The complementary components $\langle \hat{S}_y \rangle, M_y$ follow the same dynamics as $\langle \hat{S}_z \rangle, M_z$, with a $\frac{\pi}{2}$ phase shift.

4.3.2 Decoherence timescales

The decoherence of the spins can be understood in terms of the classical NMR description of T_1 and T_2 [Wangsness and Bloch, 1953; Redfield, 1957; Geva *et al.*, 1995]. Here these timescales are clarified for our specific system and experiments proposed for their observation.

In NMR, the systems are affected by relaxation processes that lead to redistribution of the two-spin components to achieve thermal equilibrium and the steady value M_0. The relaxation time of the spins defines the T_1 timescale, as described by [Ithier *et al.*, 2005] for a superconducting two-level qubit. In the Rydberg spin case, the spins evolve towards a completely depolarised state with negligible population on either $|\downarrow\rangle$ and $|\uparrow\rangle$, dominated by the decay rate to the container state $|c\rangle$. The additional complexity of requiring a third state in our model implies that a T_1 for the spins, analogous to the NMR standards, cannot be determined. However, T_1^* can be defined as the time for the total population to be depleted. Thus,

$$T_1^* = \frac{1}{\Gamma_c} = \frac{2}{\Gamma_{\uparrow c}+\Gamma_{\downarrow c}} \tag{4.21}$$

This can be observed by measuring the temporal evolution of the population in the superposition state $|\hat{S}_y\rangle = \frac{1}{\sqrt{2}}(|\downarrow\rangle + i\,|\uparrow\rangle)$.

The transversal component of the decoherence, given by the decay of the off-diagonal components of the spin density matrix constitutes the T_2. This timescale can be inferred from the evolution of magnetisation in time-dependent Ramsey experiments, as performed in Section 4.6. The decoherence rate measured in such experiments is given by $\Gamma = \frac{\Gamma_{\downarrow\uparrow}+\Gamma_{\uparrow\downarrow}}{2}$. Then,

$$T_2 = \frac{1}{\Gamma_c} = \frac{2}{\Gamma_{\downarrow\uparrow} + \Gamma_{\uparrow\downarrow}} \tag{4.22}$$

It must be noted that the associated rate is different from the Γ_{dec} affecting the evolution under continuous driving due to the effect of the coupling field. In addition, the experimental realisation includes the effect of inhomogeneities in the driving field. Therefore, we will name the experimental timescale as T_2^* hereafter.

4.4 Reconstruction of the magnetisation

After developing our theoretical model, it becomes clear that it is convenient to observe the evolution of M_z, but its experimental reconstruction presents several subtleties. However, the experimental reconstruction of the magnetisation presents certain subtleties that are to be discussed. As described in Section 3.1.6, our spin detection technique relies on a global measurement of the number of spins in the excitation volume by field-ionising the Rydberg atoms above a certain energy threshold. The energy threshold is selected such that both $|\uparrow\rangle$ and $|\downarrow\rangle$ states can be ionised and detected with similar detection efficiency, which is calibrated as explained in Fig. 3.7(c). The spins can be distinguished by applying a down-pumping pulse after their dynamics was explored, as introduced in Section 3.4.

The magnetisation of the spins during the time evolution is measured to be

$$M_z(t) = \frac{N_\uparrow(t) - N_\downarrow(t)}{2 \cdot \big(N_\uparrow(t) + N_\downarrow(t)\big)} \tag{4.23}$$

Due to the lack of selectivity of our ionisation procedure, a fraction of the atoms in the container state $|c\rangle$ is measured in each experimental sequence. In Figure 4.5(b), this state is split into two different state collections, above $|a\rangle$ and below $|b\rangle$ the ionisation threshold with rates $\Gamma_{\uparrow a}, \Gamma_{\downarrow a}$ and $\Gamma_{\uparrow b}, \Gamma_{\downarrow b}$ describing the decay to ionised and non-ionised states, respectively. Therefore, during the exploration and detection of the spin dynamics, the number of atoms evolving to states above threshold produces a bias in the measurement, such as $N_{meas}(t) = N_\uparrow(t) + N_a(t)$. Precise detection of $N_\uparrow(t)$ requires to subtract N_a. Analogously, quantifying $N_\downarrow(t) = N_0 - N_\uparrow(t) - N_b(t)$

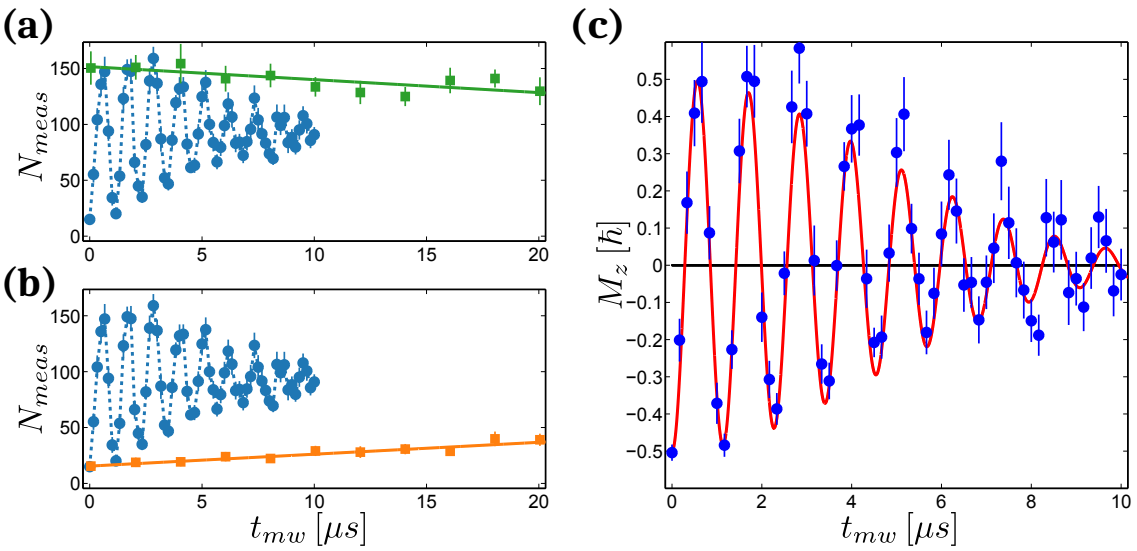

Figure 4.7: Experimental reconstruction of the spin-1/2 magnetisation. Measured Rabi oscillations between $|48S_{1/2}, m_j = 1/2\rangle \leftrightarrow |49S_{1/2}, m_j = 1/2\rangle$ (blue circles). The redistribution of atoms from $|\downarrow\rangle$ to states below **(a)** (green squares) and above **(b)** (orange squares) the ionisation threshold is quantified as detailed in Appendix C. The measured number of atoms in the Rabi oscillation is biased by the population in $|a\rangle$ (see Fig. 4.5): $N_{a(\downarrow)}(0) = 15.5 \pm 1.2$, $\Gamma_{\downarrow a} = 1.064 \pm 0.119\,\mu s^{-1}$. Analogous for the redistribution of spins in $|\uparrow\rangle$: $N_{b(\downarrow)}(0) = 151.6 \pm 3.2$, $\Gamma_{\downarrow b} = 1.159 \pm 0.317\,\mu s^{-1}$. **(c)** Evolution of the magnetisation M_z, quantified with the equations from Ap. C.0.1. Fit (red line) corresponds to a sinusoidal function with a Gaussian envelope: $\Omega = 2\pi \times (0.879 \pm 0.002)$ MHz, $\sigma_\tau = 6.26 \pm 0.32\,\mu s$. Error bars given by one standard error. Data are the average over 20 realisations.

demands an independent knowledge of the initial number of spins N_0 and the population reduction due to evolution below threshold $N_b(t)$. For that purpose, two complementary experiments are performed:

(i) Free evolution time after the spin preparation. The decay rates to states below threshold are measured: $\Gamma_{\downarrow b}, \Gamma_{\uparrow b}$.

(ii) Free evolution time after the spin preparation, with final down-pumping pulse. The initial imperfect preparation is quantified as $N_a(0)$, as well as the evolution rates $\Gamma_{\downarrow a}, \Gamma_{\uparrow a}$.
From the combination of (i) and (ii) for both $|\uparrow\rangle$ and $|\downarrow\rangle$, the initial number of spins N_0 is also extracted, providing all the ingredients to distinguish $N_\uparrow(t)$, $N_\downarrow(t)$ and $M_z(t)$. Further details can be consulted in Appendix C. Additionally, the information from the complementary experiments allows to measure T_1^*.

In Figure 4.7, an example of this reconstruction procedure is provided. Rabi oscillations between $|\downarrow\rangle = |48S_{1/2}, m_j = 1/2\rangle$ and $|\uparrow\rangle = |49S_{1/2}, m_j = 1/2\rangle$ are driven and experiments observed in (a) and (b) indicate the evolution of spins as in the descriptions (i) and (ii), respectively for spins prepared in $|\downarrow\rangle$. The evolution for spins in $|\uparrow\rangle$ is provided by the same measurements, multiplied by the theoretical correction factor $\frac{\Gamma_{\uparrow(a,b)}}{\Gamma_{\downarrow(a,b)}}$. As a consequence, the reconstructed magnetisation evolves symmetrically towards the steady state $M_z(t \to \infty) = 0$. Analogous procedure is applied to Ramsey-type experiments. This paves the path for accurate observation of the spin time-evolution with combined atomic-optical selectivity.

4.5 Tomographic control of Rydberg spins

In Section 4.1, efficient driving of Rydberg one- and two-photon transitions has been demonstrated. In this section, complete control of the quantum state of the spins is presented, in order to implement refined quantum control experimental sequences to probe the spin dynamics. In addition, the dephasing introduced by the driving pulses is quantified, as previously discussed in Section 4.2.

Applying quantum state manipulation sequences is essential to engineer logic quantum gates or to unravel the nature of spin-spin interactions [Vandersypen and Chuang, 2005]. The pulse area θ, controlled by both the pulse length and its Rabi frequency, has to be precisely controlled to rotate the spin-state (see Fig.4.1(b)). The phase of the microwave field ϕ sets the orientation of the field vector about which the spin Bloch vector rotates. Conventionally, the phase of the initial pulse is considered to be $\phi_1 = 0$. Thus, the phase introduced in subsequent pulses refers to the difference with respect to ϕ_1. A tomographic sequence relies on well-defined rotations to prepare and read out arbitrary spin states.

Our generalised tomographic experiments rely on the application of two consecutive $\frac{\pi}{2}$ pulses $\left(t_{\frac{\pi}{2}} = \frac{2\pi}{4\Omega_0}\right)$ to prepare and probe the coherent superposition state. After initialisation of the atoms in $|\downarrow\rangle$ by a two-photon excitation scheme, a first resonant microwave $\frac{\pi}{2}$-pulse rotates the spins to the equatorial xy-plane of the Bloch-Poincaré sphere. At the end of the pulse they lay in $|\hat{S}_y\rangle = \frac{1}{\sqrt{2}}(|\downarrow\rangle + i\,|\uparrow\rangle)$. A second $\frac{\pi}{2}$-pulse with a phase ϕ relative to the initial one projects the state on different directions, as described in Fig. 4.8(a). Repetitions of the experiment with different phases give a global map of the final state after arbitrary rotations. Finally, a down-pumping pulse and an ionising electric field allow to distinguish and detect the spin components. Under ideal conditions, when no dephasing mechanism limits the spin operations,

the following specific cases can be encountered:

(i) If $\phi = 0, 2\pi$, the second pulse rotates the spins about $\hat{x}$ to the final state $|\uparrow\rangle$.

(ii) If $\phi = \pi$, the second pulse imprints a rotation about $-\hat{x}$, reversing the effect of the initial pulse to achieve the final state $|\downarrow\rangle$.

(iii) If $\phi = \frac{\pi}{2}, \frac{3\pi}{2}$, the superposition state $|\hat{S}_y\rangle$ rotates about $\hat{y}$ or $-\hat{y}$, respectively, which locks the spin phase evolution. The rotation of the spin vector about its own axis constitutes the basis to apply spin-locking sequences [Redfield, 1955; Hatanaka and Hashi, 1978]. Fixing the spin-lock time to a π pulse duration can revert the acquired spin phase, as an alternative realisation of Hahn-spin-echo experiments [Hahn, 1950] by simply rotating about the perpendicular axis.

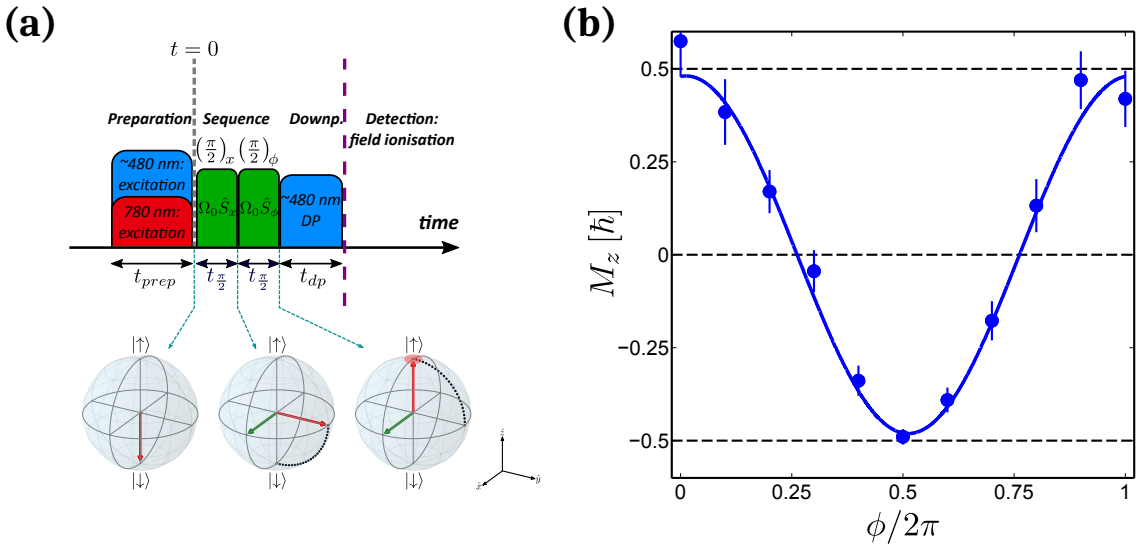

Figure 4.8: **(a)** Pulse sequence to rotate the quantum state of the spins. An initial $\frac{\pi}{2}$-pulse prepares the spins in the state $|\hat{S}_y\rangle = \frac{1}{\sqrt{2}}(|\downarrow\rangle + i\,|\uparrow\rangle)$. A second $\frac{\pi}{2}$-pulse is applied to read out the spin state, with a relative phase ϕ to the initial pulse. **(b)** Experimental demonstration of efficient spin rotation. The continuous line corresponds to a fit to the experimental function from Eq. (4.24). The contrast is measured to be $C = 96.2 \pm 2.7\,\%$ and the global phase $\phi_0 = -(0.012 \mp 0.007) \times 2\pi$. Data is averaged over 30 repetitions. Error bars correspond to one standard error of the mean.

This technique is advantageous to acquire simultaneous information on the contrast and phase-shift acquired by the spins, in opposition of Ramsey and rotary echo experiments, where only the visibility is observed. A similar technique has been

applied to probe the dynamics of dipolar-interacting polar molecules [Yan *et al.*, 2013], generalised by the implementation of an echo π-pulse between the preparation and the readout $\frac{\pi}{2}$ pulses. More complex combinations of pulses may be implemented with our experimental set-up, as discussed in Section 2.5.

In Figure 4.8(b), the experimental realisation of our tomographic sequence is demonstrated. A 1.2 µs excitation pulse prepares the Rydberg atoms in $|\downarrow\rangle = |48S_{1/2}, m_j = 1/2\rangle$. The spins are resonantly coupled with two $\nu \approx 35.2378\,\mathrm{GHz}$ photons to $|\uparrow\rangle = |49S_{1/2}, m_j = 1/2\rangle$ with microwave $\frac{\pi}{2}$-pulses of duration $t_{\frac{\pi}{2}} = 200\,\mathrm{ns}$, calibrated with complementary Rabi oscillations. A phase jump is triggered by a DDS after the first pulse, with no delay time in between. The measurements are fitted to the model

$$M_z(\phi) = C \cdot \cos(\phi + \phi_0), \tag{4.24}$$

where C is the visibility contrast and ϕ_0 is the phase-shift acquired by the spin ensemble of $N = 89.9 \pm 5.5$ spins. In the low spin-density regime, the magnetisation follows a cosinusoidal behaviour with $96.2 \pm 2.7\,\%$ contrast, oscillating between $\pm 0.481\,\hbar$. This incomplete rotation is attributed to the dephasing produced by the microwave power fluctuations (Section 4.2), 1.9 % for each $\frac{\pi}{2}$ rotation.

Precise control of the phase oscillation of the spin state may be interpreted as a basic demonstration of the spin-$\frac{1}{2}$ approximation and constitutes the fundamental tool for interferometric measurements with interacting spins.

4.6 Observation of coherence on Ramsey experiments

In section 4.4, a method to reconstruct the magnetisation of the spin ensemble was presented. As previously described, the temporal evolution of the magnetisation is not affected by the loss of spins Γ_c, but by the inter-state redistribution rate Γ, which represents the fundamental physical limitation to the spin coherence. Additionally, the effect of electric (or magnetic) field fluctuations may introduce additional dephasing sources which reduce the contrast of the magnetisation.

Ramsey interferometry [Ramsey, 1950; Riehle, 2004] constitutes a suitable platform to measure the T_2^* time associated to decoherence and dephasing of the spins. In such experiments, an initial $\frac{\pi}{2}$ driving pulse prepares the states in a coherent superposition of $|\uparrow\rangle$ and $|\downarrow\rangle$, followed by a free evolution time t_{delay}. A second $\frac{\pi}{2}$ pulse probes the final state of the system to reveal the transition probability from the initially prepared spin state to its orthogonal state. In the Bloch-sphere representation, a state initially prepared in $|\downarrow\rangle$ $(-\hat{z})$ is rotated to the equatorial xy-plane,

e.g. to the spin superposition $|\hat{S}_y\rangle = \frac{1}{\sqrt{2}}(|\downarrow\rangle + i\,|\uparrow\rangle)$. During the evolution time, the spin Bloch vector may precess around the equator with a frequency determined by the evolution frequency and the resonance $\Delta = 2\pi \times (\nu - \nu_0)$, which gives a rotation period as $T = \frac{2\pi}{\Delta}$. After the readout $\frac{\pi}{2}$ pulse, resonantly evolving spins should be transferred to the $|\uparrow\rangle$, with the Bloch vector pointing along $+\hat{z}$. However, dephasing during the evolution time may lead to spread of the spins and, therefore, reduction of the projected visibility. Figure 4.9a illustrates the evolution of the quantum state at different stages of the experimental sequence. The Ramsey technique is advantageous because of the reduced role of the driving field (limited to two fast $\frac{\pi}{2}$ pulses) on the observed coherence. It has been successfully applied to a large variety of spin systems [Treutlein *et al.*, 2004; Butscher *et al.*, 2010; Pla *et al.*, 2013].

We perform two different sets of Ramsey experiments:

(i) **Frequency-domain Ramsey evolution**. At a fixed t_{delay} the detuning Δ is varied. Ramsey fringes of width $\frac{1}{t_{\frac{\pi}{2}}+t_{delay}}$ are expected, with a spectral envelope which describes the loss of transition probability far from resonance. The experiments may be modelled by the generalised equation

$$N_\uparrow = \frac{N}{2} \cdot \mathrm{sinc}^2\left((\nu-\nu_0)\cdot t_{\frac{\pi}{2}}\right) \times \left[1+C\cdot\cos\left(2\pi(\nu-\nu_0)\cdot(t_{\frac{\pi}{2}}+t_{delay})+\phi_1-\phi_2\right)\right], \tag{4.25}$$

where N is the total number of spins, ϕ_1, ϕ_2 are the phases of the $\frac{\pi}{2}$ pulses and C indicates the contrast of the fringes [Morinaga *et al.*, 2016]. High-level of spectroscopic precision is at reach in comparison with continuous driving measurements (see Section 4.1). Large coherence times allow to increase the t_{delay} at which the Ramsey fringes are obtained. Thus, the width of the fringes decrease and the resolution of the spectroscopy increase.

(ii) **Time-domain Ramsey evolution**. At a fixed detuning Δ, variable evolution times t_{delay} are recorded. Phase oscillations along the equator can be measured, with a period $T = \frac{2\pi}{\Delta}$. A decaying envelope accounts for temporal decoherence of the spins and quantifies the transverse relaxation time T_2^*. On the one hand, if negligible or small field fluctuations are influencing the dynamics, an exponentially decaying envelope fulfils the theoretical predictions from our model (see 4.3). Otherwise, when non-negligible field inhomogeneities introduce resonant shifts of the spins, a Gaussian envelope accurately reproduces the time-evolution [Hermann-Avigliano *et al.*, 2014]. Such inhomogeneities are stronger for one-photon transitions because of the huge difference in polarisability between $|nS\rangle \leftrightarrow |nP\rangle$, whereas two-photon transitions between states

of identical angular momentum (e.g. $|nS\rangle \leftrightarrow |(n+1)S\rangle$) present a typical polarisability difference smaller than 10 %. In the experiments presented in this section, we apply the model function

$$M_z(t_{delay}) = M_z(0) \cdot \exp\left(-\frac{t}{T_2^*}\right) \cdot \cos(\Delta \cdot t_{delay}). \tag{4.26}$$

Under manipulation by ideal $\frac{\pi}{2}$ pulse sequences, $M_z(0) = \frac{\hbar}{2}$. However, the initial dephasing during the driving of the elementary pulse sequence is to be accounted for, as quantified in Section 4.5. The transverse time can be calculated as $T_2^* = \frac{1}{\Gamma}$, where the inter-state redistribution rate may be approximated as

$$\Gamma_{(1-\gamma)} = \frac{1}{2}(\Gamma_{nSnP} + \Gamma_{nPnS}) + \mathcal{O}(2) = \Gamma_{nSnP} + \mathcal{O}(2) \tag{4.27a}$$

$$\begin{aligned}\Gamma_{(2-\gamma)} =& \frac{1}{2}\Bigg(2\frac{\Gamma_{nSnP}\Gamma_{nP(n+1)S}}{\Gamma_{nSnP}+\Gamma_{nP(n+1)S}} + \frac{\Gamma_{nS(n-2)P}}{2} + \frac{\Gamma_{nS(n-1)P}}{2} + \frac{\Gamma_{nSnP}}{2} + \frac{\Gamma_{nS(n+1)P}}{2} \\ &+ \frac{\Gamma_{(n+1)S(n-1)P}}{2} + \frac{\Gamma_{(n+1)SnP}}{2} + \frac{\Gamma_{(n+1)S(n+1)P}}{2} + \frac{\Gamma_{(n+1)S(n+2)P}}{2} \\ &+ \frac{\Gamma_{nS(n-1)P}\Gamma_{(n-1)P(n+1)S}}{\Gamma_{nS(n-1)P}+\Gamma_{(n-1)P(n+1)S}} + \frac{\Gamma_{(n+1)S(n+1)P}\Gamma_{(n+1)PnS}}{\Gamma_{(n+1)S(n+1)P}+\Gamma_{(n+1)PnS}}\Bigg) \\ &+ \mathcal{O}(2) + \mathcal{O}(3)\end{aligned} \tag{4.27b}$$

For the two-photon case, all other redistribution terms in $\mathcal{O}(2)$ make a small impact on $\Gamma_{(2-\gamma)}$.

In Figure 4.9 our experimental observations are detailed. In the frequency-domain Ramsey fringes from Fig. 4.9(b), we prepare the Rydberg atoms in $|\downarrow\rangle = |42P_{1/2}, m_j = -3/2\rangle$ with a two photon transition off-resonant from the excited state of ^{87}Rb by means of a 2 µs excitation pulse. The Ramsey sequence is triggered by $t_{\frac{\pi}{2}} = 139$ ns resonant pulses, calibrated by complementary measurement of the oscillating Rabi frequency, with a waiting time $t_{delay} = 383.5$ ns. A 2 µs down-pumping pulse removes the $|42S_{1/2}, m_j = -1/2\rangle$ population, so the detected signal by field ionisation corresponds to spin states above the classical ionisation threshold [Grimmel *et al.*, 2015]. The measurement of the temporally fixed Ramsey fringes revealed a spin population offset of ~ 0.4 %, which indicates that the transition is controlled without additional coupling to nearby Rydberg states. Ramsey fringes with 95.11 ± 4.86 % contrast were measured, ensuring good coherence for hundreds of spins at short timescales. Such experiments constitute a solid benchmark to observe density dependent decay of contrast due to dipolar-exchange $\propto \frac{1}{R^3}$ interaction effects

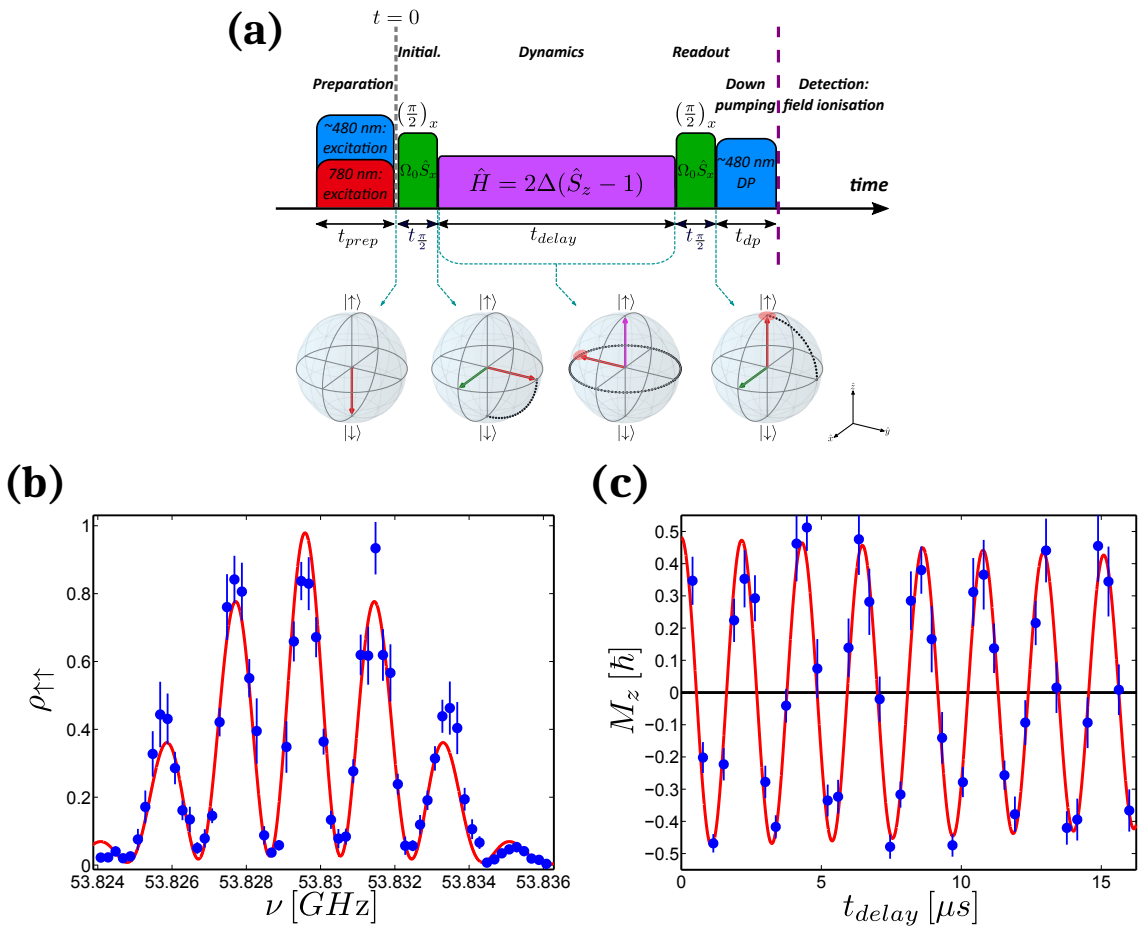

Figure 4.9: Observation of coherence on Ramsey experiments. **(a)** Ramsey experimental sequence. **(b)** Ramsey fringes between $|42S_{1/2}, m_j = -1/2\rangle$ and $|42P_{3/2}, m_j = -3/2\rangle$ for a Ramsey time $T_R = t_{\frac{\pi}{2}} + t_{delay} = 522.5 \pm 3.7\,\text{ns}$. The visibility reaches $95.1 \pm 4.9\,\%$ for $N = 390 \pm 11$ spins, extracted from a fit to Eq. (4.25) (red line). **(c)**. Coherence T_2^* time observed in a time-domain Ramsey experiment for $N = 82.7 \pm 2.2$ initial spins. The experiment is fitted to the expression from Eq. (4.26) (red line), giving $T_2^* = 126.6 \pm 58.9\,\mu\text{s}$ in an observation timescale of $16\,\mu\text{s}$. The oscillations correspond to induced precession by a detuning $\Delta = 2\pi \times 0.46\,\text{MHz}$. Data are the average over 10 **(a)** and 30 **(b)** realisations. Error bars are given by one standard error.

with higher accuracy than observing the spectral broadening [Afrousheh *et al.*, 2004; Afrousheh *et al.*, 2006a].

The time-evolution of the coherence between $|\downarrow\rangle = |48S_1/2, m_j = 1/2\rangle$ and $|\uparrow\rangle = |49S_1/2, m_j = 1/2\rangle$ (Fig. 4.9(c)) is tested by exciting the atoms to the $|\downarrow\rangle$ with a $5\,\mu\text{s}$ two-photon pulse. Calibrated Rabi pulses of duration $t_{\frac{\pi}{2}} = 640\,\text{ns}$ are used for the two-photon microwave transition, performed by two identical photons tuned at $\nu \approx 35.2376\,\text{GHz}$. After the variable time evolution, a down-pumping pulse is

applied to discriminate the spin states (see 4.4, appendix C). The atoms are ionised by means of a $\sim 86.5\,\mathrm{V/cm}$ electric field. The initial magnetisation was constraint to the value $M_z(0) = 0.481\,\hbar$, given the 1.9 % contrast reduction induced during the driving sequence. Transverse relaxation $T_2^* = 126.6 \pm 58.9\,\mu\mathrm{s}$ is extracted from the fit. This value is consistent with our theoretical calculations, which estimate an upper bound $T_2^* \approx 185\,\mu\mathrm{s}$. Thus, the observation of coherence is confirmed to be limited by inter-state redistribution Γ. Two-photon $|nS\rangle \leftrightarrow |(n+1)S\rangle$ transitions are proved to be less sensitive to strong additional dephasing mechanisms. Usage of additional spin-echo sequences is not required in our explored timescales. Thus, this spin system can be considered as a well controlled platform to study interacting Rydberg spin dynamics.

4.7 Perspectives: new platform to explore few to many-body dynamics

The presented experiments provide a precise benchmark for future explorations of few to many-body interacting sping dynamics. Sensitivity of Rydberg spins to weak microwave driving fields has been demonstrated and employed to accurately manipulate one- and two-photon Rydberg-Rydberg transitions. An important aspect to point out is the high-degree of precision in microwave field detection which correspond to measured Rabi frequencies of up to tens of kHz. Our detection method, relying on field ionisation and discrimination of the Rydberg spins states via down-pumping allows for an atomic-based approach to measure microwave fields, which is complementary to optical-based microwave electrometry, where the field strength is observed on the bandwidth of electromagnetically-induced transparency spectra [Sedlacek *et al.*, 2012; Anderson *et al.*, 2014; Anderson *et al.*, 2016]. Sensitivity to similar or even smaller field strengths was shown. At long driving times, transition spectra and Rabi oscillations have revealed limited coherence due to microwave intensity fluctuations, which enhance the dephasing of the spins under continous driving. Application of more refined NMR and quantum information protocols like BB1 composite pulse sequences [Morton *et al.*, 2005; Vandersypen and Chuang, 2005] or dynamical decoupling [Zhang *et al.*, 2014b; Souza *et al.*, 2015] will allow to overcome this and other sources of noise in the future. However, basic sequences of $\frac{\pi}{2}$ pulses have already been realised with a small contrast reduction $\sim 1.9\,\%$ per pulse, as discussed in section 4.5. As a consequence, Ramsey experiments revealed interaction-free T_2^* coherence times much larger than the typical timescales for observation

of interaction effects. The coherence of Rydberg spins was proven to be limited by intra-state black-body redistribution, which introduces dephasing in the spin ensemble. Therefore, additional sources of dephasing play a minor role. Coherence between Rydberg spins has also been observed while manipulating Rydberg spins on superconducting atom chips [Carter and Martin, 2013; Hermann-Avigliano *et al.*, 2014]. However, we are able to observe large coherence times over the full spin ensemble, whereas at the vicinity of the chip, the stray electric fields still dominate the dephasing. Additionally, by scanning the phase of our microwave pulses, we introduced a generalised rotary echo sequence which allows to simultaneously map the magnetisation contrast and small phase shifts, as an alternative route for Rydberg atom interferometry [Nipper *et al.*, 2012]. This can play an important role on the precision of Rydberg phase gates, as previously proposed by [Ryabtsev *et al.*, 2005; Paredes-Barato and Adams, 2014].

The precision of the spin detection will increase by implementing state-selective field ionisation [Jeys *et al.*, 1982; Robicheaux *et al.*, 2000; Feynman *et al.*, 2015]. Thus, additional experiments to quantify the redistribution of spins will be unnecessary, as well as the down-pumping protocol, since all Rydberg states could be distinguished in every single shot. As a consequence, the noise reduction will facilitate the reliable measurement of magnetisation variances in combination with spin tomography. Hence, observation of temporal correlations and non-equilibrium dynamical effects will become accessible.

Further investigations will focus on the effect of Rydberg-Rydberg interactions. Accurate observation of few Rydberg interacting spins has already been demonstrated [Ravets *et al.*, 2014; Barredo *et al.*, 2014; Ravets *et al.*, 2015; Barredo *et al.*, 2015; Labuhn *et al.*, 2016]. Nevetheless, the high degree of control over hundreds of Rydberg spins exhibited in the present chapter paves the way towards efficient quantum simulation of Heisenberg XX and XXZ spin Hamiltonians in the many-body regime. Preliminary results can be found in Chapter 5. In addition, structuring the spin distribution with microtrap arrays [Nogrette *et al.*, 2014; Labuhn *et al.*, 2016] and individually addressing the sites [Labuhn *et al.*, 2014] will allow to map the transition from few to many-body spin dynamics in different dimensional configurations.

Chapter 5

Interaction effects on the Rydberg spin dynamics

In this section, preliminary observations of many-body effects in Heisenberg XX and XXZ models with Rydberg spins are shown [Bettelli *et al.*, 2013; Whitlock *et al.*, 2010]. By means of the methods established and characterised in Chapter 4, like precise spectroscopy or Ramsey and tomographic techniques, the effect of spin-spin interactions on the spectrum and the decay of coherence of the spin ensemble are investigated, as an important step for further studies of quantum magnetism with Rydberg atoms.

In the first section (Sec. 5.1) the dipolar broadening of the Rydberg transitions is measured [Afrousheh *et al.*, 2004; Afrousheh *et al.*, 2006a], revealing an anisotropic effect arising from the angular dependence of the pair interactions. The decay of the coherence due to $1/R^3$ interactions is also presented and the role of the disorder on the observation is suggested. In Section 5.2, the $1/R^6$ spin system with two different $|nS\rangle$ states is explored by means of spin-locking techniques, showing the magnetisation curve of a Rydberg spin ensemble evolving under the Heisenberg XXZ dynamics.

5.1 Interaction effects on a Rydberg interacting XX-model

As discussed in Sec. 2.2.2, a direct dipole-dipole coupling between two different states of different angular momenta can be mapped onto a spin-exchange Heisenberg XX model wit $\propto 1/R^3$ interactions, which presents an very rich dynamics. Previous

experiments have revealed that the dephasing of Rabi oscillations in such interacting regime cannot be explained by a simple mean field description, since quantum correlations play an important role on its non-equilibrium properties and needs to be modelled with more refined method like Moving-Average Cluster Expansion (MACE) or Truncated Wigner Approximation (TWA) [Piñeiro Orioli *et al.*, 2017]. In this section, further observations of many-body effects on the spin dynamics are introduced, which will lead to spectral broadening of the Rydberg atomic transition and decay of the T_2^* characterised by Ramsey experiments.

5.1.1 Asymmetric spectral broadening

Here, spectroscopic measurements of the spin-exchange interaction effect are presented. The spins are prepared in the state $|\downarrow\rangle = |42S_{1/2}, m_j = 1/2\rangle$ and spectroscopically probed to address the transition to $|\uparrow\rangle = |42P_{3/2}, m_j = 3/2\rangle$ by a single microwave photon, as previously described in Section 4.1.2 (see Fig. 4.2).

Due to the anisotropy inherent to $|nP\rangle$ states [Walker and Saffman, 2008; Paris-Mandoki *et al.*, 2016], the dipole-dipole interaction amongst Rydberg pairs is strongly dependent on the orientation of the spins [Carroll *et al.*, 2004; Ravets *et al.*, 2015; Bigelow *et al.*, 2016]. Thus, pairs of atoms can interact with $J_\perp(\theta_{i,j}) = C_3(\theta_{i,j})/R_{ij}^3 < 0$, whereas different pairs present an interaction strength $J_\perp(\theta_{i,j}) > 0$. In case of a disordered sample of spins, where all possible angular configurations are equiprobable, integration of the dipole-dipole interaction coefficient $C_3(\theta)$ over all of them shows that the average $\tilde{C}_3 = \int d\theta C_3(\theta)$ interaction shift depends on the selection of Zeeman sub-states. Nonetheless, considering equiprobable coupling to the three possible sub-levels, the average interaction shift is zero, resulting in a symmetric spectral broadening due to both read and blue shifts, which has been observed to be proportional to the Rydberg atom density [Afrousheh *et al.*, 2004; Afrousheh *et al.*, 2006a].

In Figure 5.1, the spectral broadening of driven transition is presented, where the described predominance of the blue energy shift is clearly observed. This seems to confirm in good agreement with the theoretical expectation. This allows us to spectroscopically determine the sign of the interaction strength of Rydberg spins and, thus, reducing the number of unknown parameters for more complex investigations of the spin dynamics.

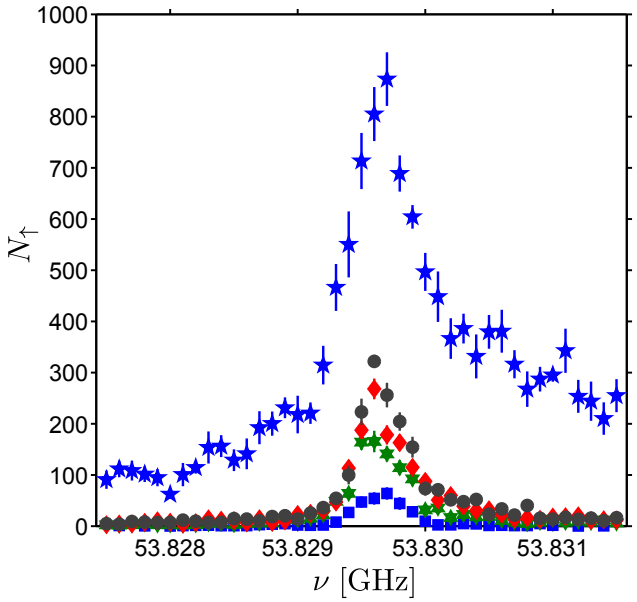

Figure 5.1: Asymmetric dipolar broadening of the spectrum of the driven spin dynamics. The transition between $|\downarrow\rangle = |42S_{1/2}, m_j = 1/2\rangle$ and $|\uparrow\rangle = |42P_{3/2}, m_j = 3/2\rangle$ is driven for 2 µs by a resonant microwave field. The asymmetry is attributed to the angular dependency of the dipole-dipole interactions. The integration over all possible angles results in a favourable repulsive interaction, such that most of the pair energy shifts are induced towards higher energies. Data are the average over 15 realisations.

5.1.2 Reduction of contrast on Ramsey fringes

In order to understand some basic features of dipolar interacting spin systems, we realise Ramsey experiments and observe the coherence of the spin ensemble under the effect of spin-exchange interactions. For such purpose, the experimental sequence discussed in Sec. 4.6 is applied to obtain frequency-domain Ramsey fringes in the transition $|\downarrow\rangle = |42S_{1/2}, m_j = 1/2\rangle \leftrightarrow |\uparrow\rangle = |42P_{3/2}, m_j = 3/2\rangle$. After a microwave $\frac{\pi}{2}$ pulse of duration $t_{\frac{\pi}{2}} = 230\,\text{ns}$, the spins freely evolve for $t_{delay} = 1.78\,\mu\text{s}$ and a second $\frac{\pi}{2}$ pulse allows to read out the contrast. The fringes are fitted to the model function

$$N_\uparrow = N_0 + A \cdot \text{sinc}^2\left[(\nu - \nu_0)t_{\frac{\pi}{2}}\right] \cdot \left[\frac{1-C}{1+C} + \frac{2\cdot C}{1+C} \cdot \cos^2\left(\pi(\nu-\nu_0)(t_{\frac{\pi}{2}} + t_{delay}) + \phi_0\right)\right], \tag{5.1}$$

proposed by [Nipper *et al.*, 2012]. The experiment is repeated at increasing number of Rydberg spins within a volume $V \approx 2.2 \cdot 10^{-6}\,\text{cm}^{-3}$, estimated by means of the Depletion Imaging technique (3.1.2). As a result, the contrast of the Ramsey fringes decays with the increase of the number of spins, as shown in Figure 5.2(a). The

temporal coherence of the spins is also probed by means of the generalised sequence which was introduced in Sec. 4.5, revealing a complex dynamics which cannot be explained by a typical exponential decay (Fig. 5.2(c).

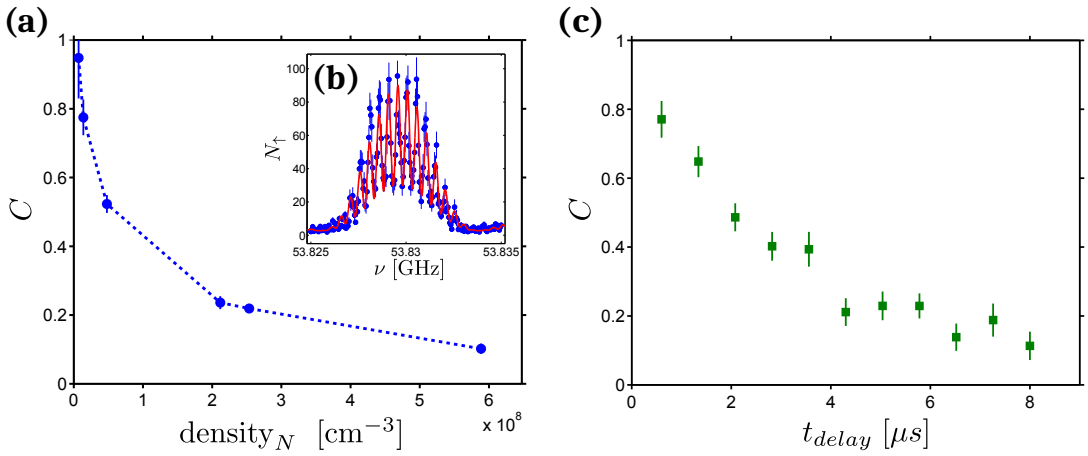

Figure 5.2: Decay of contrast in Ramsey experiments (a) Decay of the spin coherence for increasing density of spins. **(c)** Inset: frequency-dependent Ramsey fringe from (a). Fitted to Eq. (5.1) with results: $\nu_0 = 53.8297\,\mathrm{GHz}$, $C = 52.3 \pm 2.6$. **(c)** Temporal spin dynamics, obtained with the generalised sequence from Sec. 4.5. The delay in between both pulses is varied at a fixed density of spins $n_N \approx 1.2 \cdot 10^{-8}\,\mathrm{cm}^{-3}$. The contrast C correspond to the experimental fit of the Ramsey fringes, whereas the errorbars are the standard error.

In similar experiments exploring the dynamics of a dipolar XX model with polar molecules in spatially ordered optical lattices [Yan *et al.*, 2013], investigations of such temporal evolution have shown a combination of exponential decay related to the T_2^* coherence of the system and coherent oscillations due to the interaction strength amongst neighbouring molecules in the lattice, which, in our case, is partially hidden due to the disorder of the spin ensemble, since there is not such a well-defined nearest-neighbour distance that determines the dynamics. Structuring the spin distribution by means of arrays of micro-traps with tunable configuration [Labuhn *et al.*, 2016; Bernien *et al.*, 2017] would allow us to distinguish the transition from fully coherent temporal dynamics to the coherent superposition of multiple contributions.

5.2 Towards quantum magnetism with an XXZ Rydberg magnet

In this section, we present the characterisation of the magnetisation curve of a Rydberg spin system with $1/R^6$ XXZ interaction terms. To perform such measurements by means of an spin-locking technique. In such experiments, we leverage the generalised sequence explained in Section 4.5 and introduce a strong driving pulse oriented in the direction of the spins in between the preparation and the readout pulses, as depicted in Figure 5.3(a). The results show a surprising asymmetry and an important phase acquired by the spin components under absence of any competing driving.

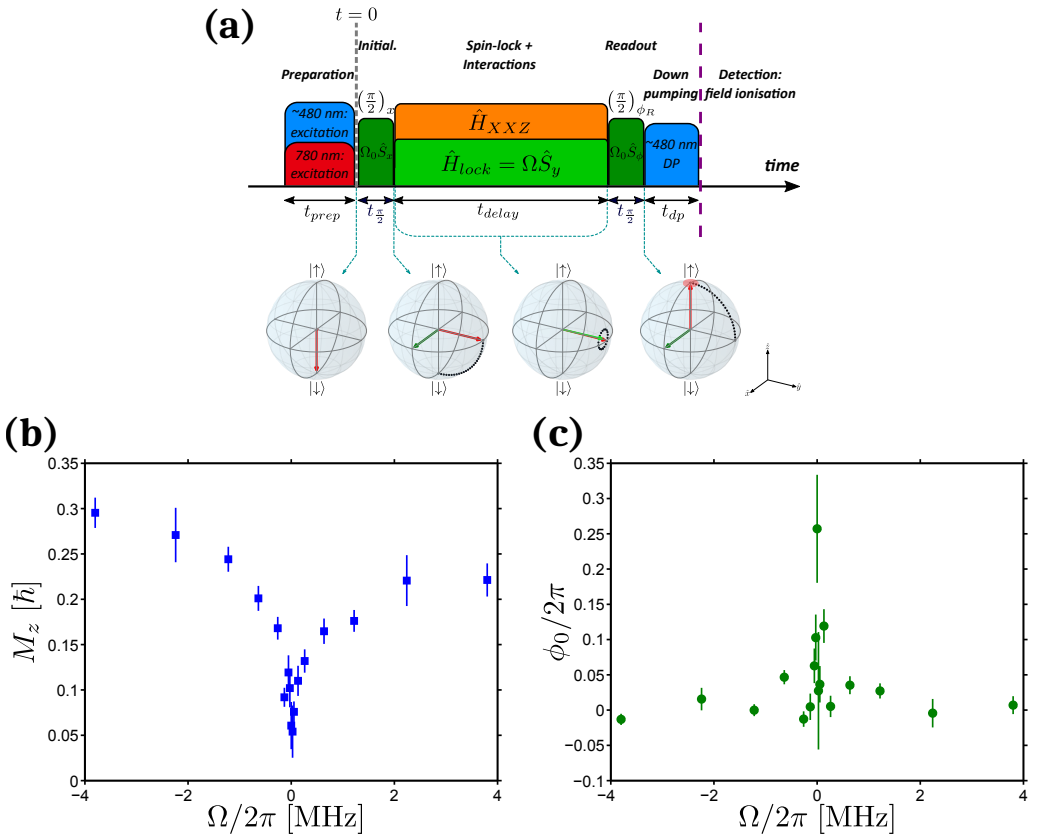

Figure 5.3: Spin-lock experiment on the transition between $|\downarrow\rangle = |48S_{1/2}, m_j = -1/2\rangle$ and $|\uparrow\rangle = |49S_{3/2}, m_j = 1/2\rangle$. (a) After preparing the spins in a superposition $|\hat{S}_y\rangle = \frac{1}{\sqrt{2}}(|\downarrow\rangle + i\,|\uparrow\rangle)$, a field is aligned or anti-aligned with such state to measure the competition between the XXZ interactions and the driving field. **(b)** Magnetisation of the spins, showing an asymmetric magnetisation curve. **(c)**. Phase aquired by the spin ensemble.

This observation constitutes the basis for our future investigations in quantum magnetism with Rydberg atoms.

5.3 Prospects

In this chapter, preliminary experiments of the dynamics of XX and XXZ Heisenberg models with Rydberg atoms has been presented. By means of spectroscopic methods and Ramsey techniques, indications of many-body dynamics have been observed. Measuring the density dependence of the spectra under continuous driving and under the effect of resonant dipole-exchange interactions, the observations suggest the important role of the combination of Zeeman sub-states on the sign of the interaction strength, leading to favourable red or blue shifts in average. The loss of coherence of the spins has been characterised by means of Ramsey techniques, leading to a complex decay pattern, in which the disordered character of the sample may play an important role. Additionally, studies of the $1/R^6$ XXZ dynamics of spins allowed us to measure the magnetisation curve of the ensemble and the competing behaviour of the driving field and the spin-spin interactions. An important question to address in future experiments is the nature of the observed effect. Since our characterisation has been realised only for the XXZ system, the observation of a similar behaviour driven by isolated spin-exchange XX interactions would be an important step forward to distinguish the subtleties of both Hamiltonians.

In order to fully understand the richness of the spin dynamics, further studies will be convenient. One striking topic of future investigation is related to the possible conditions for the spins to aggregate in magnetic domains. This could be answered by measuring the spatial correlations between the Rydberg spins Schwarzkopf *et al.*, 2011; Schauß *et al.*, 2012, which may be feasible by means of advanced imaging techniques, as can be consulted in the following chapter. The implementation of spatial order in the spin system [Labuhn *et al.*, 2016; Bernien *et al.*, 2017] would allow to explore the transition from a few-to-many body regime and efficiently characterise the role of disorder and dimensionality.

Chapter 6

Interaction Enhanced Imaging of Rydberg atoms

This chapter is partially based on the following publications, from which parts of the text are reproduced verbatim:

Interaction-Enhanced Imaging of Rydberg P states
V. Gavryusev, M. Ferreira-Cao, A. Kekić, G. Zürn and A. Signoles
Eur. Phys. J. ST **225**, 15 (2016)

Long-range interactions arising in Rydberg atoms [Saffman *et al.*, 2010] enable to study non-equilibrium properties of highly-correlated systems [Hazzard *et al.*, 2014b]. Multiple interesting phenomena can be observed like the formation of ultracold plasmas [Vanhaecke *et al.*, 2005; Vrinceanu *et al.*, 2009; Pohl *et al.*, 2011; Robert-de Saint-Vincent *et al.*, 2013], the emergence of correlated nonlinear optical effects [Pritchard *et al.*, 2010; Peyronel *et al.*, 2012; Firstenberg *et al.*, 2013; Busche *et al.*, 2017] , the creation of crystalline structures [Pohl *et al.*, 2010; Schauß *et al.*, 2012; Levi *et al.*, 2015] or the transport of energy through Rydberg aggregates [Schönleber *et al.*, 2015]. Nevertheless, only few techniques are suited to spatially image Rydberg atoms. In Section 3.1, a new imaging technique , based on the depletion of absorption of ground state atoms in presence of Rydberg atoms, has been introduced. This technique is suited to investigate the local dynamics and correlations of the excitation process , but its sensitivity is limited and it is not state selective, barring single-shot detection of low Rydberg atom numbers.

Rydberg atom imaging based on field ion microscopy [Schwarzkopf *et al.*, 2011] has been applied to measure spatial pair correlations and van der Waals interactions

between Rydberg atoms [Schwarzkopf *et al.*, 2013; Thaicharoen *et al.*, 2015; Weber *et al.*, 2015; Manthey *et al.*, 2015]. Here, cold Rydberg atoms are ionised by a inhomogeneous electric field and the resulting ions are guided along the divergent field lines towards a fluorescent multichannel plate (MCP). Each ion is revealed by a bright spot of light onto a CCD camera, allowing for few µm resolution. However, the detection efficiency is limited to $\leq 50\,\%$ by the quantum efficiency of the MCP.

Concerning optical approaches, Rydberg atoms in optical lattices have been imaged with nearly single-site spatial resolution [Schauß *et al.*, 2012]. The technique consists in de-exciting the Rydberg atoms towards a short-lived intermediate state (similar to the experiments in Sec. 3.4) and captured in an optical lattice, where high-resolution fluorescence imaging on the ground to excited state reveals the atom position. Spatial correlations have been observed with a detection efficiency of $\sim 75\,\%$. Similarly, Rydberg atoms trapped in two-dimensional arrays have been detected with $\sim 97\,\%$ efficiency [Labuhn *et al.*, 2016]. However, this method destroys the Rydberg state.

Several techniques have been introduced for alkaline-earth atomic species. Scanning autoionisation microscopy allowed to resolve the local atom number distribution with 10 µm spatial resolution [Lochead *et al.*, 2013]. This takes advantage of a tightly focused laser beam and of the large autoionisation probability of the Rydberg state when the core electron is excited, so local autoionisation is stimulated. A different technique uses the laser-induced fluorescence light of an optical transition of the core electron, which is sensitive to the second electron, previously excited to a Rydberg state [McQuillen *et al.*, 2013]. This provides high temporal resolution ($\sim 10\,\mathrm{ns}$), but limited spatial resolution ($\sim 200\,\mu\mathrm{m}$).

In this chapter detailed research on the Interaction Enhanced Imaging technique (IEI) [Günter *et al.*, 2012; Gavryusev *et al.*, 2016a; Günter, 2014; Gavryusev, 2016] is presented. It is applied as a sensitive technique for state-resolved detection of Rydberg spins (hereafter called impurities) with high spatial and temporal resolution and it is particularly suitable to observe time-resolved transport of Rydberg excitations mediated by dipolar exchange interactions [Schönleber *et al.*, 2015; Westermann, S. *et al.*, 2006; Schempp *et al.*, 2015]. The main physical principle of the technique is explained in Section 6.1. A formal model of IEI is introduced in Section 6.2 in order to estimate the effect of Rydberg impurities and the sensitivity of the technique. Then experimental results are presented in Section 6.4, both for the first average measurements of reduced numbers of nP states (Sec. 6.3.1), and for single-shot measurements of nS and nP impurities (Sec. 6.3.2).

6.1 Working principle of Interaction Enhanced Imaging

Interaction-enhanced imaging was developed and implemented within our research group to study the dynamics of dipole-mediated energy transport processes in Rydberg gases [Günter *et al.*, 2013] and, potentially, can be applied to resolve single rydberg spins with state selectivity. Aiming to combine single-particle sensitivity and high time-space resolution, the original proposal offered the possibility to detect Rydberg atoms embedded in an atomic gas, hereafter called impurities, based on differential absorption imaging, with potential resolution smaller than their Rydberg blockade radius [Günter *et al.*, 2012]. The IEI technique, similar to the proposal by Olmos *et al.* [Olmos *et al.*, 2011], is based on detecting the change in absorption of a probe light beam induced by the presence of the Rydberg impurities. Therefore, using the background atoms as a contrast medium can reveal the difference of absorption due to the effect of impurities. For such purpose, the cold atomic gas is coupled under EIT conditions (see Section 3.2) to an auxiliary "probe" state and rendered transparent to the probe light [Fleischhauer *et al.*, 2005; Pritchard *et al.*, 2011; Sevinçli *et al.*, 2011]. Priorly excited impurities interact with the auxiliary probe state, leading to local van der Waals or dipole-dipole interactions which shift the energy of the probe atoms, breaking the EIT [Hofmann *et al.*, 2013; Gärttner *et al.*, 2014]. Thus, a shadow is cast in the absorption profile, which allows to spatially map the impurity location, as described in Fig. 6.1(a). The method has been implemented with Rubidium Rydberg atoms [Günter *et al.*, 2013; Gavryusev *et al.*, 2016a] but has the potential to be applied to any particle which presents strong coupling to a medium.

Amongst the advantages of the method, it is worth stressing the applicability to investigate interaction-induced dynamics of Rydberg atoms. Since the signal is given by the background atoms in the vicinity of each impurity, it can be strongly enhanced to increase the efficiency of the detection. This amplification factor is determined by the number of additional absorbers per impurity, which is equivalent to the number of probe atoms per blockade sphere. In a hard-sphere picture, the critical distance R_{ir} defines the range below which probe atoms are considered as absorbers. Therefore, the amplification can be tuned to strongly enhance the absorption. This makes the IEI technique a pontential candidate for single-impurity sensitive imaging. Ideally, a single snapshot might reveal the presence of impurities, as will be discussed in Section 6.4.

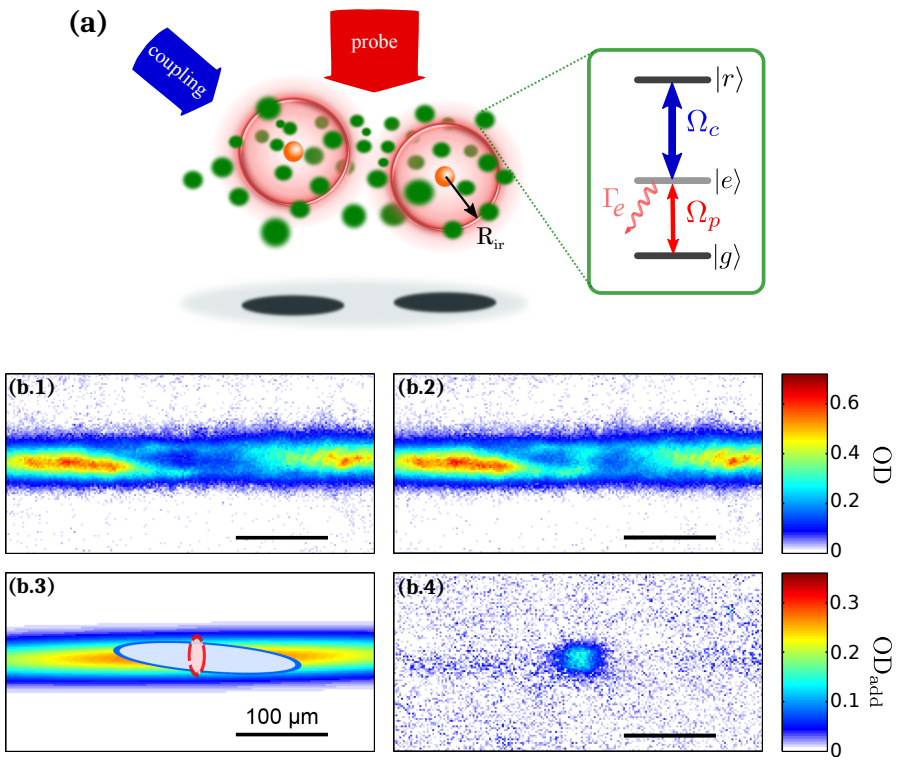

Figure 6.1: **(a)** Principle of interaction-enhanced imaging of Rydberg impurities (orange spheres) within a gas of probe atoms (green spheres). Two resonant "probe" (Ω_p) and "coupling" (Ω_c) fields, coherently couple the ground state $|g\rangle$ of the probe atoms to a Rydberg state $|r\rangle$, rendering the atoms far from any impurity transparent to the probe light field. Each impurity strongly interacts with the surrounding atoms within $r \leq R_{ir}$, leading to an energy shift of the Rydberg state $|r\rangle$, which locally becomes absorptive. The presence of an impurity casts a shadow on the camera which collects the probe light transmitted through the atomic cloud. **(b)** Absorption images acquired for interaction-enhanced imaging experiments (reproduced from Günter, 2014). **(b.1)** Atoms illuminated by a strong coupling beam, with $\Omega_c \sim 2\pi \cdot 9\,\mathrm{MHz}$ in the central region become transparent. **(b.2)** Absorption image performed with Rydberg impurities pre-excited in the center. The local breakdown of EIT can be observed. **(b.3)** Sketch showing the spatial distribution of the atomic cloud and the positions of the EIT-coupling (blue) and excitation (red) beams. The ellipses indicate the regions corresponding to $1.5 \cdot \sigma$ of the intensity profiles. **(b.4)** Difference in absorption between (b.1) and (b.2), which contains spatially-resolved information about the number of additional absorbers and the distribution of the Rydberg impurities. The images are averaged over 150 repetitions, with an exposure time of $5\,\mu\mathrm{s}$. ~ 300 impurities estimated.

6.1.1 Experimental realisation of IEI

The first successful implementation of IEI measured the spatial distribution of impurities in an ultracold Rubidium gas [Günter *et al.*, 2013]. Atoms initially prepared in the ground-state in an ODT at few μK were illuminated by a uniform 780 nm probe laser beam and a 480 nm blue laser beam focused in a smaller region, as displayed in (Fig.6.1(b.3)). Therefore, the atoms were coupled to the $|37S\rangle$ probe Rydberg state, inducing EIT on the $|5S\rangle \leftrightarrow |5P\rangle$ transition (Fig.6.1(b.1)). In a second experimental run, impurities were pre-excited in the state $|50S\rangle$ in the central region by a two-photon transition. When the EIT coupling was turned on, a drop in transparency was observed due to the presence of impurities (Fig.6.1(b.2)). The final distribution of additional absorption is obtained from the difference between both images (Fig.6.1(b.4)), in a similar way to the procedure in Sec. 3.1.

This experiment illustrates how IEI allows to map the distribution of Rydberg impurities embedded in an atomic gas. The technique has been already used to investigate classical [Günter *et al.*, 2013] and quantum [Schempp, 2014, Chapter 6] diffusion induced by dipole-dipole interactions.

6.2 Model for Interaction Enhanced Imaging

Here, we present a brief description of a hard-sphere model that captures the main features of the IEI technique that allows for an intuitive understanding of the impact of probe-probe and impurity probe interactions. The system is considered in the steady state in a quasi-frozen regime, where thermal and mechanical motion can be neglected [Amthor *et al.*, 2007; Teixeira *et al.*, 2015]. Quantitative analysis of the IEI technique is introduced, applicable to experiments and theory.

6.2.1 Rydberg-Rydberg interactions

In order to include the effect of probe-probe and impurity-probe interactions, we assume previous knowledge of the two-level and three level optical response of the medium, which have been previously described in Eq. 3.2 and Eq. 3.17.

It has been demonstrated in several investigations that the transparency in EIT media breaks down at large Rydberg atomic density [Sevinçli *et al.*, 2011; Pritchard *et al.*, 2010; Pritchard *et al.*, 2011; Hofmann *et al.*, 2013; DeSalvo *et al.*, 2016; Han *et al.*, 2016]. Then, van der Waals interactions introduce an energy shift in the transition, which is approximated to be $\Delta_{int} = V_{rr}$ [Gärttner *et al.*, 2014; Ates *et al.*,

2011]. This shift introduces a detuning $\Delta_c = \Delta_{int}$ of the coupling light that modifies the effective dephasing $\gamma_{gr} \to \gamma_{gr} + 2i\Delta_{int}$ in Eq. (3.17), inducing absorption. For large shifts V_{rr} the susceptibility converges to the the resonant two-level susceptibility.This can be observed in Figure 6.2(a).

We generalise a hard-sphere approach to describe the effect of both probe-probe and impurity-probe interactions [Petrosyan *et al.*, 2011; Sevinçli *et al.*, 2011; Parigi *et al.*, 2012] (see Fig. 6.2). Whenever the atoms experience an energy shift larger than half of the EIT bandwidth $\sigma_{eit}/2$, they are considered as two-level absorbers, whereas they are still considered as transparent for $\Delta_c \leq \sigma_{eit}/2$. Impurities interacting with a bath of EIT-coupled atoms introduce a level shift V_{ir} which renders the cloud absoptive within a distance R_{ir}, enhancing the signal. Analogously, probe-probe interactions break the EIT condition within the probe-probe blockade R_{rr}, reducing the IEI amplification and, thus, the contrast.

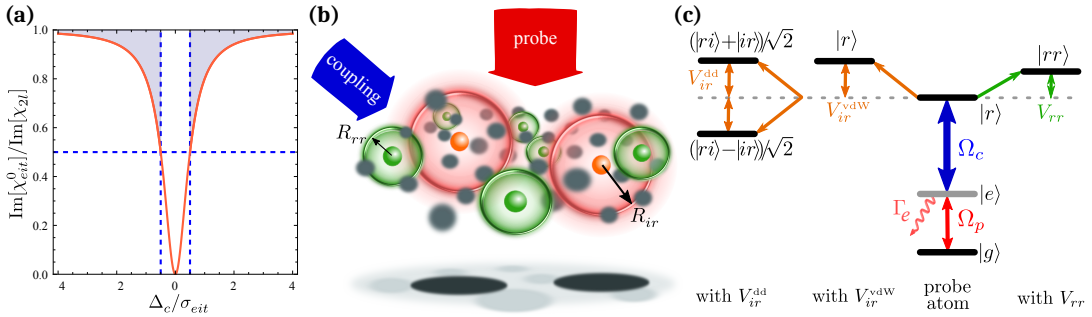

Figure 6.2: Hard-sphere description of IEI. (a) Normalised EIT absorption as a function of the detuning Δ_c of the $|e\rangle \leftrightarrow |r\rangle$ transition, normalized by the FWHM of the EIT transparency window. For $\Delta_c \leq \sigma_{eit}/2$ atoms are considered transparent, whereas for larger detuning, they are treated as two-level absorbers. **(b)** Hard-sphere description of the interactions: the impurities (orange) interact with the bath of probe atoms (grey and green dots for $|g\rangle$ or $|r\rangle$, respectively). The induced a level shift V_{ir} breaks the EIT within a distance R_{ir}. An absorption spot appears on the CCD camera when the probe light is collected. Probe-probe interactions reduce the transparency within a distance R_{rr} around each $|r\rangle$ Rydberg polariton. **(c)** The states $|g\rangle$, $|e\rangle$, $|r\rangle$ of the probe atoms are coherently coupled by two resonant light fields with Rabi frequencies Ω_p and Ω_c. Probe-probe interactions induce a level shift of V_{rr} on $|r\rangle$ (right). When impurities $|i\rangle$ are pre-located, interactions can cause state-dependent effect: a van der Waals shift V_{ir}^{vdW} in case of $|nS\rangle$ impurities or mixing of the eigenstates accompanied by an energy split $2V_{ir}$ for $|nP\rangle$ impurities (left).

Probe-probe interactions

To describe the probe-probe interactions, the EIT susceptibility can be expressed as

$$\chi_{eit} = f_{rr}\chi_{2l} + (1 - f_{rr})\,\chi^0_{eit}, \tag{6.1}$$

where f_{rr} is the effective fraction of volume blockaded by the probe-probe interactions [Ates *et al.*, 2011]. Then, f_{rr} is given as

$$f_{rr} = \frac{n\rho^0_{rr} - n\rho_{rr}}{n\rho^0_{rr}} = 1 - \frac{\rho_{rr}}{\rho^0_{rr}}. \tag{6.2}$$

ρ^0_{rr} and ρ_{rr} are the Rydberg population matrix elements in the non-interacting and interacting regime, respectively. Thus, f_{rr} is expressed through the normalised difference between $n\rho^0_{rr}$, the density of Rydberg atoms that can be ideally excited, and $n\rho_{rr}$, the effectively excited density of Rydberg atoms. The probe-probe van der Waals interactions define the Rydberg blockade radius

$$R_{rr} = \left(\frac{2C_6^{rr}}{\sigma_{eit}}\right)^{\frac{1}{6}}, \tag{6.3}$$

which establishes the limit for atoms in the volume $V_{bl} = 4/3 \cdot \pi R^3_{rr}$ considered as absorbers, leading to a Rydberg fraction $f_{rr} = n\rho_{rr}V_{bl}$. By substituting it in Eq. (6.2) we can extract the density matrix element ρ_{rr}

$$\rho_{rr} = \frac{\rho^0_{rr}}{1 + n\rho^0_{rr}V_{bl}} \tag{6.4}$$

and obtain an analytical expression for the optical susceptibility in presence of probe-probe interactions.

Impurity-probe interactions

Following a similar procedure, the optical response in presence of impurities $|i\rangle$ can be incorporated as a balanced combination of the two level susceptibility (Eq. (3.2)) and the generalised EIT susceptibility with probe-probe interactions (Eq. (6.1)), such that

$$\chi_{imp} = f_{ir}\chi_{2l} + (1 - f_{ir})\,\chi_{eit}. \tag{6.5}$$

The fraction of volume blockaded by impurity-probe interactions is considered to be $f_{ir} = n_i V_{bl,i}$, where n_i is the density of impurities and $V_{bl,i} = 4/3 \cdot \pi R^3_{ir}$ is the volume in each impurity sphere. Therefore, f_{ir} consistently defines the effect of impurities and can be expressed as $f_{ir} = 1 - 1/(1 + n_i V_{bl,i})$.

In order to quantify the critical impurity-probe radius, two particular cases are considered, as shown in Fig. 6.2(c):

(i) For $|i\rangle = |nP\rangle$, using probe atoms in a Rydberg S state, resonant $|i\rangle \leftrightarrow |r\rangle$ dipole-dipole interactions separate the pair eigenstates in a symmetric and antisymmetric state combination $(|ri\rangle \pm |ir\rangle)/\sqrt{2}$, whose energy differs by $\pm\Delta_{int} = \pm V_{ir} = \pm C_3^{ir}(\theta)/R^3$ [Lukin *et al.*, 2001; Comparat and Pillet, 2010]. The critical blockade radius R_{ir} which determines the hard-sphere absorption condition is defined as

$$R_{ir} = \left(\frac{2\tilde{C}_3^{ir}}{\sigma_{eit}}\right)^{\frac{1}{3}} . \tag{6.6}$$

The anisotropy of the interactions for P states leads to an interaction strength $C_3^{ir}(\theta)$, which we reduce to $\tilde{C}_3^{ir}$ by averaging over the total solid angle.

(ii) For $|i\rangle = |nS\rangle$, using probe atoms in a different S state, van der Waals interactions generated by the impurity in the probe state produce an energy shift $V_{rr} = C_6^{ir}/R^6$. Thus, the impurity-probe critical radius is given by

$$R_{ir} = \left(\frac{2C_6^{ir}}{\sigma_{eit}}\right)^{\frac{1}{6}} . \tag{6.7}$$

In both situations, we attribute two-level response at $r \leq R_{ir}$ and three-level EIT response at $r > R_{ir}$.

6.2.2 Detection method

To probe the impurity distribution we measure the absorption of the probe light induced by the atomic cloud, analogously to the method described in Sec. 3.1.2, where the light absorption is collected by a CCD camera (see Eq. 3.3). To collect only information about the impurities embedded in the atomic gas, we compare the collected light under EIT without impurities I_{eit}, and with impurities I_{imp}. Their presence can therefore be revealed through an additional absorption $A_{add} = (I_{eit} - I_{imp})/I_{eit}$

$$A_{add} = 1 - e^{-\Delta OD} \quad \text{with} \quad \Delta OD = OD_{imp} - OD_{eit} , \tag{6.8}$$

which represents the signal emerging from the impurities. The effective number N_{add} of absorptive atoms due to the presence of impurities (otherwise transparent) is calculated with pixel resolution (pixel area $a_{px} = 4.3\,\mu\text{m}^2$ in the object plane) as

$$N_{add} = \frac{a_{px}(1+s_0)}{\sigma_0}\Delta OD = \frac{a_{px}(1+s_0)}{\sigma_0}\ln\left[(1-A_{add})^{-1}\right] = \frac{a_{px}(1+s_0)}{\sigma_0}\ln\left[\frac{I_{eit}}{I_{imp}}\right] . \tag{6.9}$$

6.2.3 Experimental observation of the optical response

In order to verify the optical response predicted by the model, an IEI experiment is performed in the large optical dipole trap (see Sec. 2.4). The atoms are initially prepared in the ground state $|g\rangle$ at a temperature $T \approx 40\,\mu\text{K}$. The atomic cloud exhibits a Gaussian profile of width $\sigma_x = 41.2\,\mu\text{m}$ $(1/e^2)$ and of tunable density, with peak densities in the center of the cloud n_0 up to $1.5 \cdot 10^{11}\,\text{cm}^{-3}$. After the atomic preparation, the trap is released and the response of the atomic cloud is probed by measuring the absorption in three different configurations: without coupling light nor impurities (two-level response), with the coupling light turned on but no impurities (EIT response), and finally with both the coupling light and the impurities present. The probe light absorption A (Eq. (3.3)) is measured by recording the probe intensity I_{trans} as well as the intensity I_{in} after 10 ms when all the atoms have fallen below the light path because of gravity.

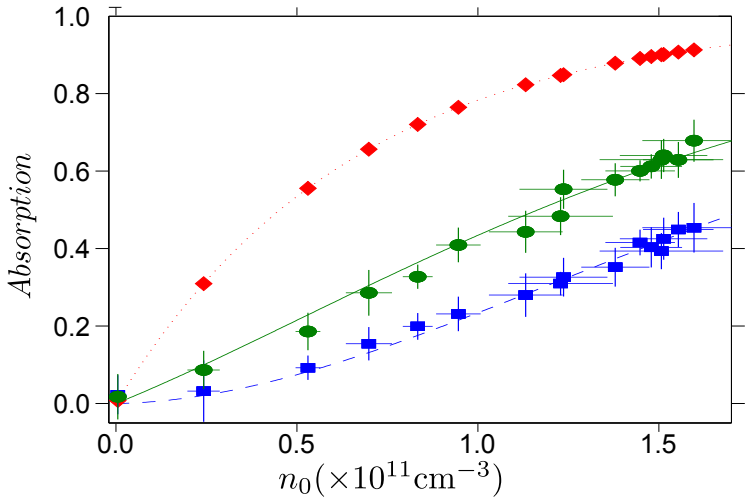

Figure 6.3: Absorption of the probe light as a function of peak atomic density n_0 in a large ODT. The atomic response is shown under three conditions: two-level (red), EIT (blue) and EIT in presence of $|42P_{3/2}, m_j = 3/2\rangle$ impurities (green). The absorption is measured on a 3x3 pixels region at the center of the cloud. Data are averaged over 10 repetitions. Error bars are given by one standard error. The lines present a comparison to the hard-sphere model, where the absorption is calculated from the corresponding optical susceptibility.

The two-level optical response, in absence of coupling field, allows to map the absorption A_{2l} (Eq. 3.2) accounting for the Rabi frequency $\Omega_p/2\pi = 1.14 \pm 0.02\,\text{MHz}$ (which introduces a 7 % correction). This measurement, shown in Figure 6.3 (red diamonds), coincides with the theoretical two-level predictions.

For a different realisation of the experiment, the coupling laser resonantly addresses the state $|r\rangle = |42S_{1/2}, m_j = 1/2\rangle$ and induces the EIT condition. The absorption A_{eit} (blue squares) is recorded in a small region in the center of the atomic cloud. The coupling beam was independently calibrated (Sec. 3.2) to deliver a Rabi frequency $\Omega_c/2\pi = 9.45 \pm 0.74\,\mathrm{MHz}$. For increasing atomic density, loss of transparency is observed, as expected in presence of emerging probe-probe van der Waals interactions. The data is compared to the hard-sphere model (blue dashed line)and good agreement is achieved considering a Rydberg blockade of $R_{rr} = 3.6 \pm 0.3\,\mu\mathrm{m}$, higher than the theoretical expectation ($\sim 2.5\,\mu\mathrm{m}$). The blockaded fraction f_{rr} increments up to 0.31 ± 0.03 as a function of density.

As a last step, impurities are pre-excited to the state $|i\rangle = |42P_{3/2}, m_j = 3/2\rangle$ during a fixed excitation time $t_{exc} = 5\,\mu\mathrm{s}$ and the optical response is measured (green circles). The larger absorption compared to the previous case is caused by the impurities. The density dependent absorption A_{imp} is compared to the hard-sphere model, where the interaction strength is considered to be $\tilde{C}_3^{ir} = 2\pi \times 1.7\,\mathrm{GHz} \cdot \mu\mathrm{m}^3$ including an angular averaging factor [Walker and Saffman, 2008]. This leads to a blockade radius of $R_{ir} = 6.1\,\mu\mathrm{m}$, roughly 2 times larger than R_{rr}. The model reproduces well the data assuming a constant fraction of volume blockaded by the impurities of $f_{ir} = 0.24 \pm 0.02$, resulting in 26 ± 5 Rydberg impurities embedded in the whole sample. From the field ionisation we estimate the number of impurities to be ~ 20, which is consistent with the optical measurement.

In the density range explored in Figure 6.3, the increase of effective signal with the peak atomic density indicates an increment of the amplification factor (expressed as the number of additional absorbers per impurity) and the SNR, which is enhanced from 0 to ~ 5. The atomic density fluctuations are estimated to be on the 8 % level by analysis of the shot-to-shot variations in the two-level case. The measurements presented here demonstrate qualitative agreement with the hard-sphere model predictions. However, additional effects evidence an increase of probe-probe interactions that lower the amplification factor in IEI experiments.

6.3 Sensitive detection of $|nS\rangle$ and $|nP\rangle$ states

In this section, recent studies of IEI using dipolar-interacting $|nP\rangle$ states as impurities are introduced in Section 6.3.1 including a characterisation of the average sensitivity for small number of impurities. Complementary investigations of the single-shot sensitivity are carried out for van der Waals interacting $|nS\rangle$ states and

compared to nP states (Section 6.3.2). These studies pave the way for probing spin models implemented with Rydberg atoms at the single spin level with high spatial and temporal resolution.

6.3.1 Averaged imaging of few $|nP\rangle$-state impurities

Here observations of a small number of impurities are presented, under conditions which restrict the diffusion of impurities outside their volume [Günter *et al.*, 2013], necessary prerequisite to implement and probe Rydberg spin systems at the single spin level. Our set of IEI experiments is performed in a mesoscopic dense atomic sample of $\sim 8 \times 8 \times 22\,\mu$m Gaussian widths ($1/e^2$), prepared in a tight ODT (see Section 2.4.1).

The atoms are prepared in the ground state $|g\rangle$ at a temperature of $\sim 1\,\mu$K with a peak density of $n_0 = (1.4 \pm 0.3) \cdot 10^{11}\,\mathrm{cm}^{-3}$. Rydberg impurities are prepared via three-photon excitation in the state $|i\rangle = |42P_{3/2}, m_j = 3/2\rangle$ (Sec. 3.3). EIT couples the probe atoms to $|r\rangle = |42S_{1/2}, m_j = 1/2\rangle$. The average number of impurities N_i is varied by the duration time t_{exc} of the three-photon excitation and is independently determined via field-ionization. For each t_{exc} the optical response under EIT conditions is recorded and compared to the response of the unperturbed EIT background to deduce the additional absorption A_{add}. Given the high-density of the sample, the coupling Rabi frequency Ω_c is increased and calibrated (see Sec.3.2) to a peak value $26.2 \pm 2.3\,$MHz, which we assume quasi-homogeneous over the extension of the cloud. Under this conditions, the cloud presents good transparency conditions even with the effect of probe-probe interactions [Hofmann *et al.*, 2013].

In Fig. 6.4(a), we present the spatially resolved additional absorption. The integrated number of additional absorbers along the vertical axis is plotted in Fig. 6.4(b) (red line) and is compared to a Gaussian fit (blue line). After averaging 50 repetitions, we observe that the signal is ≥ 3 times higher than the noise level for $N_i = 2$ impurities. The total number of additional absorbers ΣN_{add} is extracted through a 2D Gaussian fit over the absorption area and displayed in Fig. 6.4(c) as a function of the mean number of impurities N_i. The measurements show a linear increase followed by saturation at ~ 40 for $N_i > 4$.

The observation of saturation is consistent with the theoretical predictions. For our large Ω_c, we can assume $\chi^0_{eit} \approx 0$ and, since $f_{rr} \approx 0.02 \ll 1$, probe-probe interactions are negligible. According to the IEI model described in Sec. 6.2, the increase of absorption can be simply described by the relation $\Sigma N_{add} = f_{ir} N = N_i \cdot n_0 V_{bl,i}$, linear with the number of ground-state atoms N and the impurity number N_i. The

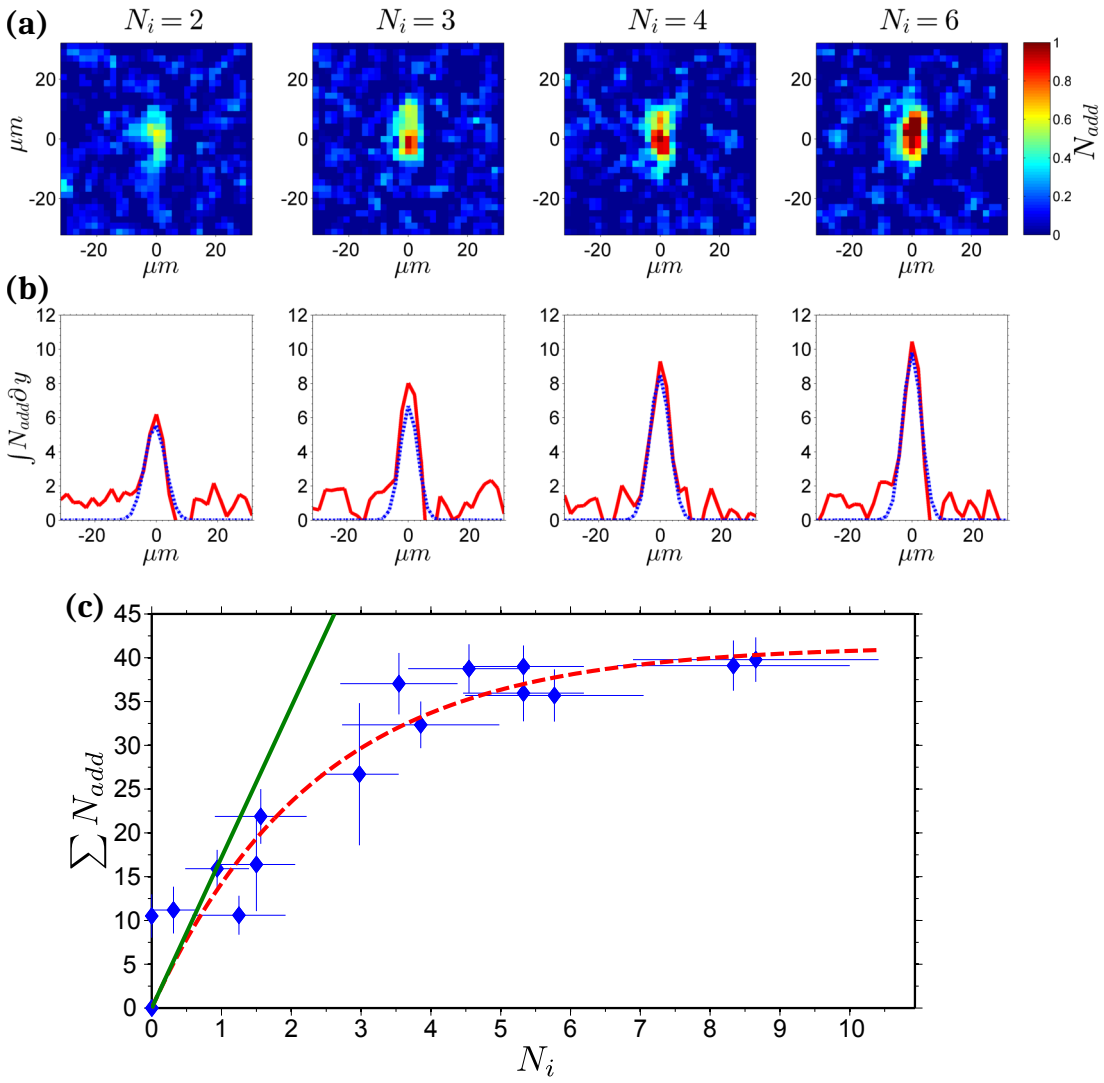

Figure 6.4: Interaction-enhanced imaging of $|42P_{3/2}\rangle$ Rydberg atoms in a mesoscopic cloud. **(a)** Spatial distribution of the additional absorbers N_{add} for increasing average number of impurities $N_i = 2,\ 3,\ 4,\ 6$. Measurements averaged over 50 repetitions with $t_{exp} = 30\,\mu$s exposure time. **(b)** Additional absorbers integrated over the vertical direction of the images from (a) (solid red). The blue dashed line correspond to a 2D Gaussian fit to the data. The fit integral allows us to extract ΣN_{add}, reducing the noise outside the region of interest. **(b)** Detected additional absorbers ΣN_{add} as a function of the mean number of impurities N_i. The initially linear growth of additional absorbers is followed by exponential saturation around 40 absorbers as a result of Rydberg impurity blockade. Data are fit to a saturating exponential model, which delivers an initial slope of 17.4 ± 0.2, in agreement with our model that predicts an amplification factor of 17.1. Error bars correspond to one standard error of the mean.

amplification factor $n_0 V_{bl,i} \approx 17$ predicted by this formula is presented in the figure (green line) and describes well the initial slope of the plot. Given $N \approx 400$ atoms and saturation around $N_{i_{sat}} \approx 40$, the fraction of volume blockaded by impurity-probe interactions is $\leq 10\,\%$. The observed deviation at larger number of impurities may be interpreted as a Rydberg blockade effect amongst impurities in the center of the absorptive region, estimated to be significant above ~ 10 impurities. Then, the excitation saturates in the center of the sample, while it would be still possible in the tails, where the density is low and thus the change in the optical response negligible. Since in our case $R_{ii} \gg R_{ir}$, only a small fraction of the total volume is effectively blockaded.

These measurements demonstrate the suitability of IEI to detect single Rydberg impurities with an average sensitivity close to 1, using 50 repetitions. In the regime of strong EIT coupling and few impurities, the number of additional absorbers changes linearly with the number of impurities and depends only on the atomic density n_0 and the EIT bandwidth σ_{eit} through the blockade volume. This relationship allows to directly estimate the number of impurities without considering the microscopic details of the imaging. Increasing the number of ground-state atoms within each blockade sphere could enhance the sensitivity of the technique. This can be obtained by increasing the R_{ir} blockade radius through an optimal choice of impurity probe state pairs.

6.3.2 Single-shot imaging of few $|nS\rangle$-state impurities

Since our spin experiments explore the dynamics of $|nS\rangle - |n'S\rangle$ or $|nS\rangle - |nP\rangle$ state combinations, IEI will have to be applied to observe $|nS\rangle$ spins. Now we will investigate the question of single-shot detection of impurities, focusing on measurements of $|nS\rangle$ impurities in a dense small sample, in similar conditions to the reported experiments in Sec. 6.3.1 for $|nP\rangle$ impurities. Measurements of the detected distributions are reported and the single-shot sensitivity $\mathcal{S}$ is analysed by means of the threshold method, previously applied in Section 3.1. Deviations from expected electromagnetically-induced transparency conditions are presented, which are not included in the hard-sphere approach.

The following IEI experiments are performed, coupling the ground state to the Rydberg state $|r\rangle = |42S_{1/2}, m_j = 1/2\rangle$ by means of an homogeneous probe beam with $\Omega_p/2\pi = (1.20 \pm 0.05)\,\mathrm{MHz}$ and a coupling beam with a peak Rabi frequency $\Omega_c/2\pi = (10 \pm 2)\,\mathrm{MHz}$ at various densities. Figure 6.5(b), shows the time-dependent increase of absorption (red) for a peak density $n_0 = (7.0 \pm 0.2) \cdot 10^{11}\,\mathrm{cm}^{-3}$, which

is accompanied by an increase of the number of excitations (blue). Whereas the initial conditions at $t_{exp} = 2\,\mu s$ can be explained with the hard-sphere predictions (OD= 0.14, $N_{ions} = 12.4$), the additional increase cannot be explained by standard probe-probe van der Waals interactions. Such observation is compatible with a spurious seeding effect due to black-body-induced transfer of population to nearby P states [Gallagher, 1994; Beterov *et al.*, 2009; Branden *et al.*, 2010]. The stimulated decay of probe states to nearby Rydberg states would originate undesired impurities which reduce the transparency of the EIT medium. Thus, black-body induced redistribution has a negative impact not only on the spin dynamics, but also on the their optical detection.

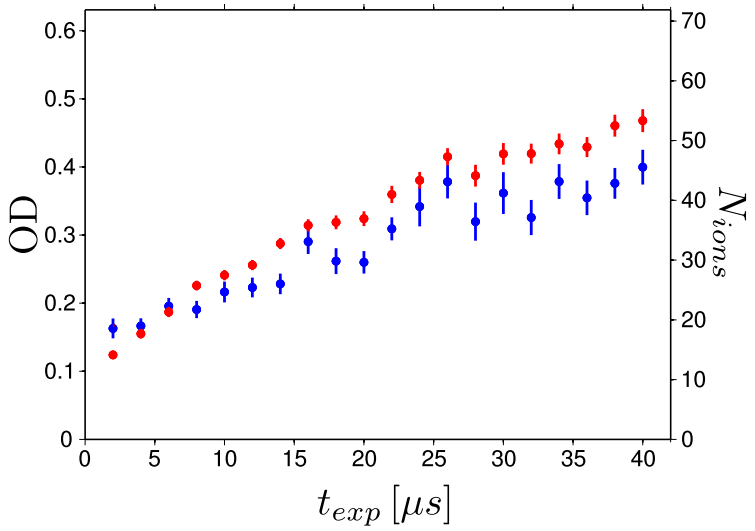

Figure 6.5: Increase of optical density (red) and probe Rydberg atom population (blue) as a function of exposure time t_{exp} under EIT conditions. Impurities are prepared in $|i\rangle = |43S_{1/2}, m_j = 1/2\rangle$, whereas probe atoms are coupled to $|r\rangle = |42S_{1/2}, m_j = 1/2\rangle$ in the "tight" dipole trap with peak atomic density $n_0 = (1.2 \pm 0.1) \cdot 10^{11}\,\mathrm{cm}^{-3}$. The Rabi frequencies are $\Omega_p/2\pi = (1.20 \pm 0.05)\,\mathrm{MHz}$ and $\Omega_c/2\pi = (10 \pm 2)\,\mathrm{MHz}$. Taken and adapted from [Gavryusev, 2016].

Since probe-probe interactions make a extremely small effect in the optical absorption for densities $\leq 3 \cdot 10^{10}\,\mathrm{cm}^{-3}$ (see Fig. 6.4), given the present conditions and probe quantum state, the increase of absorption at long exposure times has not been observed in such regime.

For subsequent measurements, the probe Rabi frequency Ω_p is lowered and the coupling Rabi frequency Ω_c is increased in order to reduce probe-probe interactions. In order to analyse the sensitivity of IEI for each individual experimental realisation, the single-shot fidelity (as defined in [Bochmann *et al.*, 2010]) is calculated by

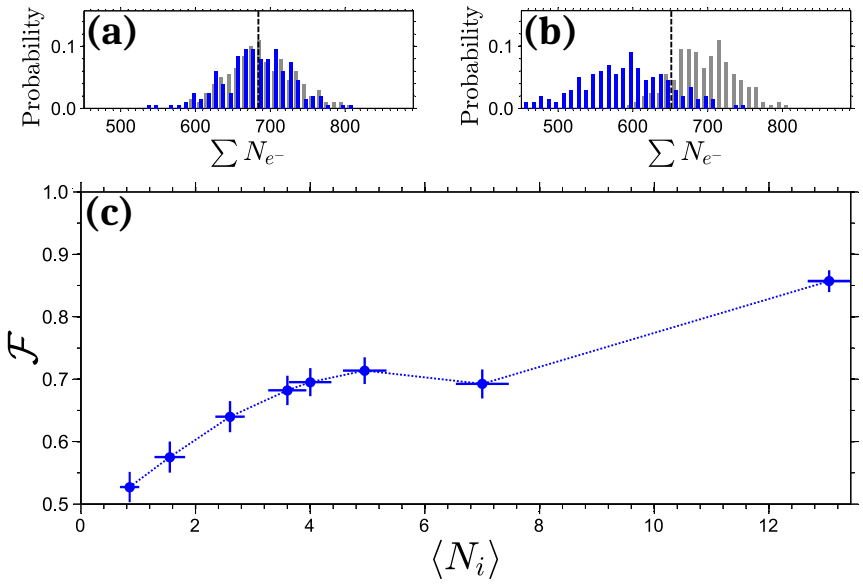

Figure 6.6: Distribution of measured counts on the CCD camera and single-shot fidelity detection for a variable number of impurities. IEI experiment realised in a dense mesoscopic sample with impurities in the state $|i\rangle = |43S_{1/2}, m_j = 1/2\rangle$ and EIT bath coupled to the probe state $|r\rangle = |42S_{1/2}, m_j = 1/2\rangle$. The normalised distributions over 200 repetitions show the number of generated counts in the CCD camera in presence (blue) and absence (grey) of impurities. Each distribution corresponds to an average number of impurities $\langle N_i \rangle$: **(a)** $\langle N_i \rangle = 0.8 \pm 0.2$. **(b)** $\langle N_i \rangle = 13.1 \pm 0.4$. **(c)** Fidelity calculated with the threshold method (see Sec.3.1.5). For $\langle N_i \rangle = 13.1 \pm 0.4$, the fidelity threshold is crossed, giving $\mathcal{F} = 0.86 \pm 0.2$. Sensitivity of $\mathcal{S} \sim 12$ impurities. Errorbars of $\mathcal{F}$ are estimated with the bootstrap method [Efron and Tibshirani, 1994]. Taken and adapted from [Gavryusev, 2016].

means of the threshold method [Cowan, 1998], which allows us to discriminate how distinguishable the distribution of impurity transmission is with respect to the distribution of transmission under EIT. The procedure can be consulted in more detail in Section 3.1, as it has been used to optically distinguish Rydberg atoms through Depletion Imaging. Further details can be found in [Gavryusev, 2016, Ch. 5].

In Figure 6.6, single-shot sensitivity analysis of IEI experiments is presented. In this experiment, $|i\rangle = |43S_{1/2}, m_j = 1/2\rangle$ and $|p\rangle = |42S_{1/2}, m_j = 1/2\rangle$. The small atomic sample (see Sec. 6.3.1) has a peak density $n_0 = (7.0 \pm 0.2) \cdot 10^{11}\,\mathrm{cm}^{-3}$ and is coupled with Rabi frequencies $\Omega_p/2\pi = (0.30 \pm 0.05)\,\mathrm{MHz}$ and $\Omega_c/2\pi = (20 \pm 1)\,\mathrm{MHz}$ during an exposure time $t_{exp} = 10\,\mu\mathrm{s}$. The transmission is acquired in a region of 4×5 pixels of the CCD camera, corresponding to $8.25 \times 10.35\,\mu\mathrm{m}^2$ in the object plane. Varying the average number of impurities detected by field ionisation $\langle N_i \rangle$, we

observe an increase of fidelity up to $\mathcal{F} = 0.86 \pm 0.2$ for $\langle N_i \rangle = 13.1 \pm 0.4$. The single shot detection sensitivity (defined as in Ch. 3.1.5) for $|43S_{1/2}, m_j = 1/2\rangle$ impurities in such conditions is measured to be $\mathcal{S} = 12$.

Analogously, the presented fidelity analysis with the threshold method has been applied to analyse the single-shot sensitivity of $|43P_{3/2}, m_j = 3/2\rangle$ impurities embedded in a probe EIT gas coupled to $|42S_{1/2}, m_j = 1/2\rangle$, as for the experiments in Sec. 6.3.1. This lead to $\mathcal{S} \sim 4$ impurities per single-shot, which represents the highest sensitivity of IEI to date. Nevertheless, achieving good transparency conditions and high probe-light signal simultaneously is a challenging task at high densities, where additional effects, as the one observed in Fig 6.5, quickly increase the absorption of the probe atoms and consequently reduce the detection sensitivity of IEI.

6.4 Prospects: enhancement of the sensitivity to observe spin dynamics

This chapter introduced an overview of Interaction Enhanced Imaging to observe Rydberg atoms, as well as the latest progress towards single-impurity sensitivity. Since this method relies on mapping the presence of Rydberg impurities on the increase of absorption of an EIT gas of cold atoms, a consistent characterisation of EIT was beneficial (Section 3.2). At increasing density, Rydberg-Rydberg interaction effects degrade the good transparency conditions and limit the IEI signal range (Fig. 6.4 ,Fig. 6.5(a)). Selecting optimal conditions, optical imaging of $|42P_{3/2}\rangle$ and $|43S_{1/2}\rangle$ Rydberg impurities has been demonstrated with good spatial resolution and few atom sensitivity (Fig. 6.4), in a dense mesoscopic sample with size of few impurity-impurity blockade radii R_{ii}. Both the spatial resolution and the sensitivity of IEI are comparable to the resolution of other Rydberg atom imaging methods [Schwarzkopf *et al.*, 2011; Schauß *et al.*, 2012; McQuillen *et al.*, 2013; Lochead *et al.*, 2013]. However, this technique does not destroy the Rydberg state due to the measurement procedure.

Competition amongst several non-linear effects plays a key role in the signal-to-noise ratio of IEI. Therefore, achieving single-shot sensitivity constitutes a big challenge. For instance, increasing the cloud density has been proven essential to increment the amplification factor per impurity, but concurrently the impact of probe-probe interactions rises, which reduces the achievable contrast. Single-impurity sensitivity per single-shot has been reported in the context of creating optical transistors controlled by a single stored photon (stored impurity) [Baur *et al.*, 2014;

Strongest impurity-probe pairs for IEI	
$\|i\rangle - \|r\rangle$	R_{ir}/R_{rr}
$\|43S\rangle - \|42S\rangle$	1.38
$\|79S\rangle - \|57S\rangle$	1.67
$\|69S\rangle - \|67S\rangle$	2.00
$\|39S\rangle - \|38S\rangle$	2.72

Table 6.1: Ratio between impurity-probe R_{ir} and probe-probe R_{rr} Rydberg blockade for the state pair combinations $|i\rangle - |r\rangle$. The calculations of both R_{ir} and R_{rr} assume $\propto \frac{1}{R^6}$ scaling of van der Waals interactions. Only pairs with stronger ratio than the first state combination of the list are presented in this table.

Tiarks *et al.*, 2014; Gorniaczyk *et al.*, 2014]. Spatially resolved and single particle sensitive imaging as in IEI is a highly demanding task, since it requires to detect a higher number of photons to resolve the particles, but this also increases the undesired probe-probe interactions. So far, a single-shot sensitivity of $\mathcal{S} = 4$ impurities has been achieved for $|42P_{3/2}\rangle - |42S_{1/2}\rangle$ and $\mathcal{S} = 12$ for $|43S_{1/2}\rangle - |42S_{1/2}\rangle$. To further enhance the IEI sensitivity, the density and probing and coupling Rabi frequencies have to be carefully optimised, after choosing impurity-probe Rydberg state combinations that present optimal interaction strength ratios. In fact, the ratio between impurity-probe R_{ir} (Eq. (6.7), Eq. (6.6)) and probe-probe R_{rr} (Eq. (6.3)) critical radii is a key figure of merit. Whereas in the case of resonant dipole-dipole impurity probe interaction, an increase of principal quantum number of the $|nS\rangle - |nP\rangle$ pair is enough to raise the SNR and, consequently, the sensitivity, the case of van der Waals interactions for $|nS\rangle - |n'S\rangle$ pairs presents additional subtleties, discussed more in detail in [Gavryusev, 2016]. The optimal choices are state combinations that present a small Förster defect, which extraordinarily enhances the interaction strength, and the most promising state combinations are listed in Table 6.1.

Achieving an SNR $\gg 1$ would allow to recover spatial resolution below the Rydberg blockade radius R_{ii}, thus, permitting to follow the local evolution of single spins. This would enable new observations of Rydberg dynamics and formation of correlations mediated by dipolar or van der Waals interactions. Studies of diverse phenomena like energy transport [Schönleber *et al.*, 2015; Schempp *et al.*, 2015; Fahey *et al.*, 2015; Yu and Robicheaux, 2016], formation of Rydberg aggregates [Malossi *et al.*, 2014; Schempp *et al.*, 2014; Urvoy *et al.*, 2015] or evolution of Rydberg dynamics under Ising or Heisenberg Hamiltonians [Hazzard *et al.*, 2014b; Glaetzle *et al.*, 2015; van Bijnen and Pohl, 2015; Barredo *et al.*, 2015; Labuhn *et al.*, 2016;

Whitlock *et al.*, 2017] will be subject of future investigations mediated by IEI.

Observing the dynamics of two spin components

As a specially interesting application of the IEI technique, I propose its use to follow the evolution of a two-component spin ensemble. For such purpose, the principles of IEI must be generalised to include three spin components: two Rydberg spins and a probe Rydberg state $|r\rangle$. As both spins interact with the probe EIT medium, a clever selection of states must be realised to maximise the interaction between the probe state and the spin-state of interest while minimising the interaction to the other spin component. In this three-state imaging process, an interesting option is to excite the $|\downarrow\rangle$ state to a Rydberg level close to a Förster resonance with the $|r\rangle$ state and to leverage this feature to follow the temporal evolution of $|\downarrow\rangle$. A suitable combination of states is given by the strongly interacting $|\downarrow\rangle = |79S\rangle$ and $|r\rangle = |57S\rangle$, with a ratio $R_{\downarrow r}/R_{rr} = 1.67$. To minimise the interaction between the probe state and the other spin component, the spin-up state can be chosen to be $|\uparrow\rangle = |77P\rangle$ or $|\uparrow\rangle = |78S\rangle$ to explore the XX and XXZ dynamics, respectively. For $|\uparrow\rangle = |78S\rangle$ the C_6 interaction coefficient between $|\uparrow\rangle - |r\rangle$ is several orders of magnitude smaller than the interaction amongst $|\downarrow\rangle - |r\rangle$ states, thus, leading to a spin-probe blockade radius with ratio $R_{\uparrow r}/R_{rr} = 0.51$. This indicates that the effect of $|\uparrow\rangle$ on the absorption is even smaller than that of probe-probe interactions, whereas the impact of $|\downarrow\rangle$ is 3.29 times higher. However, the residual absorption induced by the presence of $|\uparrow\rangle$ states must still be subtracted from the calculated additional absorption, as in Eq. (6.8). For this, a separate calibration of the absorption under the presence of each component and under the bare effect of the probe state are required, which modifies Eq. (6.8) into the effective expression

$$\Delta OD = OD_{\downarrow} - OD_{eit} - OD_{\uparrow} \, . \tag{6.10}$$

Such experiments could reveal the formation of magnetic phases in the XX and XXZ Heisenberg models, and would open the way for an enormous variety of investigations.

Chapter 7

Conclusion and outlook

In the scope of this thesis, I investigated the mapping of a spin-1/2 system onto two Rydberg states and the usage of such platform to study many-body dynamics amongst dipole-interacting Rydberg atoms and its relation to several spin Heisenberg Hamiltonians. These studies were possible due to the implementation of refined control of the microwave field that couples the relevant excited atomic levels and allows to establish complex sequential protocols to manipulate the quantum state of the Rydberg spins, with independent amplitude, frequency and phase control for each pulse of an arbitrary experimental sequence.

To prepare the spin system, accurate implementation and characterisation of several Rydberg atom excitation schemes was necessary. Here, two-photon optical excitation of Rydberg $|nS\rangle$ states was optimised to accurately prepare the $|\downarrow\rangle$ state, whereas combined three-photon excitation of $|nP\rangle$ Rydberg levels, with two optical photons and a microwave field, was introduced as a possibility to independently address a potential $|\uparrow\rangle$ of the spin system. Additionally, an optical scheme to de-excite one spin state before detection was optimised, in order to render the spin states distinguishable. By means of a new Depletion Imaging technique, which relies on the lack of absorption from Rydberg atoms, the excitation dynamics has been locally resolved. This evidenced the emergence of Rydberg blockade during the excitation and thus the spatial self-ordering of Rydberg spins at high densities was revealed. This technique also provided information about the regime of excitation of Rydberg atoms by locally mapping the excitation rates. Furthermore, the Depletion Imaging technique provides a precise method to calibrate the global Rydberg spin number detected through field-ionisation and identify its spatial distribution.

Addressing Rydberg-Rydberg transitions to manipulate the selected spin states has been proven feasible with negligible decoherence effects in short timescales

compared to the spins' life-time and being able to use the Rydberg atoms as a sensitive probe to measure weak microwave fields ($|E| \sim 1\,\frac{\mu V}{cm}$). With this level of control of the Rydberg spin platform, it was possible to benchmark the dynamics of non-interacting spins with a theoretical model governed by the dynamics of the single-spin, demonstrating efficient manipulation of the quantum state of the spin ensemble by tomographic sequences and finding an excellent coherence time of the spins ($\sim 127\,\mu m$ for $n = 48$). I quantified the experimental limitations, thus enabling our first observations of interaction effects amongst the spins in the many-body regime. Spectroscopy methods provided a tool to experimentally determine the sign of the average dipole-dipole interaction strength $\tilde{J}_\perp$, which is found to strongly depend on the selection of quantum numbers. The application of Ramsey techniques allowed to characterise the strength of the interaction in different configurations, as well as the phase shift produced on the spins. Finally, we could measure the effect the competition of XXZ interactions with a driving field, which lead to an asymmetry of the spin magnetisation curve. This paves the way to explore non-linear dynamical effects and possible phase transitions within Rydberg XXZ Heisenberg models.

In addition, the application of another imaging technique called Interaction Enhanced Imaging, with potential to achieve few-to-single spin spatial resolution per single shot, has been tested to image Rydberg spins, leading to a single-shot sensitivity $\mathcal{S} \approx 4$ for $|42P\rangle$ states. This technique makes use of the strong interactions of the spins to map their position on the absorption profile of an otherwise transparent atomic gas (by being under EIT coupling). Optimising the selection of Rydberg states, single-spin sensitive measurements may be rendered possible. Using the same principles of the imaging technique, I propose a method to measure the local spin dynamics in a two-spin component ensemble.

In the future, the range of application of Depletion Imaging may be successfully extended to reveal the number, size and local distribution of Rydberg aggregates in combination with full counting statistics (FCS) [Schempp *et al.*, 2014; Malossi *et al.*, 2014; Urvoy *et al.*, 2015] and could give insight into the seeding mechanism that leads to the formation of crystalline structures [Pohl *et al.*, 2010; Schauß *et al.*, 2015]. The potential achievement of single-atom resolution with Interaction Enhanced Imaging could be also utilized to map the emergent correlations [Schwarzkopf *et al.*, 2011; Schauß *et al.*, 2012] in such systems, as well as the evolution of magnetic domains in spin experiments. Moreover, it can be used to measure the transport of energy carried by the spins [Günter *et al.*, 2013; Robicheaux and Gill, 2014; Schönleber *et al.*, 2015; Fahey *et al.*, 2015; Yu and Robicheaux, 2016] with a high spatial and temporal resolution.

The different excitation techniques described in the course of this thesis can be jointly applied in the future to independently create spins after the initial preparation, inducing fluctuations and imbalance of the spin magnetisation which may play an important role in non-linear spin dynamics of the system in both the XX and XXZ Heisenberg models. An step forward in the control of the spin preparation would consist in structuring the optical fields in order to address specific regions of the atomic cloud [Lu *et al.*, 2015], which can be obtained by using a spatial light modulator (SLM) [van Bijnen, 2013; Bowman *et al.*, 2015; Naber *et al.*, 2016]. Thus, our experiments would achieve a higher level of control over the disordered distribution of spins, engineering their initial configuration.

Making use of our high-degree of control over the microwave field, more complex quantum control protocols can be applied to probe the spin dynamics in future experiments. On the one hand, an important goal in our spin experiments will be to distinguish the nature of the observed asymmetry with respect to the orientation of the competing field in the XXZ experiments. The dependence on the properties of the spin-exchange (XX part of the Hamiltonian) may be easier to confirm by repeating the experiments in a direct dipole-dipole interacting configuration (e.g. $|\downarrow\rangle = |nS\rangle$, $|\uparrow\rangle = |nP\rangle$). The transition between the few to many-body behaviour could be explored by increasing the principal quantum number, where a smaller total number of spins is accessible without reducing the interaction strength and the longer coherence of the spin system allows for longer evolution and observation times. By adiabatically ramping the competing microwave driving field, the ground state of the system could be revealed. Introducing spatial structure on the spin distribution will also provide a consistent framework to distinguish the effect of disorder from the inherent few-to-many body effects [Labuhn *et al.*, 2016; Bernien *et al.*, 2017]. On the other hand, the observation of time-crystalline structures and temporal correlations on Rydberg spin systems may soon become possible [Zhang *et al.*, 2017; Choi *et al.*, 2017]. Ultimately, the reduction of technical noise in the detection, provided by state-selective field ionisation, would give access to precise variance measurements of the magnetisation of the spin ensemble, which can potentially reveal rich non-linear dynamics and the development of squeezed states and entanglement or the spread of correlations [Hazzard *et al.*, 2013; Hazzard *et al.*, 2014b].

Appendices

Appendix A

IQ double mixing to suppress undesired side-bands

IQ-mixing provides a manner to realise frequency up-conversion with additional suppression of the side-bands of either higher or lower energy of the spectrum. Such suppression allows us to avoid the driving of undesired Rydberg transitions. IQ-mixing relies on the cancellation of signals by two 90° phase-shifts of the mixing components, creating a 180° shifted signal which adds up to the original signal. Thus, a typical IQ-mixer consists of two internal mixers. Each of them is fed with a local oscillator (LO) signal provided by the carrier signal, which is previously split and 90° phase-shifted. Similarly the modulating intermediate frequency (IF) for each mixer is split and 90° phase shifted. The output radio-frequency (RF) signal from both I and Q branches is added up by means of an in-phase combiner (as observed in figure [A.1]) and the resulting signal cancels out the low side-band components.

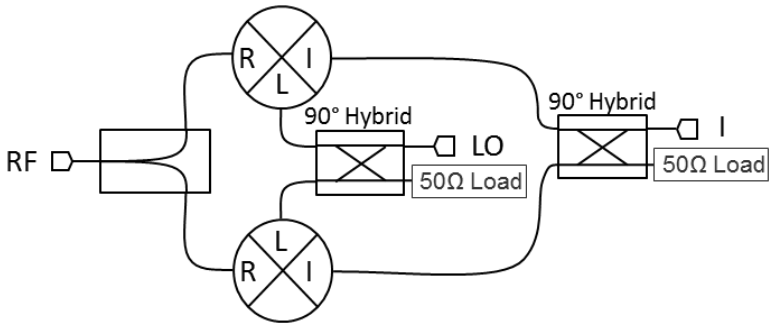

Figure A.1: Working scheme of a general IQ-mixer. The IF and LO signals are split for into two paths with a 90° relative phase. Individual mixing processes are recombined to produce the global RF output. Figure taken and adapted from "Marki microwave".

Mathematically, the IF signals (analogously, the LO inputs) of a perfect mixing process can be described for each branch as

$$I(t) = \frac{A_{IF}}{2}\cos(2\pi\nu_{IF}t) \tag{A.1a}$$

$$Q(t) = \frac{A_{IF}}{2}\sin(2\pi\nu_{IF}t) \tag{A.1b}$$

Depending on the sign of the 90° phase shift, we can suppress the low or the high-frequency components.

Hence, the output given by each of the mixers presents the following shape

$$\begin{aligned} P_I &= \frac{A_{LO}}{2}\cos(2\pi\nu_{LO}t)\cdot\frac{A_{IF}}{2}\cos(2\pi\nu_{IF}t) \\ &= \frac{A_{LO}A_{IF}}{4}\big[\cos(2\pi(\nu_{LO}+\nu_{IF})t)+\cos(2\pi(\nu_{LO}-\nu_{IF})t)\big] \end{aligned} \tag{A.2a}$$

$$\begin{aligned} P_Q &= -\frac{A_{LO}}{2}\sin(2\pi\nu_{LO}t)\cdot\frac{A_{IF}}{2}\sin(2\pi\nu_{IF}t) \\ &= \frac{A_{LO}A_{IF}}{4}\big[\cos(2\pi(\nu_{LO}+\nu_{IF})t)-\cos(2\pi(\nu_{LO}-\nu_{IF})t)\big] \end{aligned} \tag{A.2b}$$

Finally, the recombination of both branches allow us to get a global RF output such like

$$P_{RF} = \frac{A_{LO}A_{IF}}{2}\cos(2\pi(\nu_{LO}+\nu_{IF})t), \tag{A.3}$$

where only the high-frequency side-band is present.

The experimental characterisation realised with the IQ-mixer *Marki MLIQ-1845L* confirm the benefits of such mechanism to suppress one side of the modulated spectrum with respect to standard mixers.

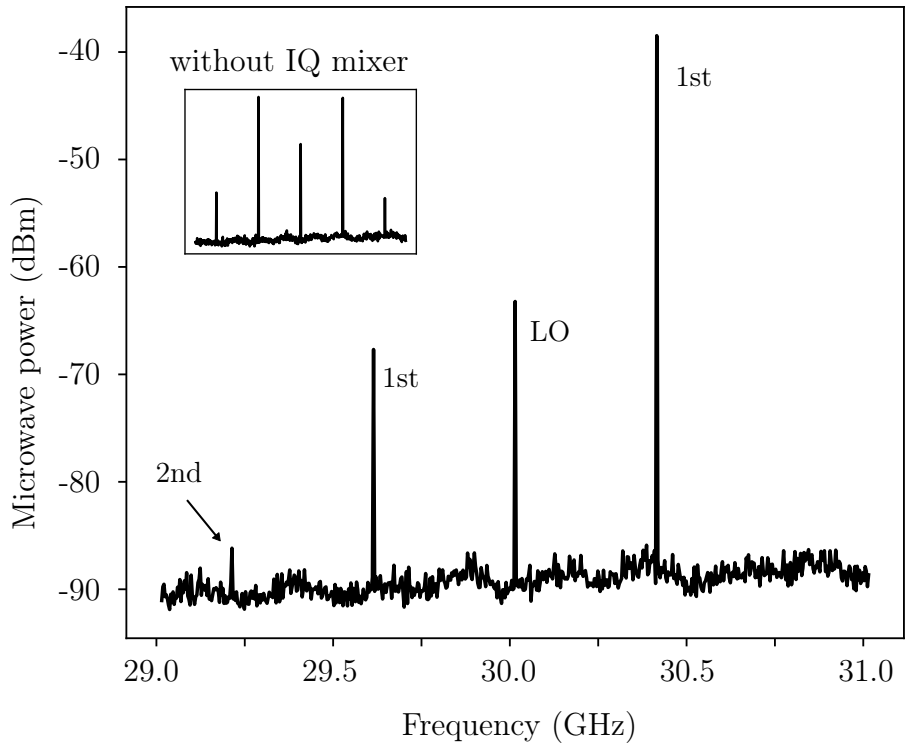

Figure A.2: Power spectral measurement of the IQ-mixer *Marki MLIQ-1845L* radio-frequency (RF) output for a carrier local oscillator (LO) frequency $\nu_{LO} = 30.04\,\mathrm{GHz}$ and input power $P_{LO} = 16\,\mathrm{dBm}$. The DDS provides a mixing intermediate frequency (IF) signal at a frequency $\nu_{IF} = 400\,\mathrm{MHz}$. The local oscillator (LO), first and second side-bands from the up-conversion process are observed. Inset: power spectral measurement of the mixer *M4-0165*, relying on standard frequency up-conversion. The amplitude of the low-frequency side-bands is strongly suppressed by means of the IQ-mixer.

Appendix B

Coupling between $|nS_{j,m_j}\rangle$ and $|n'P_{j',m_j}\rangle$ states

As evidenced in the previous chapters of this thesis, extensive use of ^{87}Rb Rydberg $|nS\rangle$ and $|n'P\rangle$ Zeeman sub-states has been employed. In Ch. (3.3, 6, 4, 5), Rydberg $|nS_{1/2}, m_j\rangle$ states are coupled to $|n'P_{j'}, m'_j\rangle$ by either a microwave field of the desired polarisation (Ch. (3.3, 4)) or by means of dipole-dipole interaction due to the strong dipole matrix elements (Ch. (6, 5)). To quantify the coupling between the involved states, the dipole operator is described as $\mu = e\vec{r}\cdot\hat{e}$ in terms of polarisation vector $\hat{e}$, so it can be transformed into the spherical basis operators μ_q, given by

$$\mu_q = er\sqrt{\frac{4\pi}{3}}Y_1^{-q}(\theta,\phi), \tag{B.1}$$

where q describes the polarisation dependence: $q = \{+1, 0, -1\} \Rightarrow \{\sigma_+, \pi, \sigma_-\}$ transitions. The Wigner-Eckart theorem provides a mechanism to separate the dipole matrix element into a radial contribution and an angular pre-factor [Weissbluth, 1978; Sobelman, 1979]. Thus, the reduced matrix element between the states $|1\rangle$ and $|2\rangle$ in the total angular momentum basis $\{n, l, j, m_j\}$ and $\{n', l', j', m'_j\}$, respectively, is expressed as

$$\langle j\|\mu\|j'\rangle = (-1)^{l+s+j'+1}\cdot\delta_{S,S'}\sqrt{(2j+1)(2j'+1)}\begin{Bmatrix} j & 1 & j' \\ l' & -q & l \end{Bmatrix}\langle l\|\mu\|l'\rangle\,, \tag{B.2}$$

where

$$\langle l\|\mu\|l'\rangle = (-1)^l\sqrt{(2l+1)(2l'+1)}\begin{Bmatrix} l & 1 & l' \\ 0 & 0 & 0 \end{Bmatrix}\langle nl|er|n'l'\rangle\,. \tag{B.3}$$

The overlap between the radial wavefunctions and the dipole moment of the involved

$\langle nljm_j\|\mu_q\|n'l'j'm'_j\rangle$						
$\times\mathcal{R}_{n,0\to n',1}$	$P_{1/2,-1/2}$	$P_{1/2,+1/2}$	$P_{3/2,-3/2}$	$P_{3/2,-1/2}$	$P_{3/2,+1/2}$	$P_{3/2,+3/2}$
$S_{1/2,-1/2}$	$\frac{1}{3}$	$-\frac{\sqrt{2}}{3}$	$-\frac{1}{\sqrt{3}}$	$\frac{\sqrt{2}}{3}$	$-\frac{1}{3}$	0
$S_{1/2,+1/2}$	$\frac{\sqrt{2}}{3}$	$-\frac{1}{3}$	0	$-\frac{1}{3}$	$\frac{\sqrt{2}}{3}$	$-\frac{1}{\sqrt{3}}$

Table B.1: Dependence of the coupling between nS and $n'P$ states with the quantum numbers $\{j, m_j\}$. The table represents the total pre-factor from Eq. (B.5) which multiplies the overlap between the dipole moments (Eq.(B.4)).

states, independent of the spin-orbit coupling, is calculated as

$$\langle nl|er|n'l'\rangle = \mathcal{R}_{nl\to n'l'} = \int_{r_i}^{r_0} \mathcal{R}_{n,l}(r) er \mathcal{R}_{n',l'}(r) r^2 dr, \tag{B.4}$$

by numerical integration, performed using the Numerov algorithm, as described in [**S**ibalić *et al.*, 2017]. Finally, the dipole matrix element on the $\{n, l, j, m_j\}$ basis is given by the expression

$$\begin{aligned}\langle nljm_j\|\mu_q\|n'l'j'm'_j\rangle = (-1)^{j-m_j+s+j'+1}\sqrt{(2j+1)(2j'+1)(2l+1)(2l'+1)} \\ \times \begin{Bmatrix} j & 1 & j' \\ l' & s & l \end{Bmatrix} \begin{pmatrix} j & 1 & j' \\ -m_j & -q & m'_j \end{pmatrix} \begin{pmatrix} l & 1 & l' \\ 0 & 0 & 0 \end{pmatrix} \langle nl|er|n'l'\rangle .\end{aligned} \tag{B.5}$$

The angular and radial contributions [Paris-Mandoki *et al.*, 2016] are noted as

$$\mathcal{C}^q_{1,2} = (-1)^{j-m_j+s+j'+1} \begin{pmatrix} j & 1 & j' \\ -m_j & -q & m'_j \end{pmatrix} \tag{B.6a}$$

$$\tilde{\mu}_{1,2} = \sqrt{(2j+1)(2j'+1)(2l+1)(2l'+1)} \begin{Bmatrix} j & 1 & j' \\ l' & s & l \end{Bmatrix} \begin{pmatrix} l & 1 & l' \\ 0 & 0 & 0 \end{pmatrix} \mathcal{R}_{nl\to n'l'}. \tag{B.6b}$$

Therefore, the radial components $\tilde{\mu}_{nS_{1/2},n'P_{1/2}} = -\sqrt{\frac{2}{3}}\mathcal{R}_{n,0\to n',1}$ and $\tilde{\mu}_{nS_{1/2},n'P_{1/2}} = \frac{2}{\sqrt{3}}\mathcal{R}_{n,0\to n',1}$. For the nS-nP transitions broadly used along this thesis:

	$n = 42$	$n = 48$
$\mathcal{R}_{n,0\to n',1}$	$1733.7 \cdot ea_0$	$2339.5 \cdot ea_0$

Appendix C

Rate model for the evolution of populations

In order to reconstruct the magnetisation of the spin ensemble, complementary information about the fraction of detected population which does not belong to the $|\uparrow\rangle$ state is required, as discussed in Section 4.4. For such purpose, the decay rates of $|\downarrow\rangle$ and $|\uparrow\rangle$ to $|a\rangle$ and $|b\rangle$ are measured with additional experiments, as defined in Figure 4.5(b). In this appendix, the three-level rate equation model [Tsai and Morse, 1979; Zizak *et al.*, 1980] employed to quantify the redistribution of populations is described.

Analogous considerations are valid for $|\downarrow\rangle$ and $|\uparrow\rangle$, so only the evolution of $|\downarrow\rangle$ is explained. The notation employed refers to the total population in the states $|\downarrow\rangle$, $|\uparrow\rangle$, $|a\rangle$ and $|b\rangle$ as $N_\downarrow$, $N_\uparrow$, N_a and N_b populations, respectively. Populations decay with rates $\Gamma_{\downarrow a}$, $\Gamma_{\downarrow b}$ (from $|\downarrow\rangle$) and $\Gamma_{\uparrow a}$, $\Gamma_{\uparrow b}$ (from $|\uparrow\rangle$).

Additionally, second-order temporal redistribution of population between the states $|\downarrow\rangle$ is neglected. Thus, it is valid as $\frac{1}{\Gamma_{\downarrow a}}, \frac{1}{\Gamma_{\downarrow b}} \gg t$.

C.0.1 General dynamics

Experimental procedure to measure the spin populations $N_\downarrow$, $N_\uparrow$ and the magnetisation of the spin ensemble, M_z:

(i) Rydberg preparation pulse.

(ii) Spin-manipulation sequence with variable time t_{ev}.

(iii) Down-pumping pulse during a fixed time t_{dp}, selected at the steady state of experiment A.

After ionising the spin populations, all spin states above the ionisation threshold are detected, so

$$N_{meas}(t) = N_{\uparrow}(t) + N_a(t) = N_{\uparrow}(t) + N^*_{a(\uparrow)}(t) + N^*_{a(\downarrow)}(t) + N_{a\downarrow}(0), \tag{C.1}$$

where $N_{a(\uparrow)}$ and $N_{a(\downarrow)}$ are the populations from $|\downarrow\rangle$ and $|\uparrow\rangle$, respectively, decaying to $|a\rangle$. Terms labelled as $^{(*)}$ are to be weighted by the fraction of time the spin spends in the state $|\uparrow\rangle$ or $|\downarrow\rangle$. 50 % contribution from both spin states is assumed.

Therefore, spin-up population is subtracted as

$$N_{\uparrow}(t_{ev}) = N_{meas}(t_{ev}) - N_0 \cdot (\Gamma_{\uparrow a} + \Gamma_{\downarrow a}) \cdot t_{ev} - N_a(0) \tag{C.2}$$

To quantify $N_{\downarrow}$, the fraction of atoms decaying to $|b\rangle$ must be subtracted, as

$$N_{\downarrow}(t_{ev}) = N_0 - N_0 \frac{\Gamma_{\downarrow a} + \Gamma_{\downarrow b} + \Gamma_{\uparrow a} + \Gamma_{\uparrow b}}{2} t_{ev} - N_{\uparrow}(t_{ev}) \tag{C.3}$$

Hence, the magnetisation can be reconstructed as

$$M_z(t) = \frac{N_{\uparrow}(t) - N_{\downarrow}(t)}{2(N_{\uparrow}(t) + N_{\downarrow})(t)}. \tag{C.4}$$

C.0.2 Experiment A: Down-pumping

Experimental procedure to understand the redistribution of Rydberg states during a down-pumping experiment (Fig. C.1(a)):

(i) Rydberg preparation pulse.

(ii) Down-pumping pulse with variable time t_{dp}.

As the population decays, a residual amount of Rydberg atoms can be measured: $N_{res}(t_{dp}) = N_a(t_{dp}) + N_{\downarrow}(t_{dp})$.

The temporal evolution of the populations obey the following rate equations

$$\frac{dN_{\downarrow}}{dt} = -(\Gamma_{dp} + \Gamma_{\downarrow a} + \Gamma_{\downarrow b}) \cdot N_{\downarrow} \tag{C.5a}$$

$$\frac{dN_a}{dt} = \Gamma_{\downarrow a} \cdot N_{\downarrow} \tag{C.5b}$$

$$\frac{dN_b}{dt} = (\Gamma_{\downarrow b} + \Gamma_{dp}) \cdot N_{\downarrow}, \tag{C.5c}$$

where $\Gamma_{tot} = \Gamma_{dp} + \Gamma_{\downarrow a} + \Gamma_{\downarrow b}$.

Therefore, each individual population is integrated as

$$N_{\downarrow}(t_{dp}) = N_0 \cdot \exp(-\Gamma_{tot} t_{dp}) \tag{C.6a}$$

$$N_a(t_{dp}) = -N_0 \frac{\Gamma_{\downarrow a}}{\Gamma_{tot}} [\exp(-\Gamma_{tot} t_{dp}) - 1] + N_a(0) \tag{C.6b}$$

$$N_b(t_{dp}) = -N_0 \frac{\Gamma_{\downarrow b} + \Gamma_{dp}}{\Gamma_{tot}} [\exp(-\Gamma_{tot} t_{dp}) - 1] + N_b(0) \tag{C.6c}$$

$$N_{res}(t_{dp}) = N_{\downarrow}(0) \cdot \left[\exp(-\Gamma_{tot} t_{dp}) + \frac{\Gamma_{\downarrow a}}{\Gamma_{tot}} \big(1 - \exp(-\Gamma_{tot} t_{dp})\big) \right] + N_a(0), \tag{C.6d}$$

assuming initial Rydberg preparation $N_0 = N_{\downarrow}(0)$.

For large time, as $t_{dp} \to \infty$, the steady-state solutions describing the population in states above threshold and the residual measured populations are found to be

$$N_{\downarrow}(t_{dp} \to \infty) \approx 0 \tag{C.7a}$$

$$N_a(t_{dp} \to \infty) \approx \frac{\Gamma_{\downarrow a}}{\Gamma_{tot}} N_0 + N_a(0) \tag{C.7b}$$

$$N_b(t_{dp} \to \infty) \approx \frac{\Gamma_{\downarrow b} + \Gamma_{dp}}{\Gamma_{tot}} N_0 + N_b(0) \tag{C.7c}$$

$$N_{res}(t_{dp} \to \infty) \approx \frac{\Gamma_{\downarrow a}}{\Gamma_{tot}} N_0 + N_a(0). \tag{C.7d}$$

C.0.3 Experiment B: Redistribution to $|b\rangle$

Experimental procedure to understand the redistribution of Rydberg states to non-detected states $|b\rangle$ during the evolution time at which the dynamics occurs (Fig. C.1(b)):

(i) Rydberg preparation pulse.

(ii) Free evolution with variable time t_{ev}.

The temporal evolution of populations during t_{ev} follows the rate equations

$$\frac{dN_{\downarrow}}{dt} = -(\Gamma_{\downarrow a} + \Gamma_{\downarrow b}) \cdot N_{\downarrow} \tag{C.8a}$$

$$\frac{dN_a}{dt} = \Gamma_{\downarrow a} \cdot N_{\downarrow} \tag{C.8b}$$

$$\frac{dN_b}{dt} = \Gamma_{\downarrow b} \cdot N_{\downarrow}. \tag{C.8c}$$

Therefore, the populations present the temporal dependence

$$N_{\downarrow}(t_{ev}) = N_0 \cdot \exp[-(\Gamma_{\downarrow a} + \Gamma_{\downarrow b})t_{ev}] \tag{C.9a}$$

$$N_a(t_{ev}) = N_0 \frac{\Gamma_{\downarrow a}}{\Gamma_{\downarrow a} + \Gamma_{\downarrow b}} \big(1 - \exp[-(\Gamma_{\downarrow a} + \Gamma_{\downarrow b})t_{ev}]\big) + N_a(0) \tag{C.9b}$$

$$N_b(t_{ev}) = N_0 \frac{\Gamma_{\downarrow b}}{\Gamma_{\downarrow a} + \Gamma_{\downarrow b}} \big(1 - \exp[-(\Gamma_{\downarrow a} + \Gamma_{\downarrow b})t_{ev}]\big) + N_b(0) \tag{C.9c}$$

$$N_{res}(t_{ev}) = N_0 \frac{\Gamma_{\downarrow a}}{\Gamma_{\downarrow a} + \Gamma_{\downarrow b}} + N_0 \cdot \big(1 - \frac{\Gamma_{\downarrow a}}{\Gamma_{\downarrow a} + \Gamma_{\downarrow b}}\big) \cdot \exp[-(\Gamma_{\downarrow a} + \Gamma_{\downarrow b})t_{ev}] + N_a(0). \tag{C.9d}$$

Consequently, the first-order Taylor expansion in t_{ev} delivers

$$N_{\downarrow}(t_{ev}) = -N_0 \cdot (\Gamma_{\downarrow a} + \Gamma_{\downarrow b}) \cdot t_{ev} \tag{C.10a}$$

$$N_a(t_{ev}) = N_0 \frac{\Gamma_{\downarrow a}}{\Gamma_{\downarrow a} + \Gamma_{\downarrow b}} + N_0 \cdot \Gamma_{\downarrow a} \cdot t_{ev} + N_a(0) \tag{C.10b}$$

$$N_b(t_{ev}) = N_0 \frac{\Gamma_{\downarrow b}}{\Gamma_{\downarrow a} + \Gamma_{\downarrow b}} + N_0 \cdot \Gamma_{\downarrow b} \cdot t_{ev} + N_b(0) \tag{C.10c}$$

$$N_{res}(t_{ev}) = N_0 \frac{\Gamma_{\downarrow a}}{\Gamma_{\downarrow a} + \Gamma_{\downarrow b}} - N_0 \cdot \Gamma_{\downarrow b} \cdot t_{ev} + N_a(0). \tag{C.10d}$$

C.0.4 Experiment C: Redistribution to $|a\rangle$

Experimental procedure to measure the redistribution of Rydberg spins to detectable states above the ionisation threshold, $|a\rangle$. It requires to combine the experiments from appendices (C.0.3, C.0.2), as observed in Figure C.1(c):

(i) Rydberg preparation pulse.

(ii) Free evolution with variable time t_{ev}.

(iii) Down-pumping pulse during a fixed time t_{dp}, selected at the steady state of experiment A.

Hence, the rate equations which describe the evolution of such experiment are identical to those from Eq. (C.5). Nevertheless, the initial state is given by the

output from Eq. (C.9). Thus,

$$N_{\downarrow}(t_{ev}+t_{dp}) = N_{\downarrow}(t_{ev})\cdot \exp(-\Gamma_{tot}t_{dp}) \tag{C.11a}$$

$$N_{a}(t_{ev}+t_{dp}) = -N_{\downarrow}(t_{ev})\frac{\Gamma_{\downarrow a}}{\Gamma_{tot}}[\exp(-\Gamma_{tot}t_{dp})-1] + N_{a}(t_{ev}) \tag{C.11b}$$

$$N_{b}(t_{ev}+t_{dp}) = -N_{\downarrow}(t_{ev})\frac{\Gamma_{\downarrow b}+\Gamma_{dp}}{\Gamma_{tot}}[\exp(-\Gamma_{tot}t_{dp})-1] + N_{b}(t_{ev}) \tag{C.11c}$$

$$N_{res}(t_{ev}+t_{dp}) = N_{\downarrow}(t_{ev})\cdot\left[\exp(-\Gamma_{tot}t_{dp}) + \frac{\Gamma_{\downarrow a}}{\Gamma_{tot}}\big(1-\exp(-\Gamma_{tot}t_{dp})\big)\right] + N_{a}(t_{ev}). \tag{C.11d}$$

Analogously, the Taylor-expanded steady-state solutions are described as

$$N_{\downarrow}(t_{ev}, t_{dp}\to\infty) \approx 0 \tag{C.12a}$$

$$N_{a}(t_{ev}, t_{dp}\to\infty) \approx N_{0}\left[\left(\Gamma_{\downarrow a} - \frac{\Gamma_{\downarrow a}}{\Gamma_{tot}}(\Gamma_{\downarrow a}+\Gamma_{\downarrow b})t_{ev}\right)t_{ev} + \frac{\Gamma_{\downarrow a}}{\Gamma_{\downarrow a}+\Gamma_{\downarrow b}}\right] + N_{a}(0) \tag{C.12b}$$

$$N_{b}(t_{ev}, t_{dp}\to\infty) \approx N_{0}\left[\left(\Gamma_{\downarrow b} - \frac{\Gamma_{\downarrow b}+\Gamma_{dp}}{\Gamma_{tot}}(\Gamma_{\downarrow a}+\Gamma_{\downarrow b})t_{ev}\right)t_{ev} + \frac{\Gamma_{\downarrow b}}{\Gamma_{\downarrow a}+\Gamma_{\downarrow b}}\right] + N_{b}(0) \tag{C.12c}$$

$$N_{res}(t_{ev}, t_{dp}\to\infty) \approx N_{a}(t_{ev}, t_{dp}\to\infty). \tag{C.12d}$$

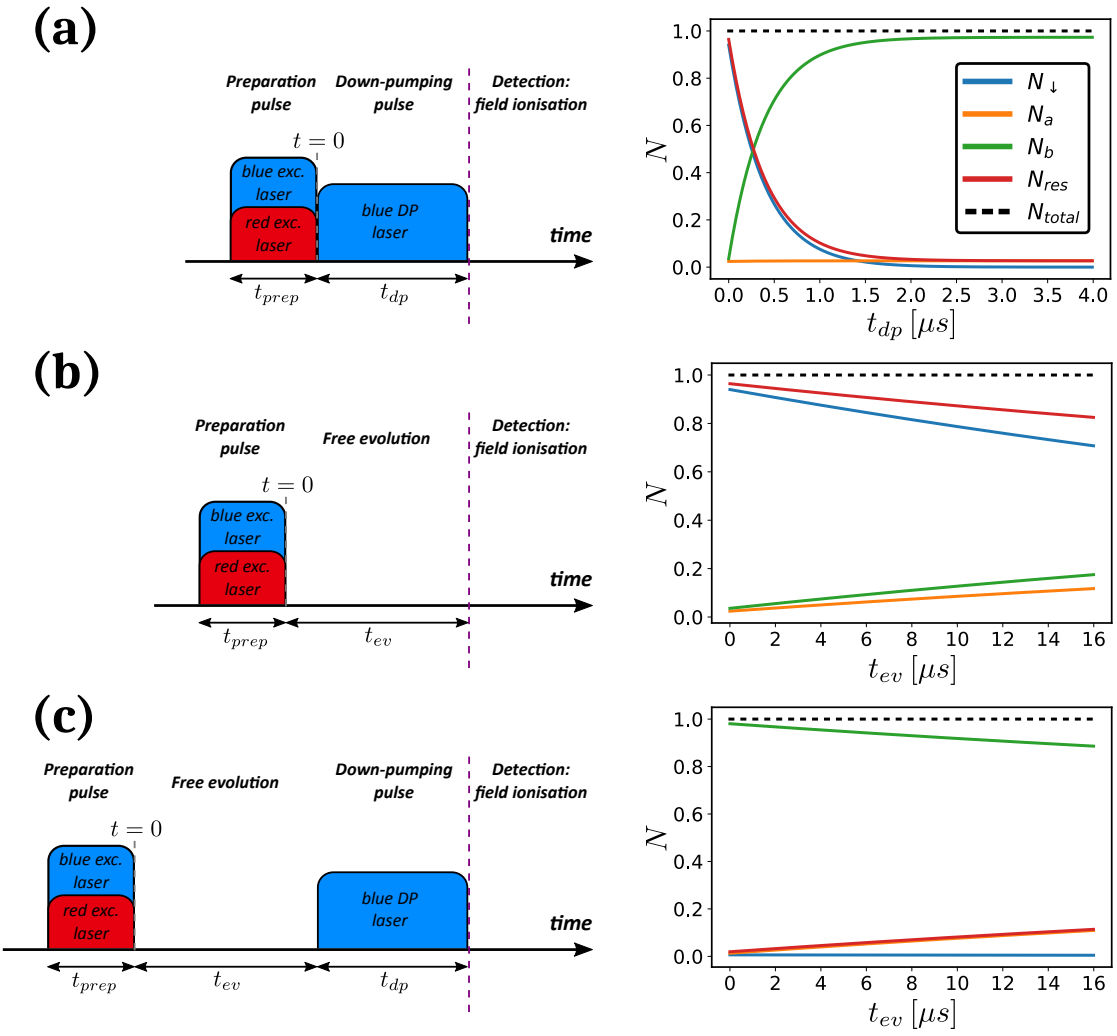

Figure C.1: Rate equation description for the redistribution of $|\downarrow\rangle$ Rydberg spins to experimentally ionised $|a\rangle$ and non-ionised $|b\rangle$ states. (a) Down-pumping characterisation (Eq. (C.6)). After the experimental preparation of $|\downarrow\rangle$ states, a coupling blue laser pumps the $N_\downarrow$ population to a fast-decaying state (see Fig. [3.15]) below the ionisation threshold, increasing N_b. Down-pumping rate $\Gamma_{dp} = 2.5\,\mathrm{MHz}$. The steady-state is achieved at $t_{dp} \approx 2\,\mu\mathrm{s}$, with detected population $N_{res} \approx N_a$. **(b)** Characterisation of decay to states below the ionisation threshold, $|b\rangle$ (Eq. (C.9)). The population in the initially prepared state freely evolves from $|\downarrow\rangle$ towards $|a\rangle$ and $|b\rangle$ with rates $\Gamma_{\downarrow a}$, $\Gamma_{\downarrow b}$. The depletion of detected population N_{res} is equivalent to the increase of N_b, allowing for experimental measurement of $\Gamma_{\downarrow b}$. **(c)** Characterisation of decay to states above the ionisation threshold, $|a\rangle$. After **(b)**, the remaining $N_\downarrow$ population is depleted by means of a $2\,\mu\mathrm{s}$ down-pumping pulse. Therefore, N_{res} evolves in accordance to $\Gamma_{\downarrow b}$ (Eq. (C.11d)). Simulations consider an initial fraction $N_\downarrow(0) = 0.94$ atoms in $|\downarrow\rangle$, whereas the remaining $6\,\%$ is distributed amongst $|a\rangle$ and $|b\rangle$, proportionally to the decay fraction to each of those states. Decay rates selected for the first-order transitions from $|\downarrow\rangle = |48S_{1/2}\rangle$: $\Gamma_{\downarrow a} = 7.1345\,\mathrm{kHz}$, $\Gamma_{\downarrow b} = 10.6288\,\mathrm{kHz}$.

Bibliography

Afrousheh, K., Bohlouli-Zanjani, P., Carter, J. D., Mugford, A., and Martin, J. D. D. (2006a). *Resonant electric dipole-dipole interactions between cold Rydberg atoms in a magnetic field.* Phys. Rev. A, **73**, 063403.

Afrousheh, K., Bohlouli-Zanjani, P., Petrus, J. A., and Martin, J. D. D. (2006b). *Determination of the ^{85}Rb ng-series quantum defect by electric-field-induced resonant energy transfer between cold Rydberg atoms.* Phys. Rev. A, **74**, 062712.

Afrousheh, K., Bohlouli-Zanjani, P., Vagale, D., Mugford, A., Fedorov, M., and Martin, J. D. D. (2004). *Spectroscopic Observation of Resonant Electric Dipole-Dipole Interactions between Cold Rydberg Atoms.* Phys. Rev. Lett., **93**, 233001.

Aikawa, K., Kobayashi, J., Oasa, K., Kishimoto, T., Ueda, M., and Inouye, S. (2011). *Narrow-linewidth light source for a coherent Raman transfer of ultracold molecules.* Opt. Express, **19**, 14479.

Amthor, T., Reetz-Lamour, M., Westermann, S., Denskat, J., and Weidemüller, M. (2007). *Mechanical Effect of van der Waals Interactions Observed in Real Time in an Ultracold Rydberg Gas.* Phys. Rev. Lett., **98**, 023004.

Anderson, D. A., Miller, S. A., and Raithel, G. (2014). *Photoassociation of Long-Range nD Rydberg Molecules.* Phys. Rev. Lett., **112**, 163201.

Anderson, D. A., Miller, S. A., Raithel, G., Gordon, J. A., Butler, M. L., and Holloway, C. L. (2016). *Optical Measurements of Strong Microwave Fields with Rydberg Atoms in a Vapor Cell.* Phys. Rev. Applied, **5**, 034003.

Anderson, M. H., Ensher, J. R., Matthews, M. R., Wieman, C. E., and Cornell, E. A. (1995). *Observation of Bose-Einstein Condensation in a Dilute Atomic Vapor.* Science, **269**, 198.

Anderson, W., Veale, J., and Gallagher, T. (1998). *Resonant dipole-dipole energy transfer in a nearly frozen Rydberg gas.* Phys. Rev. Lett., **80**, 249.

Anderson, W. R., Robinson, M. P., Martin, J. D. D., and Gallagher, T. F. (2002). *Dephasing of resonant energy transfer in a cold Rydberg gas.* Phys. Rev. A, **65**, 063404.

Angström, A. J. (1855). *XLVIII. Optical researches.* Philosophical Magazine, **9**, 327.

Ashkin, A. (1978). *Trapping of Atoms by Resonance Radiation Pressure.* Phys. Rev. Lett., **40**, 729.

Ates, C., Sevinçli, S., and Pohl, T. (2011). *Electromagnetically induced transparency in strongly interacting Rydberg gases.* Phys. Rev. A, **83**, 041802.

Balmer, J. J. (1885). *Notiz über die Spectrallinien des Wasserstoffs.* Annalen der Physik, **261**, 80.

Barredo, D., Labuhn, H., Ravets, S., Lahaye, T., Browaeys, A., and Adams, C. S. (2015). *Coherent Excitation Transfer in a Spin Chain of Three Rydberg Atoms.* Phys. Rev. Lett., **114**, 113002.

Barredo, D., Ravets, S., Labuhn, H., Béguin, L., Vernier, A., Nogrette, F., Lahaye, T., and Browaeys, A. (2014). *Demonstration of a Strong Rydberg Blockade in Three-Atom Systems with Anisotropic Interactions.* Phys. Rev. Lett., **112**, 183002.

Barreiro, J. T., Muller, M., Schindler, P., Nigg, D., Monz, T., Chwalla, M., Hennrich, M., Roos, C. F., Zoller, P., and Blatt, R. (2011). *An open-system quantum simulator with trapped ions.* Nature, **470**, 486.

Bartenstein, M., Altmeyer, A., Riedl, S., Jochim, S., Chin, C., Denschlag, J. H., and Grimm, R. (2004). *Crossover from a Molecular Bose-Einstein Condensate to a Degenerate Fermi Gas.* Phys. Rev. Lett., **92**, 120401.

Baur, S., Tiarks, D., Rempe, G., and Dürr, S. (2014). *Single-Photon Switch Based on Rydberg Blockade.* Phys. Rev. Lett., **112**, 073901.

Bendkowsky, V., Butscher, B., Nipper, J., Shaffer, J. P., Löw, R., and Pfau, T. (2009). *Observation of ultralong-range Rydberg molecules.* Nature, **458**, 1005 .

Bernien, H., Schwartz, S., Keesling, A., Levine, H., Omran, A., Pichler, H., Choi, S., Zibrov, A. S., Endres, M., Greiner, M., Vuletić, V., and Lukin, M. D. (2017). *Probing many-body dynamics on a 51-atom quantum simulator.* ArXiv e-prints.

Beterov, I. I., Ryabtsev, I. I., Tretyakov, D. B., and Entin, V. M. (2009). *Quasiclassical calculations of blackbody-radiation-induced depopulation rates and effective lifetimes of Rydberg nS, nP, and nD alkali-metal atoms with n <= 80.* Phys. Rev. A, **79**, 052504.

Bethe, H. (1931). *Zur Theorie der Metalle.* Zeitschrift für Physik, **71**, 205.

Bettelli, S., Maxwell, D., Fernholz, T., Adams, C. S., Lesanovsky, I., and Ates, C. (2013). *Exciton dynamics in emergent Rydberg lattices.* Phys. Rev. A, **88**, 043436.

Bigelow, J. L., Paul, J. T., Peleg, M., Sanford, V. L., Carroll, T. J., and Noel, M. W. (2016). *Simulations of the angular dependence of the dipole–dipole interaction among Rydberg atoms.* Journal of Physics B: Atomic, Molecular and Optical Physics, **49**, 164003.

Black, E. D. (2001). *An introduction to Pound-Drever-Hall laser frequency stabilization.* American Journal of Physics, **69**, 79.

Blatt, R. and Roos, C. F. (2012). *Quantum simulations with trapped ions.* Nat Phys, **8**, 277.

Bloch, I., Dalibard, J., and Nascimbène, S. (2012). *Quantum simulations with ultracold quantum gases.* Nature Physics, **8**, 267.

Bloch, I., Dalibard, J., and Zwerger, W. (2008). *Many-body physics with ultracold gases.* Rev. Mod. Phys., **80**, 885.

Blum, K. (2012). *Density Matrix Theory and Applications*, Vol. 64 of *Springer Series on Atomic, Optical, and Plasma Physics.* Springer-Verlag Berlin Heidelberg. 3 edition.

Bochmann, J., Mücke, M., Guhl, C., Ritter, S., Rempe, G., and Moehring, D. L. (2010). *Lossless State Detection of Single Neutral Atoms.* Phys. Rev. Lett., **104**, 203601.

Bohnet, J. G., Sawyer, B. C., Britton, J. W., Wall, M. L., Rey, A. M., Foss-Feig, M., and Bollinger, J. J. (2016). *Quantum spin dynamics and entanglement generation with hundreds of trapped ions.* Science, **352**, 1297.

Bohr, N. (1913). *I. On the constitution of atoms and molecules.* Philosophical Magazine, **26**, 1.

Bowman, D., Ireland, P., Bruce, G. D., and Cassettari, D. (2015). *Multi-wavelength holography with a single spatial light modulator for ultracold atom experiments*. Opt. Express, **23**, 8365.

Bradley, C. C., Sackett, C. A., Tollett, J. J., and Hulet, R. G. (1995). *Evidence of Bose-Einstein Condensation in an Atomic Gas with Attractive Interactions*. Phys. Rev. Lett., **75**, 1687.

Branden, D. B., Juhasz, T., Mahlokozera, T., Vesa, C., Wilson, R. O., Zheng, M., Kortyna, A., and Tate, D. A. (2010). *Radiative lifetime measurements of rubidium Rydberg states*. Journal of Physics B: Atomic, Molecular and Optical Physics, **43**, 015002.

Breit, G. and Rabi, I. I. (1931). *Measurement of Nuclear Spin*. Phys. Rev., **38**, 2082.

Brion, E., Pedersen, L. H., and Mølmer, K. (2007). *Adiabatic elimination in a lambda system*. Journal of Physics A: Mathematical and Theoretical, **40**, 1033.

Britton, J. W., Sawyer, B. C., Keith, A. C., Wang, C.-C. J., Freericks, J. K., Uys, H., Biercuk, M. J., and Bollinger, J. J. (2012). *Engineered two-dimensional Ising interactions in a trapped-ion quantum simulator with hundreds of spins*. Nature, **484**, 489.

Browaeys, A., Barredo, D., and Lahaye, T. (2016). *Experimental investigations of dipole–dipole interactions between a few Rydberg atoms*. Journal of Physics B: Atomic, Molecular and Optical Physics, **49**, 152001.

Buluta, I. and Nori, F. (2009). *Quantum Simulators*. Science, **326**, 108.

Busche, H., Huillery, P., Ball, S. W., Ilieva, T., Jones, M. P. A., and Adams, C. S. (2017). *Contactless nonlinear optics mediated by long-range Rydberg interactions*. Nat Phys, **13**, 655.

Butscher, B., Nipper, J., Balewski, J. B., Kukota, L., Bendkowsky, V., Low, R., and Pfau, T. (2010). *Atom-molecule coherence for ultralong-range Rydberg dimers*. Nature Physics, **6**, 970.

Carroll, T. J., Claringbould, K., Goodsell, A., Lim, M. J., and Noel, M. W. (2004). *Angular dependence of the dipole-dipole interaction in a nearly one-dimensional sample of Rydberg atoms*. Phys. Rev. Lett., **93**, 2.

Carter, J. D. and Martin, J. D. D. (2013). *Coherent manipulation of cold Rydberg atoms near the surface of an atom chip.* Phys. Rev. A, **88**, 043429.

Cheng, C. H., Lee, C. Y., and Gallagher, T. F. (1994). *Production of Circular Rydberg States with Circularly Polarized Microwave Fields.* Phys. Rev. Lett., **73**, 3078.

Choi, J.-H., Knuffman, B., Liebisch, T. C., Reinhard, A., and Raithel, G. (2006). *Cold Rydberg Atoms.* Vol. 54 of *ADVANCES IN ATOMIC, MOLECULAR AND OPTICAL PHYSICS*, , pp. 131–202. Academic Press.

Choi, S., Choi, J., Landig, R., Kucsko, G., Zhou, H., Isoya, J., Jelezko, F., Onoda, S., Sumiya, H., Khemani, V., von Keyserlingk, C., Yao, N. Y., Demler, E., and Lukin, M. D. (2017). *Observation of discrete time-crystalline order in a disordered dipolar many-body system.* Nature, **543**, 221.

Clément, J.-F., Brantut, J.-P., Robert-de Saint-Vincent, M., Nyman, R. A., Aspect, A., Bourdel, T., and Bouyer, P. (2009). *All-optical runaway evaporation to Bose-Einstein condensation.* Phys. Rev. A, **79**, 061406.

Comparat, D. and Pillet, P. (2010). *Dipole blockade in a cold Rydberg atomic sample.* J. Opt. Soc. Am. B, **27**, A208.

Cowan, G. (1998). *Statistical data analysis.* Oxford University Press.

Cubel, T., Teo, B. K., Malinovsky, V. S., Guest, J. R., Reinhard, A., Knuffman, B., Berman, P. R., and Raithel, G. (2005). *Coherent population transfer of ground-state atoms into Rydberg states.* Phys. Rev. A, **72**, 023405.

Davis, K. B., Mewes, M. O., Andrews, M. R., van Druten, N. J., Durfee, D. S., Kurn, D. M., and Ketterle, W. (1995). *Bose-Einstein Condensation in a Gas of Sodium Atoms.* Phys. Rev. Lett., **75**, 3969.

Debnath, S., Linke, N. M., Figgatt, C., Landsman, K. A., Wright, K., and Monroe, C. (2016). *Demonstration of a small programmable quantum computer with atomic qubits.* Nature, **536**, 63.

Deiglmayr, J., Reetz-Lamour, M., Amthor, T., Westermann, S., de Oliveira, A., and Weidemüller, M. (2006). *Coherent excitation of Rydberg atoms in an ultracold gas.* Optics Communications, **264**, 293 .

DeMarco, B. and Jin, D. S. (1999). *Onset of Fermi Degeneracy in a Trapped Atomic Gas.* Science, **285**, 1703.

DeSalvo, B. J., Aman, J. A., Gaul, C., Pohl, T., Yoshida, S., Burgdörfer, J., Hazzard, K. R. A., Dunning, F. B., and Killian, T. C. (2016). *Rydberg-blockade effects in Autler-Townes spectra of ultracold strontium.* Phys. Rev. A, **93**, 022709.

Dieckmann, K., Spreeuw, R. J. C., Weidemüller, M., and Walraven, J. T. M. (1998). *Two-dimensional magneto-optical trap as a source of slow atoms.* Phys. Rev. A, **58**, 3891.

Dudin, Y. O., Li, L., Bariani, F., and Kuzmich, A. (2012). *Observation of coherent many-body Rabi oscillations.* Nature Physics, **8**, 790.

Efron, B. and Tibshirani, R. (1994). *An Introduction to the Bootstrap.* Chapman & Hall/CRC Monographs on Statistics & Applied Probability. Taylor & Francis.

Ernst, R. R. (1992). *Nuclear Magnetic Resonance Fourier Transform Spectroscopy (Nobel Lecture).* Angewandte Chemie International Edition in English, **31**, 805.

Fahey, D. P., Carroll, T. J., and Noel, M. W. (2015). *Imaging the dipole-dipole energy exchange between ultracold rubidium Rydberg atoms.* Phys. Rev. A, **91**, 062702.

Fano, U. (1961). *Effects of Configuration Interaction on Intensities and Phase Shifts.* Phys. Rev., **124**, 1866.

Feynman, R., Hollingsworth, J., Vennettilli, M., Budner, T., Zmiewski, R., Fahey, D. P., Carroll, T. J., and Noel, M. W. (2015). *Quantum interference in the field ionization of Rydberg atoms.* Phys. Rev. A, **92**, 043412.

Feynman, R. P. (1982). *Simulating physics with computers.* International Journal of Theoretical Physics, **21**, 467.

Firstenberg, O., Adams, C. S., and Hofferberth, S. (2016). *Nonlinear quantum optics mediated by Rydberg interactions.* Journal of Physics B: Atomic, Molecular and Optical Physics, **49**, 152003.

Firstenberg, O., Peyronel, T., Liang, Q.-Y., Gorshkov, A. V., Lukin, M. D., and Vuletic, V. (2013). *Attractive photons in a quantum nonlinear medium.* Nature, **502**, 71.

Fleischhauer, M., Imamoglu, A., and Marangos, J. P. (2005). *Electromagnetically induced transparency: Optics in coherent media.* Rev. Mod. Phys., **77**, 633.

Gaëtan, A., Miroshnychenko, Y., Wilk, T., Chotia, A., Viteau, M., Comparat, D., Pillet, P., Browaeys, A., and Grangier, P. (2009). *Observation of collective excitation of two individual atoms in the Rydberg blockade regime.* Nature Physics, **5**, 115.

Gaj, A., Krupp, A. T., Balewski, J. B .and Löw, R., Hofferberth, S., and Pfau, T. (2014). *From molecular spectra to a density shift in dense Rydberg gases.* Nature Communications, **5**, 4546.

Gallagher, T. F. (1994). *Rydberg Atoms.* Cambridge University Press.

Gallagher, T. F. and Cooke, W. E. (1979). *Interactions of Blackbody Radiation with Atoms.* Phys. Rev. Lett., **42**, 835.

Gallagher, T. F. and Pillet, P. (2008). *Dipole-Dipole Interactions of Rydberg Atoms.* In: et al, A. (Ed.), *Advances in Atomic, Molecular, and Optical Physics*, Vol. 56 of *Advances In Atomic, Molecular, and Optical Physics*, , pp. 161 – 218. Academic Press.

Gallagher, T. F., Safinya, K. A., Gounand, F., Delpech, J. F., Sandner, W., and Kachru, R. (1982). *Resonant Rydberg-atom–Rydbert-atom collisions.* Phys. Rev. A, **25**, 1905.

García-Ripoll, J. J., Zoller, P., and Cirac, J. I. (2005). *Quantum information processing with cold atoms and trapped ions.* Journal of Physics B: Atomic, Molecular and Optical Physics, **38**, S567.

Gärttner, M. and Evers, J. (2013). *Nonlinear absorption and density-dependent dephasing in Rydberg electromagnetically-induced-transparency media.* Phys. Rev. A, **88**, 033417.

Gärttner, M., Whitlock, S., Schönleber, D. W., and Evers, J. (2014). *Semianalytical model for nonlinear absorption in strongly interacting Rydberg gases.* Phys. Rev. A, **89**, 063407.

Gavryusev, V. (2016). *Imaging of Rydberg Impurities in an Ultracold Atomic Gas.* PhD thesis, Fakultat fur Physik, Ruprecht-Karls-Universität Heidelberg.

Gavryusev, V., Ferreira-Cao, M., Kekić, A., Zürn, G., and Signoles, A. (2016a). *Interaction Enhanced Imaging of Rydberg P states.* The European Physical Journal Special Topics, **225**, 2863.

Gavryusev, V., Signoles, A., Ferreira-Cao, M., Zürn, G., Hofmann, C. S., Günter, G., Schempp, H., de Saint-Vincent, M. R., Whitlock, S., and Weidemüller, M. (2016b). *Density matrix reconstruction of three-level atoms via Rydberg electromagnetically induced transparency.* Journal of Physics B: Atomic, Molecular and Optical Physics, **49**, 164002.

Geier, S. (2016). *Microwave control of the quantum state in a Rydberg spin-1/2 system.* Master's thesis, University of Heidelberg.

Georgescu, I. M., Ashhab, S., and Nori, F. (2014). *Quantum simulation.* Rev. Mod. Phys., **86**, 153.

Geva, E., Kosloff, R., and Skinner, J. L. (1995). *On the relaxation of a two-level system driven by a strong electromagnetic field.* The Journal of Chemical Physics, **102**, 8541.

Glaetzle, A. W., Dalmonte, M., Nath, R., Gross, C., Bloch, I., and Zoller, P. (2015). *Designing Frustrated Quantum Magnets with Laser-Dressed Rydberg Atoms.* Phys. Rev. Lett., **114**, 173002.

Goldschmidt, E. A., Boulier, T., Brown, R. C., Koller, S. B., Young, J. T., Gorshkov, A. V., Rolston, S. L., and Porto, J. V. (2016). *Anomalous Broadening in Driven Dissipative Rydberg Systems.* Phys. Rev. Lett., **116**, 113001.

Golter, D. A. and Wang, H. (2014). *Optically Driven Rabi Oscillations and Adiabatic Passage of Single Electron Spins in Diamond.* Phys. Rev. Lett., **112**, 116403.

Gorniaczyk, H., Tresp, C., Schmidt, J., Fedder, H., and Hofferberth, S. (2014). *Single-Photon Transistor Mediated by Interstate Rydberg Interactions.* Phys. Rev. Lett., **113**, 053601.

Goy, P., Raimond, J. M., Vitrant, G., and Haroche, S. (1982). *Millimeter-wave spectroscopy in cesium Rydberg states. Quantum defects, fine- and hyperfine-structure measurements.* Phys. Rev. A, **26**, 2733.

Gregory, P. D., Molony, P. K., Köppinger, M. P., Kumar, A., Ji, Z., Lu, B., Marchant, A. L., and Cornish, S. L. (2015). *A simple, versatile laser system*

for the creation of ultracold ground state molecules. New Journal of Physics, **17**, 055006.

Greiner, M., Mandel, O., Esslinger, T., Hänsch, T. W., and Bloch, I. (2002). *Quantum phase transition from a superfluid to a Mott insulator in a gas of ultracold atoms.* Nature, **415**, 39.

Greiner, M., Regal, C. A., and Jin, D. S. (2003). *Emergence of a molecular Bose-Einstein condensate from a Fermi gas.* Nature, **426**, 537.

Grimm, R., Weidemüller, M., and Ovchinnikov, Y. B. (2000). *Optical Dipole Traps for Neutral Atoms.* Vol. 42 of *Advances In Atomic, Molecular, and Optical Physics*, , pp. 95 – 170. Academic Press.

Grimmel, J., Mack, M., Karlewski, F., Jessen, F., Reinschmidt, M., Sándor, N., and Fortágh, J. (2015). *Measurement and numerical calculation of Rubidium Rydberg Stark spectra.* New Journal of Physics, **17**, 053005.

Günter, G. (2014). *Interfacing Rydberg atoms with light and observing their interaction driven dynamics.* PhD thesis, Fakultat fur Physik, Ruprecht-Karls-Universität Heidelberg.

Günter, G., Robert-de Saint-Vincent, M., Schempp, H., Hofmann, C. S., Whitlock, S., and Weidemüller, M. (2012). *Interaction Enhanced Imaging of Individual Rydberg Atoms in Dense Gases.* Phys. Rev. Lett., **108**, 013002.

Günter, G., Schempp, H., Robert-de Saint-Vincent, M., Gavryusev, V., Helmrich, S., Hofmann, C. S., Whitlock, S., and Weidemüller, M. (2013). *Observing the Dynamics of Dipole-Mediated Energy Transport by Interaction-Enhanced Imaging.* Science, **342**, 954.

Hagen, J. B. (2000). *Radio-Frequency Electronics: Circuits and Applications.* Cambridge University Press.

Hahn, E. L. (1950). *Spin Echoes.* Phys. Rev., **80**, 580.

Han, J., Jamil, Y., Norum, D. V., Tanner, P. J., and Gallagher, T. F. (2006). *Rb nf quantum defects from millimeter-wave spectroscopy of cold $\hat{8}5$Rb Rydberg atoms.* Phys. Rev. A, **74**, 054502.

Han, J., Vogt, T., and Li, W. (2016). *Spectral shift and dephasing of electromagnetically induced transparency in an interacting Rydberg gas.* Phys. Rev. A, **94**, 043806.

Han, J., Vogt, T., Manjappa, M., Guo, R., Kiffner, M., and Li, W. (2015). *Lensing effect of electromagnetically induced transparency involving a Rydberg state.* Phys. Rev. A, **92**, 063824.

Hankin, A. M., Jau, Y.-Y., Parazzoli, L. P., Chou, C. W., Armstrong, D. J., Landahl, A. J., and Biedermann, G. W. (2014). *Two-atom Rydberg blockade using direct 6S to nP excitation.* Phys. Rev. A, **89**, 033416.

Harris, S. E. (1997). *Electromagnetically Induced Transparency.* Physics Today, **50**, 36.

Hatanaka, H. and Hashi, T. (1978). *Spin-locking, spin-locked echo and rotary saturation associated with a two-quantum transition in a multilevel NMR system.* Physics Letters A, **67**, 183 .

Hauke, P., Cucchietti, F. M., Tagliacozzo, L., Deutsch, I., and Lewenstein, M. (2012). *Can one trust quantum simulators?* Reports on Progress in Physics, **75**, 082401.

Hazzard, K. R. A., Gadway, B., Foss-Feig, M., Yan, B., Moses, S. A., Covey, J. P., Yao, N. Y., Lukin, M. D., Ye, J., Jin, D. S., and Rey, A. M. (2014a). *Many-Body Dynamics of Dipolar Molecules in an Optical Lattice.* Phys. Rev. Lett., **113**, 195302.

Hazzard, K. R. A., Manmana, S. R., Foss-Feig, M., and Rey, A. M. (2013). *Far-from-Equilibrium Quantum Magnetism with Ultracold Polar Molecules.* Phys. Rev. Lett., **110**, 075301.

Hazzard, K. R. A., van den Worm, M., Foss-Feig, M., Manmana, S. R., Dalla Torre, E. G., Pfau, T., Kastner, M., and Rey, A. M. (2014b). *Quantum correlations and entanglement in far-from-equilibrium spin systems.* Phys. Rev. A, **90**, 063622.

Heidemann, R., Raitzsch, U., Bendkowsky, V., Butscher, B., Löw, R., Santos, L., and Pfau, T. (2007). *Evidence for Coherent Collective Rydberg Excitation in the Strong Blockade Regime.* Phys. Rev. Lett., **99**, 163601.

Heisenberg, W. (1928). *Zur Theorie des Ferromagnetismus.* Zeitschrift für Physik, **49**, 619.

Helmrich, S. (2013). *Improving optical resolution by noise correlation analysis.* Master's thesis, Fakultat fur Physik, Ruprecht-Karls-Universität Heidelberg.

Helmrich, S., Arias, A., Pehoviak, N., and Whitlock, S. (2016). *Two-body interactions and decay of three-level Rydberg-dressed atoms.* Journal of Physics B: Atomic, Molecular and Optical Physics, **49**, 03LT02.

Hermann-Avigliano, C., Teixeira, R. C., Nguyen, T. L., Cantat-Moltrecht, T., Nogues, G., Dotsenko, I., Gleyzes, S., Raimond, J. M., Haroche, S., and Brune, M. (2014). *Long coherence times for Rydberg qubits on a superconducting atom chip.* Phys. Rev. A, **90**, 040502.

Hofmann, C., Günter, G., Schempp, H., Müller, N., Faber, A., Busche, H., Robert-de Saint-Vincent, M., Whitlock, S., and Weidemüller, M. (2014). *An experimental approach for investigating many-body phenomena in Rydberg-interacting quantum systems.* Frontiers of Physics, **9**, 571.

Hofmann, C. S. (2013). *Emergence of correlations in strongly interacting ultracold Rydberg gases.* PhD thesis, Fakultat fur Physik, Ruprecht-Karls-Universität Heidelberg.

Hofmann, C. S., Günter, G., Schempp, H., Robert-de Saint-Vincent, M., Gärttner, M., Evers, J., Whitlock, S., and Weidemüller, M. (2013). *Sub-Poissonian Statistics of Rydberg-Interacting Dark-State Polaritons.* Phys. Rev. Lett., **110**, 203601.

Hofstetter, W., Cirac, J. I., Zoller, P., Demler, E., and Lukin, M. D. (2002). *High-Temperature Superfluidity of Fermionic Atoms in Optical Lattices.* Phys. Rev. Lett., **89**, 220407.

Holloway, C. L., Gordon, J. A., Jefferts, S., Schwarzkopf, A., Anderson, D. A., Miller, S. A., Thaicharoen, N., and Raithel, G. (2014). *Broadband Rydberg Atom-Based Electric-Field Probe for SI-Traceable, Self-Calibrated Measurements.* IEEE Transactions on Antennas and Propagation, **62**, 6169.

Isenhower, L., Urban, E., Zhang, X. L., Gill, A. T., Henage, T., Johnson, T. A., Walker, T. G., and Saffman, M. (2010). *Demonstration of a Neutral Atom Controlled-NOT Quantum Gate.* Phys. Rev. Lett., **104**, 010503.

Ithier, G., Collin, E., Joyez, P., Meeson, P. J., Vion, D., Esteve, D., Chiarello, F., Shnirman, A., Makhlin, Y., Schriefl, J., and Schön, G. (2005). *Decoherence in a superconducting quantum bit circuit.* Phys. Rev. B, **72**, 134519.

Jaksch, D., Bruder, C., Cirac, J. I., Gardiner, C. W., and Zoller, P. (1998). *Cold Bosonic Atoms in Optical Lattices.* Phys. Rev. Lett., **81**, 3108.

Jaksch, D., Cirac, J. I., Zoller, P., Rolston, S. L., Côté, R., and Lukin, M. D. (2000). *Fast Quantum Gates for Neutral Atoms.* Phys. Rev. Lett., **85**, 2208.

Jastrow, R. (1948). *On the Rydberg-Ritz Formula in Quantum Mechanics.* Phys. Rev., **73**, 60.

Jeys, T. H., McMillian, G. B., Smith, K. A., Dunning, F. B., and Stebbings, R. F. (1982). *Electric field ionization of highly excited sodium* nd *atoms.* Phys. Rev. A, **26**, 335.

Ketterle, W., Durfee, D. S., and Stamper-Kurn, D. M. (1999). *Making, probing and understanding Bose-Einstein condensates.* In: M. Inguscio, S. S. and Wieman, C. (Eds.), *Bose-Einstein condensation in atomic gases*, Proceedings of the International School of Physics "Enrico Fermi", Course CXL, , pp. 67 – 176. IOS Press, Amsterdam.

Kielpinski, D., Monroe, C., and Wineland, D. J. (2002). *Architecture for a large-scale ion-trap quantum computer.* Nature, **417**, 709.

Killian, T. C., Pattard, T., Pohl, T., and Rost, J. M. (2007). *Ultracold Neutral Plasmas.* Physics Reports, **449**, 77.

Köhl, M., Moritz, H., Stöferle, T., Günter, K., and Esslinger, T. (2005). *Fermionic Atoms in a Three Dimensional Optical Lattice: Observing Fermi Surfaces, Dynamics, and Interactions.* Phys. Rev. Lett., **94**, 080403.

Labuhn, H., Barredo, D., Ravets, S., de Léséleuc, S., Macrì, T., Lahaye, T., and Browaeys, A. (2016). *Tunable two-dimensional arrays of single Rydberg atoms for realizing quantum Ising models.* Nature, **534**, 667.

Labuhn, H., Ravets, S., Barredo, D., Béguin, L., Nogrette, F., Lahaye, T., and Browaeys, A. (2014). *Single-atom addressing in microtraps for quantum-state engineering using Rydberg atoms.* Phys. Rev. A, **90**, 023415.

Lesanovsky, I. (2011). *Many-Body Spin Interactions and the Ground State of a Dense Rydberg Lattice Gas.* Phys. Rev. Lett., **106**, 025301.

Lett, P. D., Watts, R. N., Westbrook, C. I., Phillips, W. D., Gould, P. L., and Metcalf, H. J. (1988). *Observation of Atoms Laser Cooled below the Doppler Limit.* Phys. Rev. Lett., **61**, 169.

Levi, E., Minár, J., Garrahan, J. P., and Lesanovsky, I. (2015). *Crystalline structures and frustration in a two-component Rydberg gas.* New Journal of Physics, **17**, 123017.

Li, W., Mourachko, I., Noel, M. W., and Gallagher, T. F. (2003). *Millimeter-wave spectroscopy of cold Rb Rydberg atoms in a magneto-optical trap: Quantum defects of the ns, np, and nd series.* Phys. Rev. A, **67**, 052502.

Lindblad, G. (1976). *On the generators of quantum dynamical semigroups.* Communications in Mathematical Physics, **48**, 119.

Linskens, A. F., Holleman, I., Dam, N., and Reuss, J. (1996). *Two-photon Rabi oscillationsc.* Phys. Rev. A, **54**, 4854.

Lloyd, S. (1996). *Universal Quantum Simulators.* Science, **273**, 1073.

Lochead, G., Boddy, D., Sadler, D. P., Adams, C. S., and Jones, M. P. A. (2013). *Number-resolved imaging of excited-state atoms using a scanning autoionization microscope.* Phys. Rev. A, **87**, 053409.

Löw, R., Raitzsch, U., Heidemann, R., Bendkowsky, V., Butscher, B., Grabowski, A., and Pfau, T. (2007). *Apparatus for excitation and detection of Rydberg atoms in quantum gases.* ArXiv e-prints.

Löw, R., Weimer, H., Krohn, U., Heidemann, R., Bendkowsky, V., Butscher, B., Büchler, H. P., and Pfau, T. (2009). *Universal scaling in a strongly interacting Rydberg gas.* Phys. Rev. A, **80**, 033422.

Löw, R., Weimer, H., Nipper, J., Balewski, J. B., Butscher, B., Büchler, H. P., and Pfau, T. (2012). *An experimental and theoretical guide to strongly interacting Rydberg gases.* Journal of Physics B: Atomic, Molecular and Optical Physics, **45**, 113001.

Lu, J.-T., Goy, A. S., and Fleischer, J. W. (2015). *Nonlinear digital imaging.* arXiv:1507.08601.

Lukin, M. D., Fleischhauer, M., Côté, R., Duan, L. M., Jaksch, D., Cirac, J. I., and Zoller, P. (2001). *Dipole Blockade and Quantum Information Processing in Mesoscopic Atomic Ensembles.* Phys. Rev. Lett., **87**.

Malossi, N., Valado, M. M., Scotto, S., Huillery, P., Pillet, P., Ciampini, D., Arimondo, E., and Morsch, O. (2014). *Full Counting Statistics and Phase Diagram of a Dissipative Rydberg Gas.* Phys. Rev. Lett., **113**, 023006.

Manthey, T., Niederprüm, T., Thomas, O., and Ott, H. (2015). *Dynamically probing ultracold lattice gases via Rydberg molecules.* New Journal of Physics, **17**, 103024.

Marangos, J. P. (1998). *Electromagnetically induced transparency.* J. Mod. Opt., **45**, 471.

Marki, F. and Marki, C. (2010). *Mixer Basics Primer: A Tutorial for RF and Microwave Mixers.* Marki Microwave.

Matthews, M. R., Hall, D. S., Jin, D. S., Ensher, J. R., Wieman, C. E., Cornell, E. A., Dalfovo, F., Minniti, C., and Stringari, S. (1998). *Dynamical Response of a Bose-Einstein Condensate to a Discontinuous Change in Internal State.* Phys. Rev. Lett., **81**, 243.

McQuillen, P., Zhang, X., Strickler, T., Dunning, F. B., and Killian, T. C. (2013). *Imaging the evolution of an ultracold strontium Rydberg gas.* Phys. Rev. A, **87**, 013407.

Merkt, F. and Schmutz, H. (1998). *Very high resolution spectroscopy of high Rydberg states of the argon atom.* The Journal of Chemical Physics, **108**, 10033.

Mohapatra, A. K., Jackson, T. R., and Adams, C. S. (2007). *Coherent Optical Detection of Highly Excited Rydberg States Using Electromagnetically Induced Transparency.* Phys. Rev. Lett., **98**, 113003.

Mohr, P. J., Newell, D. B., and Taylor, B. N. (2016). *CODATA recommended values of the fundamental physical constants: 2014*.* Rev. Mod. Phys., **88**, 035009.

Morinaga, A., Murakami, M., Nakamura, K., and Imai, H. (2016). *Scalar Aharonov–Bohm Phase in Ramsey Atom Interferometry under Time-Varying Potential.* Atoms, **4**.

Morton, J. J. L., Tyryshkin, A. M., Ardavan, A., Porfyrakis, K., Lyon, S. A., and Briggs, G. A. D. (2005). *High Fidelity Single Qubit Operations Using Pulsed Electron Paramagnetic Resonance.* Phys. Rev. Lett., **95**, 200501.

Moses, S. A., Covey, J. P., Miecnikowski, M. T., Yan, B., Gadway, B., Ye, J., and Jin, D. S. (2015). *Creation of a low-entropy quantum gas of polar molecules in an optical lattice.* Science, **350**, 659.

Mourachko, I., Comparat, D., de Tomasi, F., Fioretti, A., Nosbaum, P., Akulin, V., and Pillet, P. (1998). *Many-body effects in a frozen Rydberg gas.* Phys. Rev. Lett., **80**, 253.

Müller, M., Diehl, S., Pupillo, G., and Zoller, P. (2012). *Engineered Open Systems and Quantum Simulations with Atoms and Ions.* In: Paul Berman, E. A. and Lin, C. (Eds.), *Advances in Atomic, Molecular, and Optical Physics*, Vol. Volume 61, , pp. 1–80. Academic Press.

Murray, C. and Pohl, T. (2016). *Quantum and Nonlinear Optics in Strongly Interacting Atomic Ensembles.* Advances In Atomic, Molecular, and Optical Physics, , pp. –. Academic Press.

Naber, J. B., Vos, J., Rengelink, R. J., Nusselder, R. J., and Davtyan, D. (2016). *Optical techniques for Rydberg physics in lattice geometries.* The European Physical Journal Special Topics, **225**, 2785.

Nipper, J., Balewski, J. B., Krupp, A. T., Hofferberth, S., Löw, R., and Pfau, T. (2012). *Atomic Pair-State Interferometer: Controlling and Measuring an Interaction-Induced Phase Shift in Rydberg-Atom Pairs.* Phys. Rev. X, **2**, 031011.

Nogrette, F., Labuhn, H., Ravets, S., Barredo, D., Béguin, L., Vernier, A., Lahaye, T., and Browaeys, A. (2014). *Single-Atom Trapping in Holographic 2D Arrays of Microtraps with Arbitrary Geometries.* Phys. Rev. X, **4**, 021034.

Oelsner, G., Andersen, C. K., Rehák, M., Schmelz, M., Anders, S., Grajcar, M., Hübner, U., Mølmer, K., and Il'ichev, E. (2017). *Detection of Weak Microwave Fields with an Underdamped Josephson Junction.* Phys. Rev. Applied, **7**, 014012.

Olmos, B., Li, W., Hofferberth, S., and Lesanovsky, I. (2011). *Amplifying single impurities immersed in a gas of ultracold atoms.* Phys. Rev. A, **84**, 041607.

Ospelkaus, S., Ni, K.-K., Quéméner, G., Neyenhuis, B., Wang, D., de Miranda, M. H. G., Bohn, J. L., Ye, J., and Jin, D. S. (2010). *Controlling the Hyperfine State of Rovibronic Ground-State Polar Molecules.* Phys. Rev. Lett., **104**, 030402.

Paredes-Barato, D. and Adams, C. S. (2014). *All-Optical Quantum Information Processing Using Rydberg Gates.* Phys. Rev. Lett., **112**, 040501.

Parigi, V., Bimbard, E., Stanojevic, J., Hilliard, A. J., Nogrette, F., Tualle-Brouri, R., Ourjoumtsev, A., and Grangier, P. (2012). *Observation and Measurement of Interaction-Induced Dispersive Optical Nonlinearities in an Ensemble of Cold Rydberg Atoms.* Phys. Rev. Lett., **109**.

Paris-Mandoki, A., Gorniaczyk, H., Tresp, C., Mirgorodskiy, I., and Hofferberth, S. (2016). *Tailoring Rydberg interactions via Förster resonances: state combinations, hopping and angular dependence.* Journal of Physics B: Atomic, Molecular and Optical Physics, **49**, 164001.

Park, H., Tanner, P. J., Claessens, B. J., Shuman, E. S., and Gallagher, T. F. (2011). *Dipole-dipole broadening of Rb ns-np microwave transitions.* Phys. Rev. A, **84**, 022704.

Petrosyan, D., Otterbach, J., and Fleischhauer, M. (2011). *Electromagnetically Induced Transparency with Rydberg Atoms.* Phys. Rev. Lett., **107**, 213601.

Peyronel, T., Firstenberg, O., Liang, Q.-Y., Hofferberth, S., Gorshkov, A. V., Pohl, T., Lukin, M. D., and Vuletić, V. (2012). *Quantum nonlinear optics with single photons enabled by strongly interacting atoms.* Nature, **488**, 57.

Piñeiro Orioli, A., Signoles, A., Wildhagen, H., Günter, G., Berges, J., Whitlock, S., and Weidemüller, M. (2017). *Relaxation of an isolated dipolar-interacting Rydberg quantum spin system.* arXiv:1703.05957.

Pillet, P. and Gallagher, T. F. (2016). *Rydberg atom interactions from 300 K to 300 K.* Journal of Physics B: Atomic, Molecular and Optical Physics, **49**, 174003.

Pla, J. J., Tan, K. Y., Dehollain, J. P., Lim, W. H., Morton, J. J. L., Zwanenburg, F. A., Jamieson, D. N., Dzurak, A. S., and Morello, A. (2013). *High-fidelity readout and control of a nuclear spin qubit in silicon.* Nature, **496**, 334.

Pohl, T., Adams, C. S., and Sadephpour, H. R. (2011). *Cold Rydberg gases and ultra-cold plasmas.* Journal of Physics B: Atomic, Molecular and Optical Physics, **44**, 180201.

Pohl, T., Demler, E., and Lukin, M. D. (2010). *Dynamical Crystallization in the Dipole Blockade of Ultracold Atoms.* Phys. Rev. Lett., **104**, 043002.

Pritchard, Jonathan, D. (2011). *Cooperative Optical Non-linearity in a blockaded Rydberg Ensemble.* PhD thesis, Durham University.

Pritchard, J. D., Gauguet, A., Weatherill, K. J., and Adams, C. S. (2011). *Optical non-linearity in a dynamical Rydberg gas.* Journal of Physics B: Atomic, Molecular and Optical Physics, **44**, 184019.

Pritchard, J. D., Maxwell, D., Gauguet, A., Weatherill, K. J., Jones, M. P. A., and Adams, C. S. (2010). *Cooperative Atom-Light Interaction in a Blockaded Rydberg Ensemble.* Phys. Rev. Lett., **105**, 193603.

Pritchard, J. D., Weatherill, K. J., and Adams, C. S. (2013). *Annual Review of Cold Atoms and Molecules*, Vol. 1, chapter 8 - Nonlinear optics using cold Rydberg atoms, , pp. 301–350. World Scientific.

Raab, E. L., Prentiss, M., Cable, A., Chu, S., and Pritchard, D. E. (1987). *Trapping of Neutral Sodium Atoms with Radiation Pressure.* Phys. Rev. Lett., **59**, 2631.

Ramsey, N. F. (1950). *A Molecular Beam Resonance Method with Separated Oscillating Fields.* Phys. Rev., **78**, 695.

Ramsey, N. F. (1990). *Experiments with Separated Oscillatory Fields and Hydrogen Masers.* Science, **248**, 1612.

Ravets, S., Labuhn, H., Barredo, D., Beguin, L., Lahaye, T., and Browaeys, A. (2014). *Coherent dipole-dipole coupling between two single Rydberg atoms at an electrically-tuned Forster resonance.* Nature Physics, **10**, 914.

Ravets, S., Labuhn, H., Barredo, D., Lahaye, T., and Browaeys, A. (2015). *Measurement of the angular dependence of the dipole-dipole interaction between two individual Rydberg atoms at a Förster resonance.* Phys. Rev. A, **92**, 020701.

Redfield, A. G. (1955). *Nuclear Magnetic Resonance Saturation and Rotary Saturation in Solids.* Phys. Rev., **98**, 1787.

Redfield, A. G. (1957). *On the Theory of Relaxation Processes.* IBM Journal of Research and Development, **1**, 19.

Reetz-Lamour, M., Amthor, T., Deiglmayr, J., and Weidemüller, M. (2008a). *Rabi Oscillations and Excitation Trapping in the Coherent Excitation of a Mesoscopic Frozen Rydberg Gas.* Phys. Rev. Lett., **100**, 253001.

Reetz-Lamour, M., Deiglmayr, J., Amthor, T., and Weidemüller, M. (2008b). *Rabi oscillations between ground and Rydberg states and van der Waals blockade in a mesoscopic frozen Rydberg gas.* New Journal of Physics, **10**, 045026.

Reinaudi, G., Lahaye, T., Wang, Z., and Guéry-Odelin, D. (2007). *Strong saturation absorption imaging of dense clouds of ultracold atoms.* Opt. Lett., **32**, 3143.

Reinhard, A., Liebisch, T. C., Knuffman, B., and Raithel, G. (2007). *Level shifts of rubidium Rydberg states due to binary interactions.* Phys. Rev. A, **75**, 032712.

Reinhard, A., Younge, K. C., and Raithel, G. (2008). *Effect of Förster resonances on the excitation statistics of many-body Rydberg systems.* Phys. Rev. A, **78**, 060702.

Reiter, F. and Sørensen, A. S. (2012). *Effective operator formalism for open quantum systems.* Phys. Rev. A, **85**, 032111.

Rhim, W.-K., Pines, A., and Waugh, J. S. (1971). *Time-Reversal Experiments in Dipolar-Coupled Spin Systems.* Phys. Rev. B, **3**, 684.

Riehle, F. (2004). *Frequency Standards. Basics and Applications.* Wiley-VCH.

Robert-de Saint-Vincent, M., Hofmann, C. S., Schempp, H., Günter, G., Whitlock, S., and Weidemüller, M. (2013). *Spontaneous Avalanche Ionization of a Strongly Blockaded Rydberg Gas.* Phys. Rev. Lett., **110**, 045004.

Robicheaux, F. (2005). *Ionization due to the interaction between two Rydberg atoms.* Journal of Physics B: Atomic, Molecular and Optical Physics, **38**, S333.

Robicheaux, F. and Gill, N. M. (2014). *Effect of random positions for coherent dipole transport.* Phys. Rev. A, **89**, 053429.

Robicheaux, F. and Hernández, J. V. (2005). *Many-body wave function in a dipole blockade configuration.* Phys. Rev. A, **72**, 063403.

Robicheaux, F., Wesdorp, C., and Noordam, L. D. (2000). *Selective field ionization in Li and Rb: Theory and experiment.* Phys. Rev. A, **62**, 043404.

Ryabtsev, I. I. and Tretyakov, D. B. (2001). *Microwave Hanle effect in Rydberg atoms.* Phys. Rev. A, **64**, 033413.

Ryabtsev, I. I., Tretyakov, D. B., and Beterov, I. I. (2005). *Applicability of Rydberg atoms to quantum computers.* Journal of Physics B: Atomic, Molecular and Optical Physics, **38**, 421.

Rydberg, J. R. (1890). *Recherches sur la constitution des spectres d'émission des éléments chimiques.* Kongl. Svenska vetenskaps-akademiens handlingar, **23**.

Saffman, M. (2016). *Quantum computing with atomic qubits and Rydberg interactions: progress and challenges.* Journal of Physics B: Atomic, Molecular and Optical Physics, **49**, 202001.

Saffman, M., Walker, T. G., and Mølmer, K. (2010). *Quantum information with Rydberg atoms.* Rev. Mod. Phys., **82**, 2313.

Schachenmayer, J., Lesanovsky, I., Micheli, A., and Daley, A. J. (2010). *Dynamical crystal creation with polar molecules or Rydberg atoms in optical lattices.* New Journal of Physics, **12**, 103044.

Schauß, P., Cheneau, M., Endres, M., Fukuhara, T., Hild, S., Omran, A., Pohl, T., Gross, C., Kuhr, S., and Bloch, I. (2012). *Observation of spatially ordered structures in a two-dimensional Rydberg gas.* Nature, **491**, 87.

Schauß, P., Zeiher, J., Fukuhara, T., Hild, S., Cheneau, M., Macrì, T., Pohl, T., Bloch, I., and Gross, C. (2015). *Crystallization in Ising quantum magnets.* Science, **347**, 1455.

Schempp, H. (2014). *Formation of Aggregates and Energy Transport in ultracold Rydberg gases.* PhD thesis, Fakultat fur Physik, Ruprecht-Karls-Universität Heidelberg.

Schempp, H., Günter, G., Hofmann, C. S., Giese, C., Saliba, S. D., DePaola, B. D., Amthor, T., Weidemüller, M., Sevinçli, S., and Pohl, T. (2010). *Coherent Population Trapping with Controlled Interparticle Interactions.* Phys. Rev. Lett., **104**, 173602.

Schempp, H., Günter, G., Robert-de Saint-Vincent, M., Hofmann, C. S., Breyel, D., Komnik, A., Schönleber, D. W., Gärttner, M., Evers, J., Whitlock, S., and Weidemüller, M. (2014). *Full Counting Statistics of Laser Excited Rydberg Aggregates in a One-Dimensional Geometry.* Phys. Rev. Lett., **112**, 013002.

Schempp, H., Günter, G., Wüster, S., Weidemüller, M., and Whitlock, S. (2015). *Correlated Exciton Transport in Rydberg-Dressed-Atom Spin Chains.* Phys. Rev. Lett., **115**, 093002.

Schlagmüller, M., Liebisch, T. C., Engel, F., Kleinbach, K. S., Böttcher, F., Hermann, U., Westphal, K. M., Gaj, A., Löw, R., Hofferberth, S., Pfau, T., Pérez-Ríos, J., and Greene, C. H. (2016). *Ultracold Chemical Reactions of a Single Rydberg Atom in a Dense Gas.* Phys. Rev. X, **6**, 031020.

Schmidt, P. O., Rosenband, T., Langer, C., Itano, W. M., Bergquist, J. C., and Wineland, D. J. (2005). *Spectroscopy Using Quantum Logic.* Science, **309**, 749.

Schönleber, D. W., Eisfeld, A., Genkin, M., Whitlock, S., and Wüster, S. (2015). *Quantum Simulation of Energy Transport with Embedded Rydberg Aggregates.* Phys. Rev. Lett., **114**, 123005.

Schoser, J., Batär, A., Löw, R., Schweikhard, V., Grabowski, A., Ovchinnikov, Y. B., and Pfau, T. (2002). *Intense source of cold Rb atoms from a pure two-dimensional magneto-optical trap.* Phys. Rev. A, **66**, 023410.

Schwarzkopf, A., Anderson, D. A., Thaicharoen, N., and Raithel, G. (2013). *Spatial correlations between Rydberg atoms in an optical dipole trap.* Phys. Rev. A, **88**, 061406.

Schwarzkopf, A., Sapiro, R. E., and Raithel, G. (2011). *Imaging Spatial Correlations of Rydberg Excitations in Cold Atom Clouds.* Phys. Rev. Lett., **107**, 103001.

Seaton, M. J. (1983). *Quantum defect theory.* Reports on Progress in Physics, **46**, 167.

Sedlacek, J. A., Schwettmann, A., Kübler, H., Löw, R., Pfau, T., and Shaffer, J. P. (2012). *Microwave electrometry with Rydberg atoms in a vapour cell using bright atomic resonances.* Nature Physics, **8**, 819.

Sevinçli, S., Ates, C., Pohl, T., Schempp, H., Hofmann, C. S., Günter, G., Amthor, T., Weidemüller, M., Pritchard, J. D., Maxwell, D., Gauguet, A., Weatherill, K. J., Jones, M. P. A., and Adams, C. S. (2011). *Quantum interference in interacting three-level Rydberg gases: coherent population trapping and electromagnetically induced transparency.* Journal of Physics B: Atomic, Molecular and Optical Physics, **44**, 184018.

Sibalić, N., Pritchard, J., Adams, C., and Weatherill, K. (2017). *ARC: An open-source library for calculating properties of alkali Rydberg atoms.* Computer Physics Communications, **220**, 319 .

Simon, J., Bakr, W. S., Ma, R., Tai, M. E., Preiss, P. M., and Greiner, M. (2011). *Quantum simulation of antiferromagnetic spin chains in an optical lattice.* Nature, **472**, 307.

Singer, K., Reetz-Lamour, M., Amthor, T., Marcassa, L. G., and Weidemüller, M. (2004). *Suppression of Excitation and Spectral Broadening Induced by Interactions in a Cold Gas of Rydberg Atoms.* Phys. Rev. Lett., **93**, 163001.

Sobelman, I. I. (1979). *Atomic Spectra and Radiative Transitions.* Springer-Verlag.

Solomon, I. (1959). *Rotary Spin Echoes.* Phys. Rev. Lett., **2**, 301.

Somaroo, S., Tseng, C. H., Havel, T. F., Laflamme, R., and Cory, D. G. (1999). *Quantum Simulations on a Quantum Computer.* Phys. Rev. Lett., **82**, 5381.

Souza, A. M., Sarthour, R. S., Oliveira, I. S., and Suter, D. (2015). *High-fidelity gate operations for quantum computing beyond dephasing time limits.* Phys. Rev. A, **92**, 062332.

Stebbings, R. F. and Dunning, F. B. (1983). *Rydberg States of Atoms and Molecules.* Cambridge University Press.

Steck, D. A. (2007). *Quantum and Atom Optics.* revision 0.12.0, 16 May 2017.

Steer, M. (2009). *Microwave and RF Design - A Systems Approach.* Scitech publishing, Inc.

Struck, J., Ölschläger, C., Le Targat, R., Soltan-Panahi, P., Eckardt, A., Lewenstein, M., Windpassinger, P., and Sengstock, K. (2011). *Quantum Simulation of Frustrated Classical Magnetism in Triangular Optical Lattices.* Science, **333**, 996.

Teixeira, R. C., Hermann-Avigliano, C., Nguyen, T. L., Cantat-Moltrecht, T., Raimond, J. M., Haroche, S., Gleyzes, S., and Brune, M. (2015). *Microwaves Probe Dipole Blockade and van der Waals Forces in a Cold Rydberg Gas.* Phys. Rev. Lett., **115**, 013001.

Thaicharoen, N., Schwarzkopf, A., and Raithel, G. (2015). *Measurement of the van der Waals interaction by atom trajectory imaging.* Phys. Rev. A, **92**, 040701.

Tiarks, D., Baur, S., Schneider, K., Dürr, S., and Rempe, G. (2014). *Single-Photon Transistor Using a Förster Resonance.* Phys. Rev. Lett., **113**, 053602.

Tong, D., Farooqi, S. M., Stanojevic, J., Krishnan, S., Zhang, Y. P., Côté, R., Eyler, E. E., and Gould, P. L. (2004). *Local Blockade of Rydberg Excitation in an Ultracold Gas.* Phys. Rev. Lett., **93**, 063001.

Tresp, C., Bienias, P., Weber, S., Gorniaczyk, H., Mirgorodskiy, I., Büchler, H. P., and Hofferberth, S. (2015). *Dipolar Dephasing of Rydberg D-State Polaritons.* Phys. Rev. Lett., **115**, 083602.

Treutlein, P., Hommelhoff, P., Steinmetz, T., Hänsch, T. W., and Reichel, J. (2004). *Coherence in Microchip Traps.* Phys. Rev. Lett., **92**, 203005.

Tsai, T. and Morse, T. F. (1979). *Rate Equations for a Three-Level System.* IEEE Journal of Quantum Electronics, **15**, 1334 .

Urban, E., Johnson, T. A., Henage, T., Isenhower, L., Yavuz, D. D., Walker, T. G., and Saffman, M. (2009). *Observation of Rydberg blockade between two atoms.* Nature Physics, **5**, 110.

Urvoy, A., Ripka, F., Lesanovsky, I., Booth, D., Shaffer, J. P., Pfau, T., and Löw, R. (2015). *Strongly Correlated Growth of Rydberg Aggregates in a Vapor Cell.* Phys. Rev. Lett., **114**, 203002.

Valado, M. M., Malossi, N., Scotto, S., Ciampini, D., Arimondo, E., and Morsch, O. (2013). *Rydberg tomography of an ultracold atomic cloud.* Phys. Rev. A, **88**, 045401.

Valado, M. M., Simonelli, C., Hoogerland, M. D., Lesanovsky, I., Garrahan, J. P., Arimondo, E., Ciampini, D., and Morsch, O. (2016). *Experimental observation of controllable kinetic constraints in a cold atomic gas.* Phys. Rev. A, **93**, 040701.

van Bijnen, R. (2013). *Quantum Engineering with Ultracold Atoms.* PhD thesis, Eindhoven University of Technology.

van Bijnen, R. M. W. and Pohl, T. (2015). *Quantum Magnetism and Topological Ordering via Rydberg Dressing near Förster Resonances.* Phys. Rev. Lett., **114**, 243002.

Vandersypen, L. M. K. and Chuang, I. L. (2005). *NMR techniques for quantum control and computation.* Rev. Mod. Phys., **76**, 1037.

Vanhaecke, N., Comparat, D., Tate, D. A., and Pillet, P. (2005). *Ionization of Rydberg atoms embedded in an ultracold plasma.* Phys. Rev. A, **71**, 013416.

Vermersch, B., Ramos, T., Hauke, P., and Zoller, P. (2016). *Implementation of chiral quantum optics with Rydberg and trapped-ion setups.* Phys. Rev. A, **93**, 063830.

Viteau, M., Huillery, P., Bason, M. G., Malossi, N., Ciampini, D., Morsch, O., Arimondo, E., Comparat, D., and Pillet, P. (2012). *Cooperative Excitation and Many-Body Interactions in a Cold Rydberg Gas.* Phys. Rev. Lett., **109**, 053002.

Viteau, M., Radogostowicz, J., Bason, M. G., Malossi, N., Ciampini, D., Morsch, O., and Arimondo, E. (2011). *Rydberg spectroscopy of a Rb MOT in the presence of applied or ion created electric fields.* Opt. Express, **19**, 6007.

Vogt, T., Viteau, M., Chotia, A., Zhao, J., Comparat, D., and Pillet, P. (2007). *Electric-Field Induced Dipole Blockade with Rydberg Atoms.* Phys. Rev. Lett., **99**, 073002.

Vogt, T., Viteau, M., Zhao, J., Chotia, A., Comparat, D., and Pillet, P. (2006). *Dipole Blockade at Förster Resonances in High Resolution Laser Excitation of Rydberg States of Cesium Atoms.* Phys. Rev. Lett., **97**, 083003.

Vrinceanu, D., Sadeghpour, H. R., and Pohl, T. (2009). *Rydberg atom formation in ultracold plasmas: Non-equilibrium dynamics of recombination.* Journal of Physics: Conference Series, **194**, 012067.

Walker, T. G. and Saffman, M. (2008). *Consequences of Zeeman degeneracy for the van der Waals blockade between Rydberg atoms.* Phys. Rev. A, **77**, 032723.

Wangsness, R. K. and Bloch, F. (1953). *The Dynamical Theory of Nuclear Induction.* Phys. Rev., **89**, 728.

Weber, T. M., Honing, M., Niederprum, T., Manthey, T., Thomas, O., Guarrera, V., Fleischhauer, M., Barontini, G., and Ott, H. (2015). *Mesoscopic Rydberg-blockaded ensembles in the superatom regime and beyond.* Nature Physics, **11**, 157.

Weimer, H., Löw, R., Pfau, T., and Büchler, H. P. (2008). *Quantum Critical Behavior in Strongly Interacting Rydberg Gases.* Phys. Rev. Lett., **101**, 250601.

Weimer, H., Müller, M., Lesanovsky, I., Zoller, P., and Büchler, H. P. (2010). *A Rydberg quantum simulator.* Nature Physics, **6**, 382.

Weissbluth, M. (1978). *Atoms and Molecules.* Academic Press.

Westermann, S., Amthor, T., de Oliveira, A. L., Deiglmayr, J., Reetz-Lamour, M., and Weidemüller, M. (2006). *Dynamics of resonant energy transfer in a cold Rydberg gas.* Eur. Phys. J. D, **40**, 37.

Whitlock, S., Glaetzle, A. W., and Hannaford, P. (2017). *Simulating quantum spin models using Rydberg-excited atomic ensembles in magnetic microtrap arrays.* Journal of Physics B: Atomic, Molecular and Optical Physics, **50**, 074001.

Whitlock, S., Ockeloen, C. F., and Spreeuw, R. J. C. (2010). *Sub-Poissonian Atom-Number Fluctuations by Three-Body Loss in Mesoscopic Ensembles.* Phys. Rev. Lett., **104**, 120402.

Windpassinger, P. J., Oblak, D., Petrov, P. G., Kubasik, M., Saffman, M., Alzar, C. L. G., Appel, J., Müller, J. H., Kjærgaard, N., and Polzik, E. S. (2008). *Nondestructive Probing of Rabi Oscillations on the Cesium Clock Transition near the Standard Quantum Limit.* Phys. Rev. Lett., **100**, 103601.

Wineland, D. J., Drullinger, R. E., and Walls, F. L. (1978). *Radiation-Pressure Cooling of Bound Resonant Absorbers.* Phys. Rev. Lett., **40**, 1639.

Yan, B., Moses, S. A., Gadway, B., Covey, J. P., Hazzard, K. R. A., Rey, A. M., Jin, D. S., and Ye, J. (2013). *Observation of dipolar spin-exchange interactions with lattice-confined polar molecules.* Nature, **501**, 521.

Yang, C. and Yang, C. (1966). *One-dimensional chain of anisotropic spin-spin interactions.* Physics Letters, **20**, 9 .

Yu, H. and Robicheaux, F. (2016). *Coherent dipole transport in a small grid of Rydberg atoms.* Phys. Rev. A, **93**, 023618.

Zhang, H., Zhang, L., Wang, L., Bao, S., Zhao, J., Jia, S., and Raithel, G. (2014a). *Autler-Townes spectroscopy with interaction-induced dephasing.* Phys. Rev. A, **90**, 043849.

Zhang, J., Hess, P. W., Kyprianidis, A., Becker, P., Lee, A., Smith, J., Pagano, G., Potirniche, I.-D., Potter, A. C., Vishwanath, A., Yao, N. Y., and Monroe, C. (2017). *Observation of a discrete time crystal.* Nature, **543**, 217.

Zhang, J., Souza, A. M., Brandao, F. D., and Suter, D. (2014b). *Protected Quantum Computing: Interleaving Gate Operations with Dynamical Decoupling Sequences.* Phys. Rev. Lett., **112**, 050502.

Zizak, G., Bradshaw, J. D., and Winefordner, J. D. (1980). *Rate equation solution for the temporal behavior of a three-level system.* Appl. Opt., **19**, 3631.

List of Figures

List of Tables

Acknowledgements

Last but not least, I want to express my gratitude to all the people that shared this path with me and also contributed to this work or provided the indispensable encouragement to complete this stage of my life. Without your support, this would not have been possible.

My deepest thankfulness to my supervisor **Prof. Dr. Matthias Weidemüller** for taking me into your research group and giving me this great opportunity. I sincerely appreciate your honest words since our first conversation until the end of this thesis. All the ITN-COHERENCE events provided me an excellent platform to develop myself and acquire a broader perspective of science. Working in such a competitive experiment gave me an experience that I will carry with me as a treasure.

I am grateful to **Prof. Dr. Selim Jochim** for accepting to be this work's second referee and for your modest and friendly advice. Thank you also for taking part in my examination. On that regard, I also appreciate the participation of **Dr. Tilman Enss** and **Dr. Jörg Evers**, who kindly agreed to evaluate my doctoral defence.

I highly appreciate the contributions of **Adrien Signoles** to our different projects. Your guidance, pragmatic vision to solve problems and our countless discussions strengthened my physical insight and confidence to succeed in this trip. Thank you for all the funny moments... et pour la musique française!

Thanks to **Gerhard Zürn** for transferring a fraction of your incredible technical knowledge to all fellows in the Rydberg team. Learning about lasers, locking schemes, electronics, optical design, microcontrollers, etc. would have been much harder without your input and your quick answer of every question.

Thank you very much to **Shannon Whitlock** for your very kind welcome and your background support, which allowed me to grow as a researcher. I specially appreciate your wise advice to learn the German language and your tricky "kicker" playing style. I wish you much success as a Professor in Strasbourg.

I cannot acknowledge enough my great friend **Vladislav Gavryusev** with simple words of gratitude. The enormous number of anecdotes we share and the presence and help in each other's good and bad moments speak for itself. I appreciate so much your systematic approach to programming and data analysis and your detailed explanations of any tiny detail, the fun in the lab and your salsa parties outside! Our paths will cross many more times in the future. All the best for you and Elisa!

Obrigado também para **Renato Ferracini Alves** por trazer uma nova orientação para o desenvolvimento de projetos. A sua habilidade para operar em Python e realizar simulações foi uma grande ajuda para todos. Você vai ter um bom doutoramento com certeza.

I very much appreciate **Andre Salzinger** to have joined the Rydberg team. Your empathy and shrewd sense of humour kept me always ready for a telepathic moment of fun that nobody else was understanding. I hope that you keep enjoying yourself over the group meetings ;).

It was a pleasure for me to work with **Sebastian Geier**, to guide you and to supervise your successful Bachelor thesis' project. I am also happy to have cooperated with **Titus Franz** and that you decided to join the Rydberg team. It is great that my teaching skills during your opto-electronics "Praktikum" did not convince you to become a theorist ;). I wish all the best for both of you in your bright future.

Good luck to **Henrik Zahn** for continuing my project with a fresh look and thanks for reminding me of my good old times as a musician. I wish you the best with the master thesis and your French horn interpretations of Brahms and Tschaikovski.

Thank you to **Annika Tebben**, **Armin Kekić**, **Giulia Faraoni**, **Thomas Kerst**, **Philip Fabritius**, **Ingo Nosske**, **Luc Couturier**, **Yu Lu**, **Fachao Hu** and **Chang Qiao** for the time we spent in the Rydberg team. I have plenty of anecdotes involving all of you.

Thanks to **Hanna Wildhagen**, **Georg Günter** and **Christoph Hofmann**, from whom we have inherited an amazing experiment. I am also grateful to **Martin Robert-de-Saint-Vincent** for presenting me the research that had been developed in the Rydberg experiment in the past years and for your always friendy attention.

I am so pleased to have developed a good friendship with **Puneet Murthy**. Your unquestionable integrity as a person and a scientist set a wonderful example for me and showed me the way to face the difficulties of this adventure. I will keep in mind our times at the "FP-Optik" renovation, your wise advice and your attempts to scare me out in the corridor.

I will miss **Valentin Ivannikov**, **Mark Repp**, **Rico Pires**, **Juris Ulmanis**, **Eva Kuhnle**, **Stephan Häfner**, **Binh Tram**, **Manuel Gerken**, **Bing Zhu**, **Stephan Helmrich**, **Tobias Wintermantel**, **Bastian Höltkemeier** and **Jonas Tauch** and all the undergraduate students for the time together in the Quantum Dynamics group. Especialmente agradecido estoy a **Alda L. Arias Suárez** y **Henry López Carrera** por el tiempo personal que pasamos fuera del trabajo.

My sincere appreciation for **Claudia Krämer**, **Danica Subally-Haupt**, **Ralf Ziegler**, **Dominic Litsch** due to the friendy and efficient support that you give to all researchers in the group. Y por supuesto, gracias a **Esteban Rubio** por las visitas espontáneas para tomar café y charlar.

Graciñas a **María M. Valado** polo exemplo, apoio e por entenderes perfectamente a miña situación profesional e persoal ao teres vivido unha similar. A túa estadía no grupo foi auga fresca para nós. Acabaremos o "DJ Rydberg project" cando nos atopemos por casualidade en calquera rúa d'A Ponte ou noutro país do mundo.

Mi enorme agradecimiento a **María Jesús** por el ánimo en las dificultades y los momentos buenos pasados. Espero que seas, sobre todo, muy feliz en Harvard.

Graciñas **Antonio** pola benvida e acollida dada ao chegar a Heidelberg. A lista de recordos é grande... e aínda máis as ganas de chegar á liña de meta. Ánimo!

I also want to express my fondness for **all my friends**, from Heidelberg and from Galicia, who have always dedicated part of their time to catch up with each other, have some good moments of mutual understanding. For those, thank you very much!

Bei meinen **Mitbewohner/innen** möchte ich mich für das gemeinsame Leben zusammen und eure Geduld während dieser vier Jahre bedanken. Mein besonderer Dank gilt **Clara** für deine große Freundlichkeit, Interesse und Sorge für die anderen. Ohne euch wäre es auch fast unmöglich, mein Deutsch zu verbessern!

A **Santi** e **Román** polas vosas visitas e por facerdes plans cada vez que vou para a casa, polas malleiras na bici, as patadas detrás dunha bóla e por serdes das únicas amizades que teña recordos de neno, adulto e, con sorte, de vello.

Grazas á miña **familia**, aos meus **padriños** pola vosa permanente axuda e interese e, especialmente, aos meus **pais** e á miña irmá **Olalla**, por estardes pendentes e facerdes sacrificios continuos para que teñamos as mellores oportunidades, sabendo estar ao carón a pesar da distancia.

Por último, quérome acordar dos **avós** da Madanela, que marcharon antes de poderen ver este camiño realizado e que sempre tiveron fe nos seus netos.